Influence of Wake Vortices Induced by Elliptic Cylinder on Flat-Plate Boundary Layer

by

Sanchita Amin

Submitted in partial fulfillment of the requirements for the degree of

MASTER OF SCIENCE IN MECHANICAL ENGINEERING

DEPARTMENT OF MECHANICAL ENGINEERING
BANGLADESH UNIVERSITY OF ENGINEERING AND TECHNOLOGY
Dhaka, Bangladesh.

June 2011

The thesis titled "**Influence of Wake Vortices Induced by Elliptic Cylinder on Flat-plate Boundary Layer**", submitted by **Sanchita Amin, Roll no**: **100510003P** Session October, 2005 has been accepted as satisfactory in partial fulfillment of the requirements for the degree of MASTER OF SCIENCE IN MECHANICAL ENGINEERING on June 21, 2011.

BOARD OF EXAMINERS

1. _____ Chairman
Dr. Dipak Kanti Das
Professor
Department of Mechanical Engineering
Bangladesh University of Engineering and Technology (BUET)
Dhaka, Bangladesh.

2. _____ Member
Dr. Md. Quamrul Islam
Professor
Department of Mechanical Engineering
Bangladesh University of Engineering and Technology (BUET)
Dhaka, Bangladesh.

3. _____ Member
Dr. Md. Mahabubul Alam (Ex-officio)
Professor and Head
Department of Mechanical Engineering
Bangladesh University of Engineering and Technology (BUET)
Dhaka, Bangladesh.

4. _____ External
Dr. M. A. Taher Ali
Professor
House-21/A, Road-3, DRA,
Dhaka.

CANDIDATE'S DECLERATION

It is hereby declared that this thesis or any part of it has not been submitted elsewhere for the award of any degree or diploma.

_____

Author

Sanchita Amin

CERTIFICATE OF RESEARCH

This is to certify that the work presented in this Thesis is carried out by the author under the supervision of **Dr. Dipak Kanti Das**, **Professor of Department of Mechanical Engineering**, Bangladesh University of Engineering and Technology (BUET), Dhaka, Bangladesh.

_____ _____

Dr. Dipak Kanti Das **Sanchita Amin**

Dedicated To
My Son

CONTENTS

NOMENCLATURE

a	Semi-major axis length of the elliptic cylinder (m)
b	Semi-minor axis length of the elliptic cylinder (m)
c	Focal distance of the ellipse (m)
C_{fav}	Average skin friction co-efficient
C_{frms}	Root-mean-square skin friction co-efficient
C_{fx}	Skin friction Co-efficient on different on plate axial location
H	Shape factor (δ/θ)
H_{av}	Average shape factor
H_{rms}	Root mean square shape factor
Re_{2c}	Reynolds number based on cylinder distance between the foci, $\rho U(2c)/\mu$
Re_x	Local Reynolds number based on plate axial distance, $\rho ux/\mu$
t	Time (s)
U	Free stream velocity (m/s)
u	x-velocity component (m/s)
v	y-velocity component (m/s)
X	Dimensional Co-ordinate(m)
Y	Dimensional Co-ordinate(m)
x_c	Cylinder axial location from plate leading edge, (m)
y_c	Cylinder vertical location from plate leading edge, (m)
x_p	Plate streamwise location from plate leading edge, (m)
τ	Global Dimensionless time, Ut/c
α	Angle of attack of the elliptic cylinder (^{0}, deg)
δ	Displacement thickness (mm)
θ	Momentum thickness (mm)
ρ	Fluid density (kg/m^3)
μ	Kinematic viscosity of air ($N.s/m^2$)

ACKNOWLEDGEMENT

I would like to express my sincerest gratitude and appreciation to my supervisor Dr. Dipak Kanti Das, Professor, Department of Mechanical Engineering, Bangladesh University of Engineering & Technology (BUET) for his encouragement and careful supervision throughout this research work. Without his substantial as well as sustained efforts this research would not have emerged.

Sincere thanks go to my brother for his co-operation to provide me high configuration computer. I am also very much indebted to my parents, my sister and my husband for their continuous support during the period of my research works.

Special thanks also go to all my colleagues and friends.

At last and upon all, I must say, I am very much grateful to my GOD.

ABSTRACT

The present numerical study has been conducted to investigate the unsteady boundary layer characteristics over a flat plate under the influence of wake vortices induced from an elliptic cylinder positioned in the free stream by numerical computations. This flow situation is an idealization of that occurring on turbomachinery blades where unsteady wakes are generated by the preceding row of blades. The major-minor axis ratio of the elliptic cylinder is taken 0.6 and the angle of attack 0^0 positioning the cylinder at different locations from the plate. The investigation covers a Reynolds number range up to 1000 based on the focal distance of the elliptic cylinder and undisturbed free stream velocity. The Reynolds numbers are relatively low so that in the limiting case of a boundary layer undisturbed by wakes this remained laminar over the full length of the test plate. The time dependent, two dimensional flow is simulated numerically using finite element formulation. Quadratic triangular elements and discontinuous linear triangular elements are used for velocity and pressure interpolation respectively. A finite element package COMSOL Multiphysics is used for the present computation. The development of the flow field up to certain time period is considered. Instantaneous streamlines of the disturbed flow field, instantaneous velocity field, instantaneous boundary layer integral parameters, and skin friction on different plate streamwise locations are presented for all the cases. The wake vortices strongly affect the boundary layer compared to undisturbed flow over flat plate. From the above results, two types of interaction can be obtained, one is the strong wake-boundary layer interaction and another is the weak wake-boundary layer interaction depending on the cylinder to plate relative position. Comparisons are also carried out for circular cylinder having the same height of the elliptic cylinder cross-section, for a particular cylinder to plate relative position and Reynolds number.

CHAPTER 1

INTRODUCTION

Unsteady boundary layers are encountered in many engineering applications, and they are often transitional, especially in turbomachines and aeronautics, where the boundary layer transition originates from boundary layer interaction with transverse and longitudinal vortices. In turbines and compressors, the relative motion of adjacent blade rows gives rise to a variety of unsteady flow interactions. The blades in any moving blade row are continually passing through the individual wakes of the upstream blade rows. Similarly, the blades in the fixed blade rows are being struck by the wakes of the upstream moving blades. The wakes exhibit a defect in mean velocity and a superimposed high level of turbulence intensity. These conditions have a significant influence upon boundary layer transition process. The boundary layer, laminar or turbulent, strongly influences skin friction, and therefore, drag losses. Also the transition region of boundary layer affects the machine performance, the flow losses and especially the heat transfer to turbine blades. Hence, good understanding of the unsteady boundary layer behavior is important for improving the design of turbomachines.

Bluff body wakes are complex; they involve the interactions of three shear layers in the same problem, namely a boundary layer, a separating shear layer, and a wake. Considering figure 1.1, wake formation can be explained as that when flowing fluid touches the nose A of the airfoil, the flow stagnates. Between point A and B (ahead

Figure 1.1a: Flow around the airfoil.

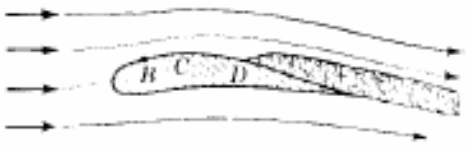

Figure 1.1b: Separation on the airfoil.

of the position of the maximum thickness C), there is a continual increase of the main- stream velocity just outside the boundary layer. Beyond point B, there is a continual decrease in the main-stream velocity so that the maximum velocity just outside the boundary layer occurs at the point B. According to Bernoulli's equation, pressure must decrease from close to the stagnation pressure at A to a minimum pressure at B and must then increase again beyond point B. Thus the boundary layer beyond B feels a pressure which is increasing in the direction of flow, and such a pressure variation is known as *adverse pressure gradient*. But since the fluid in the boundary layer has small kinetic energy, it may possibly reach a condition of stopping and reversing its direction and thus cause the boundary layer to deflect away from the boundary. This is the *onset of separation*. There may then take place a considerable readjustment of the flow, where separation having started downstream of D, results in a thick region irregular flow named as Wake.

Figure 1.2 shows a schematic diagram of the rotor-stator wake interaction which is commonly available in most of the multi-stage turbomachines.

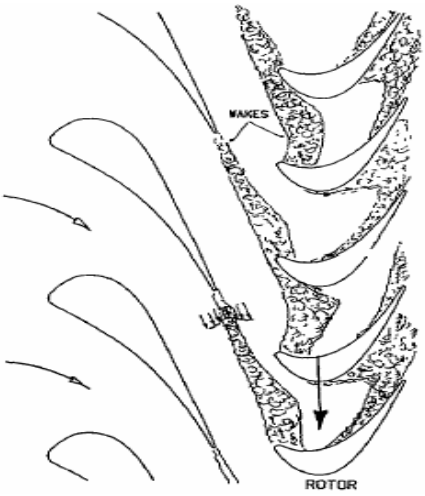

Figure 1.2: Schematic diagram of rotor-stator wake interaction in Turbomachinery [46].

In recent years gas turbine engine aerodynamicists have focused their attention on improving the efficiency and performance of the low pressure turbine (LPT) components. Normally, the LPT experiences a variation in Reynolds number ranging

from 50,000 to 250,000 depending on operational conditions. Since the major portion of the boundary layer, particularly along the suction surface, is laminar, the low Reynolds number in conjunction with the local adverse pressure gradient makes it susceptible to flow separation, thus increasing the complexity of the LPT- boundary layer aerodynamics. The periodic unsteady nature of the incoming flow associated with wakes substantially influences the boundary layer development including the onset and extent of the laminar separation and its turbulent re-attachment. The phenomenon of the unsteady boundary layer development and transition in the absence of separation zones has been the subject of intensive research that has led to better understanding of the transition phenomenon on the LPT-boundary layer.

In aeronautics, wake vortices are formed any time an aerofoil is producing lift. Lift is generated by the creation of a pressure differential over the wing surfaces. The lowest pressure occurs over the upper surface of the wing, and the highest pressure is formed under the wing. Air always wants to move towards the area of lower pressure. This causes it to move outwards under the wing towards the wingtip curl up and over the upper surface of the wing. This starts the wake vortex. The same pressure differential also causes air to move inwards over the wing. Small trailing edge vortices, formed by outward and inward moving streams of air meeting at the trailing edge, move outwards to the wingtip and join the large wingtip vortex.

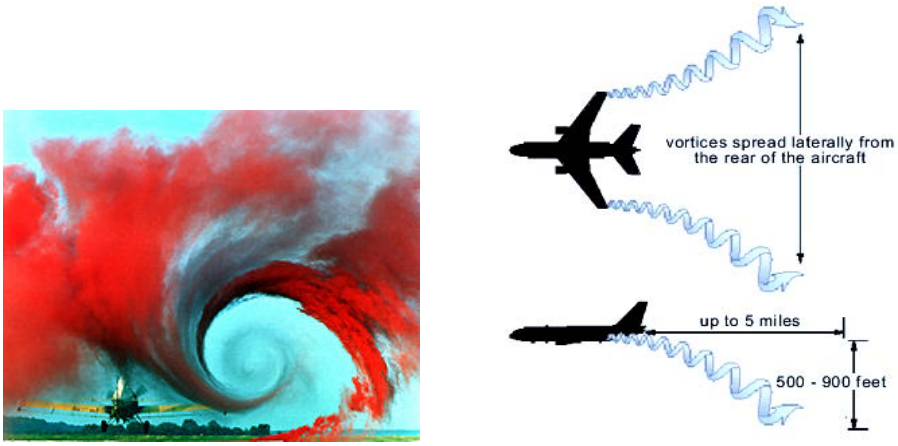

Figure 1.3: Viewed from behind the generating aircraft, the left vortex rotates clockwise and the right vortex rotates counter-clockwise [47].

Viewed from behind the left vortex rotates clockwise and the right vortex rotates counter- clockwise. They spread laterally away from the aircraft and descend 500 to 900 feet at distances of up to five miles behind it. The intensity or strength of the vortex is primarily a function of aircraft weight, wingspan and configuration (flap setting, etc). During an aircraft's critical landing phase wake vortices can endanger following aircraft. To avoid wake vortex encounters, follower aircraft must maintain a safe distance to a landing aircraft up ahead of them. With increased traffic growth and design of new high capacity aircraft, problems related to wake vortices are becoming more and more important. In order to increase airport capacities whilst at least maintaining safety levels, the knowledge of the wake vortex behavior under varying meteorological conditions achieves considerable significance over the last three decades throughout the world.

In order to understanding and provide data for verifying and improving prediction methods of so far described physical engineering problems, the present paper reports on a basic numerical study on the simplified situation of boundary layers exposed to periodic wakes induced by an elliptic cylinder passing over the plate.

1.1 MOTIVATION OF THE PRESENT RESEARCH WORK

The unsteady flow past a bluff body has received significant attention because it represents one of the most common problems in fluid structure interaction (FSI). Flow around bluff bodies such as cables, chimneys, or airfoils are generally unsteady and periodic in nature. Especially, the wake behind a circular cylinder has been studied numerically and experimentally by many investigators due to its periodic vortex shedding and simple geometry. In addition, noncircular cylinders such as elliptic and rectangular cylinders are sometimes preferred, rather than the circular cylinder, for special applications. For example, the drag coefficient of elliptic cylinders at a small angle of attack is much smaller than that of a circular cylinder in aerodynamic applications. The heat transfer coefficient of elliptic cylinders was also found to be nearly equal to or a little higher than that of a circular cylinder by Ota *et*

al. [1], [2]. Furthermore, elliptic cylinders have the general fluid dynamic features between those of a circular cylinder (Aspect Ratio, AR = 1) and a flat plate (AR $=\infty$). Hence, elliptic cylinder has wide engineering applications and can be used as an effective passive tool to control the flow nearby.

The initial development of unsteady two-dimensional uniform flow past impulsively (suddenly) started inclined elliptic cylinder was investigated by Wang [3], Dennis and Staniforth [4], Staniforth [5] and Panniker and Lavan [6]. All of these studies were carried out at high but finite values of the Reynolds number, except for Panniker and Lavan [6] in which the initial flow was investigated at a Reynolds number of 200.

Numerical solutions of laminar flow past elliptic cylinders at various angles of attack were obtained by Lugt and Haussling [7], who studied the problem of flow development past an abruptly accelerated elliptic cylinder at 45° incidence in the range of Reynolds numbers from 15 to 200. Modi &Wiland [8] and Modi & Dikshit [9, 10] studied experimentally that the flow characteristics of the wake behind elliptic cylinders located in a uniform flow are changed considerably depending on the angle of attack and the axis ratio (AR) of the cylinder. Badr, Dennis and Kocabiyik [11] solved numerically the problem of uniform flow past an impulsively started inclined elliptic cylinder for Reynolds numbers ranging from 900 to 5000 and for the range of angle of attack between 0 and 90°. The results reveal an unusual phenomenon of negative lift occurring shortly after the start of motion depending upon the value of the angle of inclination and is consistent with the experimental findings of Taneda [12, 13].

In many wall-bounded flows of engineering interest, it is often desirable to delay the onset of laminar-turbulent transition in order to reduce the skin friction drag on the surface. In aeronautical applications, drag reduction via laminar flow control is primarily relevant to the cruise configuration. Typical high-lift configurations used in commercial subsonic transports involve multi-element airfoils consisting of a leading edge slat and a trailing edge flap in addition to the wing. Flight tests suggest that

high-lift flow fields may involve large regions of laminar flow. Due to intricate coupling between transition and flow separation in such flows, accurate prediction of transition inset is crucial to the design of high-lift devices. While transition scenarios on a single airfoil have been studied in great detail, boundary layer transition due to disturbances generated by upstream geometry, as in the multi-element airfoil, has received less scrutiny.

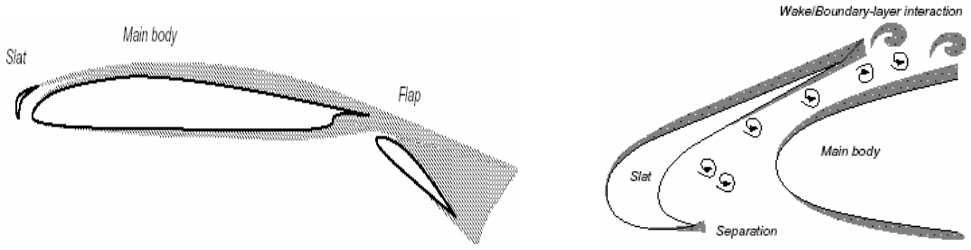

Figure 1.4: Sketch of the wake/boundary interactions on a multi-element airfoil [48].

Effects of wake/blade interaction phenomenon in turbomachines have been studied mostly from the view point of blade vibration or noise generation. Recently, they have attracted a great amount of attention from various researchers because it has become known that the wake/blade interaction affects the stage efficiency and increase the heat load on the blade much more than was expected from steady flow analysis. Hence a number of relevant studies have been carried out up to date. The existence of disturbed laminar, transitional and turbulent flow on a turbine blade had been demonstrated by Addison and Hudson [14]**.** A detailed experimental study on the behavior of the separated zone on the suction surface of a highly loaded LPT-blade under periodic unsteady wake flow was presented by Schobeiri et al. [15]. Similar problem of turbomachinery were conducted numerically by Volkov and Tau [16]. For the control and prediction of the effect of vortex generation from aircraft near a ground was studied by Lee and Gerontakos [17], Holzäpfel et al. [18], Corjon and Poinsot [19] etc.

Boundary layer disturbances by the interaction of wake vortices from circular cylinder is an interesting field of research. A study had been made of the process of laminar to turbulent transition induced by a von Karman vortex street, in the boundary layer on a flat plate by Kyriakides et al. [20]**.** From the experimental observations they developed a correlation which can predict the onset of transition under strong wake-boundary layer interaction. Choi and Lee [21] experimentally investigated the flow characteristics around an elliptic cylinder with an axis ration of AR=2 located near a flat plate. Investigations of boundary layer transition in undistributed flow and in flow periodically disturbed by wakes were carried out by Orth [22], Wu and Durbin [23], Wu et al. [24] etc. over the years.

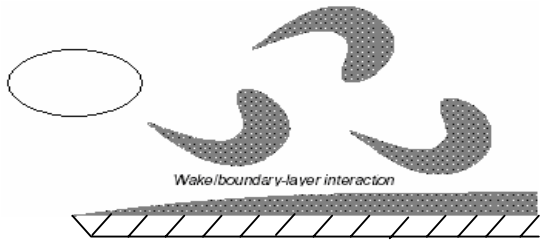

Figure 1.5: Interaction in a simplified geometry

In the current research, numerical simulations have been performed to study the interaction between the unsteady wake of an upstream element and the boundary layer over a downstream element. To study such flows in a simpler setting, a model problem is considered, illustrated in figure 1.5, which consists of an elliptic cylinder positioned over a flat plate. Although there have been a number of experimental investigations on the flow around flat plate under the influence of cylinder wake which is placed at various heights above the plate, numerical investigations is limited due to its complexity in grid generation. Also wake induced from the elliptic cylinder got less attention in this regard. A numerical study of this type of flow on laminar Reynolds number ranges will be considered in this research work. This kind of study can be applied to many engineering problems such as undersea pipelines, building constructions and heat transfer enhancement of heat exchangers.

1.2 OBJECTIVES

The specific objectives of the present research work are as follows:

i. To investigate the flow field around the elliptic cylinder for the validation of the present Finite Element model.

ii. To investigate the boundary layer development on the flat-plate under the influence of wake vortices induced from elliptic cylinder.

iii. To study the effect of Reynolds number on the flow field.

iv. To investigate the effect of the relative position (i.e. the streamwise and vertical distance) between the cylinder (center of the ellipse) and the flat plate leading edge, on the flow field.

CHAPTER 2

LITERATURE REVIEW

Boundary layer development along a flat plate under the influence of wake vortices induced from an elliptic cylinder has not been numerically investigated to a great extent mainly due to the geometrical complexity arising from grid generation and variety of influential parameter.

The literature relevant to the present study can broadly be divided into two groups: one is concerning flow past an elliptic cylinder in an otherwise uniform free stream and another is concerning with the flow over a flat plate under different influential parameters which can cause instability in the boundary layer development.

2.1 FLOW AROUND ELLIPTIC CYLINDER

The phenomenon of flow separation and bluff body wakes has long been intensely studied because of its fundamental significance in flow physics and its practical importance in aerodynamic and hydrodynamic applications. Flow behind a circular cylinder has become the canonical (reduced to the simplest and most significant form possible without loss of generality) problem for studying such external separated flows. Engineering applications, on the other hand, often involve flows over complex bodies like wings, submarines, missiles, and rotor blades, which can hardly be modelled as a flow over a circular cylinder. In such flows, parameters such as thickness ratio and angle-of-attack can greatly influence the nature of separation and the wake structure. Elliptic cylinders, which are more general geometrical configurations than the canonical circular cylinder, can provide a richer flow behavior characteristic of typical engineering flow configurations and significantly augment the understanding of wake flows. For these cylinders, changes in eccentricity allow for shapes ranging from that of a circular cylinder to a flat plate.

There have been many experimental studies of fluid flow from elliptic cylinders. Schubauer [25, 26] studied experimentally the velocity distribution and turbulence in the boundary layer on the surface of an elliptic cylinder with axes ratio (AR) of 1:2.96 at $\alpha = 0^0$, where α denotes the angle of attack. He found that the velocity distribution in the boundary layer, its thickness, and its separation from the surface of the body depend entirely on the velocity distribution in the region of potential flow, outside the boundary layer. His experiment disclose that there exists the critical Reynolds number regime, which extends from about $\mathrm{Re} = 85{,}000$ to 312,000, Re being the Reynolds number based on the major axis of the cylinder. He also observed a so-called separation bubble upstream of the turbulent boundary layer at the critical Reynolds number. However, his main purpose seems to have an investigation of the boundary layer characteristics.

The drag coefficient and Strouhal number were measured for an elliptic cylinder of axis ration 1:2 at $\alpha = 0^0$ and 90^0 by Delay and Sorensen [27]. All the result of $\alpha = 90^0$ seem to be characteristic of the subcritical flow but the data at $\alpha = 0^0$ extend from the subcritical flow to the supercritical one. The Strouhal number was found to vary discontinuously at the critical Reynolds number. Details of the flow around the cylinder, however, have not been described in their paper.

A series of experimental studies on steady and unsteady flow behaviors of elliptic cylinders have been reported by Modi and his colleagues [8-10]. The mean and fluctuating pressure distribution, the drag, lift, and moment coefficients, the Strouhal number and also the near wake features were clarified at the subcritical Reynolds number. They described that the Reynolds number range examined was included in the subcritical flow regime and that the aerodynamic characteristics exhibited no dependency upon the Reynolds number. In spite of their descriptions, the lift and moment coefficients for an elliptic cylinder of axis ratio 2:5 indicate a large variation with the Reynolds number especially at angles of attack smaller than 20^0 [9].

Yano and Kieda [28] presents an approximate method for solving Ossen's linearized

equations for 2D steady flow of incompressible viscous fluid past an inclined elliptic cylinder of aspect ration AR = 0.1 and 0.5 at Reynolds number between 0.01 and 5. The angle of attack was $\alpha = 0^0, 45^0 \, and \, 90^0$. The drag and lift coefficients have maximum values at $\alpha = 90^0$. Honji [29] observed the starting flow around a sphere and an elliptic cylinder at 45^0 and 54^0 angles of incidences.

Taneda [12] studied the relationship between the time dependent lift and flow pattern for the case of an impulsively started elliptic cylinder (AR = 2.1) at angles of incidence of 20^0 and 45^0 at Reynolds numbers 3500 and 6000 respectively. He reported very high initial lift values and a gradual downward movement of the rear stagnation point. In addition, it was pointed out that lift takes negative values in a small time interval shortly after the impulsive start in the case of angle of attack 20^0 unlike the case of angle of attack 45^0.

Shintani et al. [30] gave a detail description of the flow field near an elliptic cylinder placed perpendicularly in a uniform stream at low Reynolds number. Particular attention was given on the effects of both the shape due to the flattening of the cylinder and fluid inertia on the flow field. In this paper, Umemura's method of coordinate transformation through matching procedure was applied for the analysis of the flow past the elliptic cylinder.

Ota et al. [2] investigated experimentally the flow around an elliptic cylinder of axis ratio 1:3 in the critical Reynolds number regime, which extends from about 35,000 to 125,000. The critical Reynolds (Rec) number has been found to vary with the angle of attack α. Rec attains a minimum around $\alpha = 5^0$ to 10^0 and it increases both at smaller and larger angle of attack. The flow around the cylinder at the critical Reynolds number is very unstable. The subcritical flow state and the critical one appear alternatively and the Strouhal number reaches a maximum of about 1.0 and 1.5 depending on α. It is found , however, that the universal Strouhal number based on the velocity along the separated shear layer and the wake width is nearly equal to 0.19, on average, even in the critical Reynolds number regime. The flow at higher

Reynolds number beyond the critical one becomes relatively stable and the small separation bubble was observed on the suction side of the cylinder.

Numerical solutions for laminar incompressible fluid flows past an abruptly started elliptic cylinder at 45° incidence were obtained by Lugt and Haussling [7] in the Reynolds number range from 15 to 200. Almost steady-state solutions were obtained for *Re* = 15 and 30, whereas for *Re* = 200 a Kármán vortex street developed. Comparisons between the obtained location of the first vortex and the flow visualization results reported by Honji [29] show good agreement. However, the surface pressure distribution reported in Lugt and Haussling's paper shows some discrepancies since the pressure periodicity is not fully satisfied.

The numerical solutions to the viscous, incompressible flow over an impulsively started elliptic cylinder at 0, 30, 45 and 90° incidence were determined for moderate and large values of the time by Patel [31]. He obtained a numerical solution in the range of Reynolds number from 60 to 200. Patel's solution is based on a Fourier series approximation of stream function and vorticity.

Nair and Sengupta [32] investigated the incompressible flow past impulsively started elliptic cylinders of thickness-to-chord ratio of 0.1 and 0.25 for different angle of attack and for Reynolds number of 3000 and 10,000 by solving 2D Navier- Stokes equation. The Navier-Stokes equation is solved in stream-function-vorticity formulation using finite difference method. The resulting flows were quite complex. They found that if the angle of attack is large, then the released vortices are strong and hence remain coherent over larger distance in the wake and the stronger the vortices, the more is the tendency to form rotating pairs and triplets. In contrast, the weak vortices show multiple vortex interaction and stronger diffusion.

Badr, Dennis and Kocabiyik [11] studied the 2D unsteady viscous flow over an impulsively started inclined elliptic cylinder by numerical method. The problem is solved for axis ratio between 0.5 and 0.6, Reynolds number ranging from 900 to 5000 and angle of attack between 0^0 *and* 90^0. The direction of free stream was

normal to the cylinder axis and the flow field unsteadiness aroused from two effects, the first is due to the flow field development following the start of the motion and the second is due to vortex shedding in the wake region. A series truncation method based on Fourier series is used to reduce the governing Navier-Stokes equations to two coupled infinite sets second order differential equations. The results revealed an unusual phenomenon of negative lift occurring shortly after the start of the motion, which is consistent with the experimental findings of Taneda [12].

Mittal and Balachandar [33] conducted two and three dimensional simulations of an incompressible viscous flow over elliptic cylinders by spectral methods. The ellipse aspect ratio is AR = 2 and the span wise aspect ration (ratio of spanwise length to semi-major axis of the cylinder) is A = 2. Two angle of attack $0^0 \, and \, 45^0$ were considered. The Reynolds number is fixed at 525. The drag coefficient calculated with the three-dimensional simulation agrees better with the experimental value than that of the two-dimensional simulation. The values of the coefficient of drag obtained with the two-dimensional simulation are 74, 16, and 1.3% higher than those obtained with the three-dimensional simulation.

Allessio and Kocabiyik [34] studied numerically the flow of a viscous incompressible fluid past an inclined elliptic cylinder which starts translating and oscillating impulsively. These oscillations are allowed in a direction perpendicular to the uniform oncoming flow having a magnitude which is less than or equal to the constant translational velocity. The investigation is based on an implicit finite difference/spectral scheme for integrating the unsteady Navier-Stokes equations expressed in a stream function vorticity formulation. The Reynolds number is fixed to 1000. Two angles of attack $\alpha = 45^0$ and $\alpha = 90^0$ were considered. They examine the effect of increase of velocity ratio on the near-wake structure as well as the hydrodynamic forces acting on the cylinder. Vortex dynamics close behind the cylinder are affected by the changing acceleration of the cylinder. An interesting phenomenon has been observed in the flow pattern depending on the velocity ratio and the angle of inclination. In all cases considered in this study, the C_L curve oscillates with the forcing frequency of the cylinder whereas a switch over in the

nature of the fluctuations of the drag coefficient is observed with the increase in angle of inclination.

Johnson et al. [35] studied numerically the flow around an elliptic cylinder with spectral methods. /the aspect ratios ranging from 0.01 to 1.0 and the Reynolds number ranging from 30 to 200 was used. Six different types of flow pattern were categorized in the simulations. These are, steady flow, Von Karman-type vortex shedding, symmetric wake, transitional vortex shedding, steady secondary shedding and unsteady secondary shedding. They have shown substantial change in the shedding types caused by the convective instability interacting with the vortex shedding occurring behind the cylinder.

2.2 BOUNDARY LAYER INSTABILITY

Boundary layer transition in incompressible flow has commonly been divided into "natural" and "bypass" type. Natural transition process is based on the formation, amplification and breakdown, due to instability of Tollmein-Schlicting (T-S) waves [36]. This process culminates with the formation and growth of "turbulent spots", which finally coalesce into fully developed turbulent boundary layer flow.

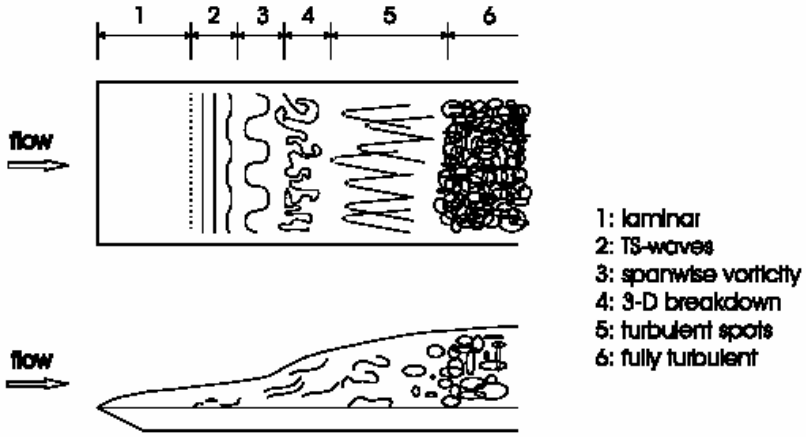

Figure 2.1: The process of natural transition

But in some conditions, transition occurs sooner, via the mechanisms not yet fully understood. Morkovin [37] called this bypass transition, a term indicative of the fact that the aforementioned natural transition path to turbulence is bypassed i.e. the formation of turbulent spots may occur without the initial amplification of T-S waves observed in natural transition. This process is characterized by growth over time scales much shorter than the viscous scale of TS waves. Transition in a boundary layer on a solid body in a stream is affected by many parameters: pressure distribution in the external flow, the nature of the wall (roughness), radius of curvature, heat transfer, suction of the boundary layer, vibration, the nature of the disturbances in the free flow (intensity of turbulence) etc. Transition induced by free-stream turbulence has become synonymous with bypass.

Mayle [38], in his description of the various modes of transition, states that the effect of unsteadiness caused by the periodic passing of wakes, from upstream airfoils or obstruction (cylinders), on transition is referred to as "wake induced transition". Transition induced by wakes or shocks, appear to bypass the first stage of natural transition. The turbulent spots are formed and immediately coalesce and then grow and propagate downstream.

2.2.1 Boundary Layer Disturbance by Cylinder wakes

Liu and Rodi [39] investigated in detail the development of boundary layer along a flat plate under the influence of periodically passing wakes by hot-wire measurements. The wakes were generated by cylinders moving on a squirrel cage in front of the plate leading edge. The Reynolds number was fairly low so that the boundary layer remained laminar over the full length when no disturbing wakes were present. The influence of wake passing frequency on the boundary-layer development and in particular on the transition processes was examined. The hot-wire signals were processed to yield ensemble-average values and the fluctuations could be separated into periodic and stochastic turbulent component. When wakes passed over the plate, the boundary layer was found to be turbulent quite early

underneath the free-stream disturbances due to wakes, while it remained initially laminar. The turbulent boundary layer stripes underneath the disturbed free-stream traveled downstream and grew together so that the embedded laminar regions disappear and the boundary layer became fully turbulent. The streamwise locations where this happened moves upstream with increasing wake-passing frequency, and a clear correlation was determined in this experiment.

Savill and Zhou [40] made an extensive study at low Reynolds numbers of various types of simple interactions, using flow visualization. These studies included interactions with a variety of wakes. Wakes formed behind a circular cylinder were examined, in order to obtain an essentially two-dimensional vortex street, with most of the turbulent energy contained in the highly coherent vortices. They studied, what they called, “slow” or “weak” interactions in which the wake was initially sufficiently far from the boundary layer and was effectively fully developed, before starting to merge with the boundary layer. In contrast to the above type of transition, “fast” or “strong” interactions were also studied. In this type of interaction, the initial vortex street was still present, when the two shear layers merged together. Savill and Zhou concluded that the main parameter governing the growth of the interaction is the level of turbulence in the interaction region.

Investigations of boundary layer transition in undistributed flow and in flow periodically disturbed by wakes were carried out based on extensive hot-wire measurements by Orth [22]. The measurements were carried out in a low speed wind tunnel with a rotating cascade upstream of the testing section, where a flat plate of 700 mm length and d = 20 mm thickness was mounted at half height. The rotating cascade consists of two disks. Three bars of 2 mm diameter were fixed between the disks. The bar moved on a circular path perpendicular to the flow in front of the plate, so that their wakes hit the plate periodically. This setup is chosen to simulate conditions in turbo machines, where the blades are often subjected to periodic wakes of upstream blade rows. In undistributed flow (Tu= 0.6 %), Tollmien-schlichting waves were observed, which are amplified and lead to transition. Under periodic flow conditions as found in turbo machinery, the observed early onset of transition is

likely to be caused by the high intensity of stochastic turbulence, and not by the periodic fluctuations. The boundary layer in flow periodically disturbed by wakes differs in two ways from a boundary layer developing in undisturbed flow. First, an early onset of transition is observed momentarily as the high turbulence level of the wake disturbs the boundary layer and leads to the formations of a turbulent patch. Second, laminar becalmed regions are formed behind the turbulent patches. The results also show that with increasing turbulence intensity, the onset of transition shifts to lower Reynolds number, and the effect of pressure gradient almost disappears. The wake turbulence leads to an earlier transition than observed in isotropic grid turbulence.

A study had been made of the process of laminar to turbulent transition induced by the von Karman vortex street, in the boundary layer on a flat plate by Kyriakides et al. [20]**.** Hot-wire measurements over a range of Strouhal frequencies and free stream velocities were used for the identification of the transition onset. It was established that, the onset of the strong von karman wake induced transition process was a function of the free stream velocity, the position of the cylinder with respect to the plate, the cylinder diameter, the drag coefficient and the minimum velocity in the developing wake at the streamwise position of the onset of the boundary layer transition. It was also established that, in the case of weak wake-boundary layer interaction, the boundary layer transition process was accelerated by the overall free stream turbulence increase due to the wake of the cylinder. From the experimental observations they also developed a correlation which can predict the onset of transition under strong wake-boundary layer interaction.

Wu et al. [24] numerically simulated the interaction between an initially laminar boundary layer developing spatially on a flat plate and wakes. The flow bared a close resemblance to the transitional boundary layer on turbomachinery blades. They found that the inlet wake disturbances inside the boundary layer evolved rapidly into longitudinal puffs during an initial receptivity phase. In the absence of strong forcing from free-stream vortices, these structures exhibited streamwise elongation with gradual decay in amplitude. Selective intensification of the puffs occurred when

certain types of turbulent eddies from free-stream wake interact with the boundary layer through a localized instability. Breakdown of the puffs into young turbulent spots was preceded by a wavy motion in the velocity field outer part of the boundary layer.

Turbulent wakes swept across a flat plate boundary layer i.e. the phenomenon of wake-induced bypass transition was simulated by Wu and Durbin [23]. Benchmark data from a direct numerical simulation of this process were presented and compared to Reynold-averaged predictions. The data were averaged skin-friction and mean velocities.

Choi and Lee [21] experimentally investigated the flow characteristics around an elliptic cylinder with an axis ratio of AR=2 located near a flat plate. The elliptic cylinder was embedded in a turbulent boundary layer whose thickness was larger than the cylinder height. The Reynolds number based on the height of the cylinder cross-section was 14000. The wake velocity profiles behind the cylinder were measured using hot-wire anemometry. In the near-wake region, the vortices were shed regularly only when the gap ratio was greater than the critical value of G/B=0.4. The critical gap ratio was larger than that of a circular cylinder. As the gap ratio increased, the drag co-efficient of the cylinder itself increased, but lift co-efficient decreases. The ground effect of the cylinder at small gap ratio constrained the flow passing through the gap, and restricted the vortex shedding from the cylinder, especially in the lower side of the cylinder wake

2.2.2 Boundary Layer Instability in Aircraft and Turbomachinery

Holzäpfel et al. [18] presented the results of high-resolution numerical simulations of aircraft wake vortex evolution and decay in different regimes and atmospheric conditions. They concluded that the stretching, tilting, and merger of ambient velocity caused by the primary vortices were the prominent mechanisms in vortex evolution and decay.

Lee and Gerontakos [17] investigated the characteristics of the unsteady boundary layer and stall events occurring on an oscillating NACA 0012 airfoil by using closely spaced multiple hot-film sensor arrays at $Re=1.35x10^5$. Aerodynamic forces and pitching moments, integrated from surface pressure measurements, and smoke-flow visualizations were presented.

The existence of disturbed laminar, transitional and turbulent flow on a turbine blade had been demonstrated by Addison and Hodson [14]**.** The measurements included time-resolved hot-wire traverses and surface hot film gage measurements at the midspan of the rotor suction surface with three different rotor-stator spacing. They found that the start of transition was unsteady and dominated by stator wake turbulence. The transition process was characterized by the appearance of high frequency bursts above the lower frequency background disturbances.

Numerical simulation on the interaction of axial compressor stator with upstream rotor wakes and tip leakage vortices were employed to elucidate their impact on the time-averaged performance of the stator by Volkov and Tau [16]. The key objectives of their computational results were (i) to identify the unsteady flow mechanisms responsible for the change of performance, (ii) quantify these changes, and (iii) translate this information into design insights. Two generic mechanisms with significant impact on the performance had been identified. These are reversible recovery of the energy in the disturbances (beneficial), and the no transitional boundary layer response (detrimental). They found that the impact of stator interaction with upstream wakes and vortices depends on the following parameters: axial spacing, loading, and the frequency of wake fluctuations in the rotor frame. At reduced spacing, this impact becomes significant. The most import aspect of the tip vortex is the relative velocity defect and the associated relative total pressure defect.

A detailed experimental study on the behavior of the separated zone on the suction surface of a highly loaded LPT-blade under periodic unsteady wake flow was presented by Schobeiri et al. [15]**.** Two-dimensional periodic unsteady inlet flow was simulated by the translational motion of a wake generator, with a series of cylindrical rods attached to two operating timing belt driven by an electric motor. One steady

and two different unsteady inlet wake flow conditions with corresponding wake frequencies, wake velocity and turbulence intensities were investigated at Re=50,000, 75,000,100,000, and 125,000 based on blade suction surface length. The surface pressure distribution showed no major changes with respect to the above Re-number changes. Passing the wake flow with its highly turbulent vortical core over the separation region caused a periodic contraction and expansion of the separation zone. They also found the periodic behavior of the boundary layer integral parameter.

Direct Numerical Simulation (DNS) of a vortex pair embedded in a stable atmospheric boundary layer were presented by Corjon and Poinsot [19]. The effects of various crosswind conditions were studied. With or without crosswind, the vortices descend toward the ground and create secondary vortices. The presence of crosswind induces a boundary layer with negative vorticity, which act on the creation of secondary vortices. There is a redistribution of the vorticity induced by the primary vortices and that contained in the boundary layer. The sudden eruption of wall vorticity is favored in one case (downwind), when the crosswind shear and the secondary vortex have the same sign, and counteract in the other (upwind), where the crosswind shear and the secondary vortex have the opposite sign. In the case of high crosswind (and high shear), the upwind vortex doesn't rebound. These computations allowed defining a new dimensionless parameter W_s, which gives the altitude of rebound as a function of crosswind and vortex characteristics. This parameter can be use in simple engineering models to predict rebound.

CHAPTER 3

MATHEMATICAL MODELLING

Unsteady boundary layers occur when the motion is started from rest or when it is periodic. When motion is started from rest both the body and the fluid have zero velocities up to a certain instant of time. The motion begins at that instant and it can be considered either that the body is dragged through the fluid at rest or that the body is at rest and that the external fluid motion varies with time. In the later case, an initially very thin boundary layer is formed near the body, and the transition from the velocity of the body to that in the external flow takes place across it and the thickness of the boundary layer increases with time.

Unsteady boundary layer development over a flat-plate under the influence of wake vortices induced from elliptic cylinder is the function of angle of attack of the cylinder, undisturbed approach velocity of the free stream, and the relative position of the elliptic cylinder from the flat-plate. Von Karman wake Vortex Street originated from the elliptic cylinder will interact with the boundary layer development over a flat-plate with different intensities depending on the impinging vortex strength as well as different cylinder-plate relative positions. In this chapter, the governing basic equations for unsteady viscous incompressible flow field with appropriate boundary conditions applicable for the present problem will be discussed briefly. The generalized governing equations are based on the conservation of mass and conservation of momentum. Also, the quantities of interest for getting the picture of the present problem will be introduced.

3.1 FUNDAMENTAL EQUATIONS

The motion in the present problem is two-dimensional. This flow field is governed by the conservation of mass and 2-D unsteady Navier-Stokes equation.

Mass Conservation:

$$\frac{\partial u}{\partial x} + \frac{\partial v}{\partial y} = 0$$

Momentum Conservation:

Unsteady 2-D Navier-Stokes equation:

X-component: $$\rho\left(\frac{\partial u}{\partial t} + u\frac{\partial u}{\partial x} + v\frac{\partial u}{\partial y}\right) = F_x - \frac{\partial P}{\partial x} + \mu\left(\frac{\partial^2 u}{\partial x^2} + \frac{\partial^2 u}{\partial y^2}\right)$$

Y-component: $$\rho\left(\frac{\partial v}{\partial t} + u\frac{\partial v}{\partial x} + v\frac{\partial v}{\partial y}\right) = F_y - \frac{\partial P}{\partial y} + \mu\left(\frac{\partial^2 v}{\partial x^2} + \frac{\partial^2 v}{\partial y^2}\right)$$

Where ρ is the fluid density, F is the body force, P is pressure field, and μ is the kinematic viscosity of the fluid.

Vector forms of these equations are,

Mass Conservation: $\nabla . V = 0$ …….. (3.1)

Navier-Stokes Equation:

$$\rho\frac{\partial V}{\partial t} + \rho\,(V.\nabla)V = -\nabla P + \mu\nabla^2 V + F$$

or, $$\rho\frac{\partial V}{\partial t} - \mu\nabla^2 V + \rho\,(V.\nabla)V + \nabla P = F$$ …..……. …… (3.2)

where $V = \begin{bmatrix} u \\ v \end{bmatrix}$

Now the gradient will be the tensor,

$$\nabla V = \begin{bmatrix} u \\ v \end{bmatrix} \begin{bmatrix} \frac{\partial}{\partial x} & \frac{\partial}{\partial y} \end{bmatrix}$$

or, $$\nabla V = \begin{bmatrix} \frac{\partial u}{\partial x} & \frac{\partial u}{\partial y} \\ \frac{\partial v}{\partial x} & \frac{\partial v}{\partial y} \end{bmatrix}$$

Now transpose of ∇U,

$$(\nabla V)^T = \begin{bmatrix} \frac{\partial u}{\partial x} & \frac{\partial v}{\partial x} \\ \frac{\partial u}{\partial y} & \frac{\partial v}{\partial y} \end{bmatrix}$$

Hence, $$\nabla V + (\nabla V)^T = \begin{bmatrix} 2\frac{\partial u}{\partial x} & \frac{\partial v}{\partial x} + \frac{\partial u}{\partial y} \\ \frac{\partial u}{\partial y} + \frac{\partial v}{\partial x} & 2\frac{\partial v}{\partial y} \end{bmatrix}$$

And,

$$\nabla . \mu \left(\nabla V + (\nabla V)^T \right) = \begin{bmatrix} \frac{\partial}{\partial x} \mu \left(2\frac{\partial u}{\partial x} \right) + \frac{\partial}{\partial y} \mu \left(\frac{\partial v}{\partial x} + \frac{\partial u}{\partial y} \right) \\ \frac{\partial}{\partial x} \mu \left(\frac{\partial u}{\partial y} + \frac{\partial v}{\partial x} \right) + \frac{\partial}{\partial y} \mu \left(2\frac{\partial v}{\partial y} \right) \end{bmatrix}$$

For incompressible/ Newtonian fluid,

$$\nabla . \mu \left(\nabla V + (\nabla V)^T \right) = \mu \nabla . \left(\nabla V + (\nabla V)^T \right)$$

$$= \begin{bmatrix} \mu \left(2\frac{\partial^2 u}{\partial x^2} + \frac{\partial^2 v}{\partial x \partial y} + \frac{\partial^2 u}{\partial y^2} \right) \\ \mu \left(\frac{\partial^2 u}{\partial x \partial y} + \frac{\partial^2 v}{\partial x^2} + 2\frac{\partial^2 v}{\partial y^2} \right) \end{bmatrix}$$

$$= \mu \begin{bmatrix} \frac{\partial}{\partial x}\left(\frac{\partial u}{\partial x}+\frac{\partial u}{\partial x}+\frac{\partial v}{\partial y}\right)+\frac{\partial^2 u}{\partial y^2} \\ \frac{\partial}{\partial y}\left(\frac{\partial u}{\partial x}+\frac{\partial v}{\partial y}+\frac{\partial v}{\partial y}\right)+\frac{\partial^2 v}{\partial x^2} \end{bmatrix}$$

$$= \mu \begin{bmatrix} \frac{\partial^2 u}{\partial x^2}+\frac{\partial^2 u}{\partial y^2} \\ \frac{\partial^2 v}{\partial x^2}+\frac{\partial^2 v}{\partial y^2} \end{bmatrix}$$

or, $\nabla.\mu\left(\nabla V+(\nabla V)^T\right)=\mu\nabla^2 V$

So, equation (3.2) comes as

$$\rho\,\frac{\partial V}{\partial t}-\mu\nabla^2 V+\rho\,(V.\nabla)V+\nabla P=F$$

or, $\rho\,\frac{\partial V}{\partial t}-\mu\nabla.\left(\nabla V+(\nabla V)^T\right)+\rho\,(V.\nabla)V+\nabla P=F$

or, $\rho\,\frac{\partial V}{\partial t}+\rho\,(V.\nabla)V=\nabla.\left[-pI+\mu\left(\nabla V+(\nabla V)^T\right)\right]+F$ .... (3.3)

Where *I* is the identity matrix.

Equation (3.3) along with the compressibility constraint, equation (3.1) will be used for the present numerical computation.

3.2 DIMENSIONLESS ANALYSIS

An elliptic cylinder having major and minor axis of lengths 2a and 2b respectively and axis ratio (AR = b/a) of 0.6, in an otherwise uniform flow, U can be modeled by unsteady 2-D Navier-Stokes equation neglecting body forces,

$$\rho\,\frac{\partial V}{\partial t}+\rho\,(V.\nabla)V=-\nabla P+\mu\nabla^2 V \quad \text{..(3.4)}$$

The dimensionless quantities are,

$$V' = \frac{V}{U} \qquad x' = \frac{x}{c} \qquad y' = \frac{y}{c} \qquad P' = \frac{P}{\rho U^2} \qquad t' = \frac{U t}{c}$$

also, $\nabla = \frac{1}{c}\nabla'$ and $\nabla^2 = \frac{1}{c^2}\nabla'^2$

where, c stands for the focal distance of the ellipse defined by, $c = \sqrt{a^2 - b^2}$.

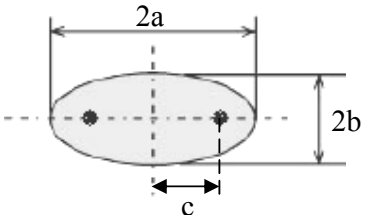

Now equation (3.4) in dimensionless form,

$$\rho \frac{\partial V' U}{\partial\left(\frac{t' c}{U}\right)} + \rho\left(V' U . \frac{1}{c}\nabla'\right) V' U = -\frac{1}{c}\nabla' P' \rho U^2 + \mu \frac{1}{c^2}\nabla^2 V' U$$

or, $$\frac{\partial V'}{\partial t'} + \left(V' . \nabla'\right) V' = -\nabla' P' + \frac{2}{\mathrm{Re}_{2c}} \nabla'^2 V' \quad \ldots\ldots\ldots\ldots\ldots\ldots\ldots\ldots\ldots\ldots\ldots\ldots (3.5)$$

where $\mathrm{Re}_{2c} = \frac{\rho U (2c)}{\mu}$

Equation (3.5) is the dimensionless form of 2-D unsteady Navier-Stokes equation.

And dimensionless form of conservation of mass,

$$\nabla' . V' = 0 \quad \ldots\ldots\ldots\ldots\ldots\ldots\ldots\ldots\ldots\ldots\ldots\ldots\ldots\ldots\ldots\ldots\ldots\ldots\ldots\ldots\ldots\ldots (3.6)$$

In the present computation dimensionless time will be considered as $\tau = \frac{Ut}{c}$ which was used by Badr, Dennis and Kocabiyik [11] where they used the vorticity/stream function formulation of unsteady 2-D Navier-Stokes equation.

3.3 BOUNDARY CONDITIONS

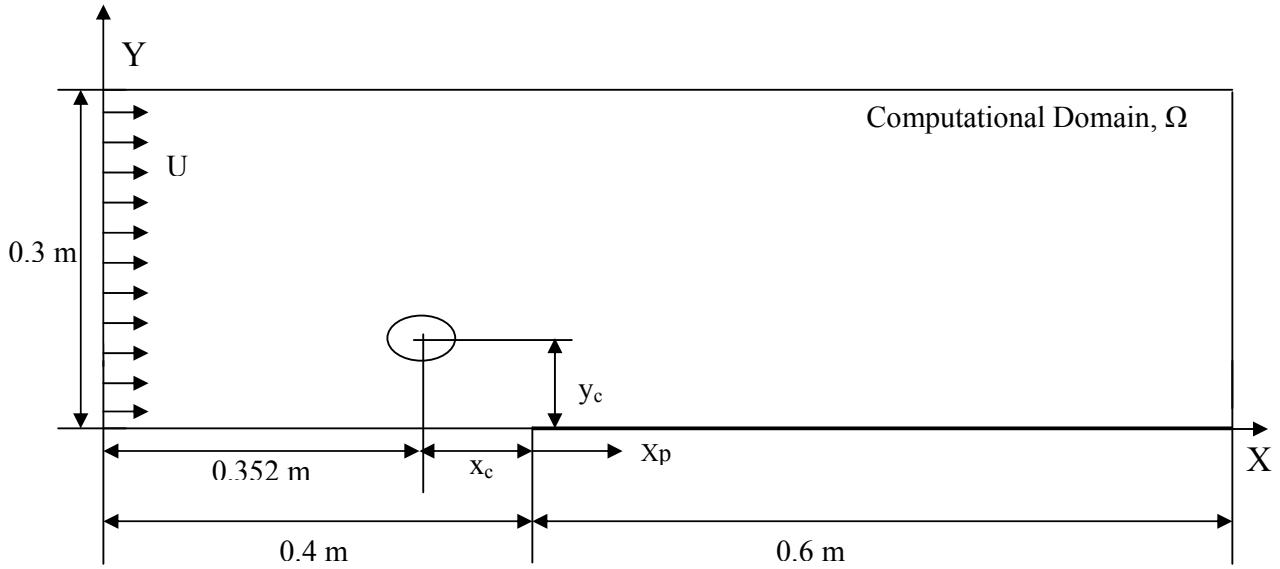

Figure 3.1: Scheme of the computational domain (not to scale)

Figure 3.1 shows the computational domain where an elliptic cylinder of axis-ratio 0.6 is placed in front of a flat plate of 0.6m length in an otherwise uniform free stream, U. In the figure, x_c is the streamwise distance and y_c is the vertical distance repectively, between the cylinder centre and the flat plate leading edge and Xp indicates different streamwise locations on the plate.

In the present finite element computation, some problems were to face for selecting the boundary conditions for different boundary of the computational domain. Some the boundaries of the domain were set with different boundary conditions and the programme was runned. Each time the undisturbed velocity profile was found to match not exactly the Blassius velocity profile for the flat plate but it overshoot i.e. $u/U > 1$ (two sample graphs are shown in figure 3.3). The results of the different trials for selecting the boundary conditions have been given in Table-3.1. To understand, each boundary is symbolized with different alphabetic numbering system as shown in figure 3.2.

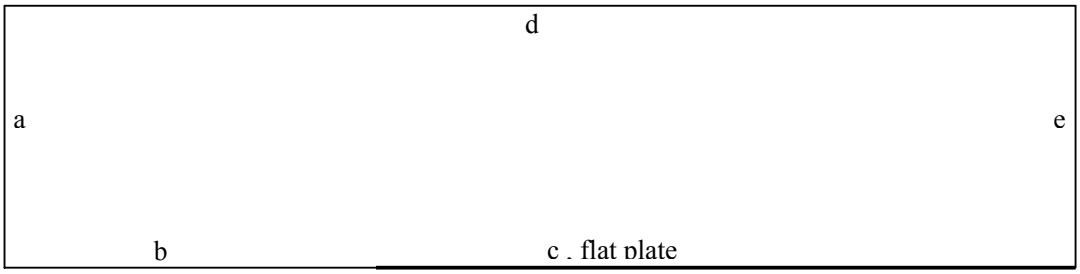

Figure 3.2: Alphabetic numbering of the boundaries of the computational domain.

Identification numbers are as follows:

a -- Left boundary

b – Lower left boundary

c – Lower right boundary (flat plate)

d – Upper boundary

e – Right boundary

The reasons of this type of discrepancy may be explained as follows:

1. Leading edge of the flat plate can affect the flow field. When the fluid touches the nose of the leading edge, the flow stagnates developing a large pressure and hence reduces the region of undistorted constant-pressure flow available on the plate. Numerically, at the point of x = 0.4 m, the computer finds two values of stream velocity; u = U for the slip condition of the lower left boundary of the domain and u = 0 for the no slip condition of the plate and this may cause a numerical error.

2. It may be the result of the boundary condition that has been chosen for the present model. In a real external flow, there is no boundary at the top and flow is permitted to pass through freely. Unfortunately, this cannot be used in our flow field without encountering convergence problems.

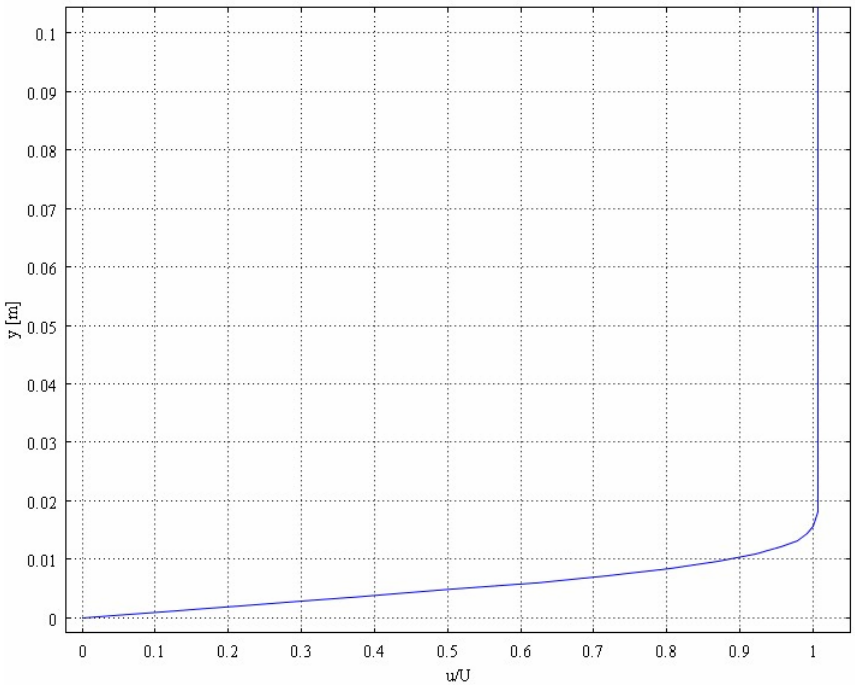

(Case-2)

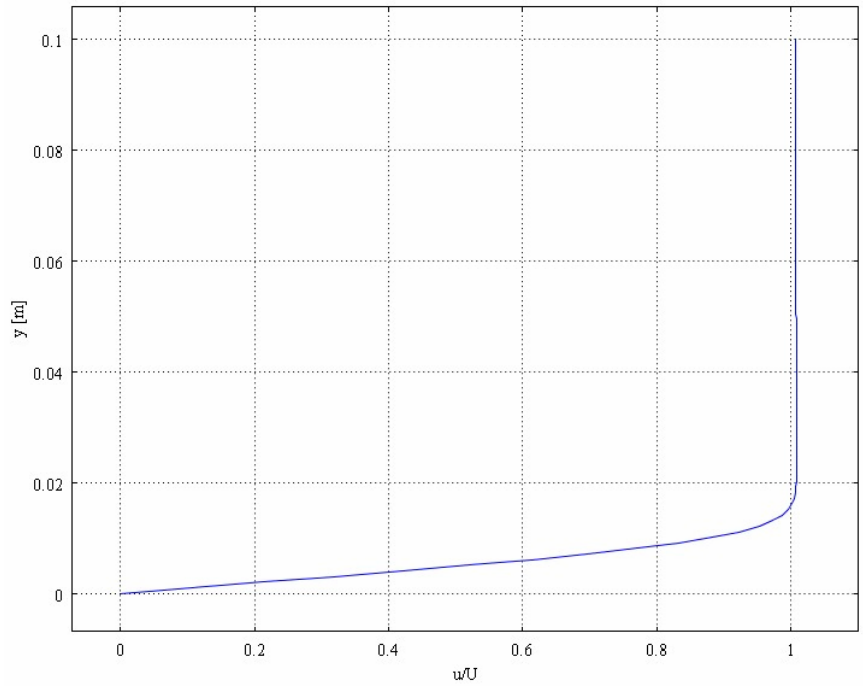

(Case-12)

Figure 3.3: Velocity profiles for two test cases of Table 3.1

Table 3.1: Different combination of boundary conditions applied to the boundaries of the computational domain with %error occurred in the velocity profile.

Inlet Velocity	Boundary Conditions					% error
	a	b	c	d	e	
U= 0.468 (m/s) (Re_{2c} = 500)	Velocity Inlet	Slip wall	No slip	Open boundary: Normal stress = 0	Pressure, No viscous stress	0.29904
	Velocity Inlet	Slip wall	No slip	Open boundary: no viscous stress	Pressure, No viscous stress	0.588
	Velocity Inlet	Symmetry	No slip	Open boundary: Normal stress = 0	Pressure	No convergence
	Velocity Inlet	Slip wall	No slip	Open boundary: no viscous stress	Pressure	No convergence
	Velocity Inlet	Slip wall	No slip	Open boundary: Normal stress = 0	No viscous stress	1
	Velocity Inlet	Slip wall	No slip	Open boundary: no viscous stress	No viscous stress	No convergence
	Velocity Inlet	Slip wall	No slip	Open boundary: Normal stress = 0	Normal stress = 0	0.545
	Velocity Inlet	Slip wall	No slip	Open boundary: no viscous stress	Normal stress = 0	0.448
	Velocity Inlet	Slip wall	No slip	Symmetry	Pressure, No viscous stress	1.58
	Velocity Inlet	Slip wall	No slip	Symmetry	Pressure	1.5
	Velocity Inlet	Slip wall	No slip	Symmetry	No viscous stress	No convergence
	Velocity Inlet	Slip wall	No slip	Symmetry	Normal stress = 0	1.52
	Velocity Inlet	Slip wall	No slip	Slip wall	Pressure, No viscous stress	1.079
	Velocity Inlet	Slip wall	No slip	Slip wall	Pressure	1.082
	Velocity Inlet	Slip wall	No slip	Slip wall	No viscous stress	No convergence
	Velocity Inlet	Slip wall	No slip	Slip wall	Normal stress = 0	1.08
	Velocity Inlet	Slip wall	No slip	Pressure outlet	Pressure outlet	No convergence

Considering the results of Table-3.1, the boundary conditions for different boundaries of the present computational domain have chosen according to the lowest %error of the velocity profile (at Xp = 300mm) of the flat plate.

.

The computational Domain subjected to **initial condition**,

$$(u,v) \mid_{t=0} = (U,V)$$

The **boundary conditions** to be considered are as follows:

1. An inflow boundary condition is applied at the left boundary:

$$\boldsymbol{V} = \mathrm{U} \quad \text{i.e.} \quad u = U \quad \text{and} \quad v = 0$$

2. Slip boundary condition is applied at the lower left boundary

$$\partial u / \partial y = 0 \ , \quad v = 0$$

3. No-slip velocity condition for all velocity components on all solid walls. So,

   a. On the plate surface, $\boldsymbol{V} = 0$ i.e. u = v =0.
   b. On the surface of the cylinder, also $\boldsymbol{V} = 0$ i.e. u = v =0.

4. An open boundary condition is applied at the upper boundary of the domain.

$$(-p\mathbf{I} + \mu(\nabla \mathbf{V} + (\nabla \mathbf{V})^{T}))\ \mathbf{n} = 0$$

5. An outflow boundary condition is applied at the right boundary

$$\mu(\nabla \mathbf{V} + (\nabla \mathbf{V})^{T})\ \mathbf{n} = 0 \quad \text{and} \quad p = p_0$$

3.4 BOUNDARY LAYER PARAMETERS

The presence of the boundary layer moves streamlines just outside the boundary layer from the body compared to the inviscid solution by an additional amount called the *displacement thickness*, δ .

$$\delta = \int_0^{\delta_1} \left(1 - \frac{u}{U}\right) dy$$

where, δ_1 is the boundary layer thickness.

Just as the boundary layer transports less mass than the undisturbed surrounding flow, it also transports less momentum. The deficit in momentum flux for the entire boundary layer is measured by the *momentum thickness*, θ. The measure of the amount by which fluid in the boundary layer loses momentum is directly related to the drag coefficient.

$$\theta = \int_0^{\delta_1} \frac{u}{U}\left(1 - \frac{u}{U}\right) dy$$

An idea of the shape of a boundary-layer velocity profile — and some idea about how likely it is to separate from the body — can be obtained from the dimensionless *shape factor*, H, which is the ratio of displacement to momentum thickness

$$H = \frac{\delta}{\theta}$$

For unsteady flow field, sometimes it is convenient to use average shape factor, H_{av}

$$H_{av} = \frac{1}{n} \sum_{i=1}^{n} H_i$$

where n is the number of sample points taken over a predetermined time.

Sometimes, the root mean square (rms**)** value is useful especially when the variates are positive and negative.

$$H_{rms} = \sqrt{\left(\sum_{i=1}^{n} H_i^2\right)} / n$$

In general, H = 2.6 indicates laminar flow and H = 1.4 for turbulent flow. It is an inverse measure of the boundary layer momentum, which increases in the turbulent regime.

Skin friction is the component of parasitic drag arising from the friction of the fluid against the "skin" of the object that is moving through it. Skin friction is a function of the interaction between the fluid and the skin of the body.

The skin friction coefficient, C_f, is defined by:

$$C_f = \frac{\tau_w}{\frac{1}{2}\rho U^2}$$

Where τ_w is the local wall shear stress, ρ is the fluid density and U is the free-stream velocity (usually taken ouside of the boundary layer or at the inlet).

For unsteady flow field, sometimes it is convenient to use average skin friction co-effecient, $C_{f_{av}}$

$$C_{f_{av}} = \frac{1}{n}\sum_{i=1}^{n} C_{fi}$$

where n is the number of sample points taken over a predetermined time.

And also the rms value of the skin friction is

$$C_{f_{rms}} = \sqrt{\left[\left(\sum_{i=1}^{n} C_{d_i}^2\right)/n\right]}$$

CHAPTER 4

COMPUTATIONAL DETAILS

Due to the complicated nature of flow field, theoretical analysis is typically limited to either flows at very low Reynolds number or flows at early times after an impulsive start. Experimental techniques have become very sophisticated in recent years but an extensive spatial and temporal analysis of the three-dimensional flow field would quickly overwhelm the available resources. Numerical simulations provide a promising approach to analyse this problem. Numerical Methods are extremely powerful problem-solving tools-capable of handling large systems of equation, complicated geometries etc. that are often impossible to solve analytically. It provides a vehicle to reinforce the understanding of mathematics.

The partial differential equations (PDE) of fluid mechanics and heat transfer are solvable for only a limited number of flows. To obtain an approximate solution numerically, we have to use discritization method which approximated the differential equations by a system of algebric equations, which can then be solved on a computer. The approximations are applied to small domains in space and/ or time so the numerical solution provides results at discrete locations in space and time. Much as accuracy of experimental data depends on the quality of the measuring instruments used, the accuracy of numerical solutions is dependent on the quality of discritization used.

The complete Navier-Stokes equations are considered to be the correct mathematical description of the governing equations of fluid motion. The most accurate numerical computations in fluid dynamics came from solving the Navier-Stokes equations. The equations represent the conservation of mass and momentum.

There are several discritization methods available for the high performance numerical computation in CFD;

- Finite volume method (FVM)
- Finite element method (FEM)
- Finite difference method (FDM)
- Boundary element method (BEM)
- Boundary volume method (BVM)

In the present numerical computation Finite element method (FEM) is used.

4.1 FINITE ELEMENT METHOD

The finite element method (FEM) is a numerical technique for solving problems which are described by partial differential equations or can be formulated as functional minimization. A domain of interest is represented as an assembly of *finite elements*. Approximating functions in finite elements are determined in terms of nodal values of a physical field which is sought. A continuous physical problem is transformed into a discretized finite element problem with unknown nodal values. For a linear problem a system of linear algebraic equations should be solved. Values inside finite elements can be recovered using nodal values.

The major steps involved in finite element analysis of a typixal problem are:

1. Discritization of the domain into a set of finite elements (mesh generation)
2. Weighted-integral or weak formulation of the differential equation to be analyzed.
3. Development of the finite element model of the problem using its weighted-integral or weak form.
4. Assembly of finite elements to obtain the global system of algebric equations.
5. Solution of equations.
6. Post-computation of solution and quantities of interest.

4.2 MESH GENERATION

In Finite element method, the mesh generation is the technique to subdivide a domain into a set of subdomains, called finite elements. Figure shows a domain, Ω is subdivided into set of subdomains, Ω^e with boundary Γ^e.

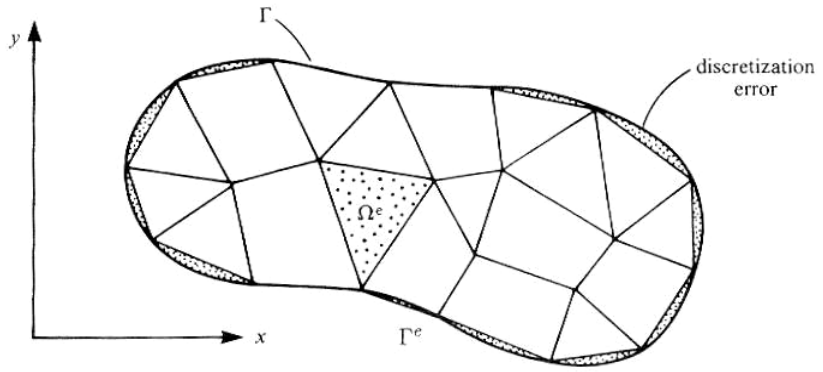

Figure 4.1: Finite element discritization of a domain [41]

The present numerical technique will discretize the computational domain into unstructured triangles by Delaunay Triangulation method. The delaunay triangulation is a geometric structure that has enjoyed great popularity in mesh generation since the mesh generation was in its infancy. In two-dimensions, the Delaunay triangulation of a vertex set maximizes the minimum angle among all possible triangulations of that vertex set.

The process of solving the linear or nonlinear systems of equations yielded by the finite element method and its brethren is simpler and faster on structured meshes, because of the ease of determining each node's neighbors. Because unstructured meshes necessitate the storage of pointers to each node's neighbors, their demands on storage space and memory traffic are greater. Furthermore, the regularity of structured meshes makes it straightforward to parallelize computations upon them, whereas unstructured meshes engender the need for sophisticated partitioning algorithms and parallel unstructured solvers. Unstructured meshes, far better than

structured meshes, can provide multiscale resolution and conformity to complex geometries.

Figure 4.2 shows the mesh mode for the present numerical computation. Special attention is given for mesh generation on the cylinder surface and on the plate surface.

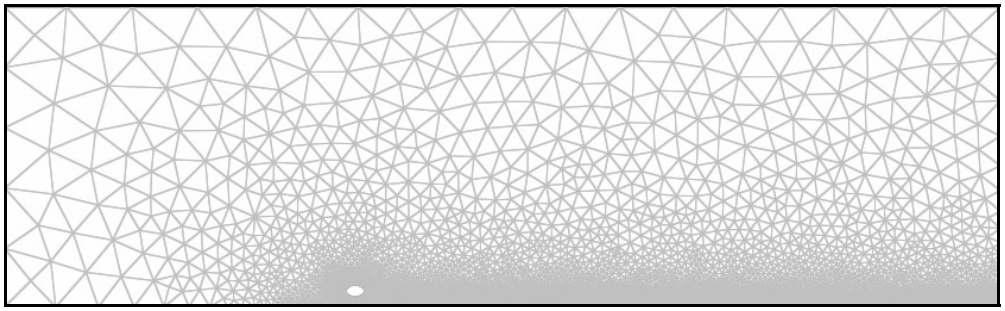

Figure 4.2: Current mesh structure with around 29,000 elements.

Numerical results greatly depend on the mesh generation. A grid sensitivity test has been carried out to find the optimum element number. 29,000 elements mesh has been selected to predict the result based based on accuracy and time.

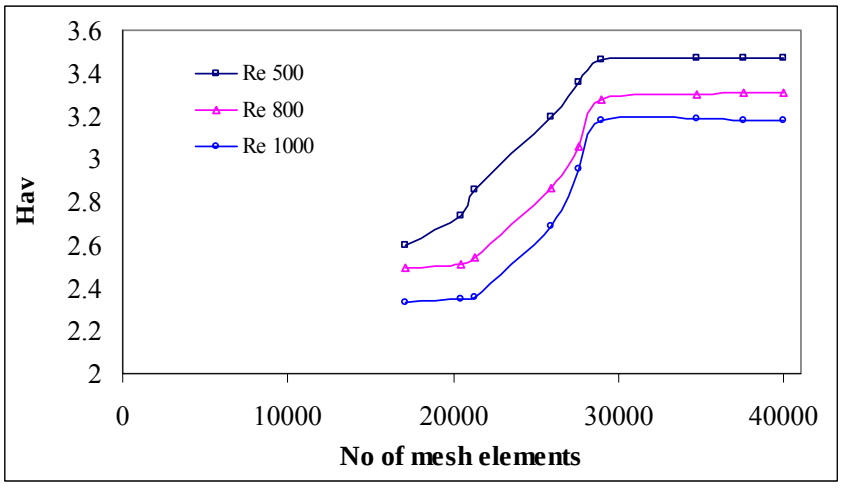

Figure 4.3: Grid Independency test for $x_c/2c = 0$ $y_c/2c = 1$, at Xp = 400mm.
(where Hav is average shape factor)

4.3 WEAK FORMULATION OF THE DIFFERENTIAL EQUATION

The motion of fluid is governed by the global laws of conservation of mass and momentum.

Conservation of mass:

$$\frac{\partial u_i}{\partial x_i} = 0 \quad \ldots\ldots\ldots\ldots\ldots\ldots\ldots\ldots\ldots\ldots\ldots\ldots\ldots\ldots\ldots\ldots\ldots\ldots\ldots\ldots \text{(4.1)}$$

Conservation of momentum:

$$\rho\left(\frac{\partial u_i}{\partial t}+u_j\frac{\partial u_i}{\partial x_j}\right)-\frac{\partial \sigma_{ij}}{\partial x_j}+\rho f_i = 0 \ldots\ldots\ldots\ldots\ldots\ldots\ldots\ldots\ldots\ldots\ldots\ldots.... \quad \text{(4.2)}$$

with constitutive equation:

$$\left.\begin{aligned} &\sigma_{ij} = \tau_{ij} - P\delta_{ij} \;\; ; \;\; \tau_{ij} = \mu D_{ij} \\ &D_{ij} = \frac{1}{2}\left(\frac{\partial u_i}{\partial x_j}+\frac{\partial u_j}{\partial x_i}\right) \end{aligned}\right\} \quad \ldots\ldots\ldots\ldots\ldots\ldots\ldots\ldots\ldots\ldots\ldots\ldots.(4.3)$$

Using the constitutive equations and deformation rate-velocity relations, equation(4.1) and (4.2) can be expressed solely in terms of the velocity component and pressure:

$$\frac{\partial u_i}{\partial x_i} = 0 \qquad \ldots\ldots\ldots\ldots\ldots\ldots\ldots\ldots\ldots\ldots\ldots\ldots\ldots\ldots\ldots \text{(4.4)}$$

$$\rho\left(\frac{\partial u_i}{\partial t}+u_j\frac{\partial u_i}{\partial x_j}\right)-\frac{\partial}{\partial x_j}\left[-P\delta_{ij}+\mu\left(\frac{\partial u_i}{\partial x_j}+\frac{\partial u_j}{\partial x_i}\right)\right]+\rho f_i = 0 \;\ldots\ldots\ldots.. \quad \text{(4.5)}$$

The starting point for the development of the finite element models of equations (4.4) and (4.5) is their weak forms. For convenience, the left side expressions of eq.(4.4) and (4.5) are denoted by f_1 and f_2.

The weighted –integral statements of the two equations over a typical element Ω^e are given by

$$\int_{\Omega^e} Q f_1 dx = 0 \quad \text{.....(4.6)}$$

$$\int_{\Omega^e} w f_2 dx = 0 \quad \text{.....(4.7)}$$

where (Q,w) are weight functions.

The following integral statements are found [42]

$$0 = \int_{\Omega^e} Q \left(\frac{\partial u_i}{\partial x_i} \right) dx \quad \text{..... (4.8)}$$

$$0 = \int_{\Omega^e} \left[\rho \left(w_i \frac{\partial u_i}{\partial t} + w_i u_j \frac{\partial u_i}{\partial x_j} \right) + \frac{\partial w_i}{\partial x_j} \left(-P\delta_{ij} + \mu \left(\frac{\partial u_i}{\partial x_j} + \frac{\partial u_j}{\partial x_i} \right) \right) - \rho w_i f_i \right] dx - \oint_{\Gamma^e} w_i T_i \, ds \quad \text{..... .(4.9)}$$

where T_i is the boundary stress components.

This completes the weak form development.

4.4 FINITE ELEMENT MODEL

Suppose that the dependent variables (u_i,P) are approximated by expansions of the form,

$$u_i(x,t) = \sum_{m=1}^{M} \Psi_m(x) u_i^m(t) = \Psi^T u_i \quad \text{..... (4.10)}$$

$$P(x,t) = \sum_{l=1}^{L} \Phi_l(x) P_l(t) = \Phi^T P \quad \text{.....(4.11)}$$

Where Ψ and Φ are (column) vectors of interpolation (or shape) function, and u_i and P are vectors of nodal values of velocity components and pressure, respectively.

The weight function (Q,w) have the following correspondence [41]

$$w \approx \psi_m \ , Q \approx \Phi_l$$

Substituting equation (4.10) and (4.11) into equation(4.8) and (4.9) the following forms are found [42]

Continuity: $- Q^T u = 0$ ……(4.12)

Momentum: $M \dot{u} + C(u)\, u + Ku - Q\, P = F$ ……...(4.13)

For two-dimensional case, equation (4.12) and (4.13) have the following explicit form,

$$\begin{bmatrix} M & 0 & 0 \\ 0 & M & 0 \\ 0 & 0 & M \end{bmatrix} \begin{Bmatrix} \dot{u}_1 \\ \dot{u}_2 \\ P \end{Bmatrix} + \begin{bmatrix} C(u) & 0 & 0 \\ 0 & C(u) & 0 \\ 0 & 0 & 0) \end{bmatrix} \begin{Bmatrix} u_1 \\ u_2 \\ P \end{Bmatrix} +$$

$$\begin{bmatrix} 2K_{11} + K_{22} & K_{21} & -Q_1 \\ K_{12} & K_{11} + 2K_{22} & -Q_2 \\ -Q_1^T & -Q_2^T & 0 \end{bmatrix} \begin{Bmatrix} u_1 \\ u_2 \\ P \end{Bmatrix} = \begin{Bmatrix} F_1 \\ F_2 \\ 0 \end{Bmatrix}$$

……. (4.14)

where the superposed dot represents a time derivative. The co-efficient matrix shown in equation (4.14) are defined by

$$M = \int_{\Omega^e} \rho \Psi \Psi^T \, dx \quad ; \quad C(u) = \int_{\Omega^e} \rho \Psi \left(\Psi^T u_j \right) \frac{\partial \Psi^T}{\partial x_j} \, dx$$

$$K_{ij} = \int_{\Omega^e} \mu \frac{\partial \Psi}{\partial x_i} \frac{\partial \Psi^T}{\partial x_j} \, dx \ ; \quad Q_i = \int_{\Omega^e} \frac{\partial \Psi}{\partial x_i} \Phi^T \, dx$$

$$F_i = \int_{\Omega^e} \rho \, \Psi f_i \, dx + \oint_{\Gamma^e} \Psi \, T_i \, ds$$

The interpolation used for the pressure variable should be different from that used for velocities, because the weak forms in equations (4.8) and (4.9)contain the first

derivative of the velocities u_i and no derivatives of pressure P. This observation lead to the conclusion that the pressure variable should be interpolated with functions that are one order less than those used for the velocity field and the approximation may be discontinuous.

In the present numerical computation, quadratic triangular element for velocity field and linear triangular element for pressure field is used. In COMSOL, it is Lagrange P2-P1 element.

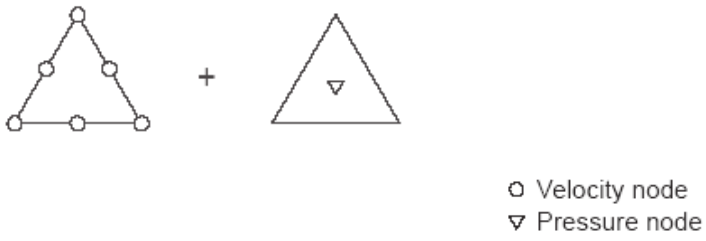

Figure 4.4: Velocity-pressure (discontinuous) interpolation

4.5 SIMPLE ALGORITHM

The acronym SIMPLE stands for Semi-Implicit Method for Pressure-Linked Equations. The principal difficulty in solving the momentum equations for incompressible flows lies in the determination of pressure. In the iterative SIMPLE-like algorithm, the discrete form of the continuity equation is converted into an equation for the pressure correction. It is essentially a guess-and-correction procedure for the calculation of pressure. The pressure corrections are then used to update the pressure and velocity fields so that the components obtained from the solution of momentum equations satisfy the continuity equation. In a short procedure is a pressure field P^* is guessed discretized momentum equations are solved using the guessed pressure field to yield velocity components u^* and v^*. The simple algorithm is shown by the flow chart below.

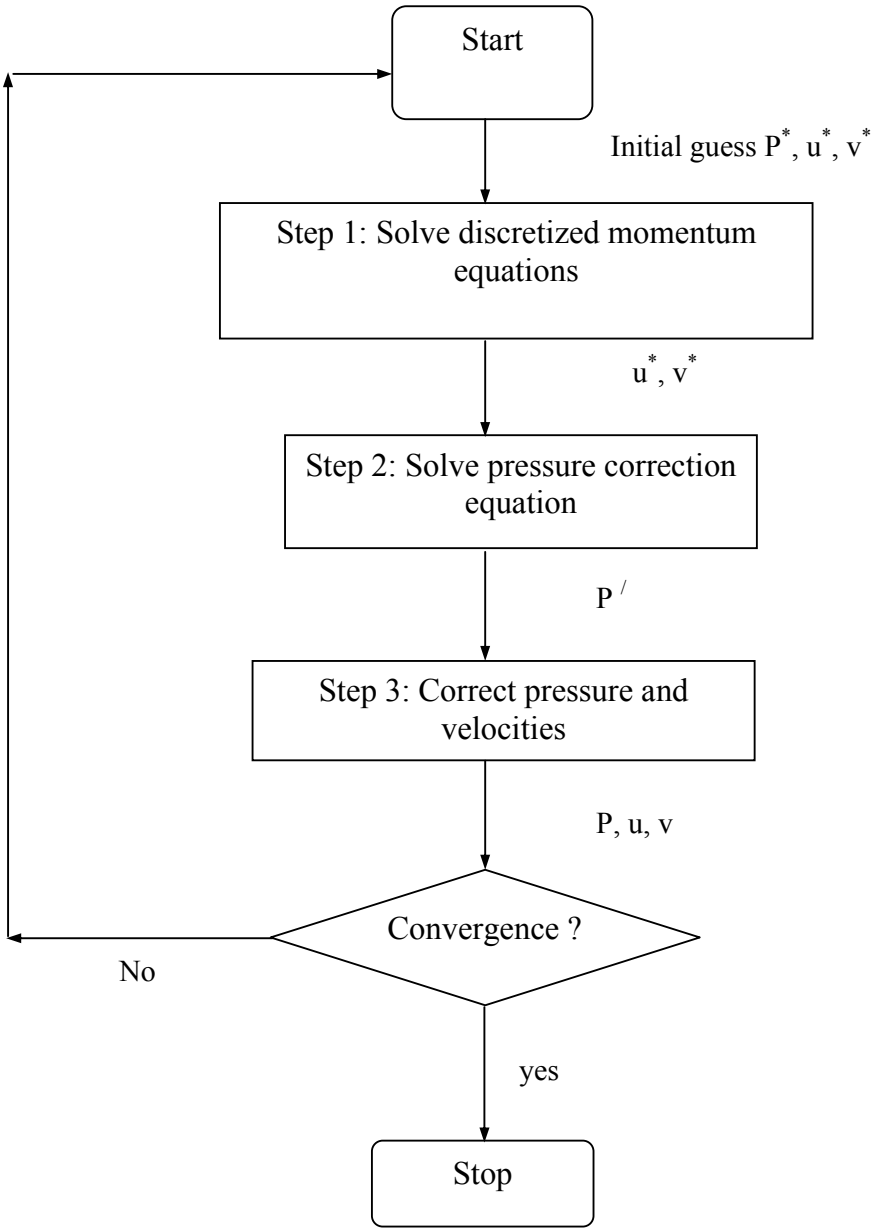

4.6 SOLUTION OF SYSTEM OF LINEAR ALGEBRIC EQUATION

As a result of the decoupling of the equation for each dependent variable and subsequent linearization, large sets of linear algebric equations are obtained. In order

to solve these equations, algebric multigrid (AMG), Unsymmetric multifrontal method (UMF), Generalized minimul residual(GMRES) –type solver are used.

The solution process in AMG, which involves relaxation, transfer of residuals from fine to coarse grid, and interpolation of corrections from coarse to fine levels, is very efficient for fine-grid problem, provided the above 'multigrid components' are properly chosen. It is also more economical for coarse grids.

The generalized minimal residual (GMRES) method is an extension of the minimal residual method (MINRES), which is only applicable to symmetric systems, to unsymmetric systems. Like MINRES, it generates a sequence of orthogonal vectors, but in the absence of symmetry this can no longer be done with short recurrences; instead, all previously computed vectors in the orthogonal sequence have to be retained. For this reason, "restarted" versions of the method are used. It is an efficient iterative process for solving systems of linear equations

UMFPACK (Unsymmetric MultiFrontal Package) is a set of routines for solving unsymmetric sparse linear systems, Ax=b, when A is sparse and unsymmetric.
It is based on the Unsymmetric-pattern MultiFrontal method. UMFPACK factorizes PAQ, PRAQ, or PR−1AQ into the product LU, where L and U are lower and upper triangular, respectively, P and Q are permutation matrices, and R is a diagonal matrix of row scaling factors (or R = I if row-scaling is not used). Both P and Q are chosen to reduce fill-in (new nonzeros in L and U that are not present in A). The permutation P has the dual role of reducing fill-in and maintaining numerical accuracy (via relaxed partial pivoting and row interchanges). UMFPACK first finds a column pre-ordering that reduces fill-in, without regard to numerical values. It scales and analyzes the matrix, and then automatically selects one of three strategies for pre-ordering the rows and columns: unsymmetric, 2-by-2, and symmetric. This solver is very efficient for solving the unstructured finite element mesh. In the present computation this direct type of solver is used.

CHAPTER 5

RESULTS AND DISCUSSION

In the previous chapter, computational technique along with detail discretization of governing equation is presented. This chapter will be divided into two sections: the first section will deal with the results obtained from the elliptic cylinder in uniform flow, comparing with the results of the published data available in literature. And in the second section, results of the present numerical simulation of the two dimensional boundary layer development on the surface of a flat plate under the influence of passing wake vortices induced from an elliptic cylinder and the effects of different parameters i.e. the relative position of the cylinder to the plate, the Reynolds number etc. will be discussed. The parameters affecting the results have been summarized in Table 5.1, where 2c stands for the distance between the foci of the ellipse. The cylinder is positioned at the non-dimensional axial distance $x_c/2c$ from the plate leading edge, while $y_c/2c$ is the non-dimensional vertical distance of the axis of the cylinder from the surface of the plate. The flat plate used in the present model is 600mm long with a sharp leading edge. The geometrical scheme of the various test cases investigated in the present numerical problem, is shown in figure 5.2.

Table 5.1: Summary of computational Conditions

	Free Stream Velocity, U (m/s)			Cylinder to Plate relative position	
	0.46875	0.75	0.9375	$x_c/2c$	$y_c/2c$
Reynolds number, Re_{2c}	500	800	1000	-3	1
	500	800	1000	0	1
	500	800	1000	3	1
	500	800	1000	0	0.75

5.1 FLOW AROUND ELLIPTIC CYLINDER

In this section, the method of the solution and the accuracy of the numerical scheme of elliptic cylinder in uniform flow will be verified for Reynolds number Re_{2c} = 1000, the angle of attack of $\alpha = 0^0$ and $\alpha = 30^0$ and cylinder axis ratio AR = 0.6.

In order to verify the present numerical scheme used in this work, the initial flow for the problem of flow field of the elliptic cylinder only is considered. The figures (figure 5.3 to 5.7) of instantaneous streamline and drag and lift coefficients found in the present problem show a good agreement with the numerical solution of Badr, Dennis and Kocabiyik.

The patterns of instantaneous streamlines for $\alpha = 0^0$ and $\alpha = 30^0$ at different times are shown in figure 5.3 and 5.5 respectively. The corresponding flow visualization by Badr, Dennis and Kocabiyik [11] are also presented for comparing or validity of the present numerical computations.

Figure 5.3 shows that at the start of motion, the wake cavity behind the cylinder (at $\alpha = 0^0$) contains a symmetrical pair of equal and opposite recirculating-flow regions (upper clockwise and lower counter-clockwise voetex pairs) on either side of the wake whose length grows (due to viscous stresses) with the increase of time τ. Eight snapshots of the flow field for the case $\alpha = 30^0$ are shown in figure 5.5. Figure 5.5(a,A) shows the formation of a separation bubble. The vortex resulting from the separation bubble develops at time $\tau = 3.0$ near the upper half of the cylinder. After a while this vortex detaches and moves downstream. During the time interval $1 < \tau < 10$, the formations and detachments of the upper (clockwise) and lower (counterclockwise) vortex pairs take place and in further time, this classical mode of vortex shedding leads to the formation of a Karman vortex street. Comparison of these figures with the corresponding ones in case of $\alpha = 0^0$ indicates that the separation point moves more toward the front of the cylinder as α increases from 0^0 to 30^0. Karman vortex street can also be found when the time is very large ($\tau >> 10$).

The fluid forces acting on the cylinder are mainly the drag and lift forces represented by D and L respectively. These forces arise from the fluid pressure and shear forces acting on the cylinder surface and are usually expressed by the coefficients named drag coefficient, C_D and lift coefficient, C_L respectively, where

$$C_D = \frac{D}{\frac{1}{2}\rho U^2 (2c)} \quad \text{and} \quad C_L = \frac{L}{\frac{1}{2}\rho U^2 (2c)}$$

The above equation can be split into two parts, one due to frictional forces and the other due to pressure forces.

$$C_D = C_{DF} + C_{DP} \quad \text{and} \quad C_L = C_{LF} + C_{LP}$$

Where, C_{DF} and C_{DP} are the friction and pressure components of the drag coefficient and C_{LF} and C_{LP} are the friction and pressure components of the lift coefficient respectively.

The calculated values of C_{DF}, C_{DP} and C_D for Re_{2c} = 1000 and $\alpha = 0^0$, when the flow is symmetric about the major axis are plotted in figure 5.4. The figure shows that the contribution of frictional force to the total drag coefficient C_D is relatively small.

In the case of flow past an inclined elliptic cylinder ($\alpha = 30^0$), lift is present unlike the symmetrical case $(\alpha = 0^0)$. The calculated values of C_D and C_L are plotted as shown in figure 5.6 and 5.7 respectively for the case of $\alpha = 30^0$. These figures indicate a periodic variation of the flow field associated with vortex shedding. The comparison of C_D found in $\alpha = 30^0$ with the corresponding one in the case of $\alpha = 0^0$ for the same time interval ($0 < \tau < 10$) indicates that the C_D curve shows non-periodic behavior in the case of $\alpha = 0^0$, whereas in the case of $\alpha = 30^0$, the C_D curve shows a periodic behavior after a transition period when $\tau = 6$. Figure 5.7 illustrates an interesting behavior of the lift coefficient, C_L, where it takes negative values almost at $\tau = 8$. This unusual behavior of negative lift was also presented by

Taneda [12, 13] experimentally. In order to explain this phenomenon, the streamlines patterns shown in figure 5.5 can be matched with the time variation of C_L given in figure 5.7. The decrease in C_L started approximately at $\tau = 5$, which marks the beginning of detachment of the first vortex and the formation of the second vortex at the upper surface of the cylinder as shown in figure 5.5(g, G). At $\tau = 8$ (approx.), the first vortex started shedding away from the surface (figure 5.5(h,H)) causing a net circulation in the reverse direction and resulting in the negative lift.

5.2 INSTANTANEOUS STREAMLINES OF THE PRESENT FLOW FIELD

Figure 5.8 to figure 5.19 represent the instantaneous stream lines development of the flow field for all test cases of the present numerical problem and figure 5.20 for a circular cylinder. Actually the wake region can be classified into some flow regimes based on the Reynolds number such as laminar steady regime, laminar vortex shedding regime, wake transition regime, shear layer transition regime, asymmetric reattachment regime (critical transition), symmetric reattachment regime (or supercritical regime) etc. From the visualization of the flow field, it can be said that for the three Reynolds numbers used in the present numerical problem, the flow fields were in the laminar vortex shedding regime. As the wake moves downstream, it starts interaction with the boundary layer on the plate by advecting low speed fluid from the wall into the outer region and high speed fluid from the core towards the wall, as rollers of alternating rotation are convected above the boundary layer and so the shape of the streamlines found in the figures are in wavy shape.. The interaction procedure of the cylinder wake and the boundary layer of the flat plate can be divided into three stages [42]. In the first stage, the wake and the boundary layer are separated and can be well represented by the usual relationships (i.e. only the wake behaviors behind an elliptic cylinder and the boundary layer on the plate for undisturbed flow individually) as shown in the figure 5.1.

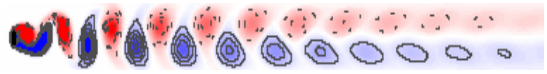

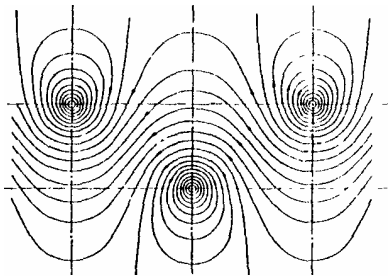

Figure 5.1a: Streamlines in a regular vortex street behind the elliptic cylinder.

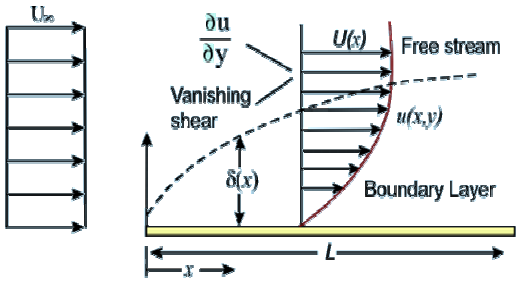

Figure 5.1b: Flow over a flat plate

The second stage corresponds to the initial merging of the wake and the boundary layer and is the most important and the most complicated in the evolution of the merging flow. Here, the outer part of the wake and the innermost part of the boundary layer are substantially unaffected by the interaction, although the flow in the merging region is completely different from that in the undisturbed flow. In the final stage, the merging flow disappears and the layer gradually reverts to a new thicker boundary layer (as found mostly in figures 5.8, 5.9, 5.10, 5.12, 5.13, 5.16, 5.17). The wake spreads outward from the source until its energy is lost, usually by friction or dispersion and becomes weaker. Strong inviscid-viscid interaction takes place in the form of an eruption in the boundary layer and these eruptions and the vortices penetrate into the wake region and weaken the vortex formation in the shear layer [43]. The merging distance depends, of course, on the spreading rate of the wake and on the boundary-layer growth (i.e. on the Reynolds number), as well as on the initial distance between the wake and the solid body. The shape of the body that forms the wake is also affect the merging distance. Under the effect of the bluff body (circular cylinder) the thickness of the boundary layer of the flat plate gets thicker than that of a streamlined body (elliptic cylinder).

An interesting feature also found in figures 5.11, 5.14, 5.15, 5.18, 5.19 and 5.20, is that when the wake interacts with the plate boundary layer, there develops some

vortices or bubbles. It can be explained as that the molecular diffusion in some places in the laminar boundary layer is often small as compared with the existing pressure gradients of the plate. The transport of streamwise momentum across the boundary layer is therefore not sufficiently large to prevent a deceleration of the innermost fluid which eventually begins to flow separation. The separated shear layer which is formed curves back to the plate surface and forms a shallow region of reverse flow called separation bubble. From the flow field it can be said that at high Reynolds numbers the size of the bubble becomes small. Figure 5.14, 5.17, 5.18 shows that the separation bubbles acts only to displace the above fluid almost without affecting the pressure distribution. These bubbles are referred to as short bubbles [44]. In the present flow cases these short bubbles are further affected by the cylinder wakes i.e. change in the flow condition occurs (according to [45] an increase of incidence or a reduction in speed) and the "short bubbles" are "burst" to form a "long bubble" (found in present numerical simulation) or an unattached free shear layer (not found here). The bursting mechanism can be stated as that the supply of kinetic energy from the shear layer to the bubble must balance the loss through viscous dissipation and that, it may be necessary for the bubble to expand to maintain equilibrium. There are always generation of this "mushroom-like" core very early stage from the leading edge and convected downstream while creating secondary instability roles over the plate. Visualizing the streamlines of the present numerical problem it is found that, as the elliptic cylinder position changes streamwise from the left to the right of the plate leading edge the size of the bubbles also increases due to the combined action of the cylinder wake and the leading edge of the plate. Again the core size was biggest when the cylinder to plate relative position was smallest i.e. at cylinder elevation of $x_c/2c = 0$ $y_c/2c = 0.75$ because of strong interaction of the wake and the boundary layer.

5.3 INSTANTANEOUS VELOCITY PROFILE

Figure 5.21 to figure 5.34 show the instantaneous velocity distribution (for undisturbed flow) at different streamwise locations on the flat plate for different Reynolds numbers and also for different cylinder to plate relative positions.

Figure 5.21 and 5.22 presents the undisturbed flow field on the flat plate. The shapes of the velocity profile for all axial locations of undisturbed flow are similar to Blassius profile. The figure 5.20 shows that the thickness of the velocity profile increases with the increase of axial distance from the leading edge of the plate for the same Reynolds number and figure 5.22 shows that the boundary layer thickness decreases with the increase in Reynolds number for same axial location of the plate.

An overall picture of the boundary layer-cylinder wake interaction could be obtained, by studying the velocity profiles. The velocity profiles of all cases, for several streamwise locations, are presented from figure 5.23 to 5.34 for a particular non-dimensional time $\tau = 800$. From the visualization of the velocity profiles, it can be said that the shape of the profiles are largely dependent on the combined effect of Reynolds number, cylinder to plate relative position, size of the wake, the presence and size of the separation bubble. But in general (Figure 5.35), in every velocity profile, two regions could be identified. The first one was a wake region; it appeared downstream of the cylinder, creating a velocity defect which gradually disappeared with the streamwise distance. The second was the boundary layer region. In this case the velocity distribution, up to the point of interaction, followed the shape of Blasius profile, indicating that the boundary layer was still laminar. As we move from the plate leading edge to the downstream, it is found that the shape of the streamlines are wavy and the velocity profile is not as Blassius because of the effect of the shed vortices to the near wall region. In this region the wake from the cylinder perturbs the boundary layer by advecting low-speed fluid from the wall into outer region and, and high speed fluid from the core towards the wall, as rollers of alternating rotation are convected above the boundary layer. Thus approximately S-shaped velocity profile under the influence of wake vortices is identified. As the wake decays, the

advection effect becomes less significant. In the low Reynolds number cases (in the present problem) the flow tends towards a more quiescent state towards the end of the computational domain and the statistics never reach turbulent level. Figure 5.35 shows the variation of the velocity profiles at a particular axial location on the plate (Xp = 100mm) as the wake vortices moves downstream the computational domain. For $\tau = 505$ it is found that the lower vortex advects the low speed fluid to the outer region and the stramlines shows a peak here. From the corresponding velocity profile it is clear that upto about the vertical distance of the domain, y = 0.0072m (or 7.2 mm) the velocity profile follows the Blassius profiles shape. After then (y > 7.2 mm) the lower vortex advects the fluid in the boundary layer to the outer region lowering the local streamwise velocity u upto y = 0.018m (indicates the presence of the lower vortex core). Further with the increase of y, u velocity increases and reaches a maximum at about y = 0.035m indicating that there is a region of high velocity above the core of the lower vortex. After then, as y increases u velocity decreases to match the flow field velocity U. According to this, the velocity profile for $\tau = 505$ found is a reversed S shape. As the time increases, the region of the lower vortex gradually shifts downstream the plate and the discrepancy between u and U decreases gradually. But as the region of lower vortex crossing the location of Xp = 100mm, upper vortex region is also moving towards that Xp gradually and at time $\tau = 508$ the upper vortex is along the line Xp = 100mm. The upper vortex tries to push the streamlines towards the plate wall advecting the high speed fluid from the outer region to the wall. In this case, as y increases from the wall, u velocity gradually increases and reaches a maximum value below the vortex core and then u velocity decreases while crossing the upper vortex core. After then, u velocity starts increasing to match the field velocity U. In this case, the velocity profile found is an S- shaped. In this present numerical simulation, the velocity profiles found in the different flow conditions almost follows the sequential behavior found in Figure 5.35.

For a particular gap ratio (cylinder to plate relative position) and Reynolds number, it is clearly observed that the boundary layer thickness increases with the increase of plate axial location. This is due to, wake vortices widen further downstream and thus

the merging of wake vortices with boundary layer occurs in large scale. More wake vorticity elements available in the boundary layer which can interact more with increasing plate axial locations. Thus velocity deficit starts (for wake region) somewhat earlier in upward direction from the plate with increasing the streamwise positions. It can be concluded that if the plate length is much more than 600mm (as in present numerical problem), there may be a region when the velocity profile will follow the Blassius profile due to weak interation of the wake and boundary layer. In some velocity profiles it is found that there is region of undershoots ($0<u/U<1$) following the overshoot region (vortex centre where $u/U > 1$) from the plate to the upward direction. In some cases, (say in figure 5.23, 5.24, 5.25 etc.) this nature is found before the wake vortex center. The reason for such behavior seems to be connected with the existence of secondary flow of a kind which is similar to that on a lift-generating body. Again some profiles exhibit a negative behavior i.e. $u/U < 0$ indicating the presence of a separation bubble on the plate surface.

While changing the cylinder to plate relative position from $x_c/2c = -3$, $y_c/2c = 1$ to $x_c/2c = 3$, $y_c/2c = 1$, i.e. from left to right of plate leading edge with same elevation, and also for $x_c/2c = 0$ $y_c/2c = 1$ to $x_c/2c = 0$ $y_c/2c = 0.75$, the boundary layer thickness for the same axial location of the plate, decreases (figure 5.27, 5.28 and 5.29) due to the effect of the wake size before coming into the contact with the plate and wake boundary layer interaction. But there were some exceptions in the case when the cylinder to plate relative position was $x_c/2c = 0$ $y_c/2c = 0.75$. When the cylinder is located at $x_c/2c = -3$ $y_c/2c = 1$, the wake size is larger before it merges the plate compared to that when the cylinder is located at $x_c/2c = 0$ $y_c/2c = 1$ and so the boundary layer thickness is large fro cylinder location at $x_c/2c = -3$ $y_c/2c = 1$ to $x_c/2c = 0$ $y_c/2c = 1$ and so on.

With the increase in Reynolds number for any comparable gap ratio, the free stream disturbance level increases due to the inherent increase in vortex street strength.

Figure 5.34 shows the comparison of velocity profile due to the effect of the wake induced from a circular cylinder (bluff body) and an elliptic cylinder (streamlined

body) with the same projected height at the centers of them (i.e. considering the diameter of the circular cylinder, d = 2b, where 2b is the minor axis of the elliptic cylinder) and for the same elevation of the location of them ($x_c/2c = -3$ $y_c/2c = 1$) and also for the undisturbed profile. The figures clearly show that the boundary is much thicker for circular cylinder than for elliptic cylinder indicating that bluff body (circular cylinder) wake size is larger than that of streamlined body (elliptic cylinder). As the flow goes downstream, the wake behind the circular cylinder is spread out toward the wall region. On the other hand, the wake behind the elliptic cylinder has less influence on the near-wall region compared to the circular cylinder. Therefore, the wake region formed inside the boundary layer is smaller than that of the circular cylinder.

5.4 BOUNDARY LAYER INTEGRAL PARAMETERS

The boundary layer integral parameter such as displacement thickness (δ_1), momentum thickness (θ), shape factor (H), are of particular interest to turbine designer, since they provide an accurate first estimation of the quality of the designed blade.

Figure 5.36 to 5.52 show the spatial and temporal variation of displacement thickness (δ), momentum thickness (θ) and shape factor (H). From this figures it is observed that the boundary layer integral parameters exhibit the fluctuating behavior. The values of boundary layer integral parameters change with time. In unsteady disturbed boundary layer, always there are some fluctuating behaviors compared to undisturbed boundary layer analysis. Table 5.2 shows the values of boundary layer integral parameters found in the present numerical simulation for undisturbed flow on flat plate for $Re_{2c} = 500$

Table 5.2: Undisturbed boundary layer integral parameter for $Re_{2c} = 500$

x_p(mm)	δ(mm)	θ (mm)	H
100	3.02	1.14	≈ 2.64
200	4.31	1.64	≈ 2.633
300	5.31	2.02	≈ 2.628
400	6.16	2.35	≈ 2.625
500	6.92	2.64	≈ 2.623
600	7.63	2.91	≈ 2.613

Figure 5.36 and 5.37 show the variation of displacement thickness, momentum thickness and shape factor with the plate axial location for undisturbed flow condition. For a particular Reynolds number (figure 5.36), both the displacement thickness and momentum thickness increases with the increase in plate axial length exponentially (for laminar flat plate both δ and θ are proportion to $Xp^{1/2}$) but ultimately their ratio i.e. the shape factor remain same i.e. H ≈ 2.6 indicating that the flow is laminar. Observing figure 5.37, it is clear that both the displacement thickness and momentum thickness decreases with the increase in Reynolds number (for laminar flat plate both δ and θ are proportional to $Re_x^{-1/2}$) but the shape factor remains constant for all the Reynolds number.

Figure 5.38 to figure 5.49 presents the temporal variation of the boundary layer integral parameters, each for a particular Reynolds number and a particular cylinder to plate relative position. From each of the figures, it is found the parameters show a regularly shaped fluctuating behavior for a definite time period and this fluctuation is due to the periodic affect of the cylinder wake on the plate boundary layer.

For a particular Reynolds number and a particular cylinder to plate relative position, the trend of graphs of thicknesses and shape factor exhibit that with the increase of plate axial distance, the amplitude of the fluctuations gradually decreases but the numerical values of the thicknesses were increases (except for the cases when the

cylinder was positioned at very near the plate leading edge i.e. $x_c/2c = 0$ $y_c/2c = 0.75$). This behavior may be due the fact that there was strong interaction near the plate leading edge where the size of the wake was small (sharp sinusoidal behavior of streamlines showing peak and valleys) and as the wake passes forward i.e. to the downstream of the plate the interaction was weaker and the wake size became larger (sinusoidal behavior of streamlines almost damped out). Negative value of momentum thickness is found when the wake from the cylinder perturbs the boundary layer by advecting low-speed fluid from the wall into outer region and positive peak is found when the wake perturbs the boundary layer by advecting high speed fluid from the core towards the wall. Other values are found for the time interval between two vortices crossing a fixed axial length of the plate. The value of shape factor is totally dependent on the ratio of the displacement and momentum thicknesses, or more clearly on the value of u/U, i.e. whether $u/U < 0$ (when separation bubble is present), or $u/U = 0$ (at the point of separation), or $0<u/U<1$ or $u/U > 1$. On average, the value of shape factor H is found about 3 (> 2.6 for laminar flat plate consideration) or more indicating that there is always a tendency of flow separation [40].

Figures 5.41, 5.45 and 5.49 for the cases when the cylinder was placed very close to the plate leading edge i.e. for $x_c/2c = 0$ $y_c/2c = 0.75$, the regular fluctuating behavior of the thicknesses was not found. Rather the thicknesses varied randomly with time and so the shape factor. This random behavior is mainly due to the strong interaction of the cylinder wake and the flat plate boundary layer. Due to this interaction, separation bubbles were found in some places on the plate and these bubbles also burst in some cases at different time.

For a particular cylinder to plate relative position, observing the figures of boundary layer integral parameter, it can be say that, as the Reynolds number increases the value of displacement and momentum thickness decreases and so the shape factor (figure 5.50), found in the plate length after Xp = 300 mm. But the case $x_c/2c = 0$ $y_c/2c = 0.75$ shows a random behavior.

Again, for particular Reynolds number, the shape factor found in the present simulation to increase as the cylinder moves closer to the flat plate (figure 5.49).

5.5 SKIN FRICTION DEVELOPMENT ON THE PLATE SURFACE

Figure 5.53 shows the variation of skin friction with the plate streamwise axial position. For the undisturbed flow case and also for the disturbed cases with the presence of cylinder wake, it is found that as the axial distance of the plate increases, skin friction decreases for a particular Reynolds number. This trend can be found in literature. For undisturbed flow case, the figure slows that, with the increase of Reynolds number, skin friction decreases. This behavior is also found for the disturbed cases of figure 5.53 (b) and (c) but not in Figure 5.53 (d) and (e) when the cylinder wake affected the boundary layer. The discrepancies for the case (d) and (e) is due to the random generation of separation bubble. At the point of separation, skin friction shows a peak, inside the bubble it drops down.

Figure 5.54 shows the variation of skin friction with different plate axial location for different cylinder to plate relative position, at a particular Reynolds number. From the figure it is clear that, as the cylinder moves closer to the plate, the interaction between the cylinder wake and plate boundary layer becomes stronger and the skin friction increases, except for case (b) and (c) for Re = 800 and also for Re = 1000, when the cylinder was plate after the leading edge of the plate at that instant for τ = 500. This behavior may not be found in another instant of time. Actually these cases are complicated to explain due to incident of combined effect of wake itself and further the wake-separation interaction. In general, the value of skin friction for undisturbed flow on the flat plate was found the below (not very large amount) the disturbed flow. In each case, the skin friction starts from a perturbed laminar value that does not coincide with the Blasius profile. This is due to the combination of the proximity to the leading edge (where Blasius similarity is invalid) and the free-stream acceleration due to the .flow obstruction by the cylinder, which causes the initial skin-friction undershoot.

Figure 5.55 shows the variation of time-average skin friction with Reynolds number for different cylinder to plate relative position. The general trend shows that as the Reynolds number increases skin friction decreases because of lower viscous effect on the plate except for the case when the cylinder was nearest to the plate. This may be due to the fact that there was much more interaction comparing the other cases and the flow may be in the transition region.

Figure 5.56 exhibit the comparison of skin friction for the cases of without cylinder i.e. undisturbed flow and with cylinder with axis ratio. From the figure it is clear that as the axis ratio increases i.e. b/a = 0 (for elliptic cylinder) to b/a = 1 (for circular cylinder), the skin friction increases. In both cases the skin friction that found was larger than the skin friction found for undisturbed case when the axis ratio is 0.

5.6 BOUNDARY LAYER TRANSITION

Wake-induced boundary-layer transition in the present configuration depends both on the physical distance from the plate leading edge, *x/D*, and on the plate Reynolds number, Re_x .The former dependence appears as an 'interaction distance', the physical streamwise distance required for the wake disturbance to contaminate the boundary layer, while the Re_x-dependence enters through the degree of boundary-layer instability, which increases with Re_x. From the above observations, we conjecture that transition may depend on a Reynolds number based on the distance from the impingement point.

In the present computation, the Reynolds number Re_{2c} is fairly low so that the boundary layer remained laminar over the full plate length when no disturbing wakes are present. When wake passes over the plate, the free stream was intermittently disturbed by wakes. Underneath the wake disturbed free stream, the boundary layer become transitional quite early.

The transition point can be identified from the skin friction plots on the plate streamwise location. In general, when the Cfx (present problem) crosses the Cf curve for the Blassius laminar flow and increase continuously and sharply after that, the x-location on the plate where the Cfx interact the Cf curve for the Blassius laminar flow, is considered as the onset of transition. From visualization of the figures 5.51, the onset of transition is typically difficult to identify. Because the curves show fluctuating behavior of laminar and turbulent region randomly. This is due to the fact that wake induced transition may be considered as bypass transition i.e. some of the initial stages of the natural transition process do not take place or bypass. This task is difficult and the underlying physics of by-pass transition is not yet very well understood. It becomes essential to capture the coupling between large freestream wake disturbances and the pretransitional boundary layer in order to correctly describe transtion.

The overall behavior of the curves of figure 5.54 show that the flow field very close to the undisturbed laminar case at that instant. The Cfx found slightly larger than the undisturbed laminar case. Although the laminar boundary layer is buffeted by the shed vortices, it remains stable and no transition is observed within the computational domain. The overall flow field may be considered laminar.

CHAPTER 6

CONCLUSION

Unsteady boundary layer development over a flat plate under the influence of wake vortices induced from an elliptic cylinder is investigated for different cylinder to plate relative positions and also for different Reynolds number. A comparison is also carried out for circular cylinder having the same height of the elliptic cylinder cross-section, for a particular cylinder to plate relative position and Reynolds number. The interaction between the boundary layer developed over a flat plate and the cylinder wake has been studied from the view-point to visualize the effect of the presence of a cylinder in the laminar boundary layer over a flat surface, where the cylinder controls the laminar boundary layer flow.

Two types of boundary layer-wake interaction are obtained from the computations, one is the strong wake-boundary layer interaction and another is the weak wake-boundary layer. The intensity of interaction greatly depends on plate streamwise location, the Reynolds number of the flow and the gap ratio between the plate and the cylinder. The higher the Reynolds number and the lower the gap ratio, the more rapidly the wake loses its coherence, and the more unstable the boundary layer is to perturbation. Despite the difference in the Reynolds number and gap ratio, the mechanism of interaction is the same for all the cases.

The impingement of wake on the boundary layer causes velocity and momentum deficit on the flow field. The boundary layer integral parameters such as displacement thicknesses, momentum thicknesses, and shape factors are also disturbed by wake vortices. The wake vortices and separation bubbles varies the thicknesses randomly and so the shape factor.

Wake vorticity elements can always generate from rotating circular cylinder and affects on the transition in boundary layers. Transitional phenomena are crucially

important to the design of the compressor and the turbines. In the former, about half the loss of stage efficiency at the design point owes to skin friction, which is several times larger in a turbulent boundary layer than in its laminar counterpart. The separation bubble, which usually is laminar at the point of separation, if transitions it will likely reattach to the blade surface and the loss in efficiency is limited. Under some circumstances, the transitional process is slow and the flow reattachment point may move far downstream on the suction surface and the large separated region cause severe losses is stage efficiency.

Bubble bursting creates an increase in drag and an undesirable change in pitching moment. If a very large bubble is formed on bursting, or if the shear layer fails to reattach, there is also an appreciable fall in lift. This is one type of stall the thin aerofoil nose stall. Hence, the technological importance of the present study is sufficiently demonstrated by transition problems on turbines and compressors and on airfoils.

CHAPTER 7

RECOMMENDATIONS FOR FUTURE WORKS

The following recommendations can be put forward for the further works as follow-ups of the present research:

1. Influence of wake generated from elliptic cylinder of different axis ratio and angle of attack, on flat plate boundary layer development.
2. Influence of wake generated from a square cylinder or hexagonal cylinder on plate boundary layer development.
3. To study the influence of a rotationally oscillating circular cylinder on the boundary layer of a flat plate.
4. To study the influence of a transversely oscillating circular cylinder on the boundary layer of a flat plate.
5. The numerical computations can be carried out at higher Reynolds number that is for turbulent region.
6. To extent this study for a sliding flat plate.
7. To investigate the effect of incorporating the turbulence intensity (Tu) on the free stream.

REFERENCES

1. Ota, T., Nishiyama, H. & Taoka, Y., (1984), 'Heat transfer and flow around an elliptic cylinder', International Journal of Heat and Mass transfer, vol. 27, pp. 1771-1779.

2. Ota, T., Nishiyama, H. and Taoka, Y., (1987), 'Flow around an elliptic cylinder in the critical Reynolds number regime', Journal of Fluids Engineering, vol. 109, pp. 149-155.

3. Wang C-Y., (1967), 'Separation and stall of an impulsively started elliptic cylinder', ASME Journal of Applied Mechanics, vol. 34, pp. 823–828.

4. Dennis SCR, Staniforth AN, (1971), 'A numerical method for calculating the initial flow past a cylinder in a viscous fluid', In Proceedings of the 2nd International Conference Numerical Methods in Fluid Dynamics, Lecture Notes in Physics, vol. 8, Holt M (ed.). Springer-Verlag: Berlin,; 343–349.

5. Staniforth AN, (1972), 'Studies of symmetrical and antisymmetrical viscous flows past impulsively started cylinders', PhD thesis, The University of Western Ontario, London, Canada,.

6. Panniker PKG, Lavan Z., (1975), 'Flow past impulsively started bodies using Green's functions', Journal of Computational Physics, vol. 18, pp. 46–65.

7. Lugt HJ, Haussling HJ., (1974), 'Laminar flow past an abruptly accelerated elliptic cylinder at 45° incidence', Journal of Fluid Mechanics, vol. 65, pp. 711–734.

8. Modi, V. J. & Wiland, E., (1970), 'Unsteady aerodynamics of stationary elliptic cylinders in subcritical flow', AIAA Journal, vol. 8, pp.1814-1821.

9. Modi, V.J., and Dikshit, A.K., (1971), "Mean aerodynamics of stationally elliptic cylinders in subcritical flow", Proc. Third Int. Conf. on Wind Effects on Buildings and Structures, Tokyo, pp. 345-355.

10. Modi, V. J. & Dikshit, A. K., (1975), 'Near wakes of elliptic cylinders in subcritical flow', AIAA Journal, vol. 13, pp. 490-497.

11. Badr H.M., Dennis S.C.R. and Kocabiyik S., (2001), "Numerical simulation of the unsteady flow over an elliptic cylinder at different orientations", International Journal for Numerical Methods in Fluids; 37: 905-931.

12. Taneda S., (1972), 'The development of the lift of an impulsively started elliptic cylinder at incidence', Journal of the Physics Society of Japan, vol. 33, pp. 1706–1711.

13. Taneda S., (1977), 'Visual study of unsteady separated flows around bodies', Progress in Aerospace Science, vol. 17, pp. 287–348.

14. Addison, J. S. & Hodson, H. P. (1990), "Unsteady Transition in an Axial-Flow Turbine: Part 1- Measurements on the Turbine Rotor", Journal of Turbomachinery, vol. **112**, pp. 206-214

15. Schobeiri, M.T., Öztürk, B. and Ashpis, D.E., (2003), "On the Physics of Flow Along a Low Pressure Turbine Blade Under Unsteady Flow Conditions", Proc. ASME Turbo Expo Power for Land, Sea and Air, pp. 1-16.

16. Valkov, T. V. & Tan, C. S. (1999), "Effect of Upstream Rotor Vortical Disturbances on the Time-Averaged performance of Axial Compressor Stators: Part 2- Rotor Tip Vortex/Streamwise Vortex-Stator Blade Interactions", Journal of Turbomachinery, vol. 121, pp. 387-397

17. Lee, T. & Gerontakos, P. (2004), "Investigation of flow over an oscillating airfoil", J. Fluid Mech., vol. 512, pp. 313-341

18. Holzäpfel, F., Hofbauer, T., Darracq, D., Moet, H., Garnier, F. & Gago, C. F. (2003), "Analysis of wake vortex decay mechanisms in the atmosphere", J. Aerospace Science and Technology, vol. **7**, pp. 263-275

19. Corjon, A. & Poinsot, T. (1997), "Behavior of Wake Vortices Near Ground", AIAA Journal, vol. **35**, pp. 789-855.

20. Kyriakides, N. K., Kastrinakis, E.G., Nychas, S.G., Goulas, A., (1996), "Boundary layer transition induced by a von karman vortex street wake", IMechE, PartG: Journal of Aerospace Engineering, vol. 210**,** pp. 167-179.

21. Choi, J.-H. and Lee, S.-J.,(2000), "Ground effect of flow around an elliptic cylinder in a turbulent boundary layer", Journal of Fluids and Structures, vol. 14**,** pp. 697-709.

22. Orth, U., (1993), "Unsteady Boundary Layer Transition in Flow Periodically Disturbed by Wakes", Journal of Turbomachinery, vol. 115**,** pp. 707-713.

23. Wu, X. and Durbin, P.A., (2000), "Boundary layer transition induced by periodic wakes", Journal of Turbomachinery, vol. 122**,** pp. 442- 449.

24. Wu, X., Jacobs, R.G., Hunt, J.C.R. and Durbin, P., (1999), "Simulation of boundary layer transition induced by periodically passing wakes", J. Fluid Mech., vol. 398**,** pp. 109-153.

25. Schubauer, G.B., (1935), "Air flow in a separating laminar boundary layer", T.R. No. 527, N.A.C.A.

26. Schubauer, G.B., (1939), "Air flow in the boundary layer of an elliptic

cylinder", T.R. No. 652, N.A.C.A.

27. Delay, N.K. and Sorensen, N.E., (1953), "Low-speed drag of cylinders of various shapes", NACA Tech. Note No. 3038.

28. Yano, H., and A. Kieda, (1980), "An approximate method for solving two-dimensional low-Reynolds-number flow past arbitrary cylindrical bodies", J. Fluid Mech., 97, pp. 157-159.

29. Honji, H., (1972), "Starting flows past spheres and elliptic cylinders", Reports of the Research Institute of applied Mechancis, Khushu University, Japan, Vol. XIX, No. 65.

30. Shintani, K., Umemura, A., and Takano, A., (1983), "Low Reynolds number flow past an elliptic cylinder", J. Fluid Mech., vol. 136, pp. 277-289.

31. Patel, V.A., (1981), "Flow around the impulsively started elliptic cylinder at various angle of attack", Computers and Fluids, vol. 9, pp. 435-462.

32. Nair, M.T., and Sengupta, T.A., (1997), "Unsteady flow past elliptic cylinders", J. Fluids and Structure, vol. 11, pp. 555-595.

33. Mittal, R. and S. Balachandar, (1996), "Direct numerical simulation of flow past elliptic cylinder", J. Computational Phys., vol. 124, pp. 351-367.

34. Allessio, S.J.D.D. and Kocabiyik, S., (2001), "Numerical simulation of the flow induced by a transversly oscillating elliptic cylinder", J. Fluids Struct., vol. 15, pp. 691-715.

35. Johnson, S.A., Thompson, M.C. and Hourigan, K., (2001), "Flow past elliptic cylinders at low Reynolds numbers", 14th Australian Fluid Mechanics Conference Adelaide University, Australia.

36. Schlicting, H., (1979), *Boundary Layer Theory,* Seventh edition, Mcgraw-Hill Inc., New York.

37. Morkovin, M. V., (1969), "On the many phases of transition", In Viscous Drag Reduction, (Ed. G.S. Wells), pp. 1-31, New York.

38. Mayle, R. E., 1991, The role of laminar-turbulent transition in gas turbine engines. *ASME paper, 91*-GT-261.

39. Liu, X., and Rodi, W., (1991), "Experiments on transitional boundary layers with wake induced unsteadyness", J.Fluid Mech., vol. 231, pp. 229-256.

40. Savill, A., and Zhou, M., (1983), "Wake/boundary layer and wake/wake interactions-smoke flow visualization and modeling", Proceedings of the second Asian Congress of Fluid Mechanics, pp. 743-754.

40. White F.M. (1999), *Fluid Mechanics,* Fourth edition, Mcgraw-Hill Companies, Inc.

41. Reddy, J. N. & Gartling, D. K. (1994), The Finite Element Method in Heat Transfer and Fluid Dynamics.

42. Squire, L. C., (1989), "Interactions between wakes and boundary layers", Prog. Aerospace Sci., vol.-26, pp.-261-288.

43. Doligalski**,** T. L. and Walker**,** J. D. A., (1984), "The boundary layer induced by a convected two-dimensional vortex". J. Fluid Mech., vol. 139, pp.1-28.

44. Walker, J., (1989), "Wall layer eruptions in turbulent flows", In Structure of turbulence and drag reduction, (Ed A. Gyr), IUTAM Symposium, Zurich, Switzerland, pp. 109-117.

45. Gaster, M., (1967), "The structure and behavior of separation bubbles" reports and Memo no. 3595.

46. Hodson H. P., Addison J. S., and Shepherdson C. A., (1992), "Models for Unsteady Wake-Induced Transition in Axial Turbomachines", J. Phys. III France vol. 2, pp. 545-574.

47. http://en.wikipedia.org/wiki/Wake_turbulence

48. Ovchinnikov Victor, (2006), "Numerical Simulation of Boundary Layer Transition Due to External Disturbances", Ph. D Thesis. University of Maryland.

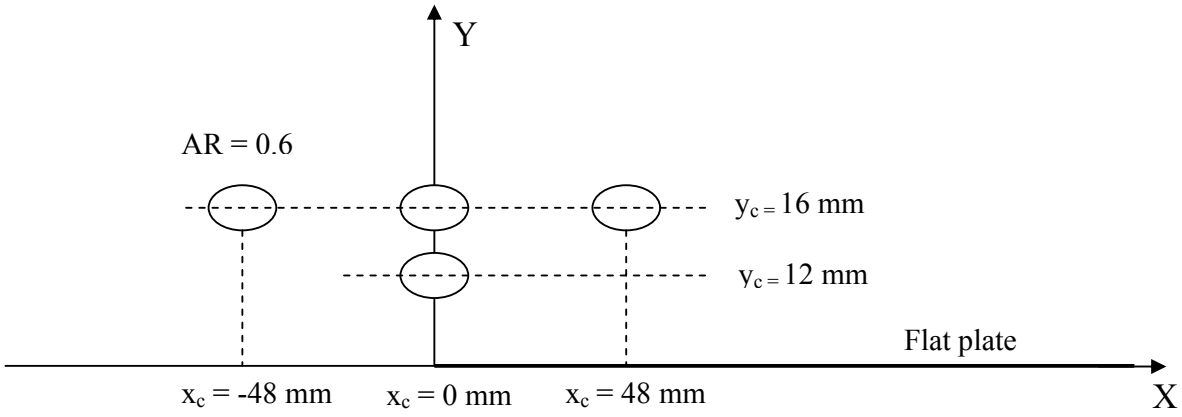

Figure 5.2: Positions of elliptic cylinder of all test cases.

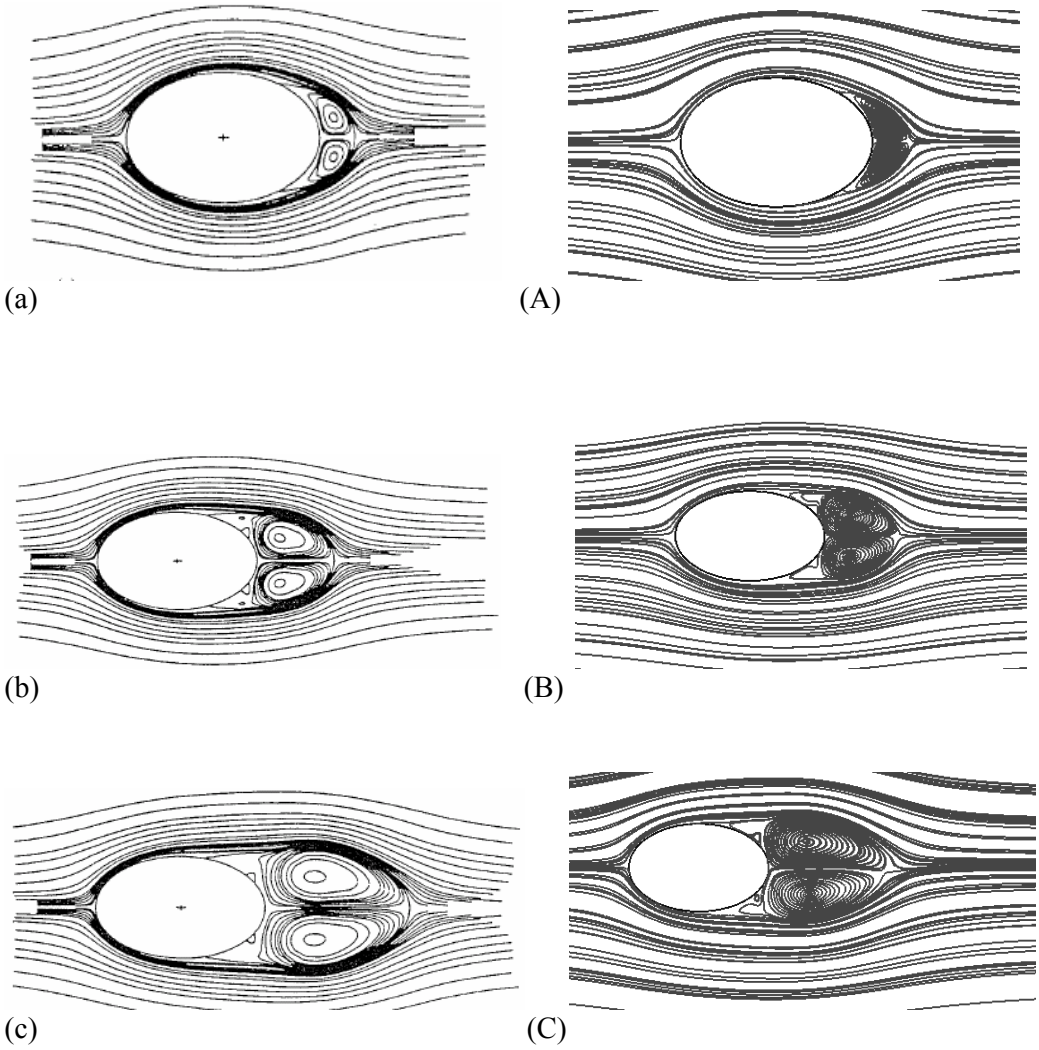

Figure 5.3: Comparison of Instantaneous streamlines of the flow for Re_{2c}=1000, and $\alpha = 0^0$: (a,A) $\tau = 2.0$; (b,B) $\tau = 5.0$; (c,C) $\tau = 10.0$. (a-c) Flow visualization by Badr, Danis and Kocabiyik and (A-C) Present Finite Element Computation.

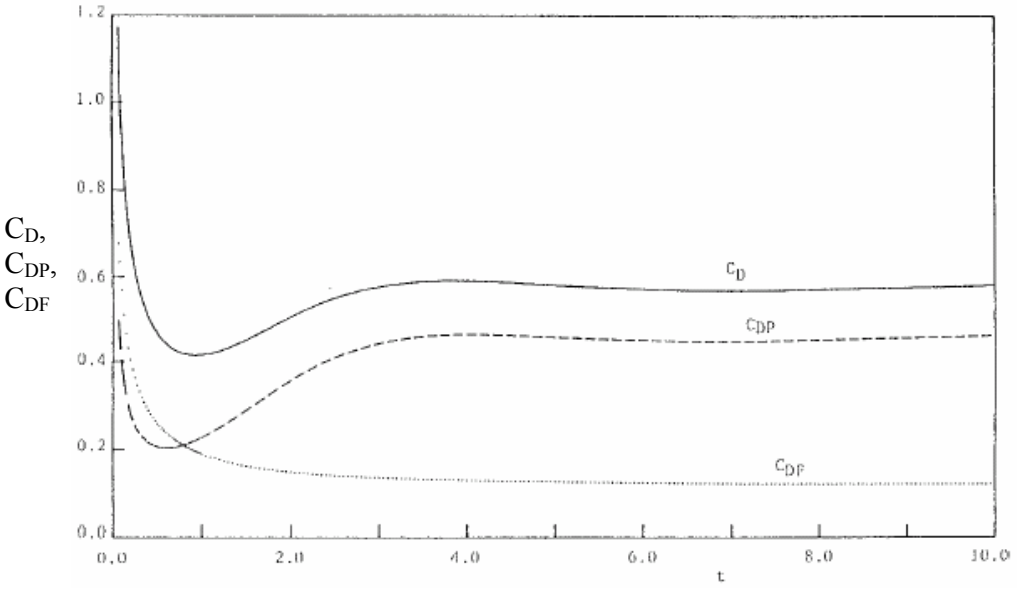

(a)

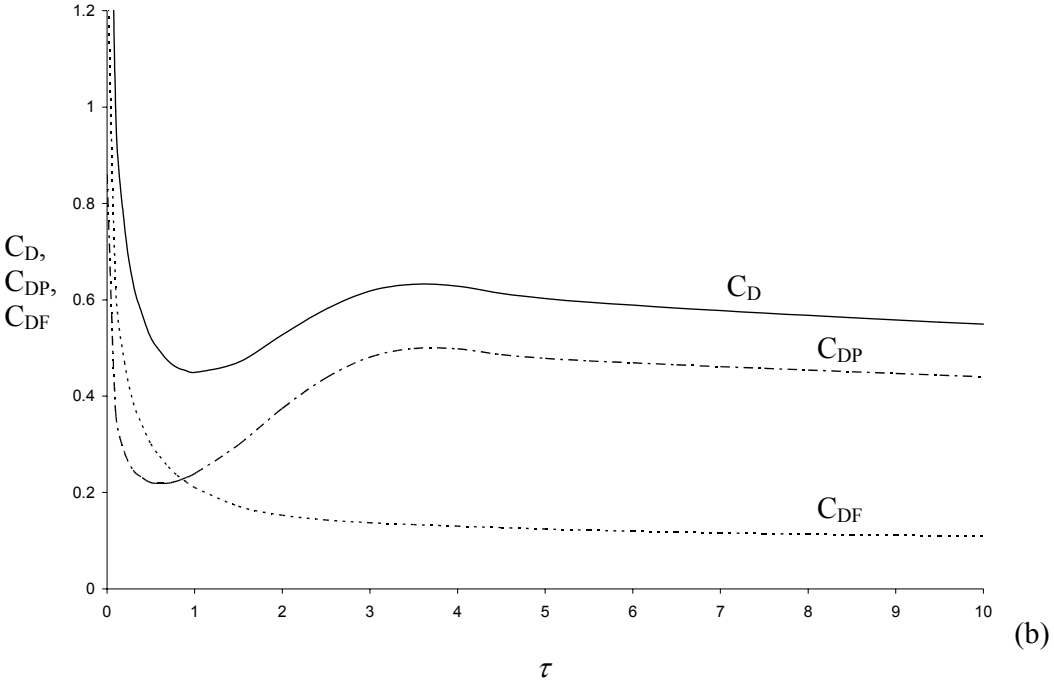

(b)

Figure 5.4: Variation of the Drag Coefficients C_D, C_{DF}, and C_{DP} with τ at Re_{2c} = 1000 and $\alpha = 0^0$. (a) results from Badr, Danis and Kocabiyik, (b) Present Finite Element Computation.

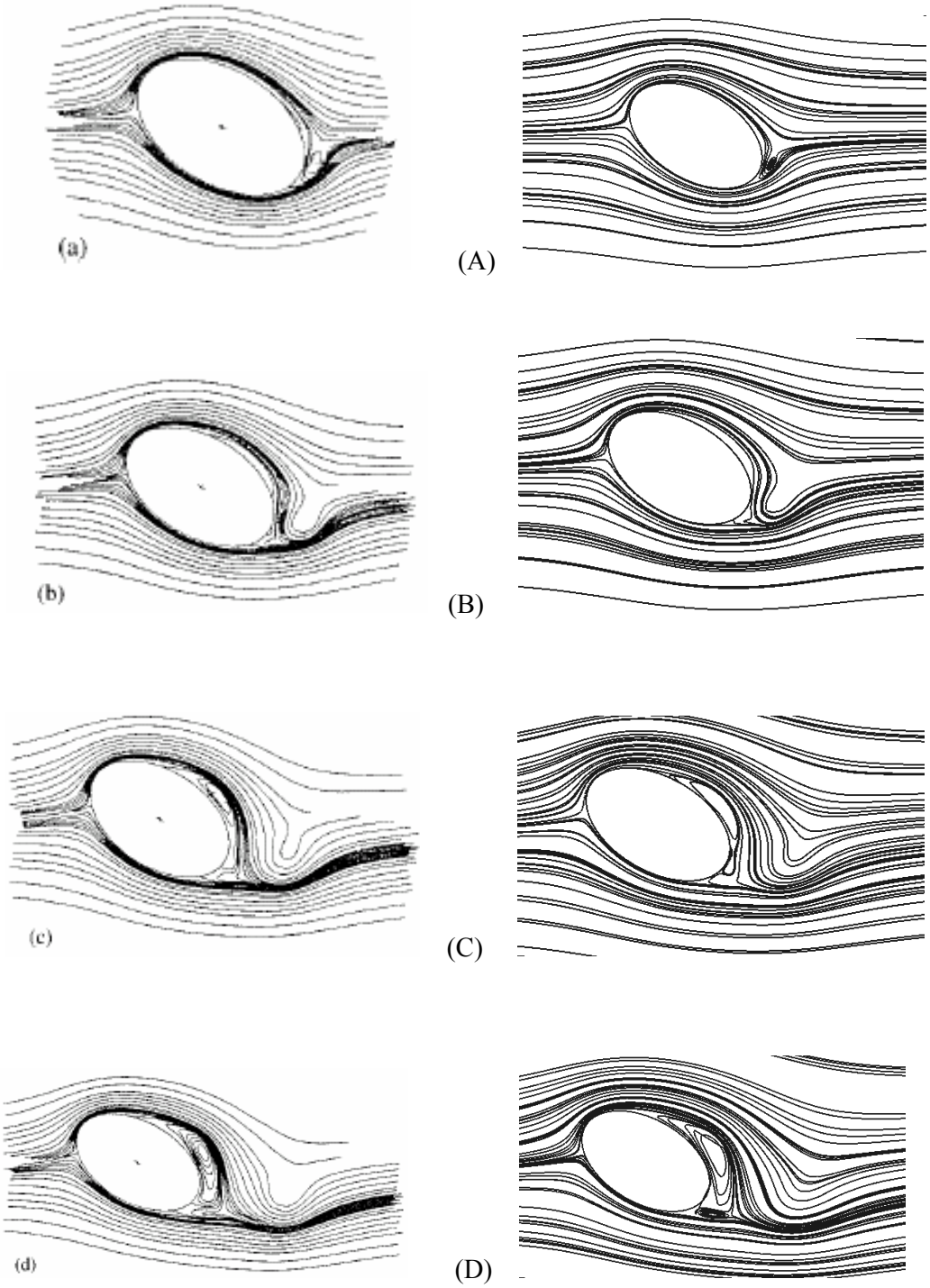

Figure 5.5: (a,A,b,B,c,C,d,D) (Continue…)

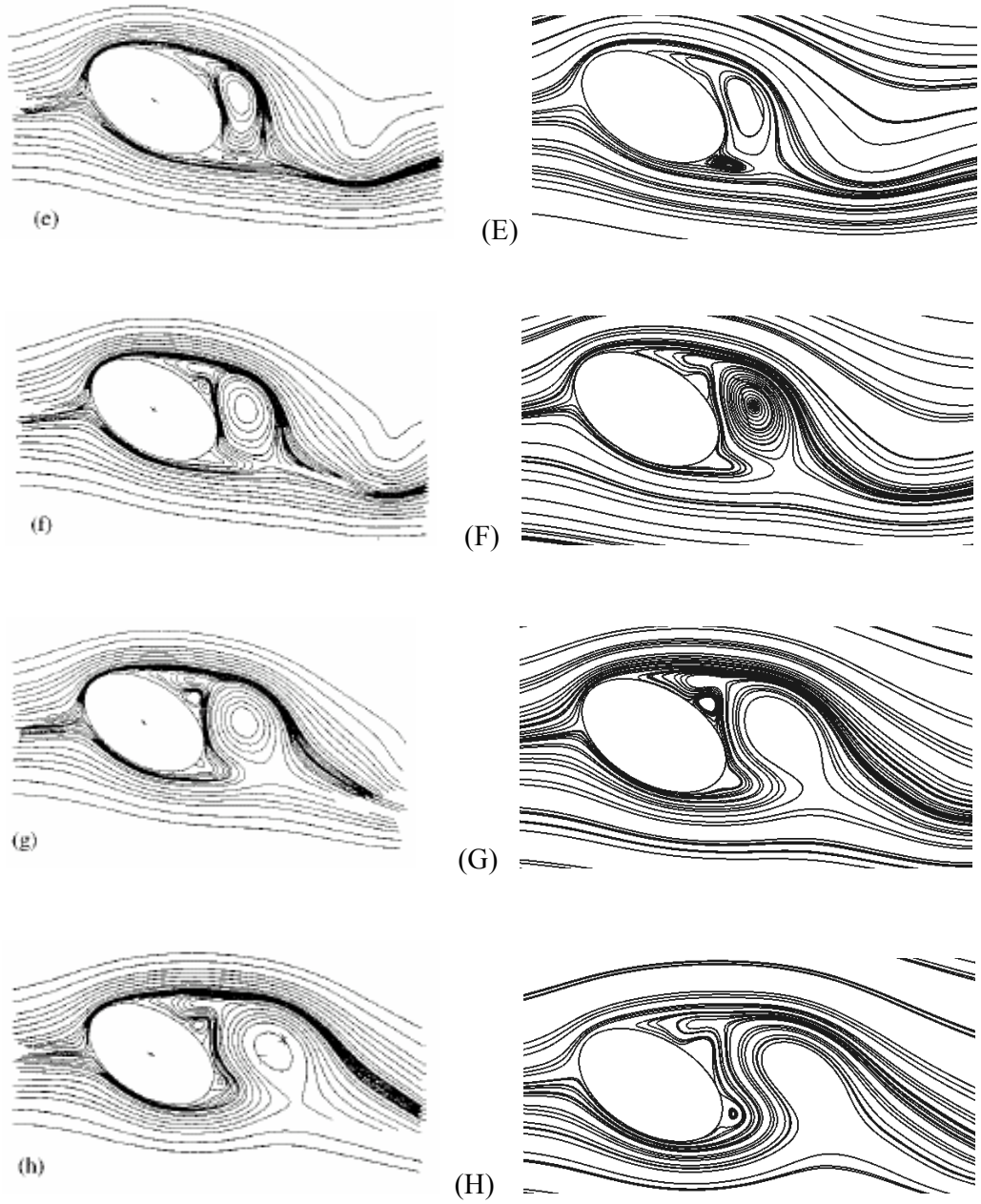

Figure 5.5: Comparison of Instantaneous streamlines of the flow for Re_{2c}=1000, and $\alpha = 30^0$: (a,A) τ = 1.0; (b,B) τ = 2.0; (c,C) τ = 3.0; (d,D) τ = 4.0; (e,E) τ = 5.0; (f,F) τ = 6.0; (g,G) τ = 7.0; (h,H) τ = 8.0. (a-h) Flow visualization by Badr, Danis and Kocabiyik and (A-H) Present Finite Element Computation.

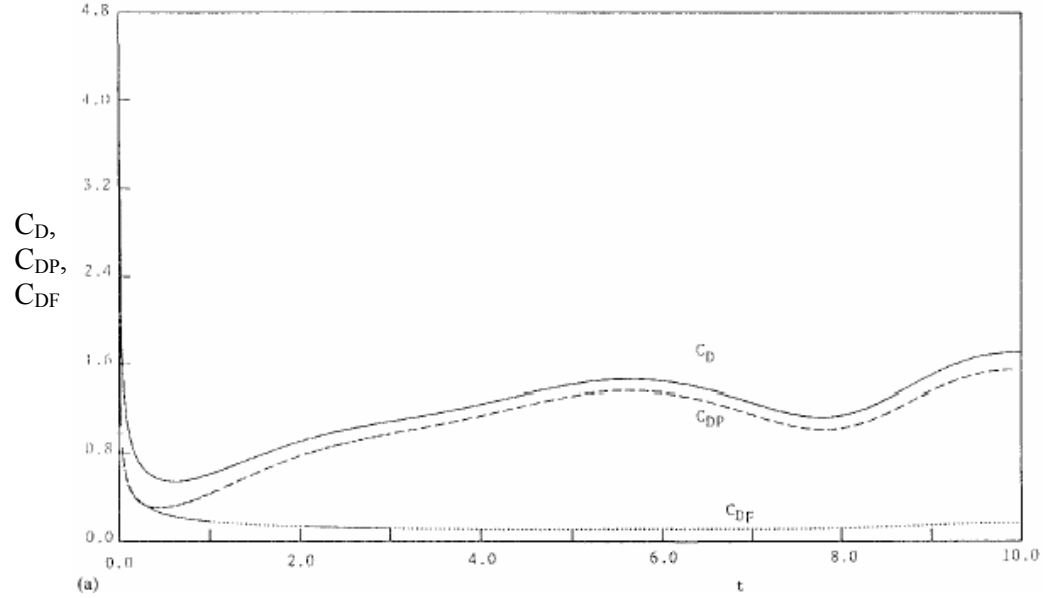

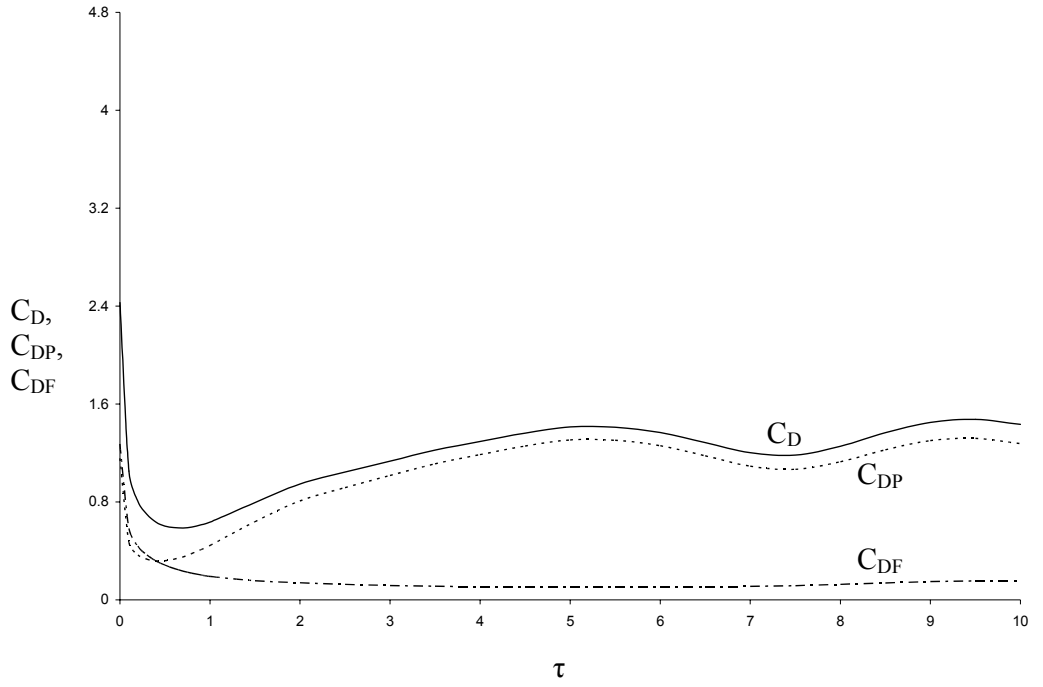

(A)

Figure 5.6: Variation of the Drag Coefficients C_D, C_{DF}, and C_{DP} with τ at Re_{2c} = 1000 and $\alpha = 30^0$. (a) results from Badr, Danis and Kocabiyik, (A) Present Finite Element Computation.

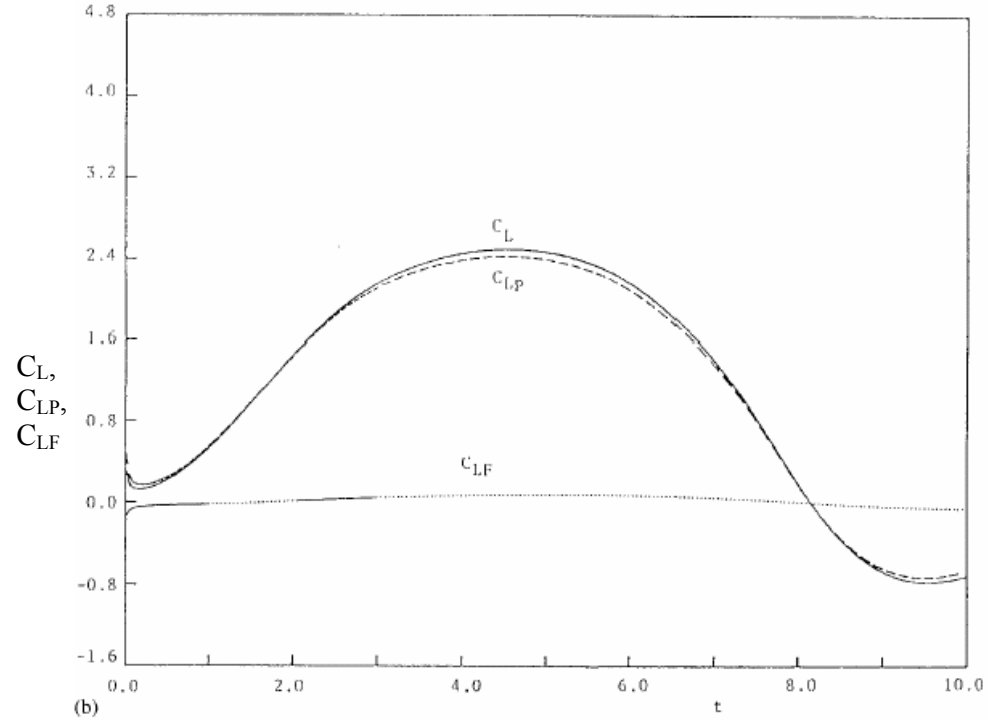

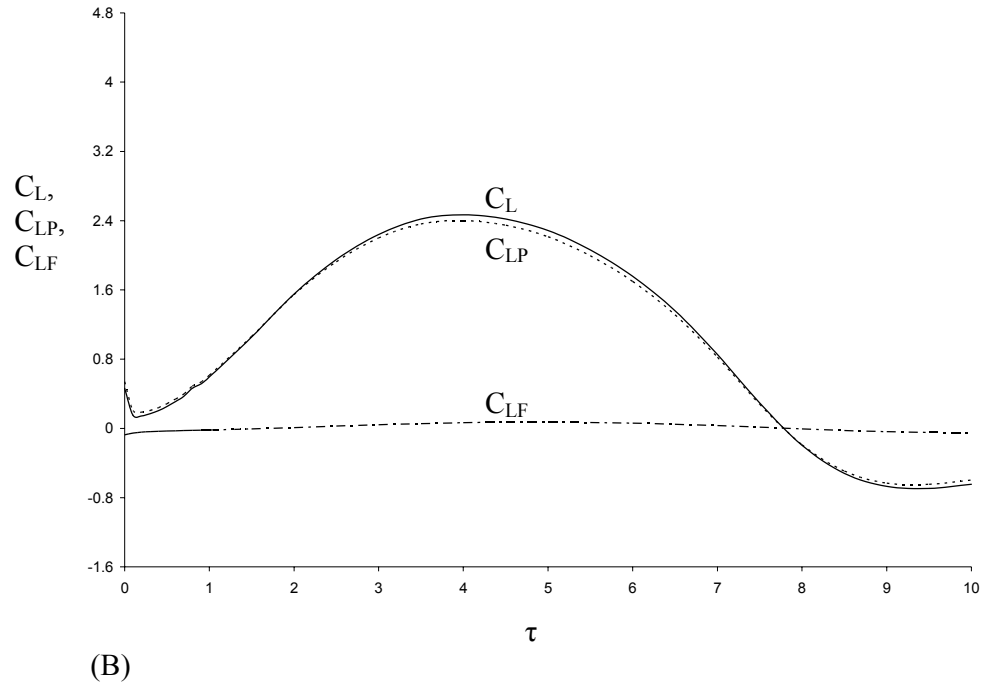

(B)

Figure 5.7: Variation of the Drag Coefficients C_L, C_{LF}, and C_{LP} with τ at $Re_{2c} = 1000$ and $\alpha = 30^0$. (b) results from Badr, Danis and Kocabiyik, (B) Present Finite Element Computation.

$\tau = 50$

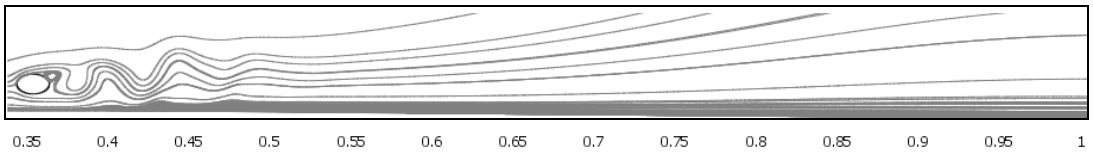

$\tau = 80$

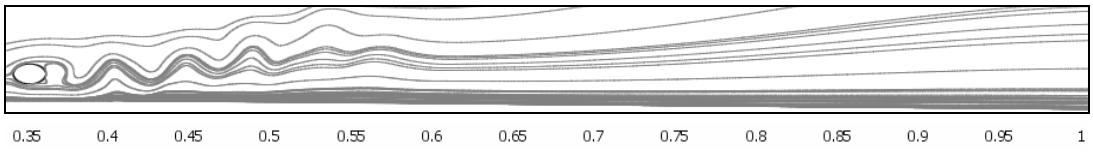

$\tau = 100$

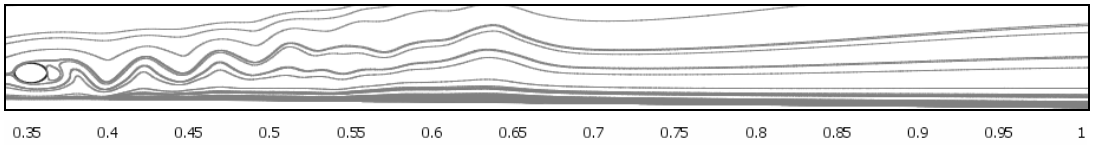

$\tau = 120$

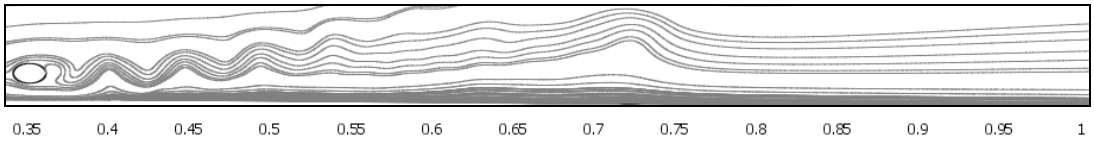

$\tau = 150$

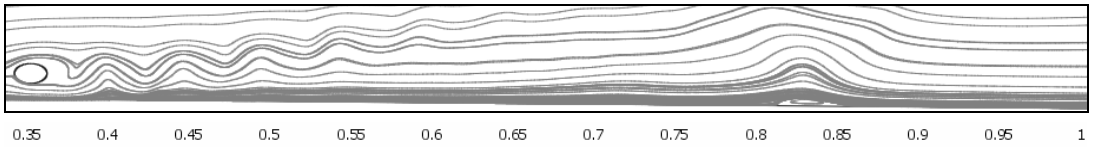

$\tau = 170$

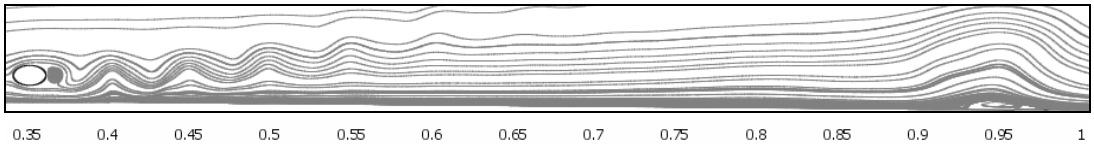

X (m)

Figure 5.8 (Continue…)

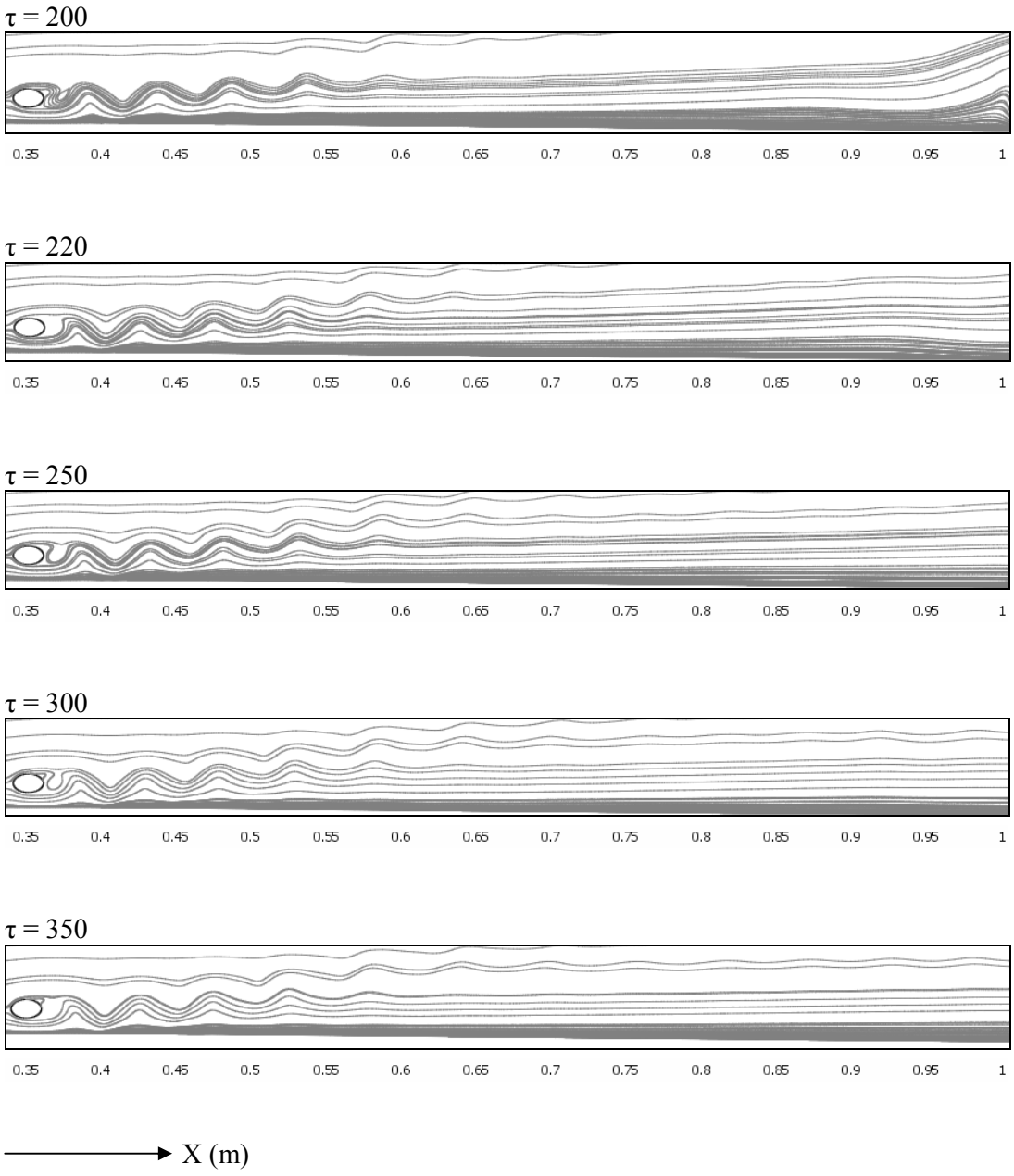

Figure 5.8: Instantaneous streamlines on the flow field for $Re_{2c} = 500$, $x_c/2c = -3$ $y_c/2c = 1$.

τ = 50

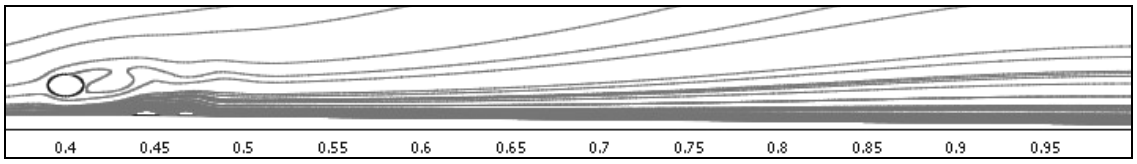

τ = 80

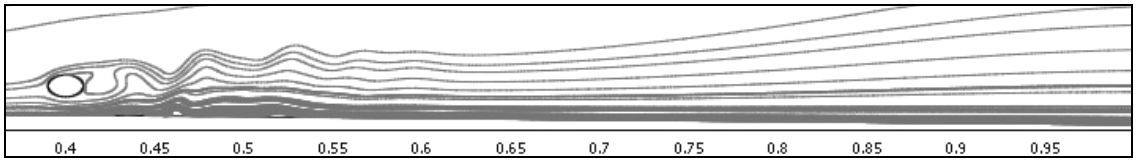

τ = 100

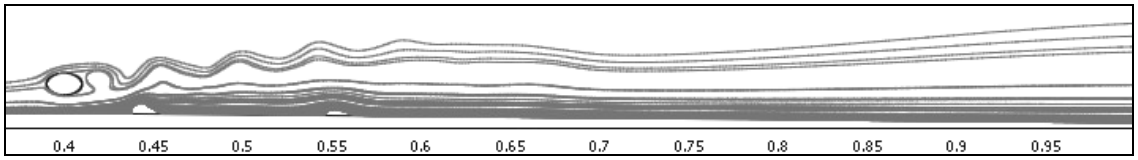

τ = 120

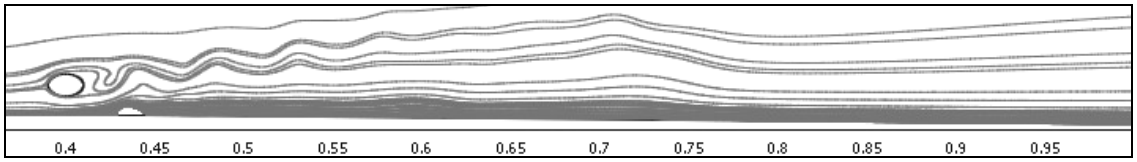

τ = 150

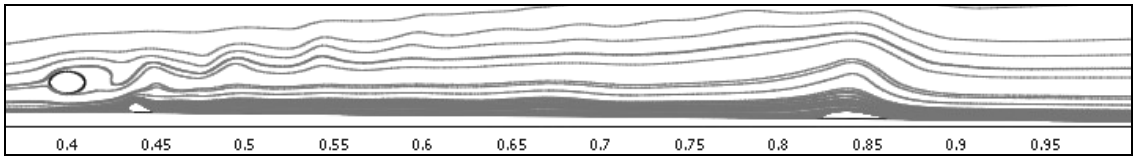

τ = 170

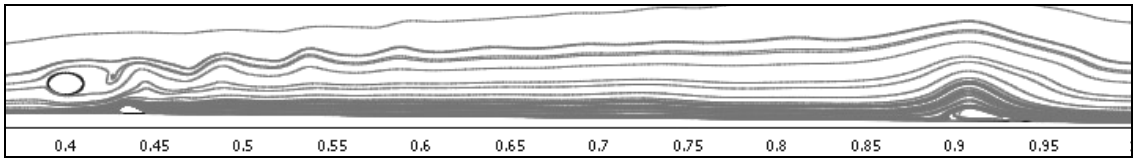

→ X (m)

Figure 5.9 (Continue…)

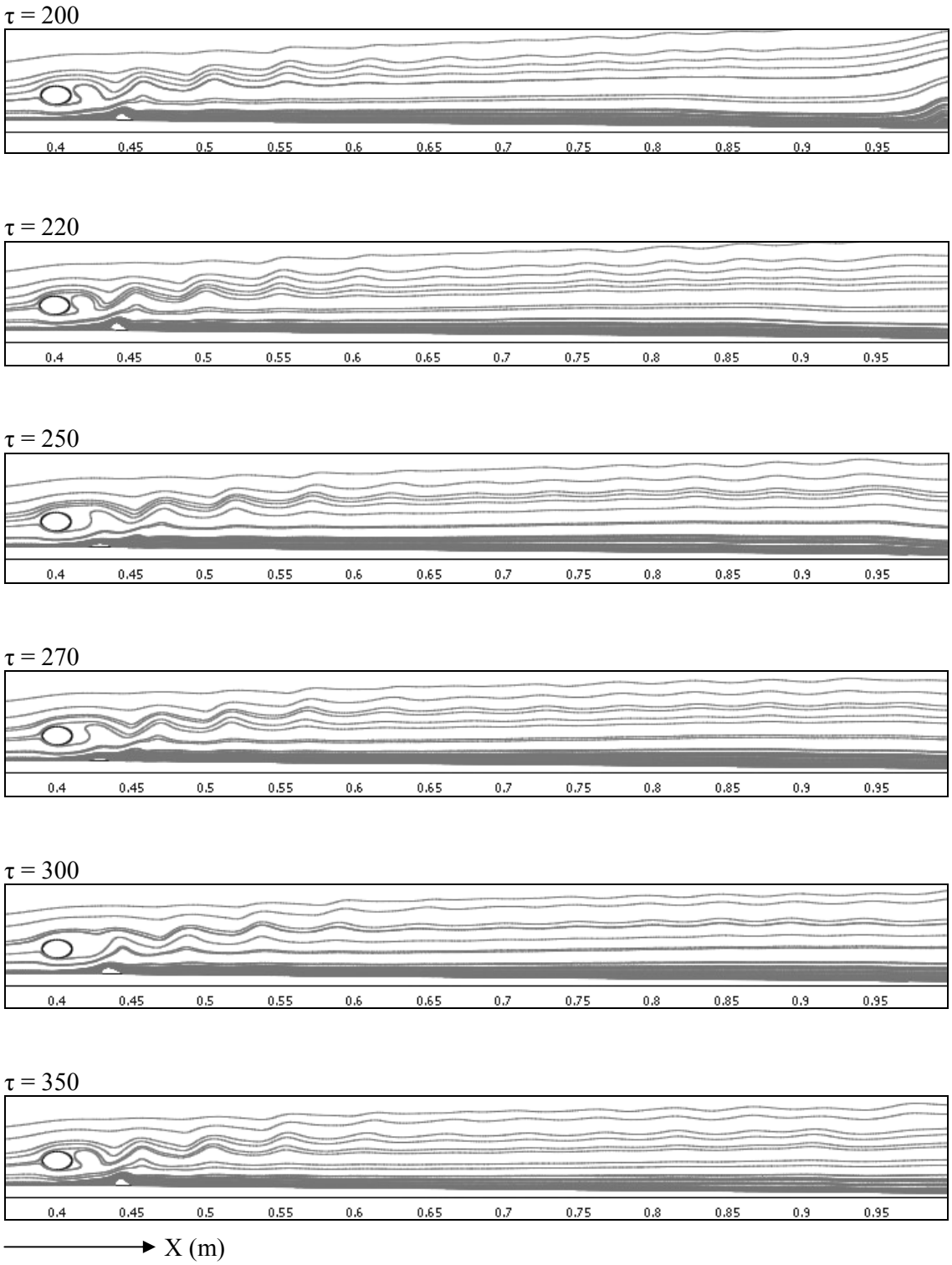

Figure 5.9: Instantaneous streamlines on the flow field for Re_{2c}=500, $x_c/2c = 0$, $y_c/2c$=1.

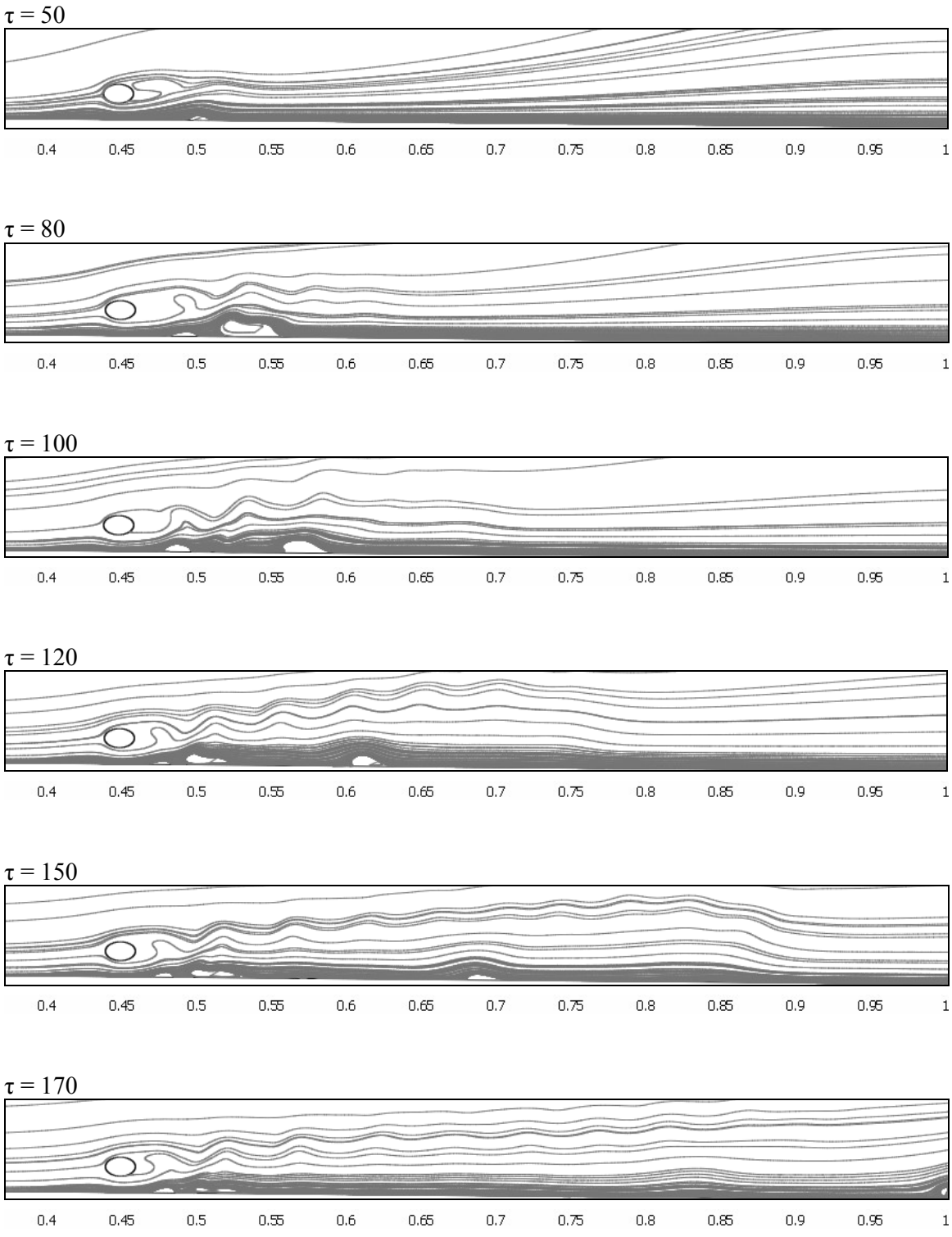

Figure 5.10 (Continue…)

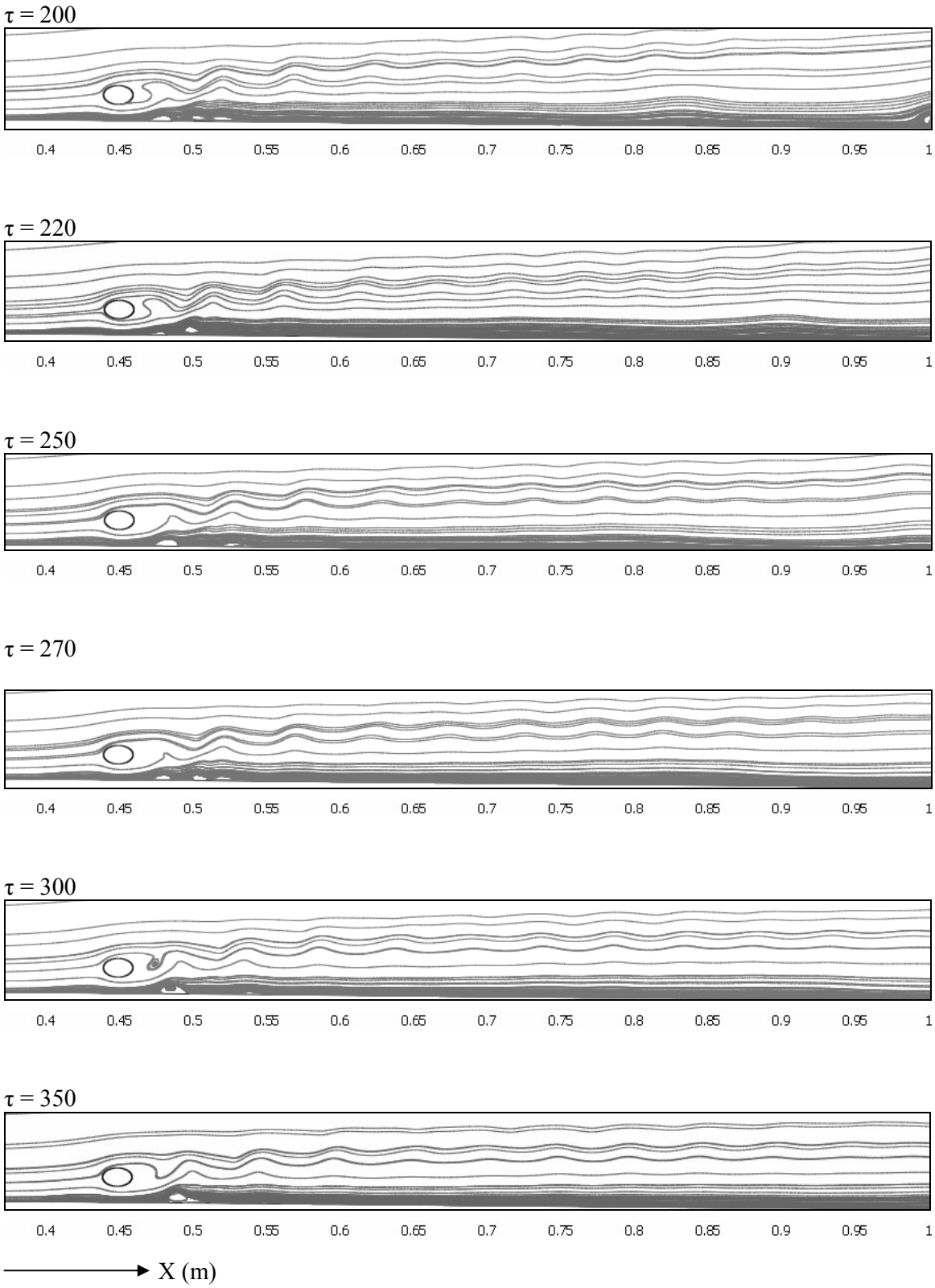

Figure 5.10: Instantaneous streamlines on the flow field for Re_{2c}=500, $x_c/2c = 3$ $y_c/2c = 1$.

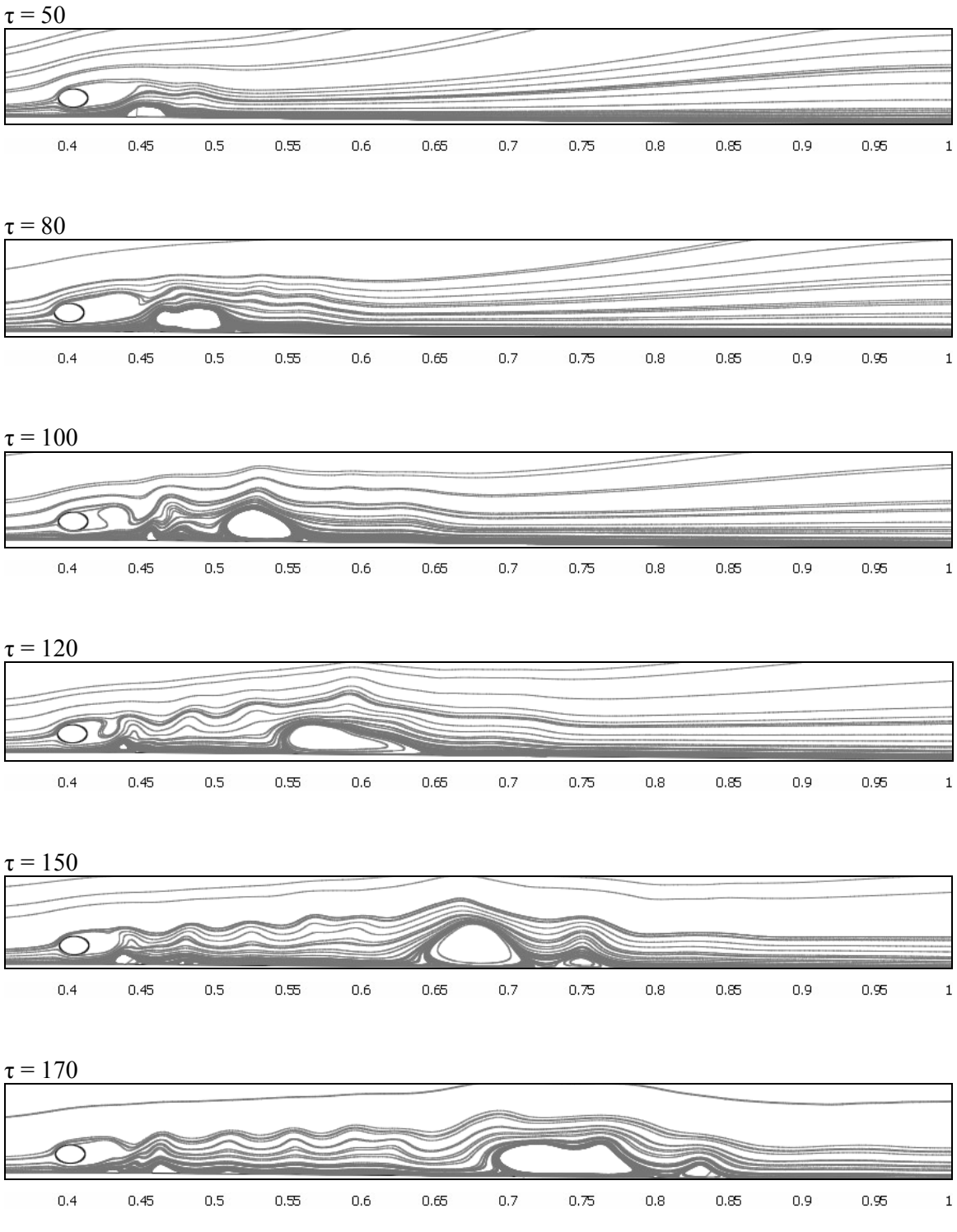

Figure 5.11 (Continue…)

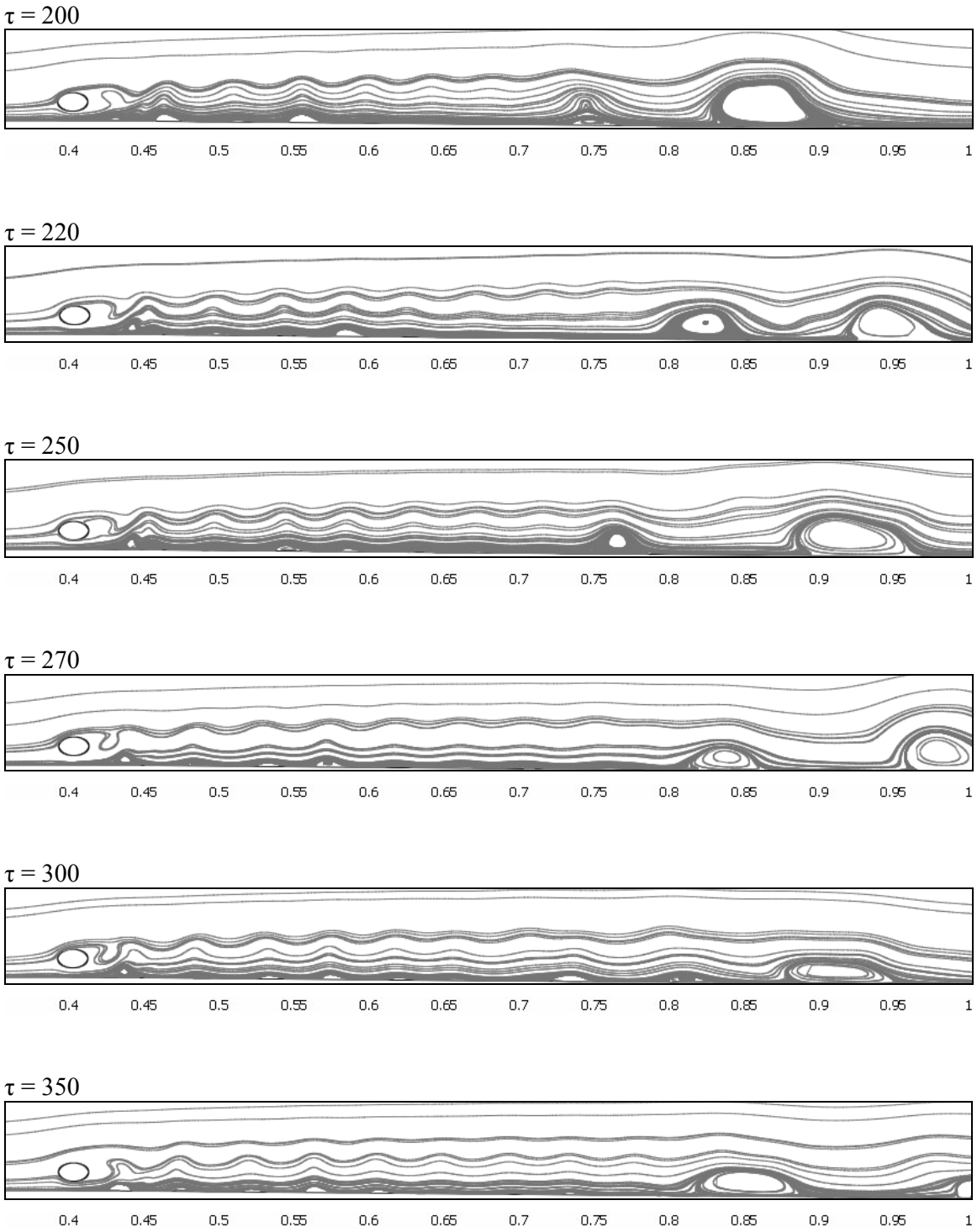

Figure 5.11: Instantaneous streamlines on the flow field for Re_{2c}=500, $x_c/2c = 0$ $y_c/2c = 0.75$.

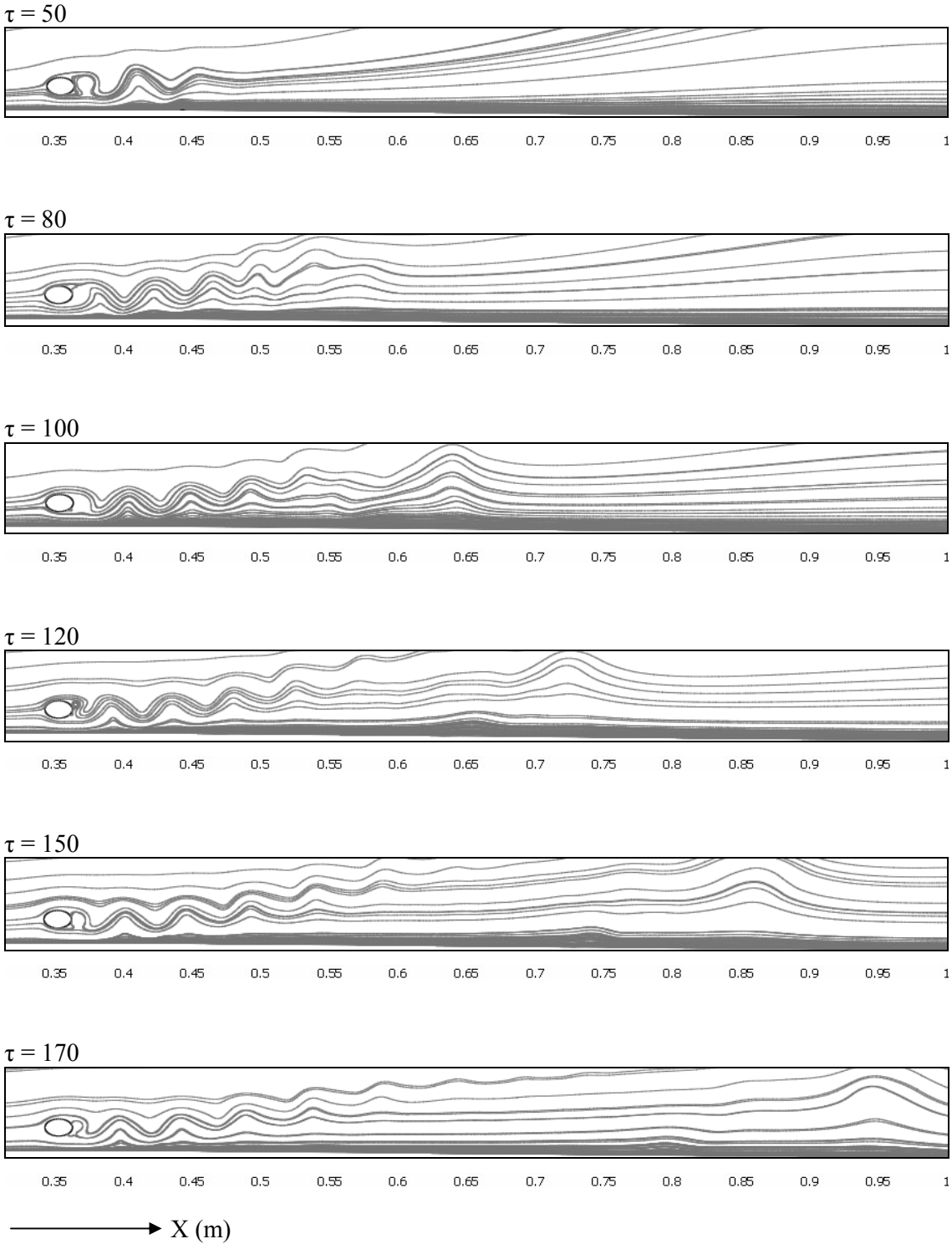

Figure 5.12 (Continue)

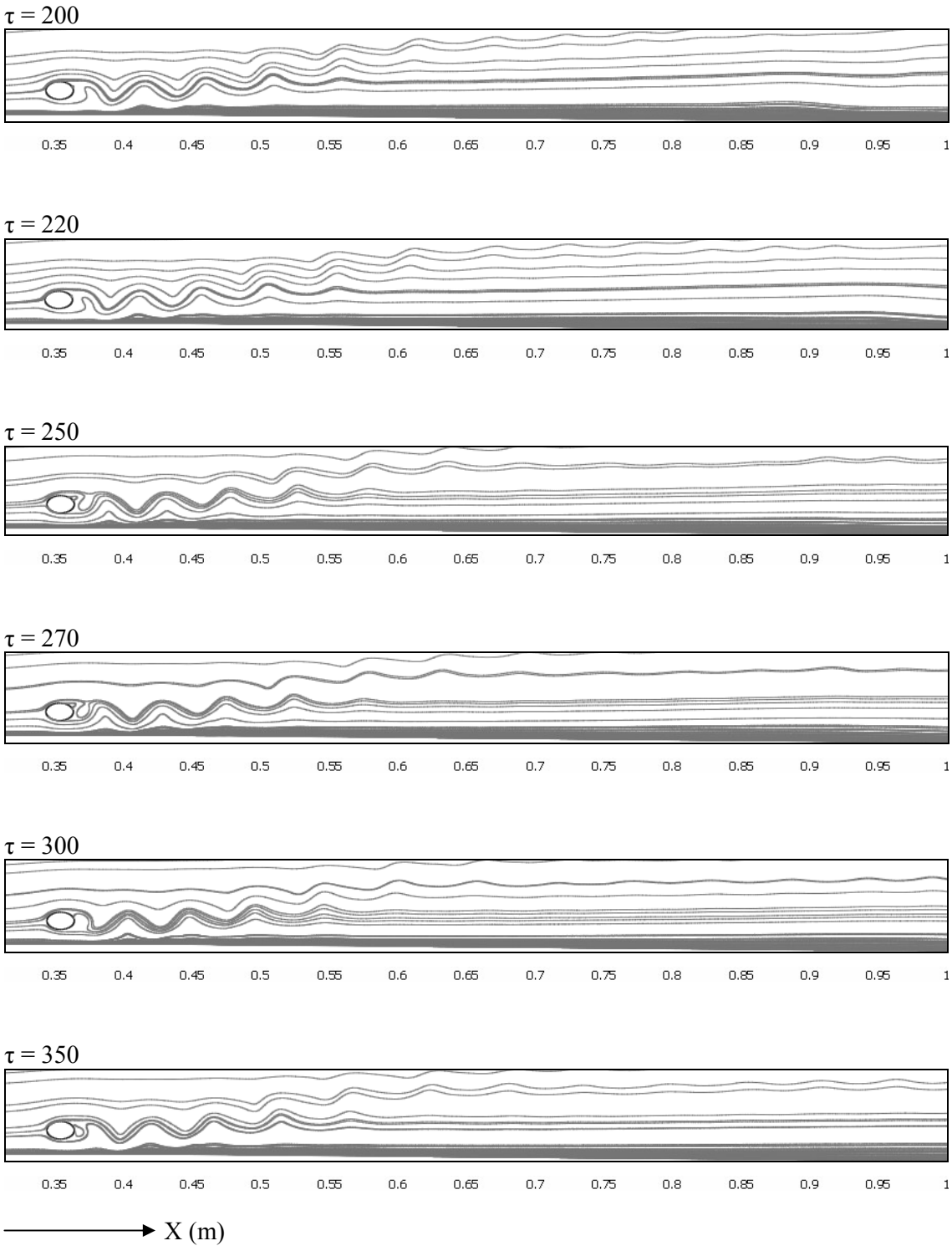

Figure 5.12: Instantaneous streamlines on the flow field for Re_{2c}=800, $x_c/2c$ = -3 $y_c/2c$ = 1.

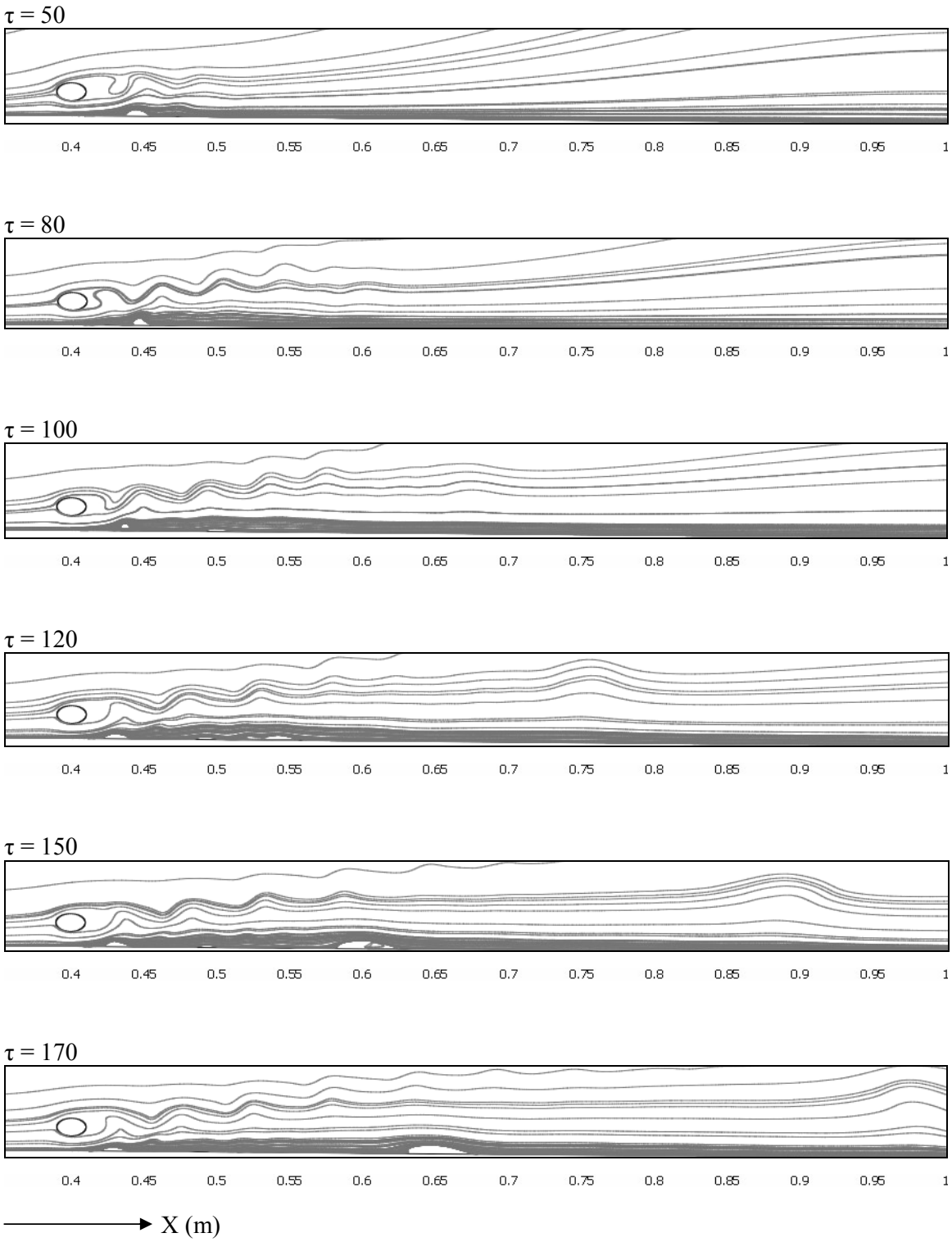

Figure 5.13 (Continue…)

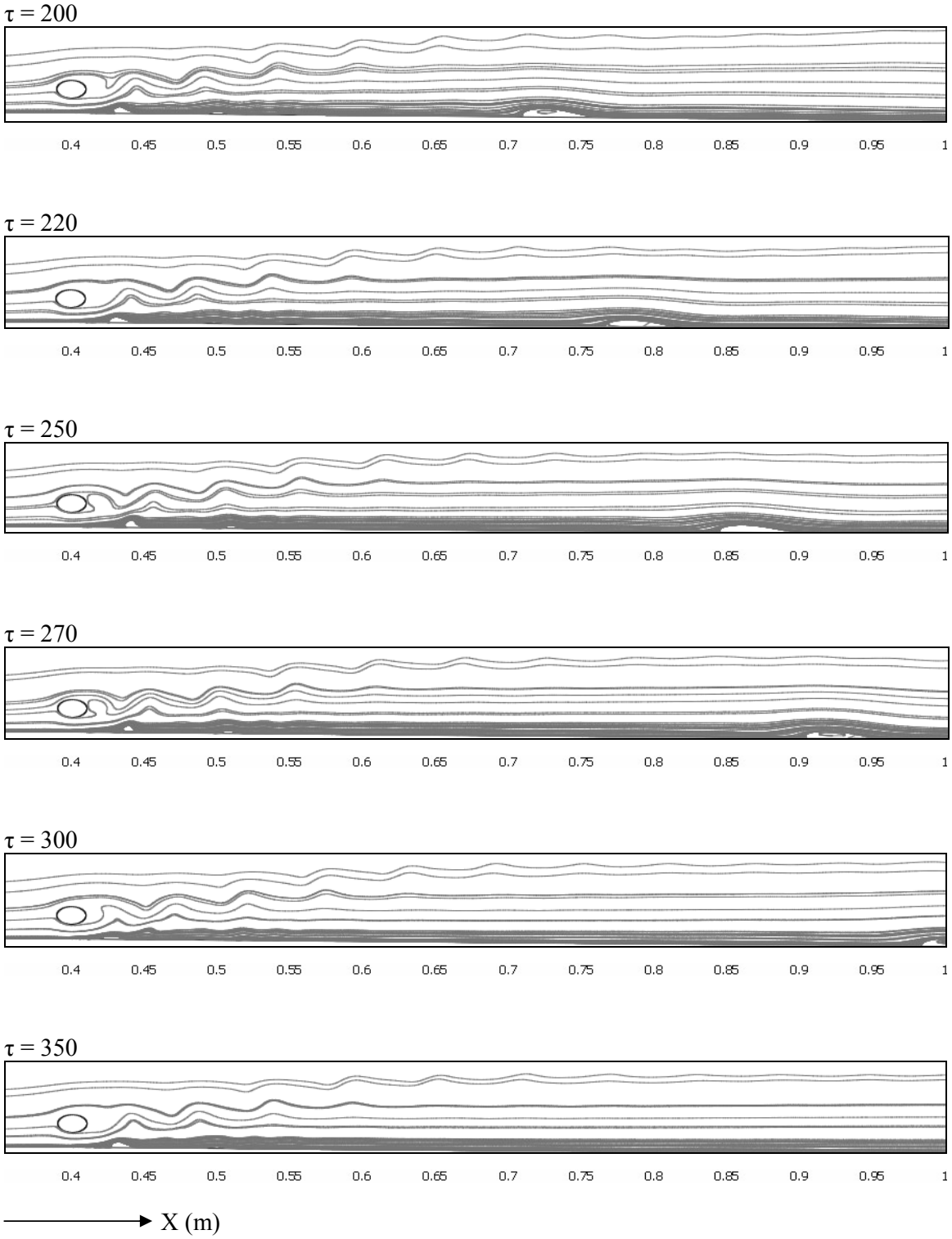

Figure 5.13: Instantaneous streamlines on the flow field for Re_{2c}=800, $x_c/2c = 0$ $y_c/2c = 1$.

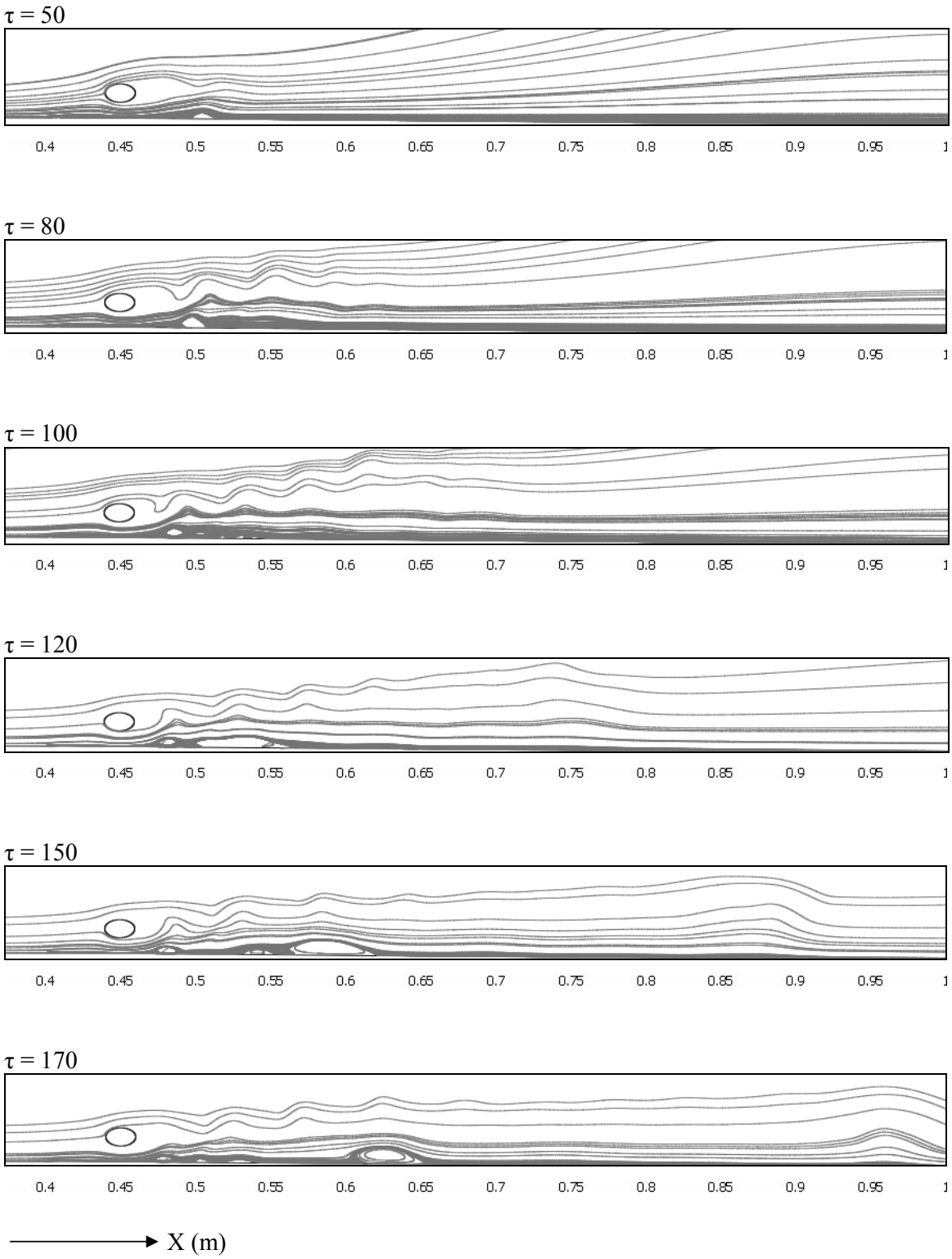

Figure 5.14 (Continue…)

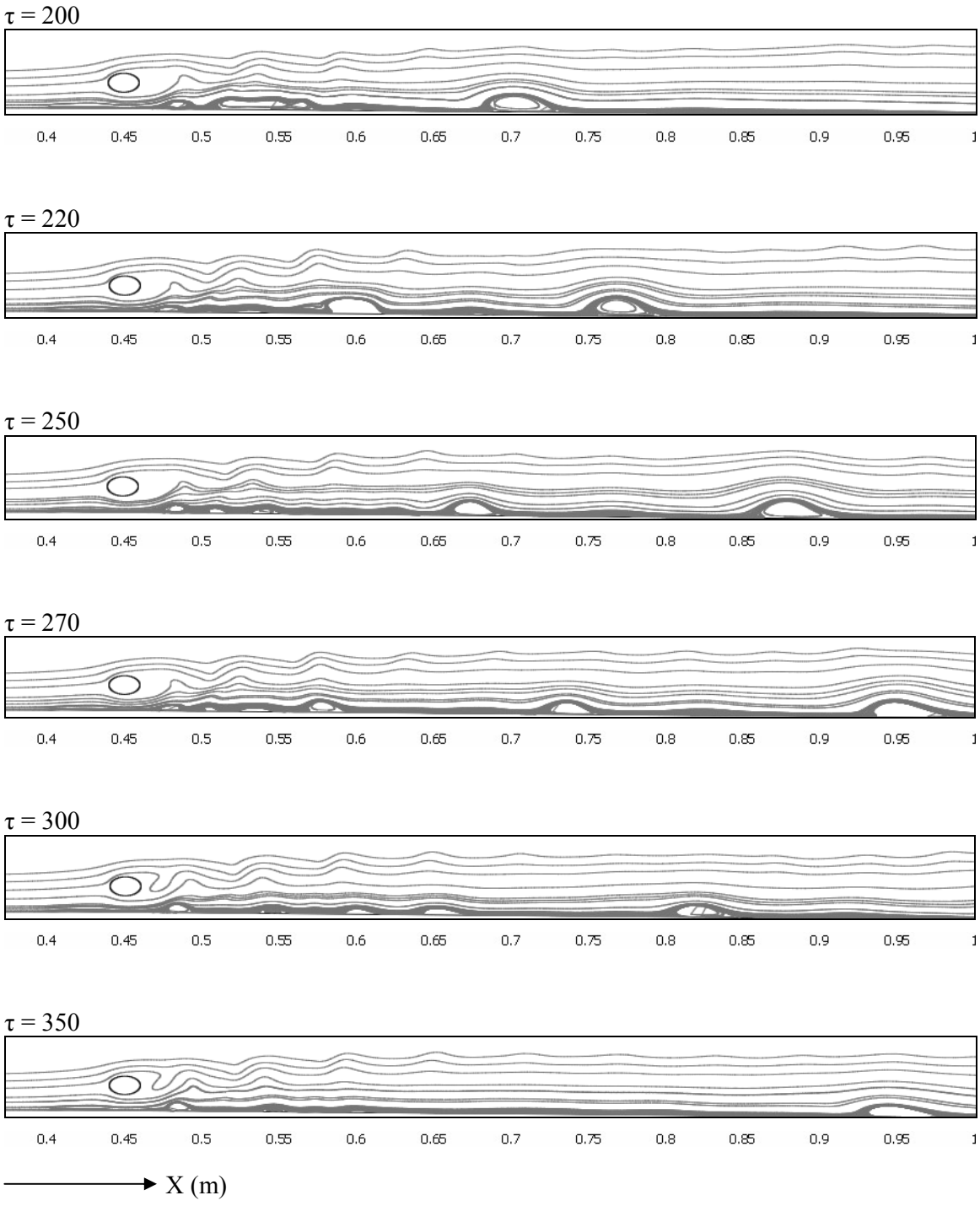

Figure 5.14: Instantaneous streamlines on the flow field for Re_{2c}=800, $x_c/2c = 3$ $y_c/2c = 1$.

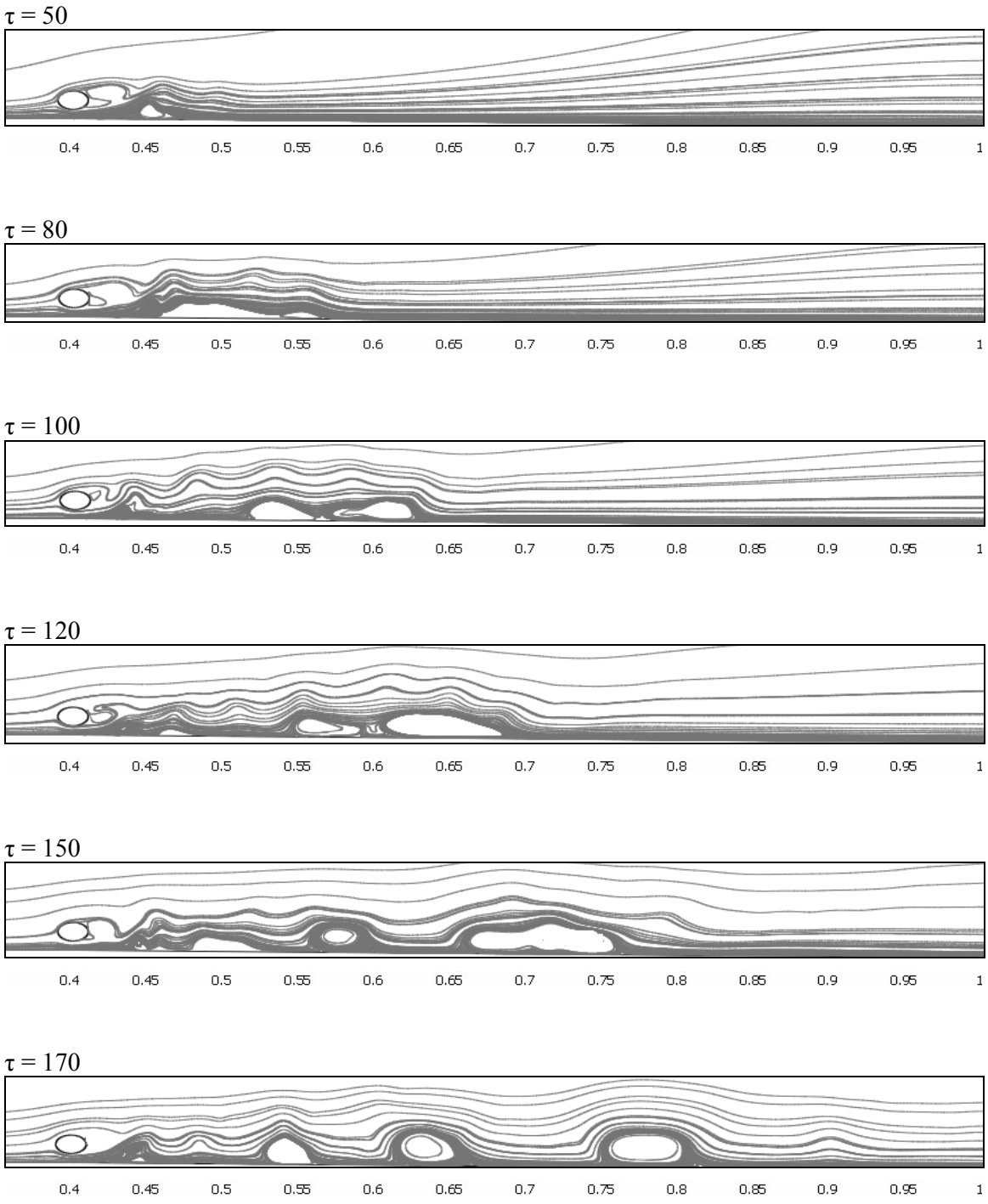

Figure 5.15 (Continue…)

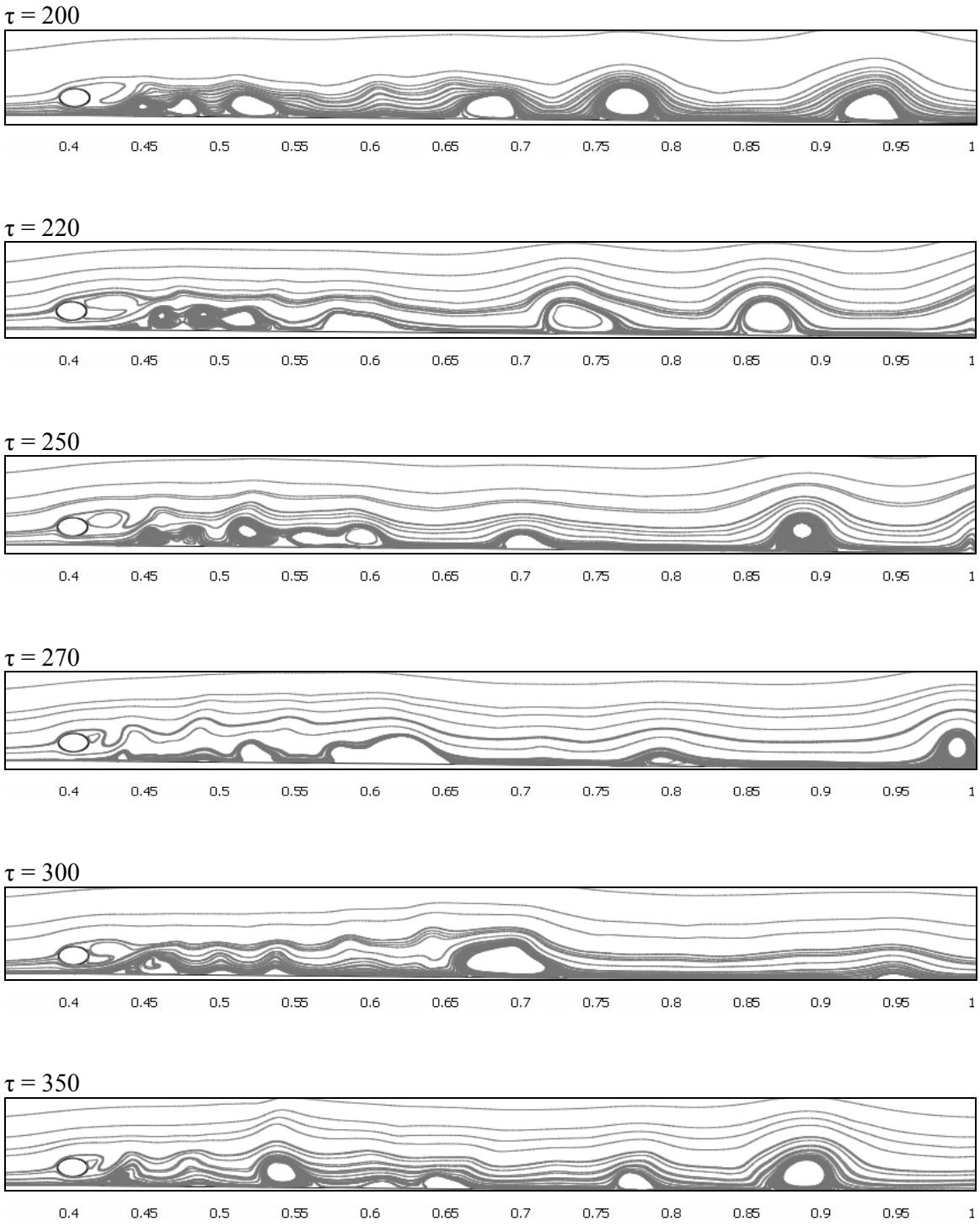

Figure 5.15: Instantaneous streamlines on the flow field for Re_{2c}=800, $x_c/2c = 0$ $y_c/2c = 0.75$.

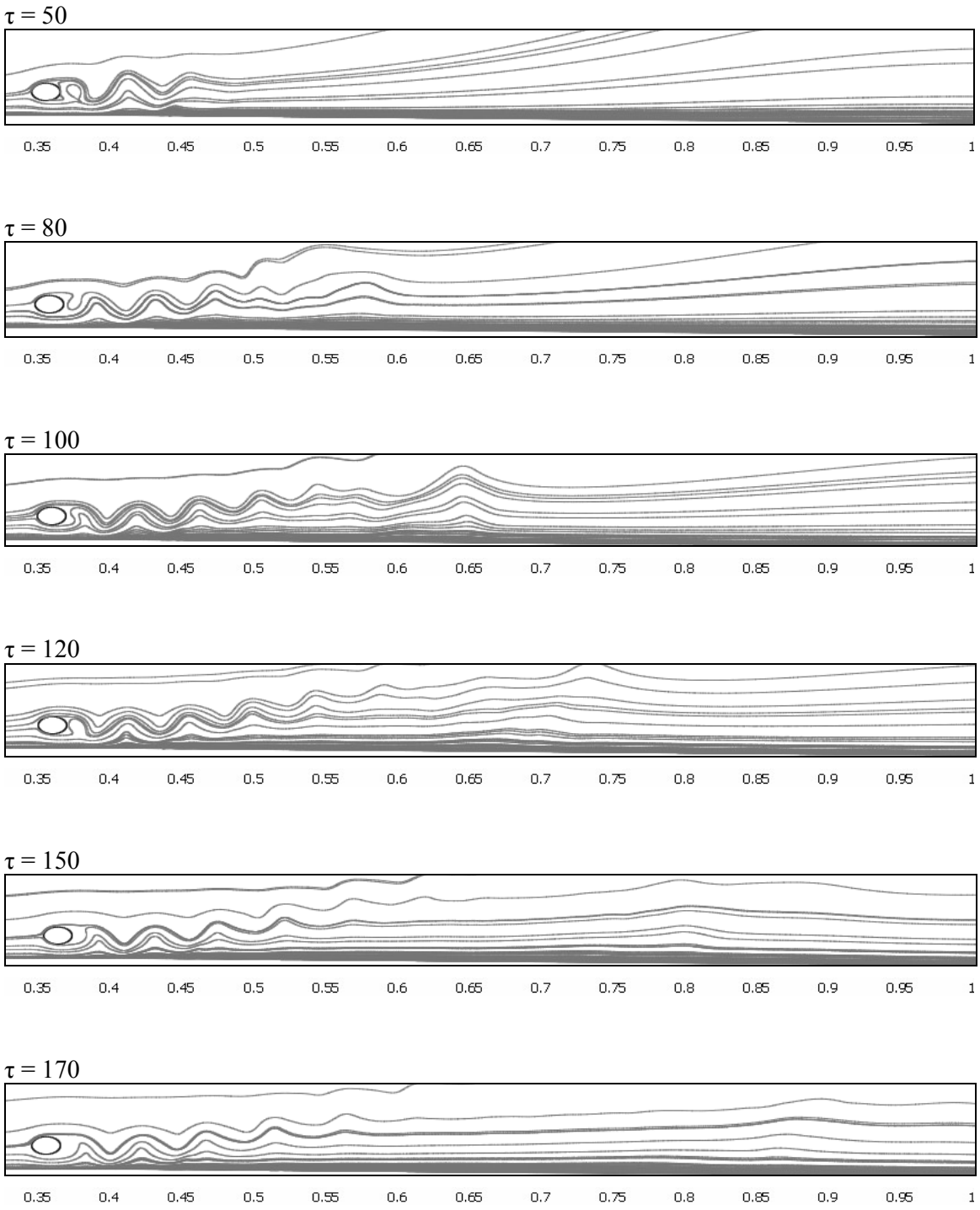

Figure 5.16 (Continue…)

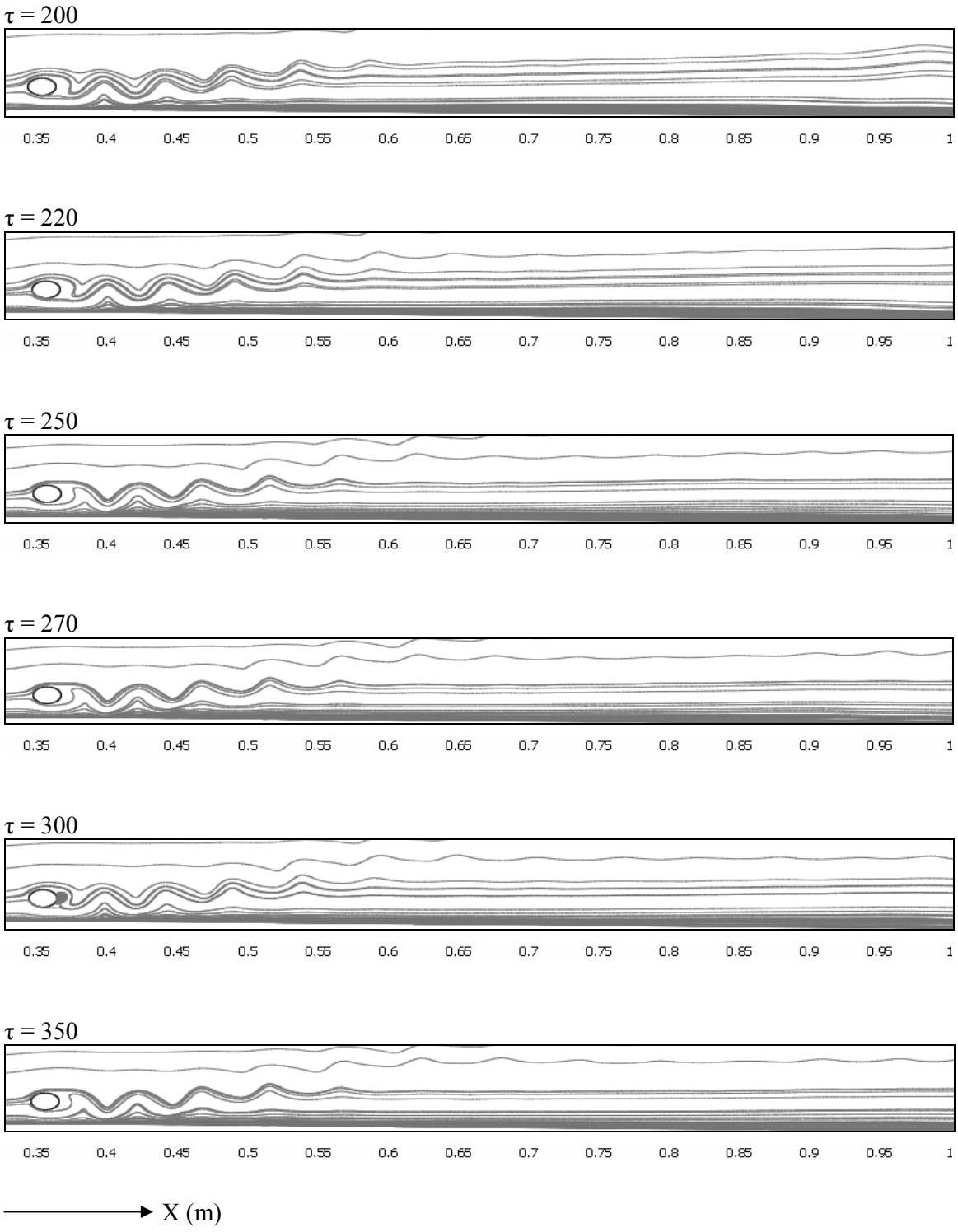

Figure 5.16: Instantaneous streamlines on the flow field for Re_{2c}=1000, $x_c/2c$ = -3 $y_c/2c$ = 1.

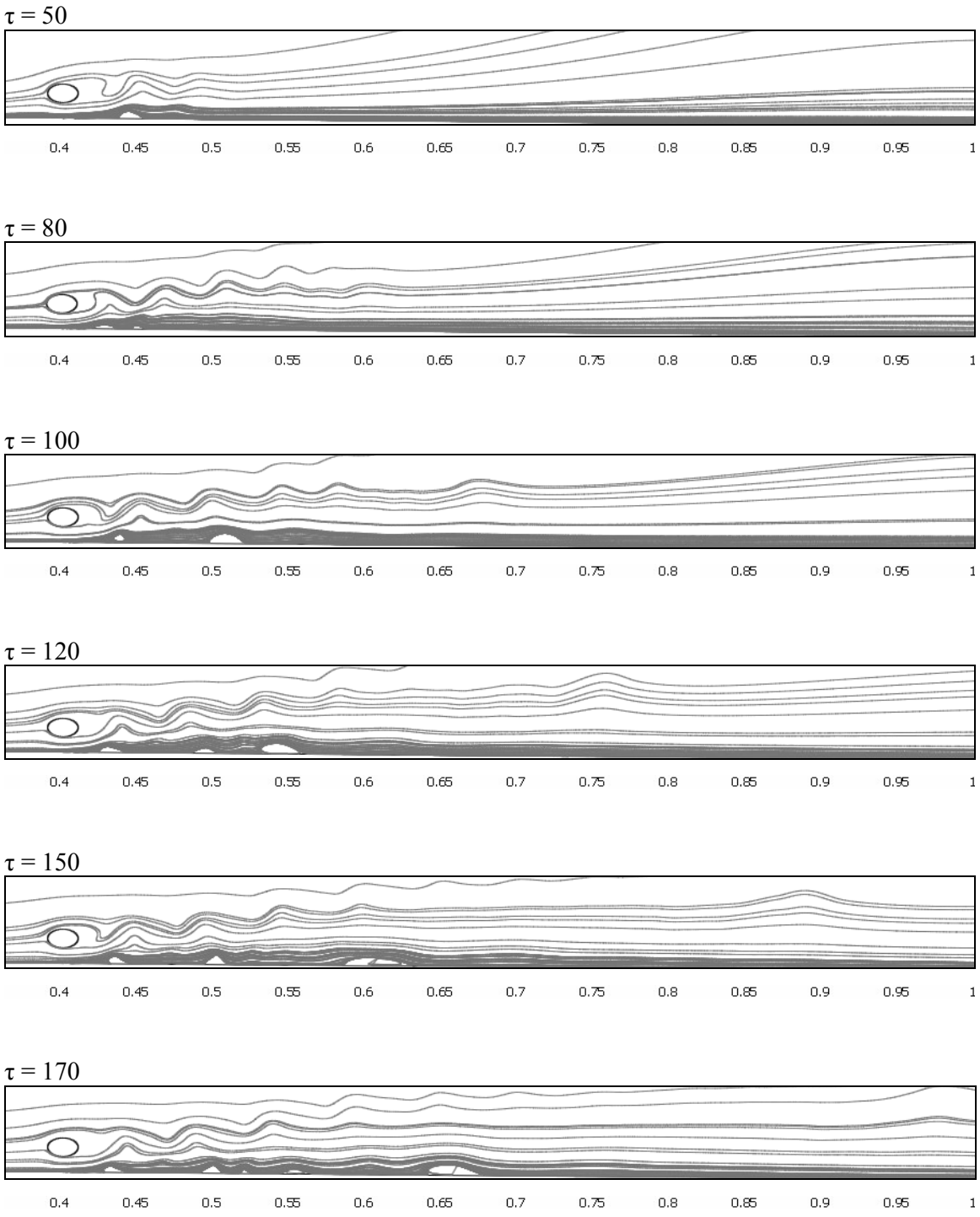

Figure 5.17 (Continue…)

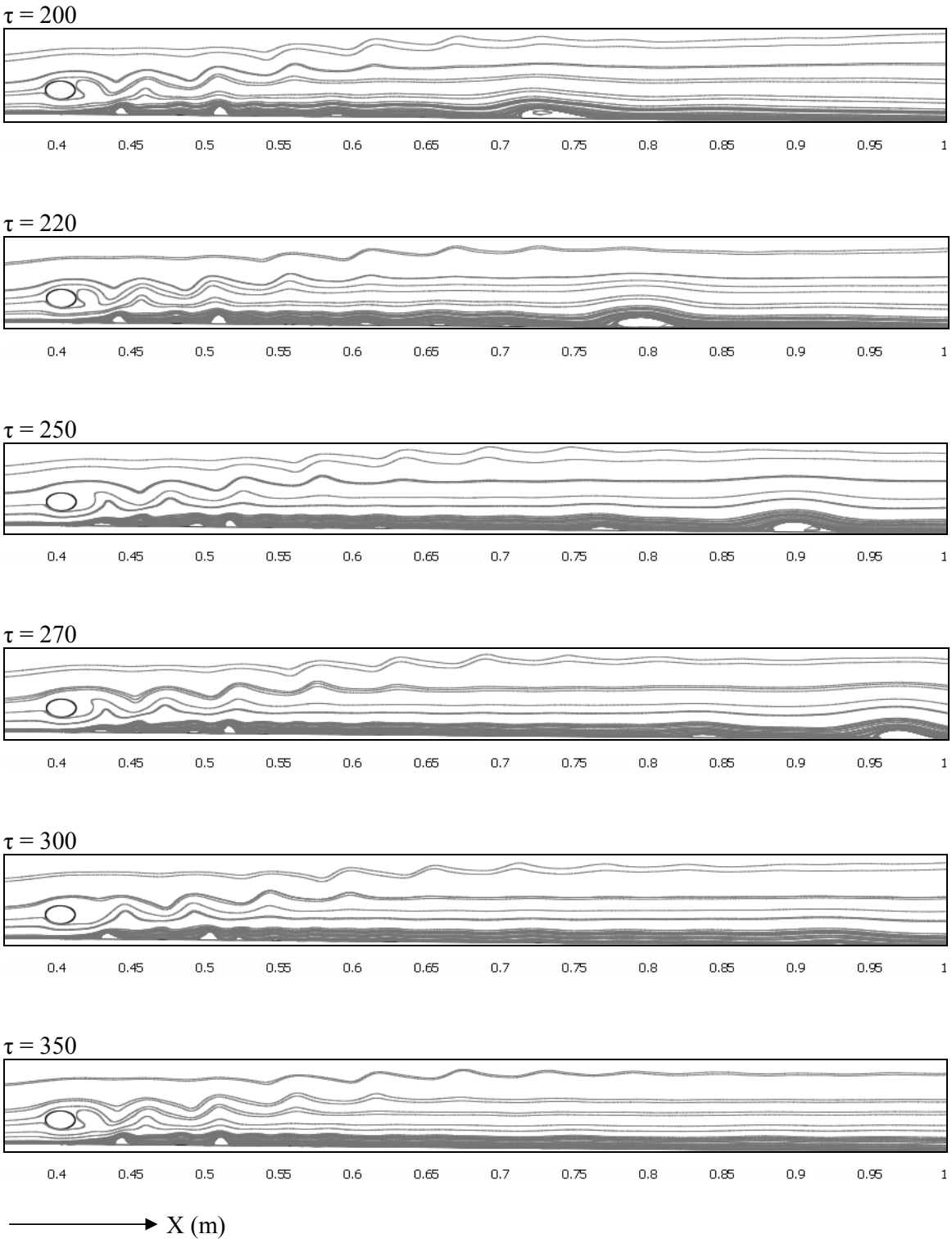

Figure 5.17: Instantaneous streamlines on the flow field for Re_{2c}=1000, $x_c/2c = 0$ $y_c/2c = 1$.

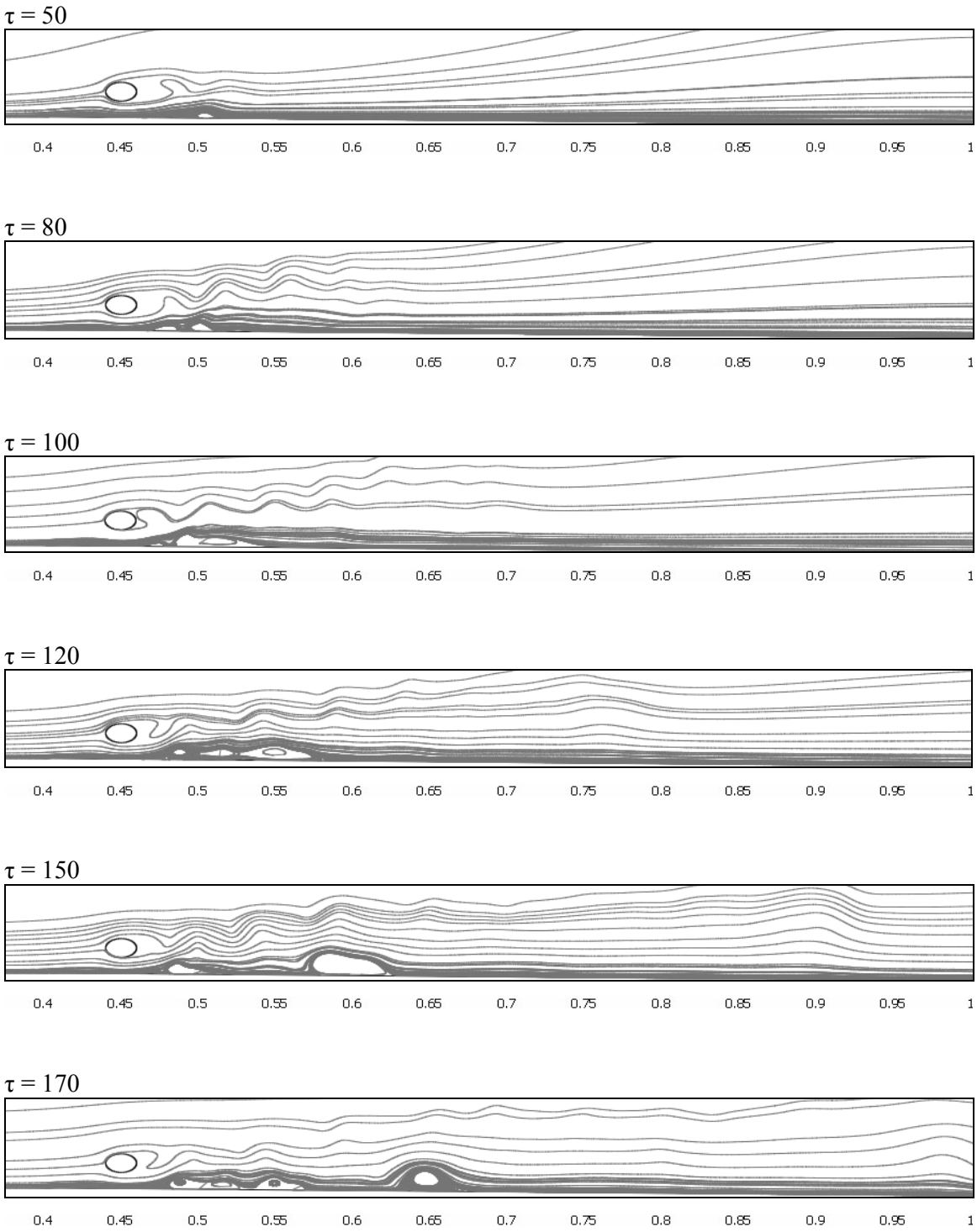

Figure 5.18 (Continue…)

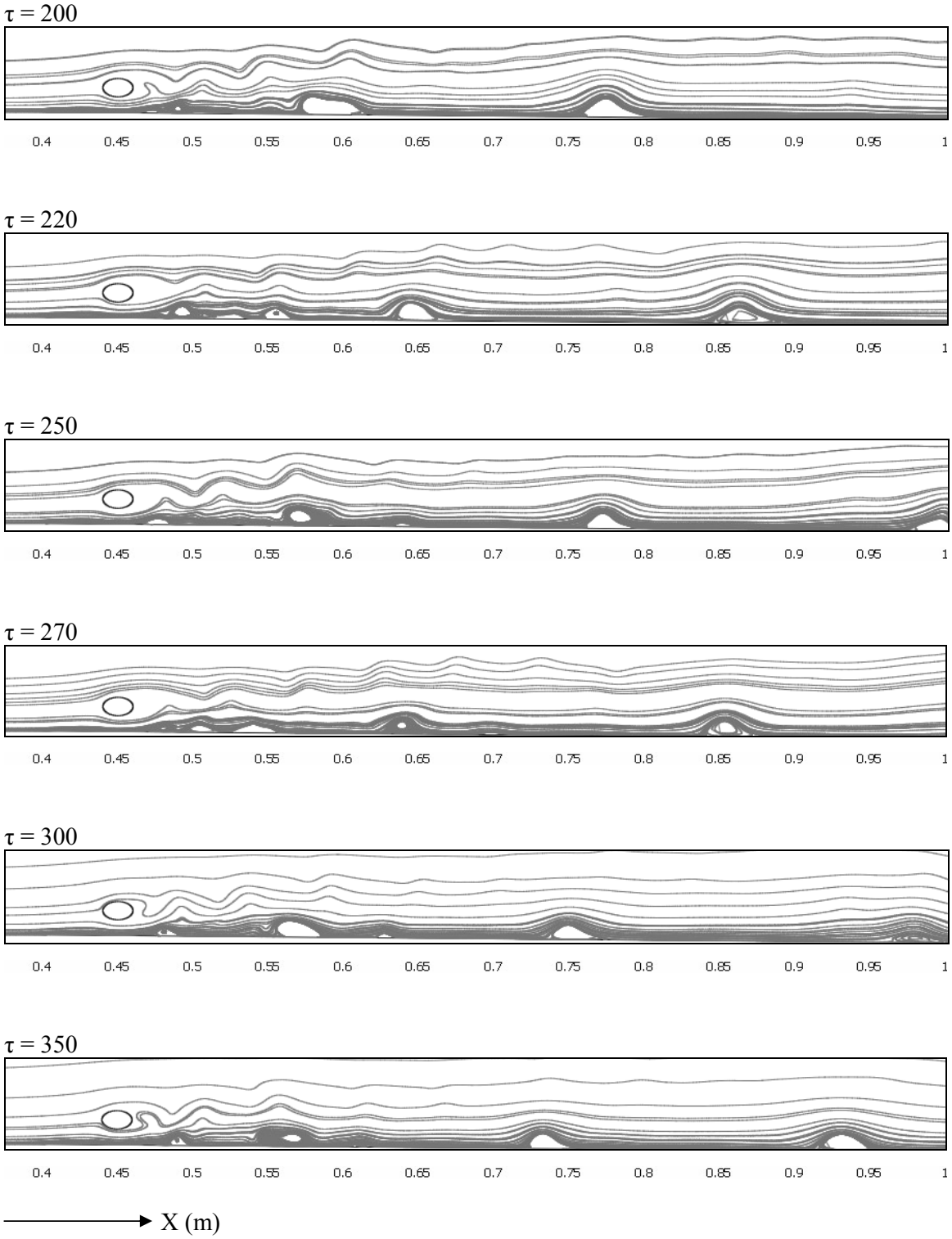

Figure 5.18: Instantaneous streamlines on the flow field for Re_{2c}=1000, $x_c/2c = 3$ $y_c/2c = 1$.

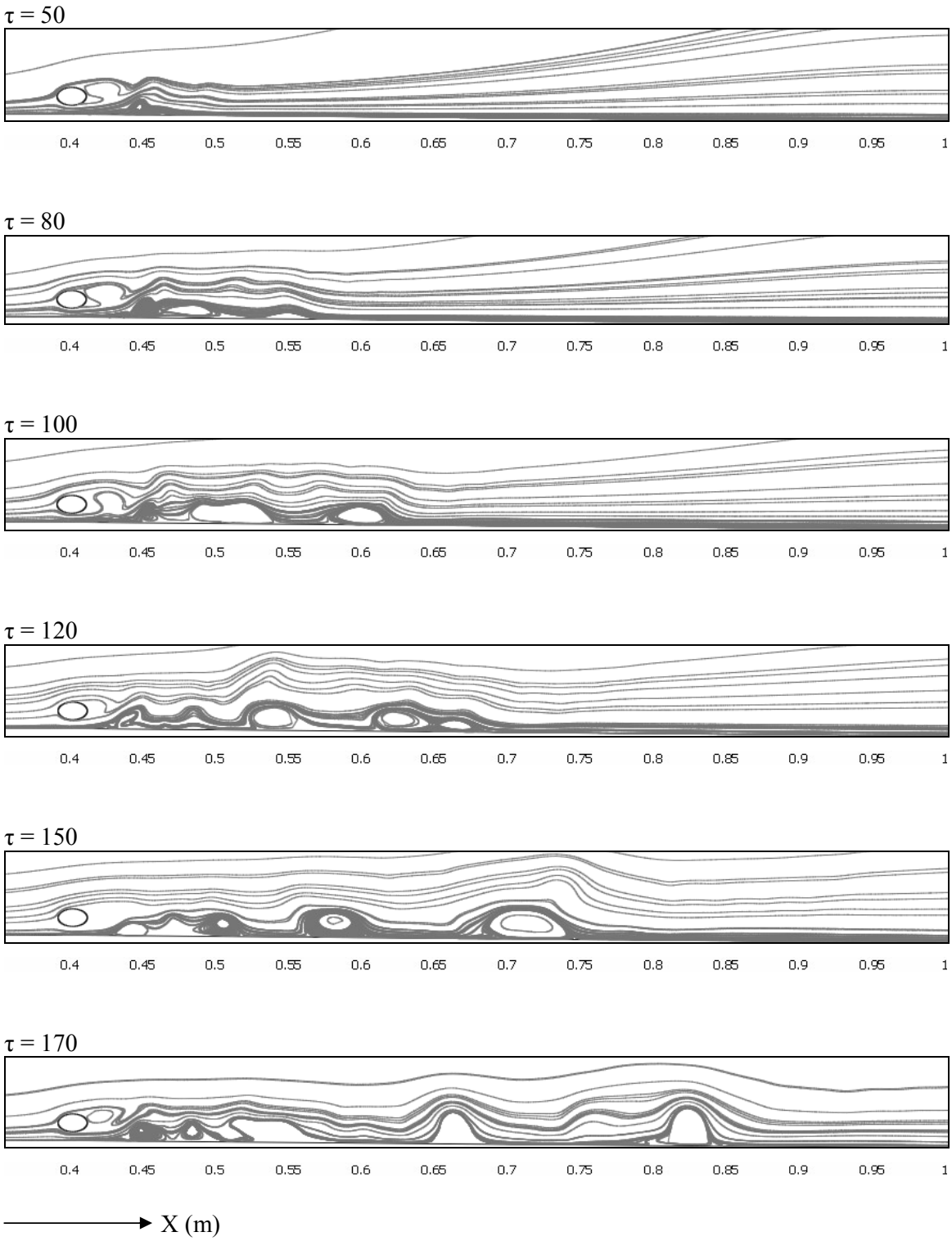

Figure 5.19 (Continue…)

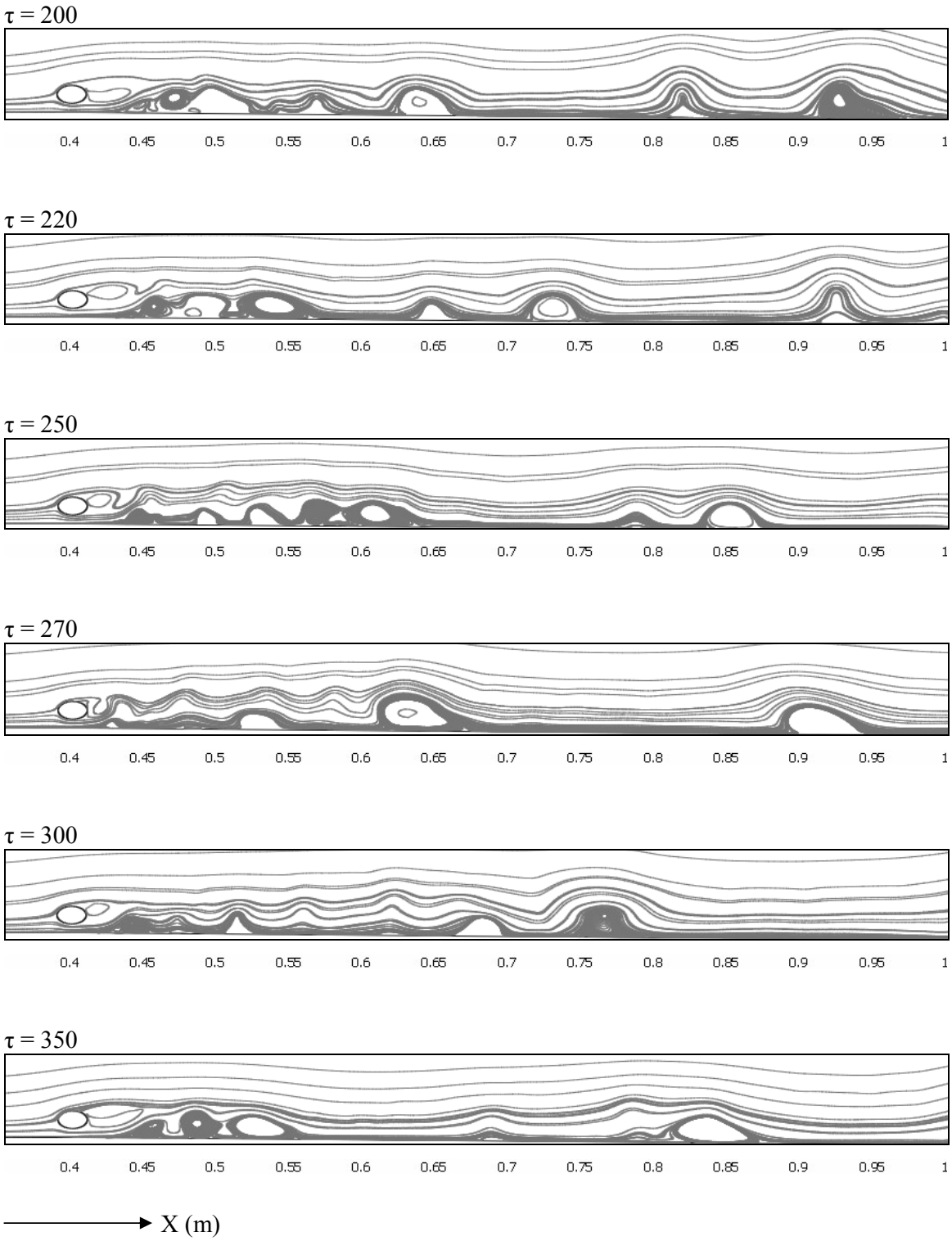

Figure 5.19: Instantaneous streamlines on the flow field for Re_{2c}=1000, $x_c/2c = 0$ $y_c/2c = 0.75$.

τ = 50

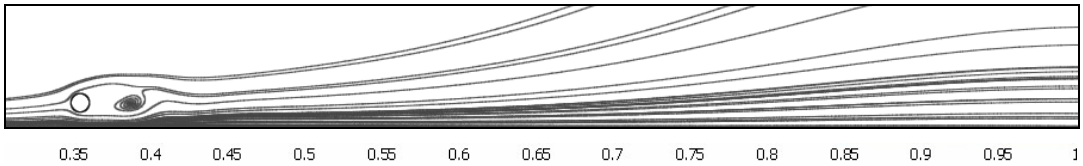

τ = 80

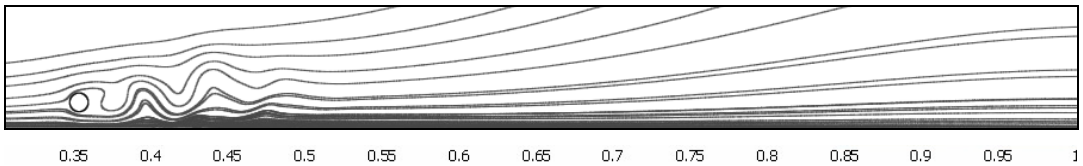

τ = 100

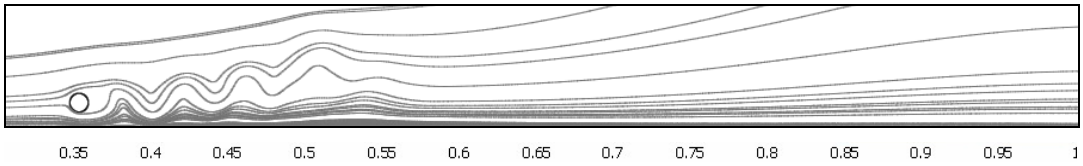

τ = 120

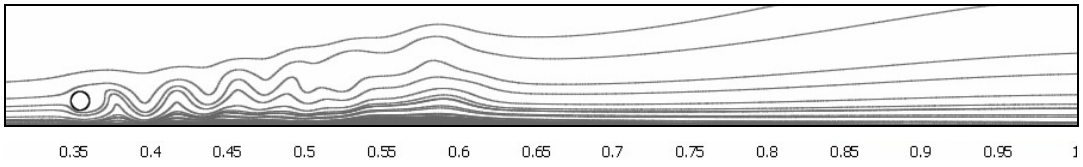

τ = 150

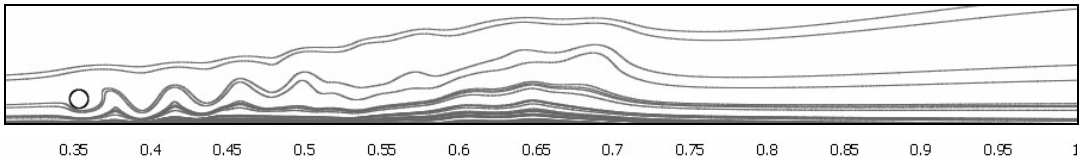

τ = 170

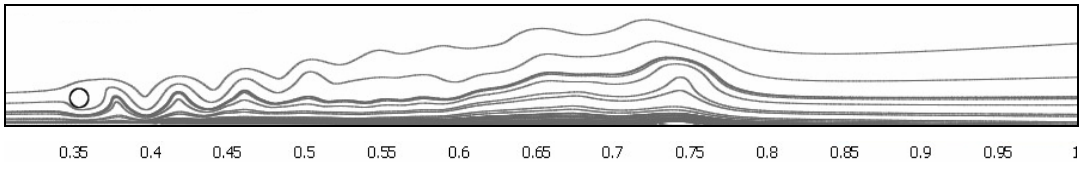

X (m)

Figure 5.20 (Continue…)

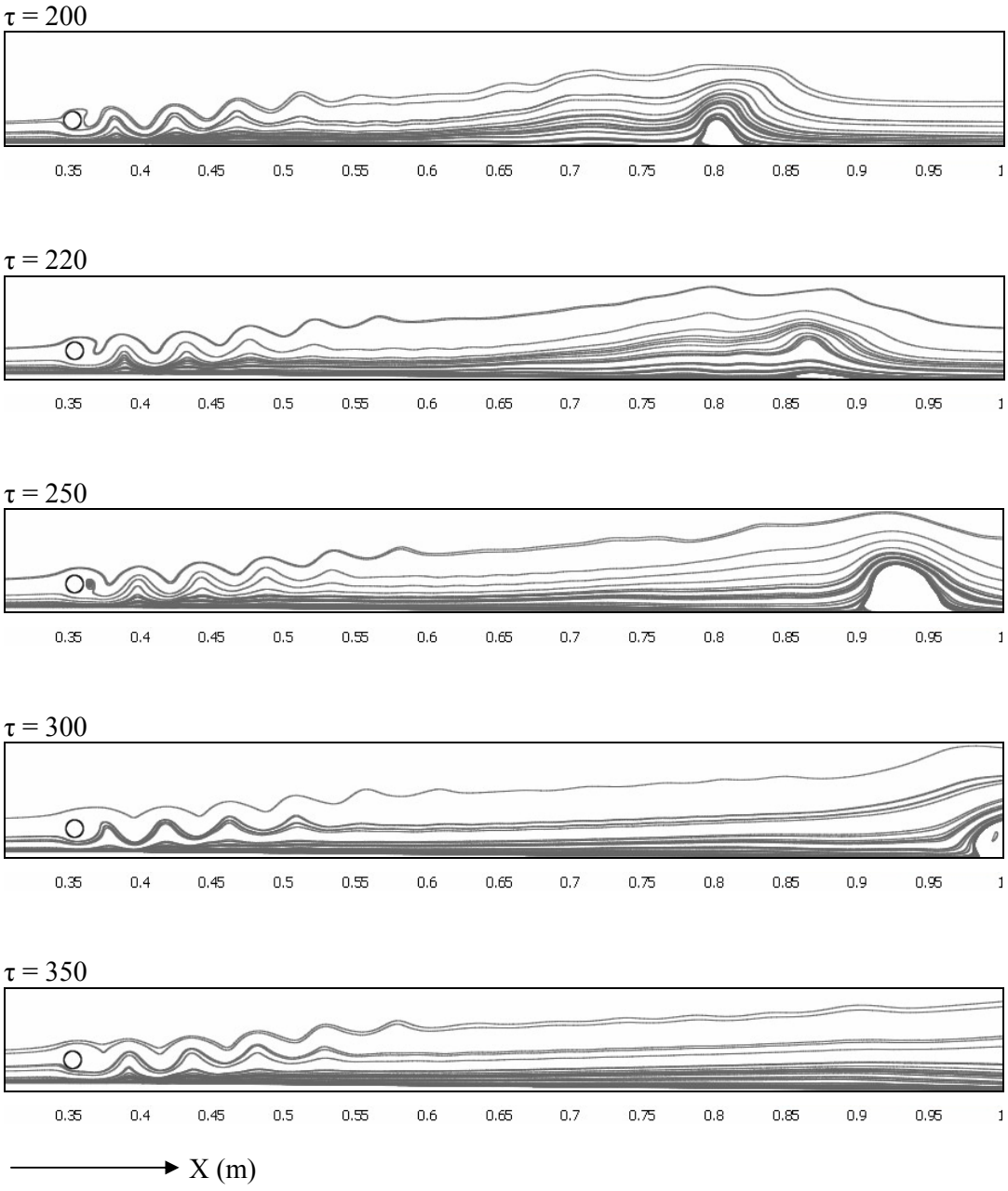

Figure 5.20: Instantaneous stream lines for the flow field Re_{2c}=500, $x_c/2c$ =-3 $y_c/2c$ = 1 for circular cylinder.

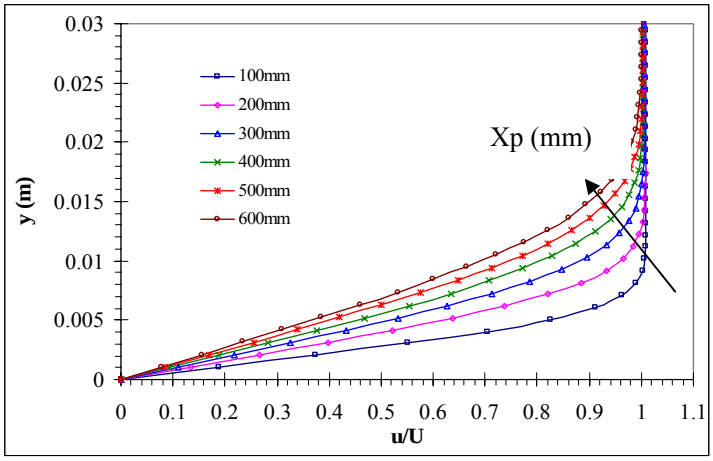

(a)

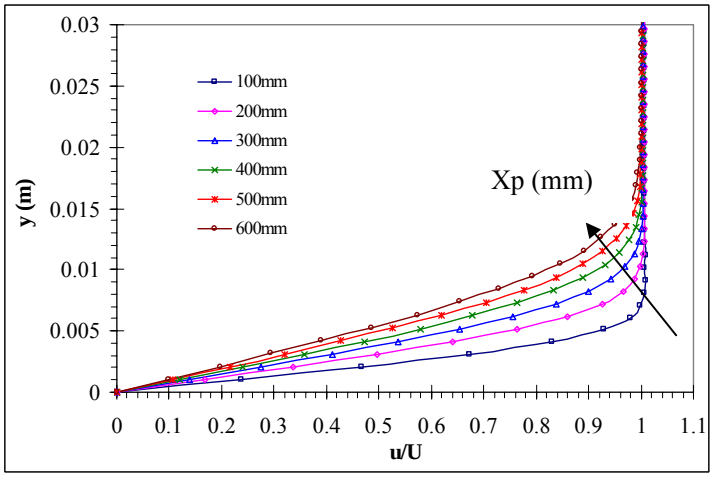

(b)

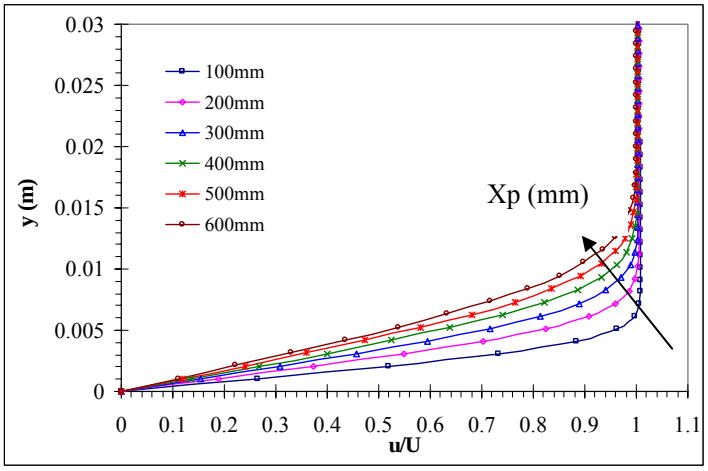

(c)

Figure 5.21: Undisturbed profile of velocity distribution on different flat plate axial location, (a) Re = 500, (b) Re = 800, (c) Re = 1000.

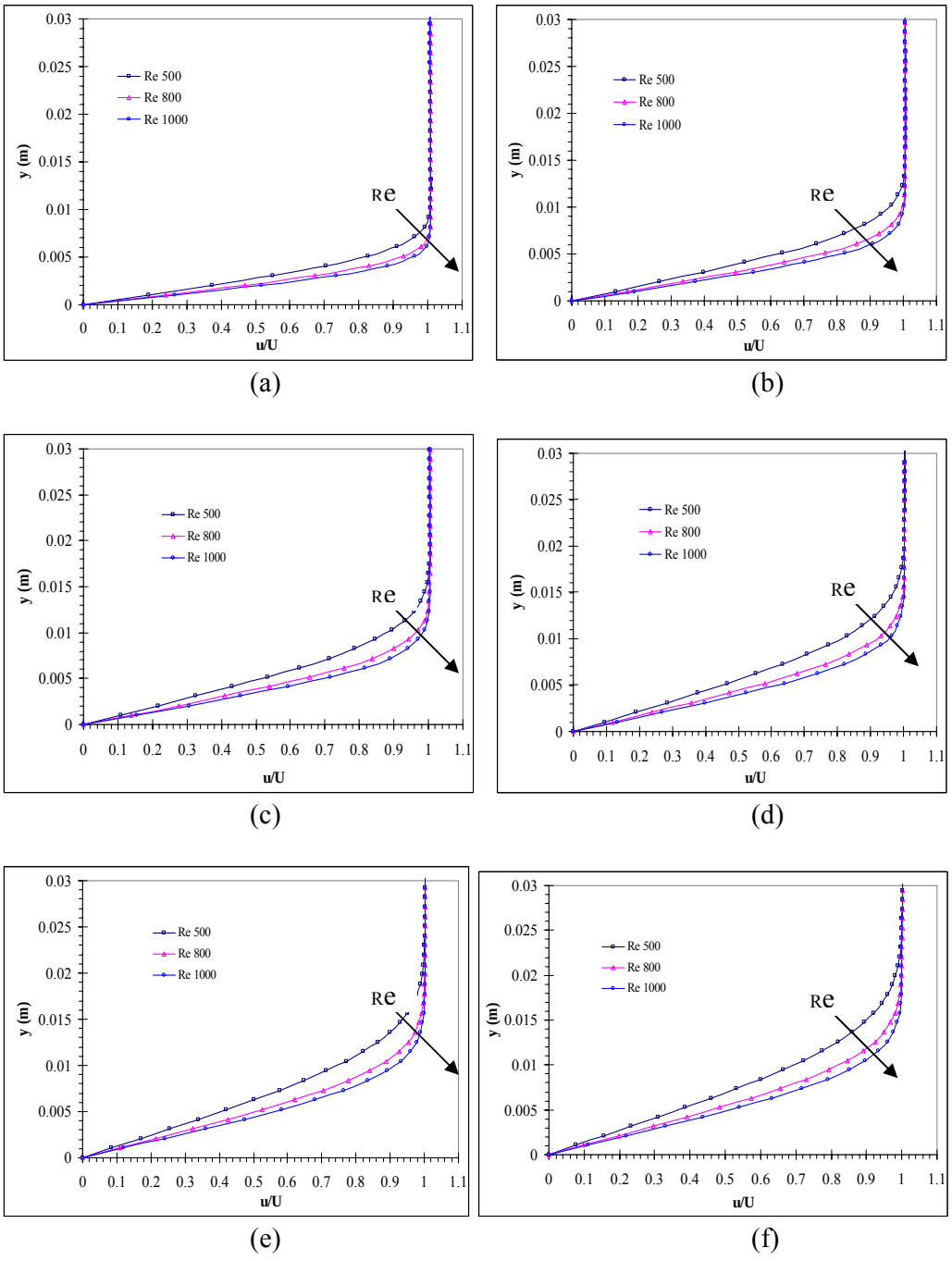

Figure 5.22: Variation of undisturbed profile of velocity distribution with respect to Reynolds number Re for different plate axial location, (a) Xp = 100mm, (b) Xp = 200mm, (c) Xp = 300mm, (d) Xp = 400mm, (e) Xp = 500mm, (f) Xp = 600mm.

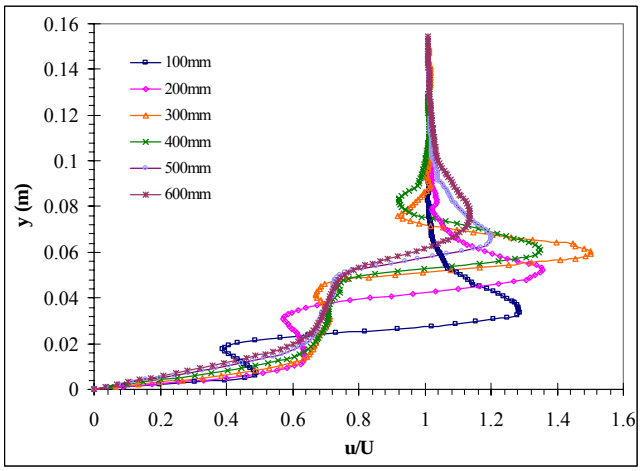

(a)

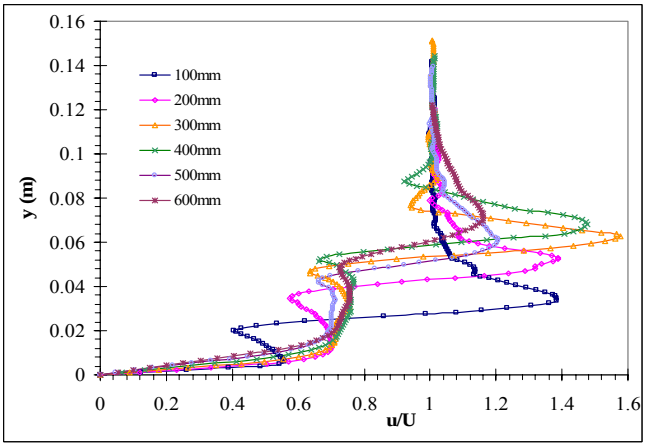

(b)

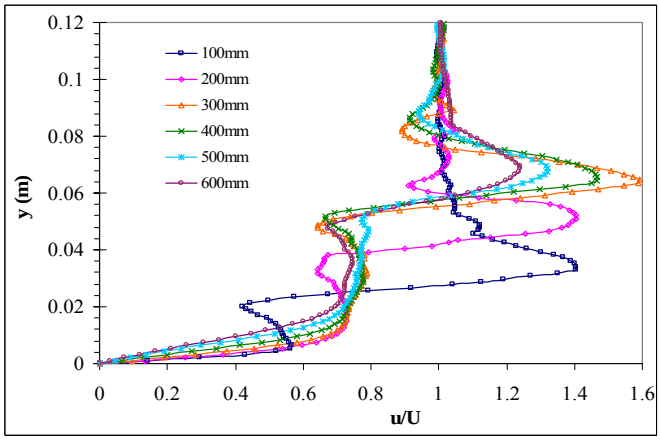

(c)

Figure 5.23: Instantaneous velocity distribution on different flat plate axial locations for $\tau = 800$, $x_c/2c = -3$ $y_c/2c = 1$ (a) Re_{2c}=500, (b) Re_{2c}=800 (c) Re_{2c}=1000.

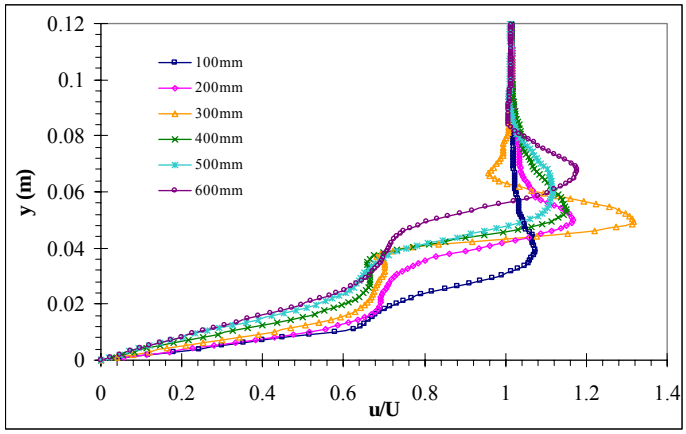

(a)

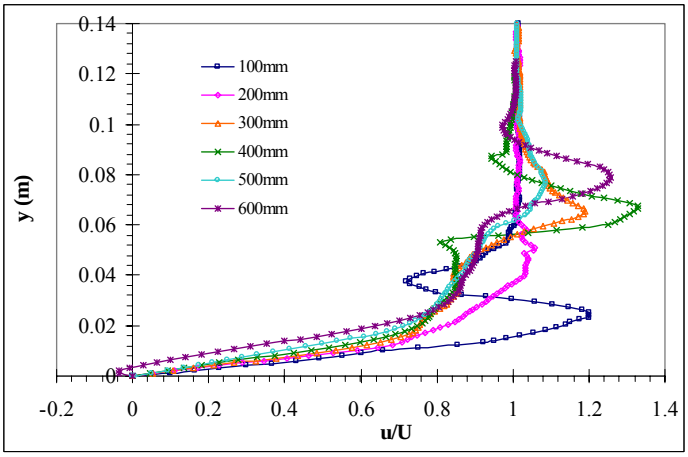

(b)

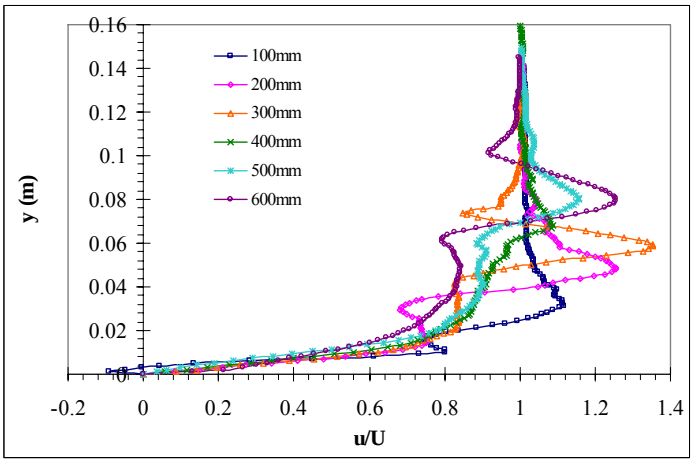

(c)

Figure 5.24: Instantaneous velocity distribution on different flat plate axial locations for $\tau = 800$, $x_c/2c = 0$ $y_c/2c = 1$ (a) Re_{2c}=500, (b) Re_{2c}=800, (c) Re_{2c}=1000.

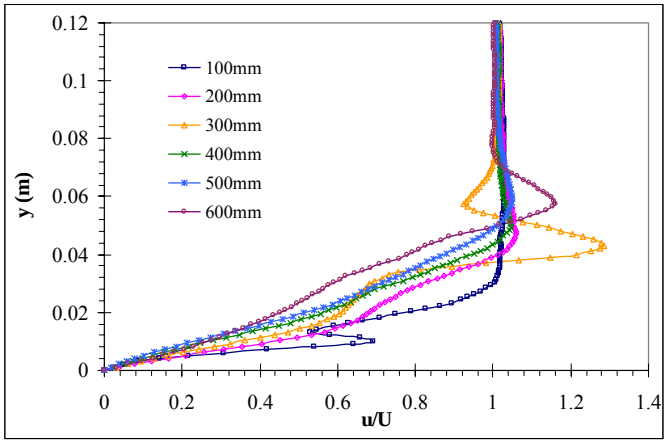

(a)

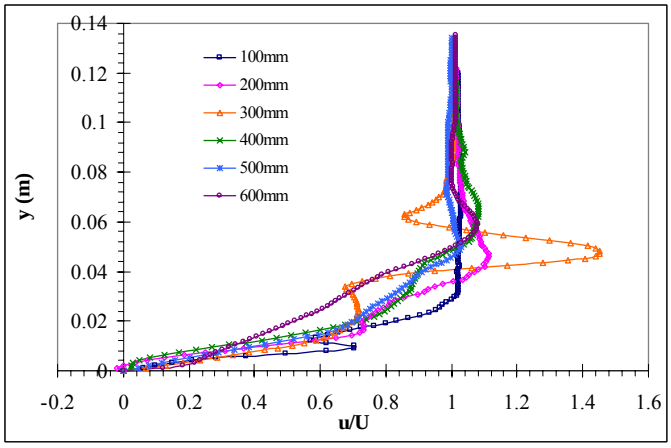

(b)

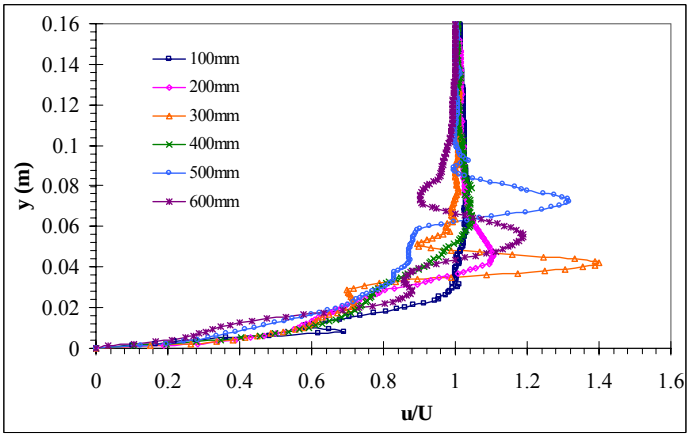

(c)

Figure 5.25: Instantaneous velocity distribution on different flat plate axial locations for $\tau = 800$, $x_c/2c = 3$ $y_c/2c = 1$ (a) Re_{2c}=500, (b) Re_{2c}=800, (c) Re_{2c}=1000.

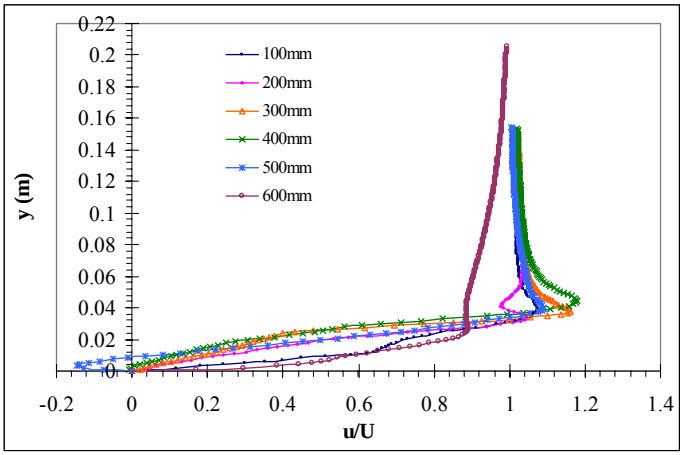

(a)

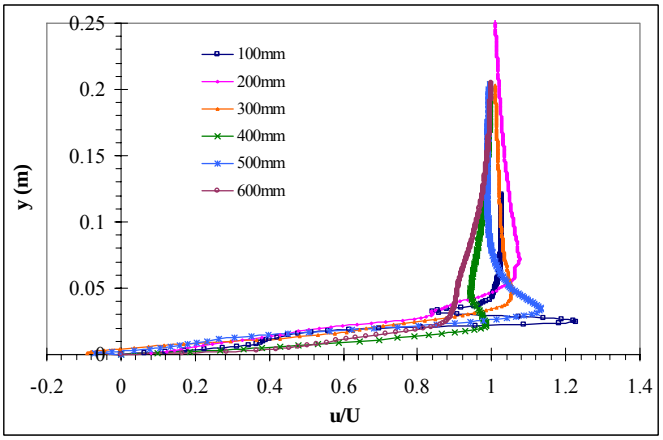

(b)

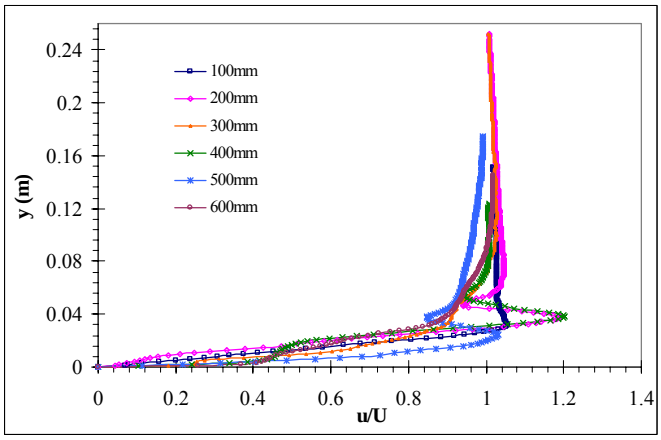

(c)

Figure 5.26: Instantaneous velocity distribution on different flat plate axial locations for $\tau = 800$, $x_c/2c = 0$ $y_c/2c = 0.75$, (a) $Re_{2c}=500$, (b) $Re_{2c}=800$, (c) $Re_{2c}=1000$.

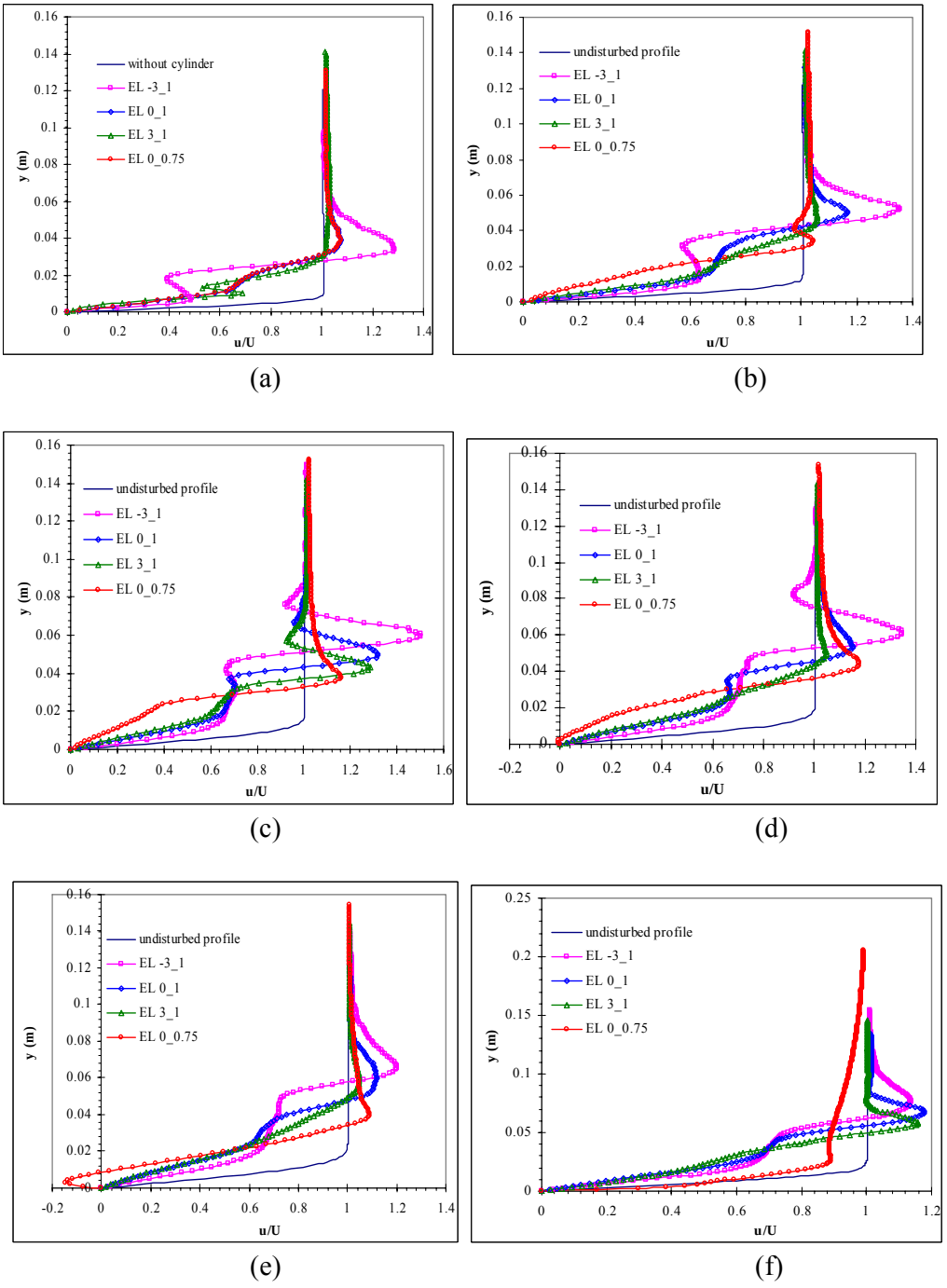

Figure 5.27: Variation of velocity profile with cylinder to plate relative positions for τ = 800, Re = 500, (a) Xp =100mm (b) Xp =200mm, (c) Xp =300mm, (d) Xp =400mm, (e) Xp =500mm, (f) Xp =600mm.

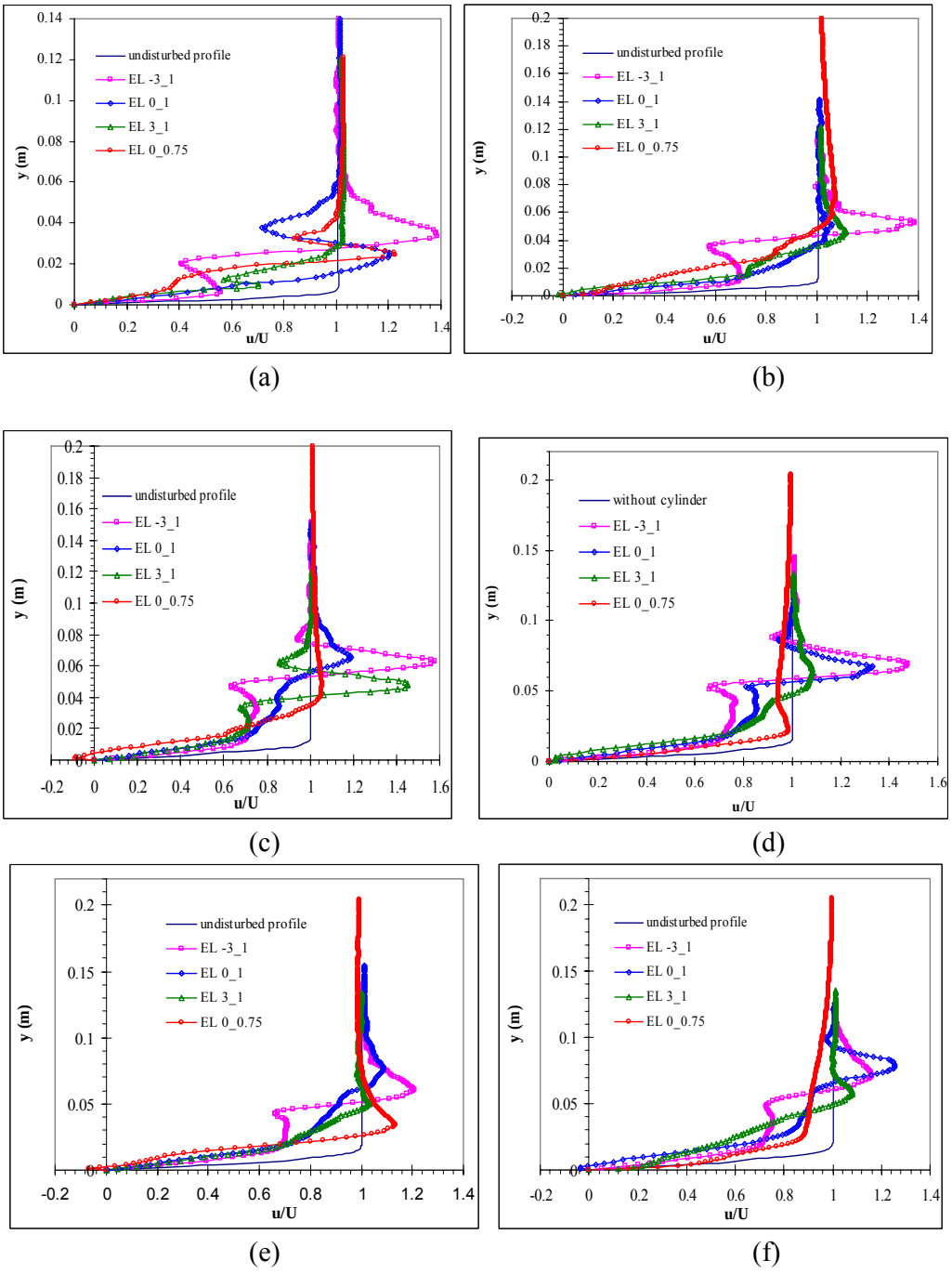

Figure 5.28: Variation of velocity profile with cylinder to plate relative positions for τ = 800, Re = 800, (a) Xp =100mm (b) Xp =200mm, (c) Xp =300mm, (d) Xp =400mm, (e) Xp =500mm, (f) Xp =600mm.

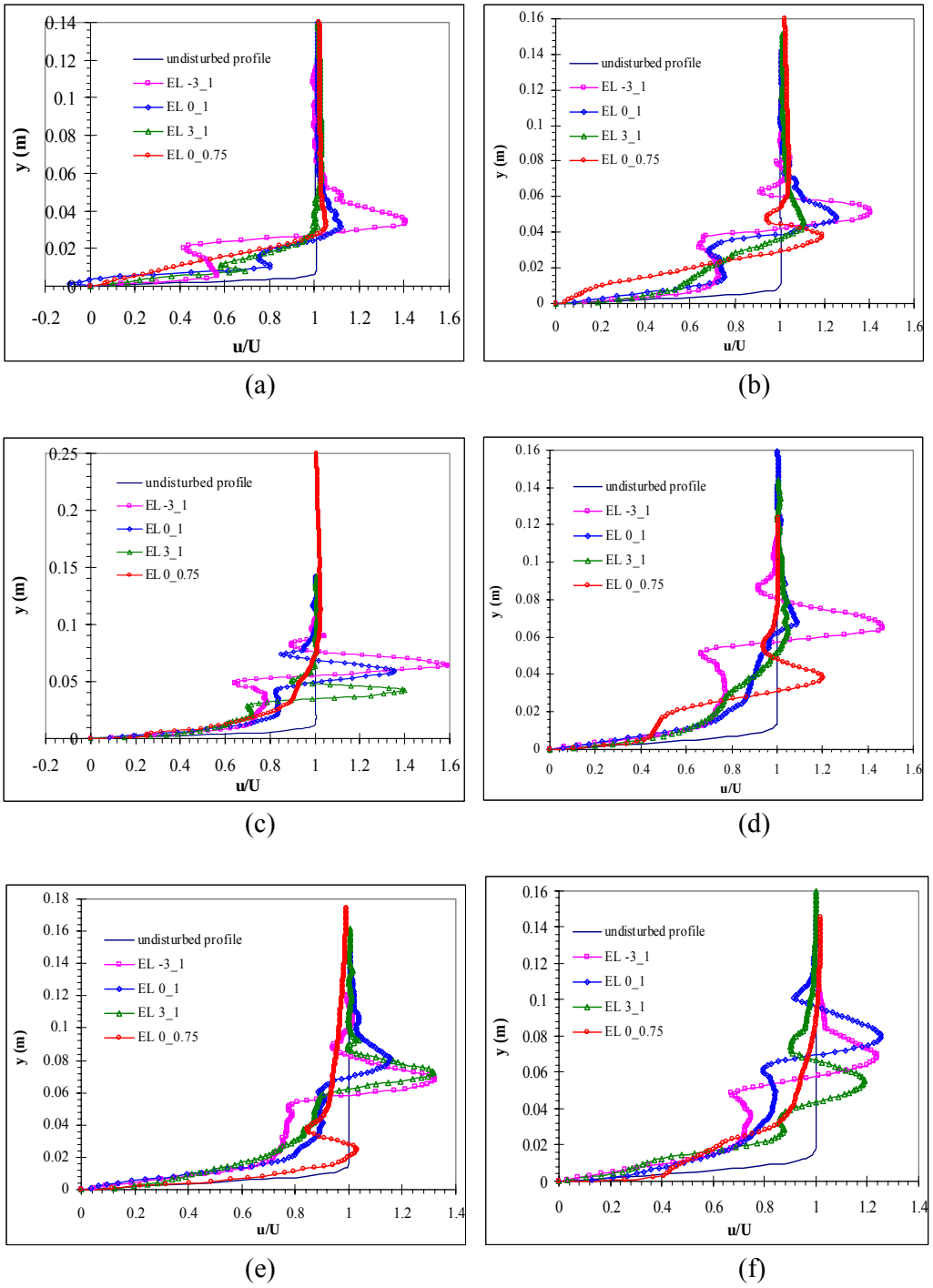

Figure 5.29: Variation of velocity profile with cylinder to plate relative positions for τ = 800, Re = 1000, (a) Xp =100mm (b) Xp =200mm, (c) Xp =300mm, (d) Xp =400mm, (e) Xp =500mm, (f) Xp =600mm.

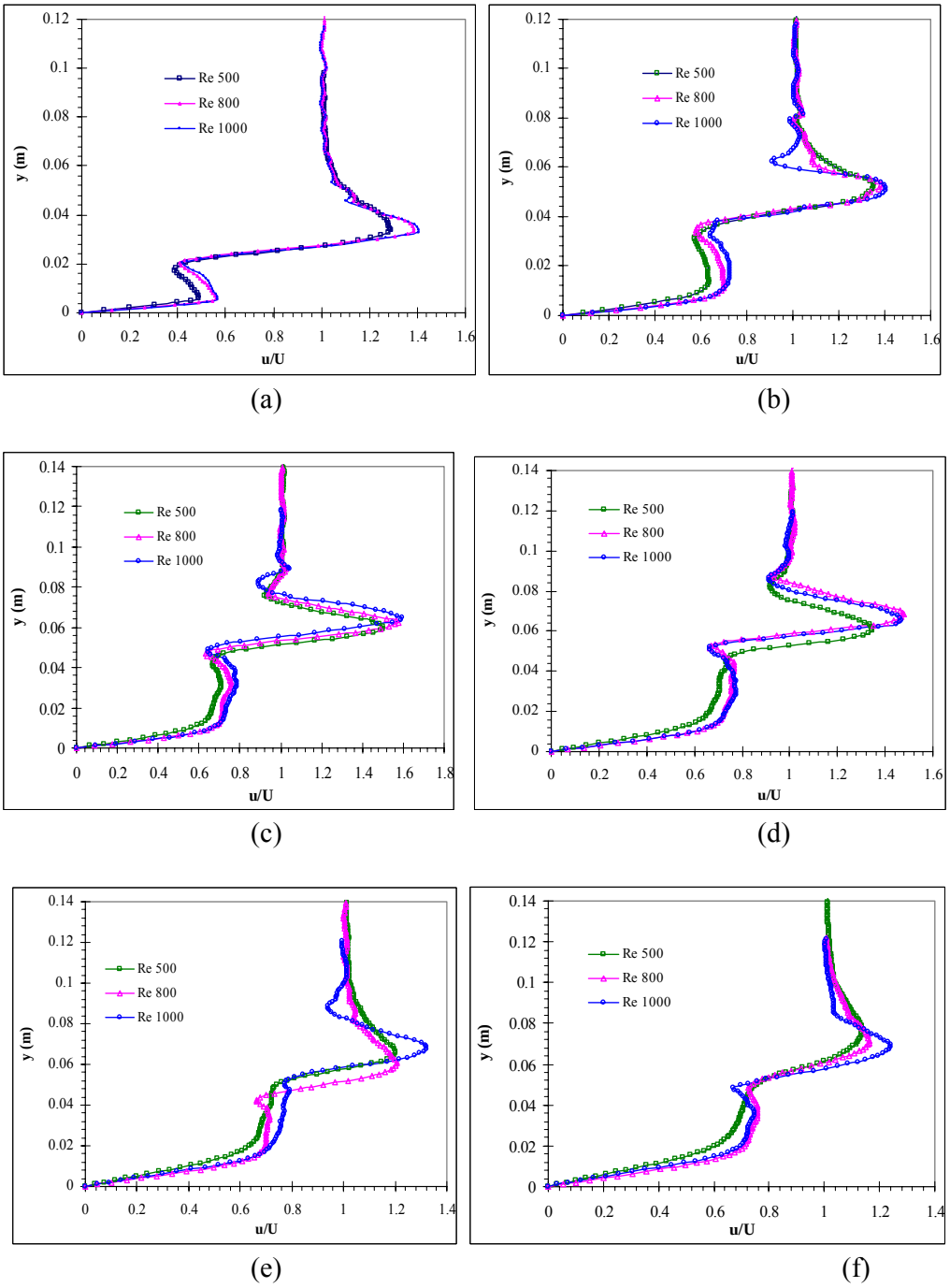

Figure 5.30: Variation of velocity profile with Reynolds number Re at cylinder to plate relative positions $x_c/2c = -3$ $y_c/2c = 1$ for $\tau = 800$ (a) Xp =100mm (b) Xp =200mm, (c) Xp =300mm, (d) Xp =400mm, (e) Xp =500mm, (f) Xp =600mm.

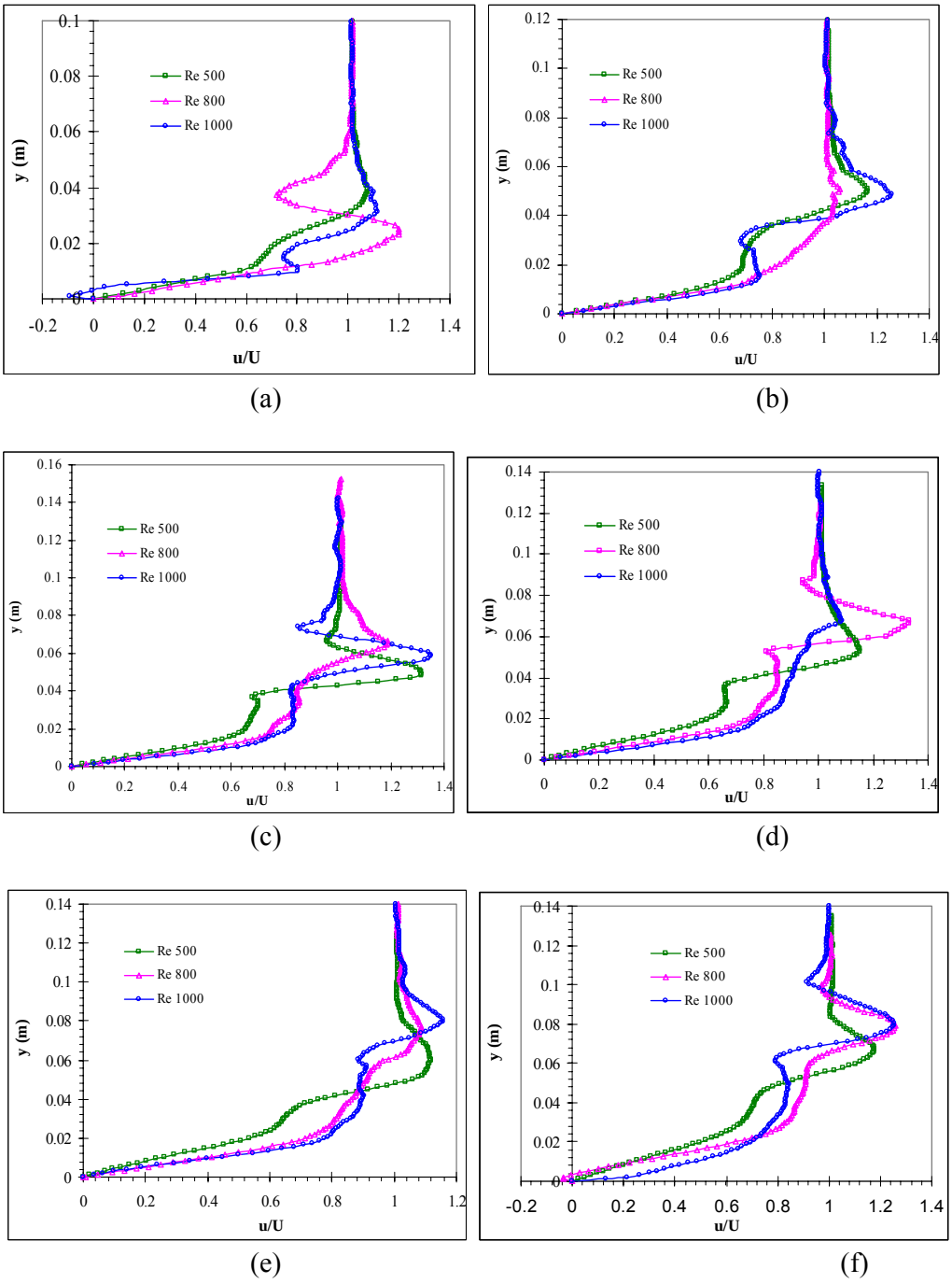

Figure 5.31: Variation of velocity profile with Reynolds number Re at cylinder to plate relative positions $x_c/2c = 0$ $y_c/2c = 1$ for $\tau = 800$ (a) Xp =100mm (b) Xp =200mm, (c) Xp =300mm, (d) Xp =400mm, (e) Xp =500mm, (f) Xp =600mm.

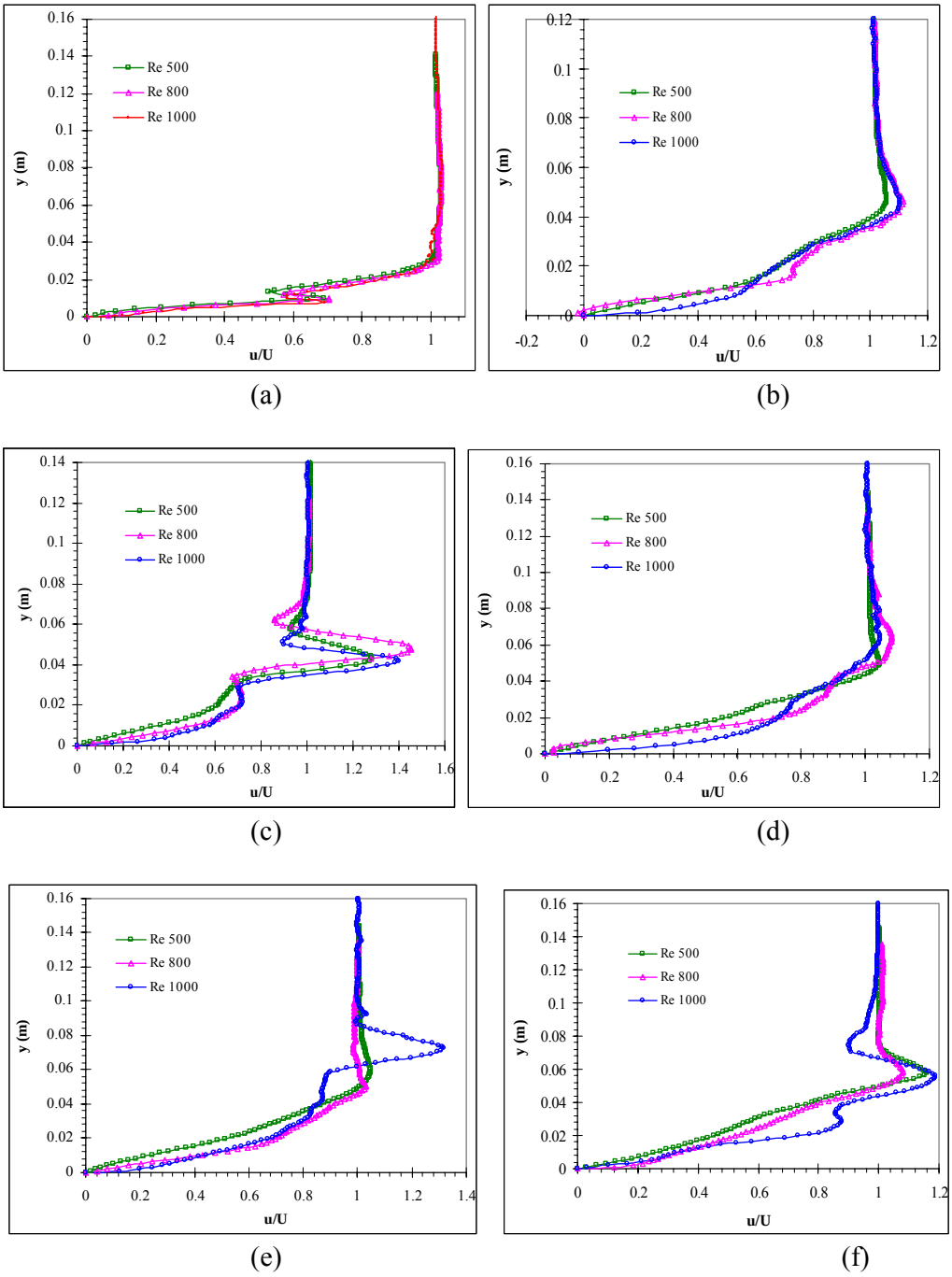

Figure 5.32: Variation of velocity profile with Reynolds number Re at cylinder to plate relative positions $x_c/2c = 3$ $y_c/2c = 1$ for $\tau = 800$ (a) Xp =100mm (b) Xp =200mm, (c) Xp =300mm, (d) Xp =400mm, (e) Xp =500mm, (f) Xp =600mm.

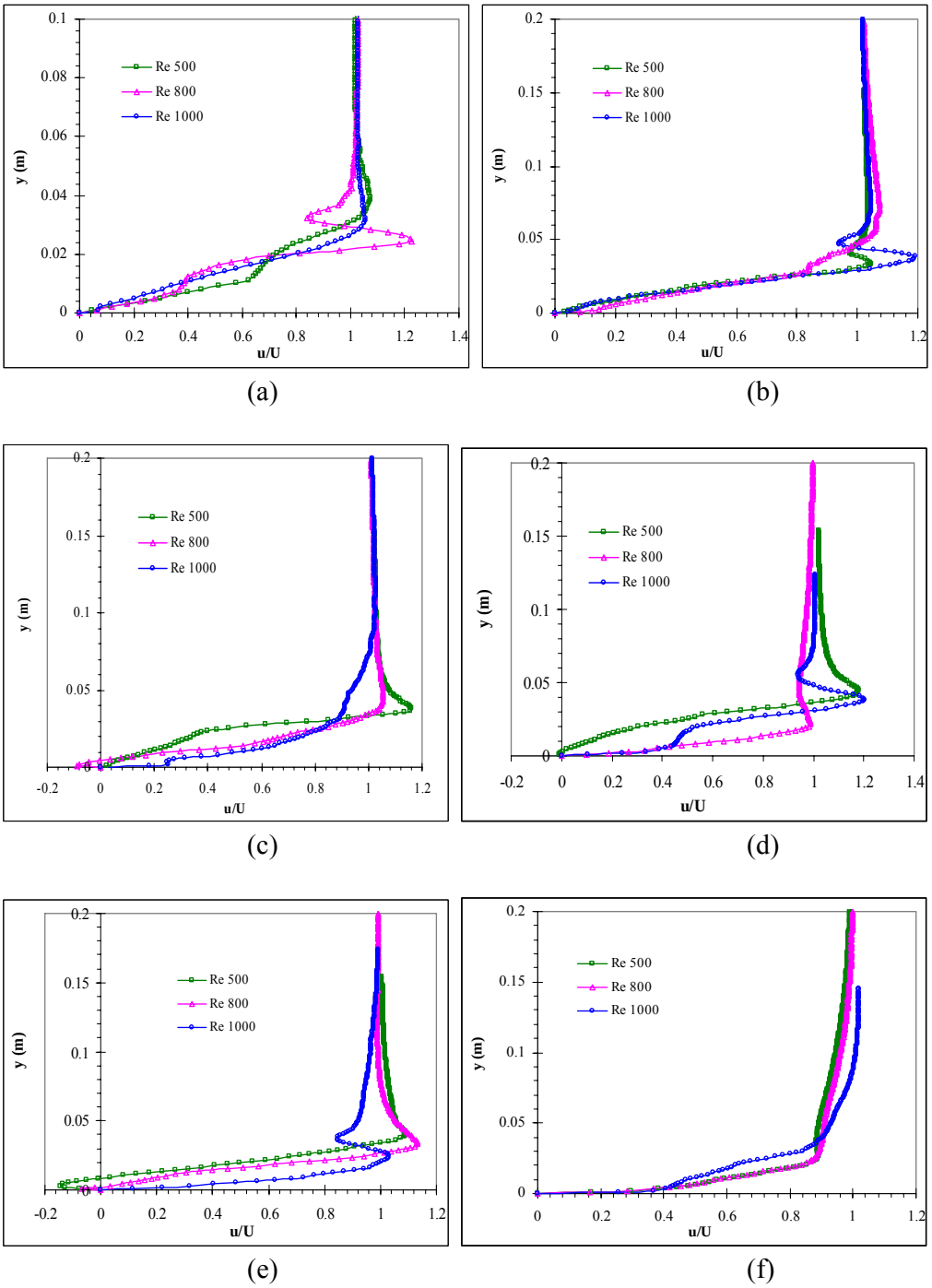

Figure 5.33: Variation of velocity profile with Reynolds number Re at cylinder to plate relative positions $x_c/2c = 3$ $y_c/2c = 1$ for $\tau = 800$ (a) Xp =100mm (b) Xp =200mm, (c) Xp =300mm, (d) Xp =400mm, (e) Xp =500mm, (f) Xp =600mm.

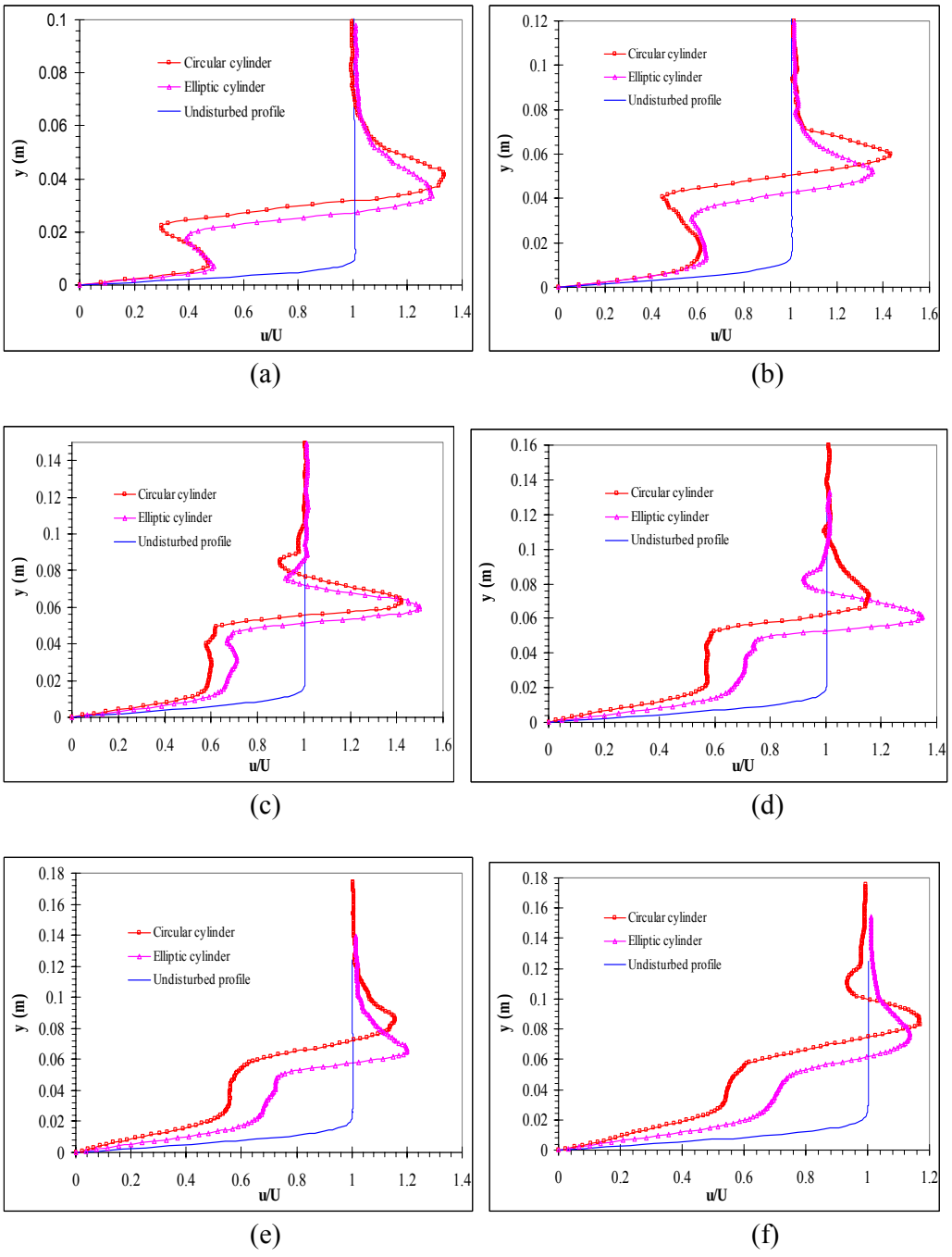

Figure 5.34: Variation of velocity distribution on the flat plate for different types of cylinder located ahead of the plate for Re_{2c} = 500, τ = 800, $x_c/2c$ = -3 y_c = 1, (a) Xp = 100mm, (b) Xp = 200mm, (c) Xp = 300mm, (d) Xp = 400mm, (e) Xp = 500mm, (f) Xp = 600mm.

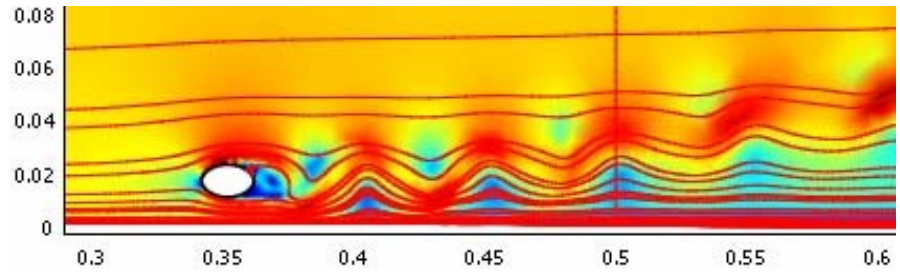

$\tau = 505$

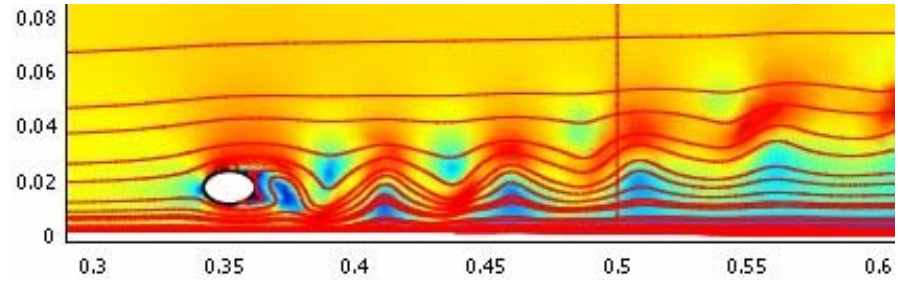

$\tau = 506$

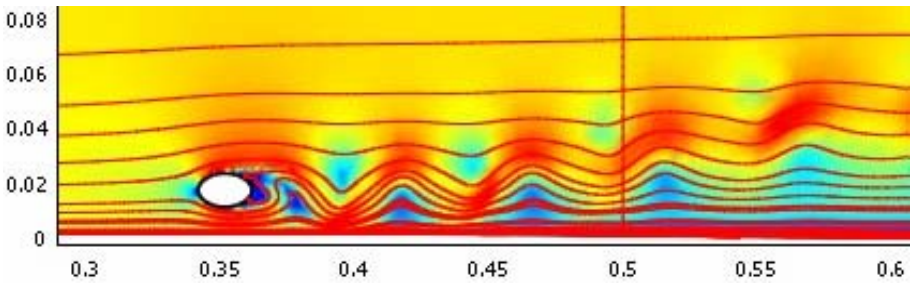

$\tau = 507$

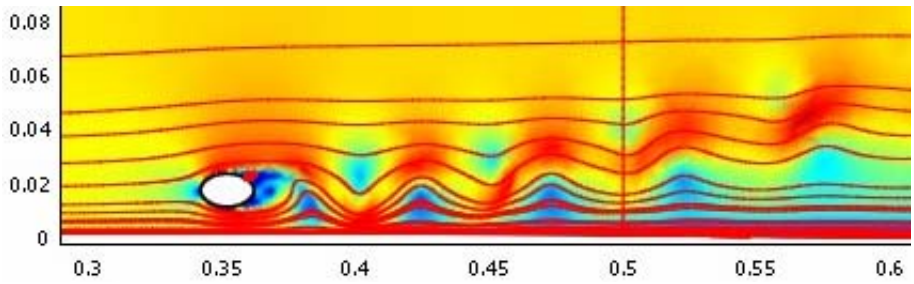

$\tau = 508$

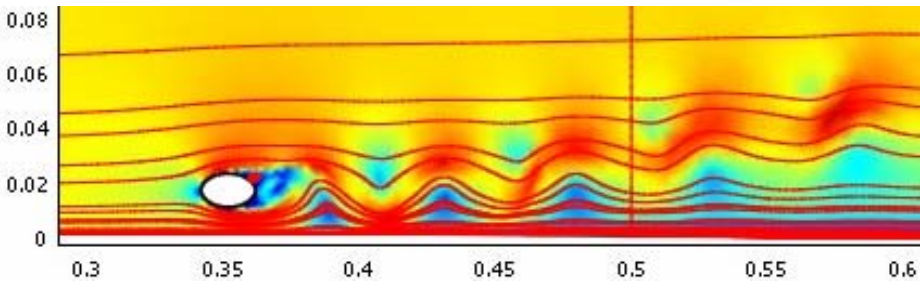

$\tau = 509$

Figure 5.35 (Continue…)

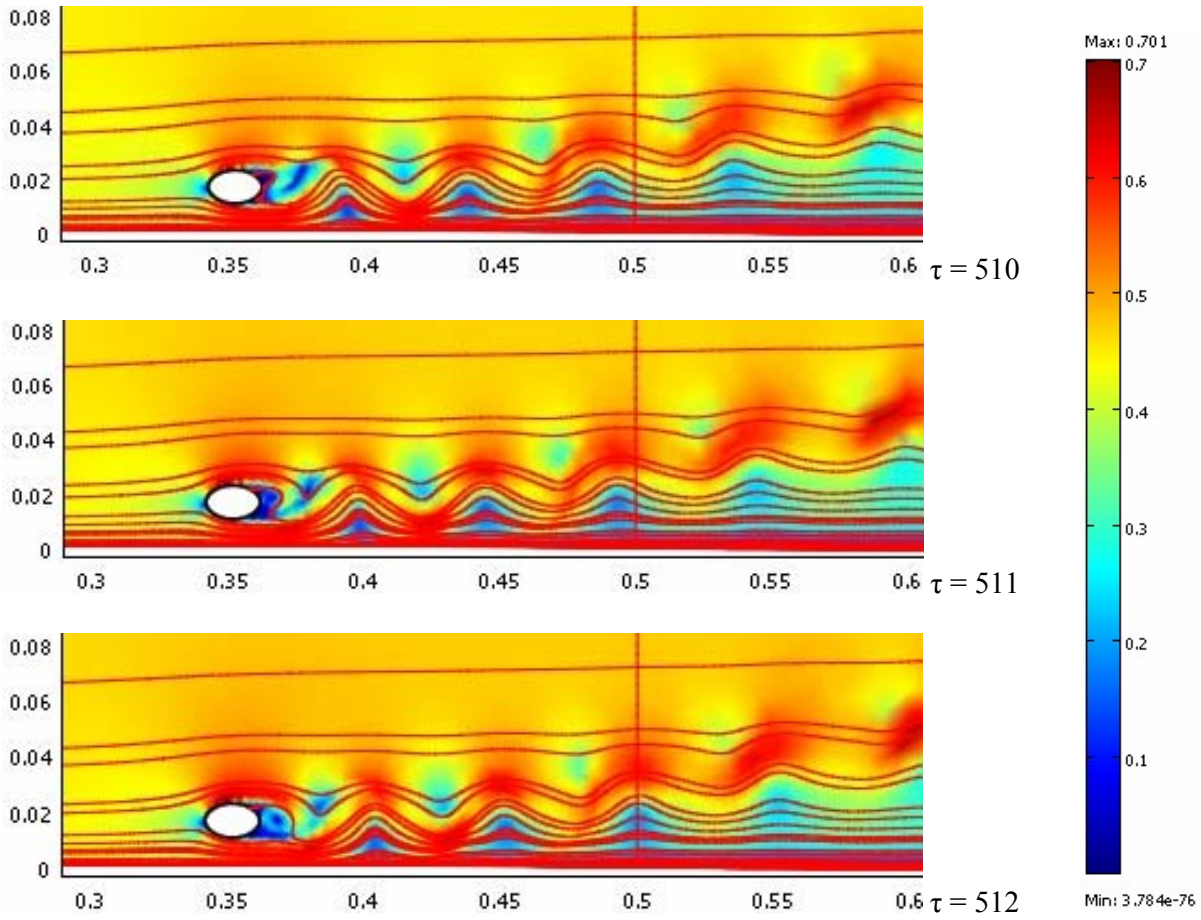

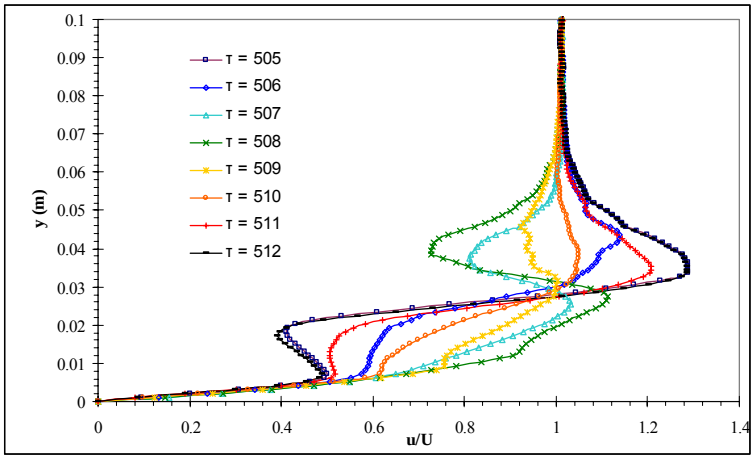

Figure 5.35: Instantaneous streamlines for sequential time interval (τ = 505 to τ = 512) and the corresponding velocity profiles of each time τ for Xp = 100 mm, Re_{2c} = 500, $x_c/2c$ = -3, $y_c/2c$ = 1.

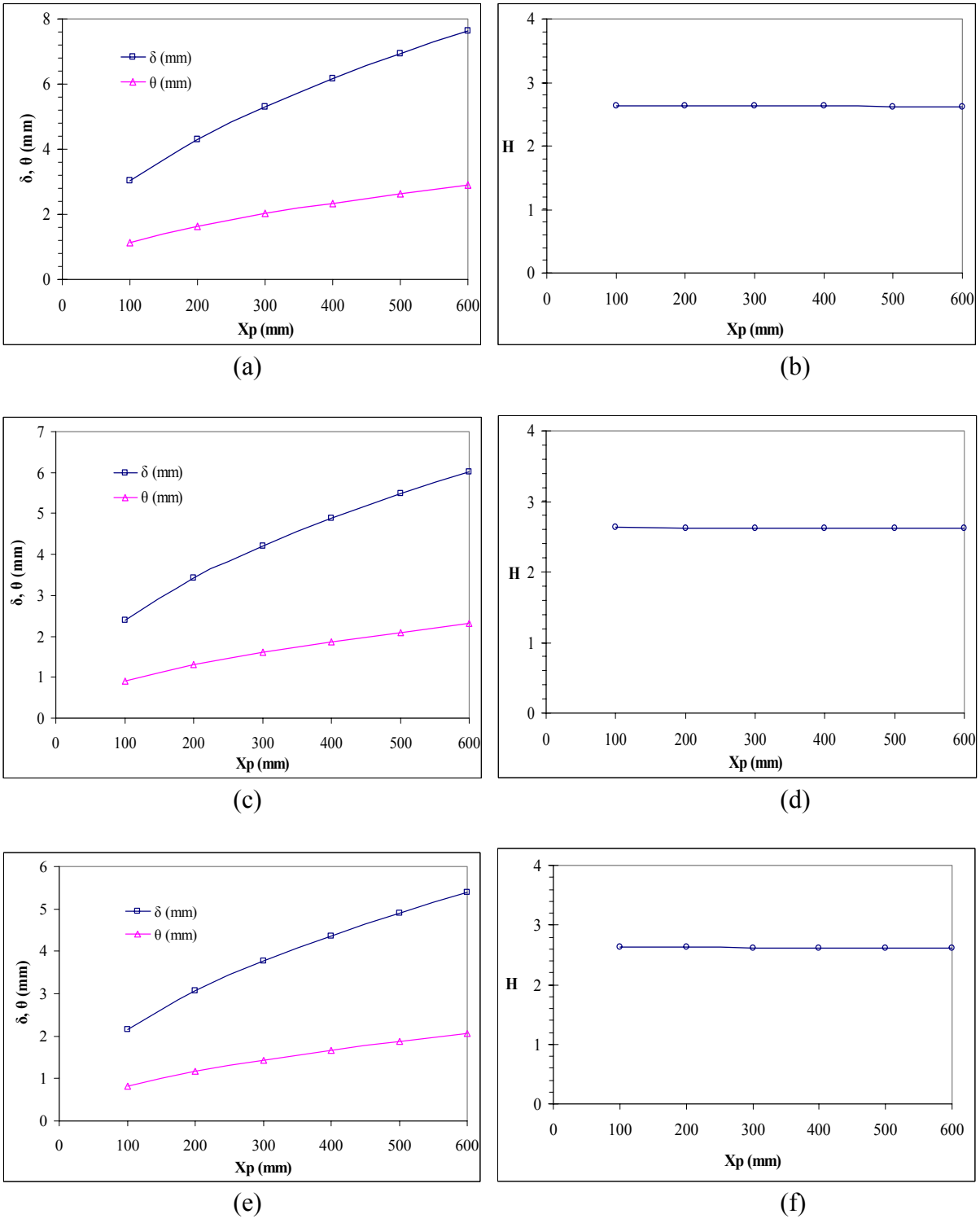

Figure 5.36: Spatial variation of □-displacement thickness (δ), Δ-momentum thickness (θ) and ○-shape factor (H) of undisturbed flow over the flat plate for (a,b) Re_{2c} = 500, (c,d) Re_{2c} = 800 and (e,f) Re_{2c} = 1000.

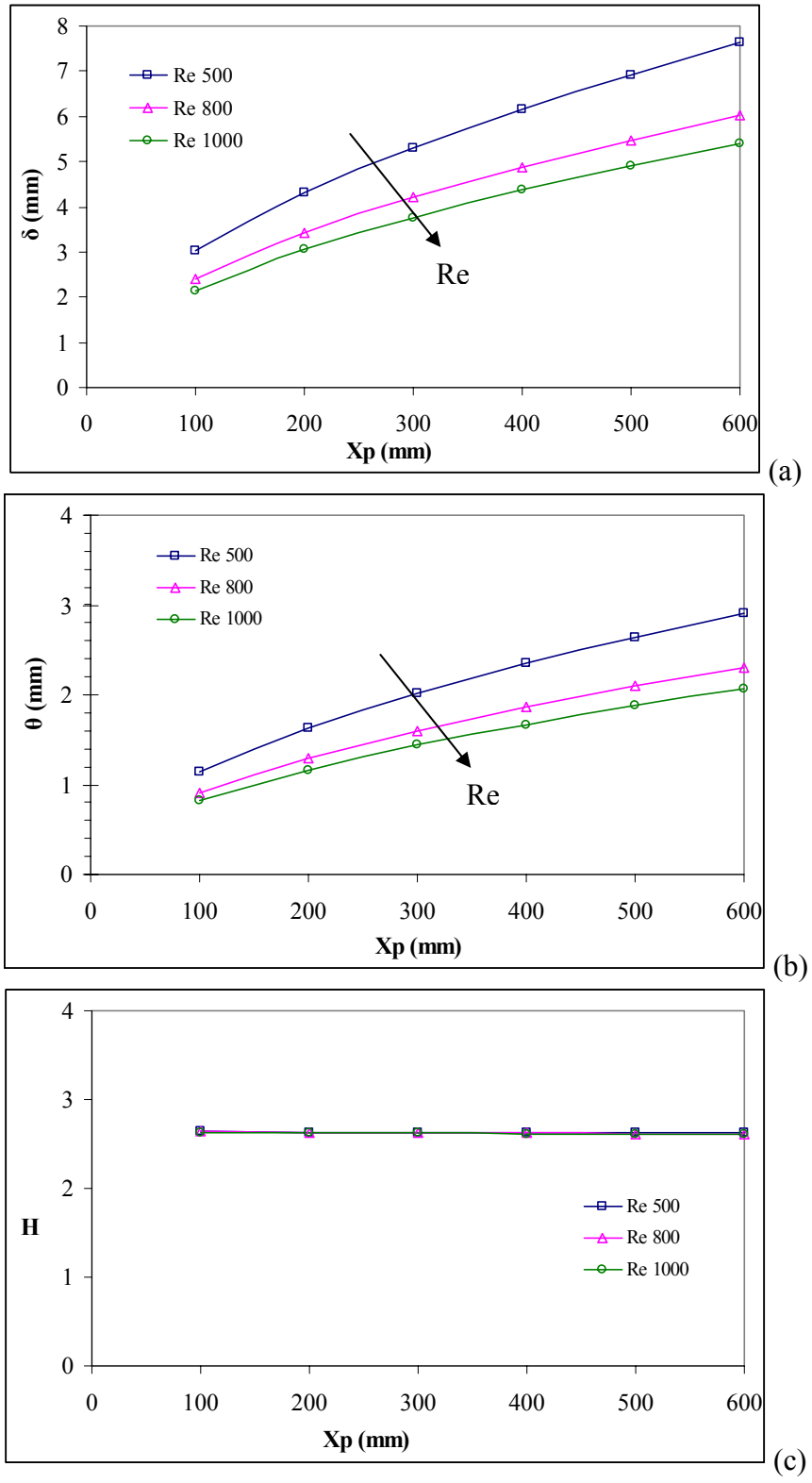

Figure 5.37: Comparison of displacement thickness (δ), momentum thickness (θ) and shape factor (H) for different Reynolds number of undisturbed flow over the flat plate, (a) displacement thickness (δ), (b) momentum thickness (θ) and (c) shape factor (H).

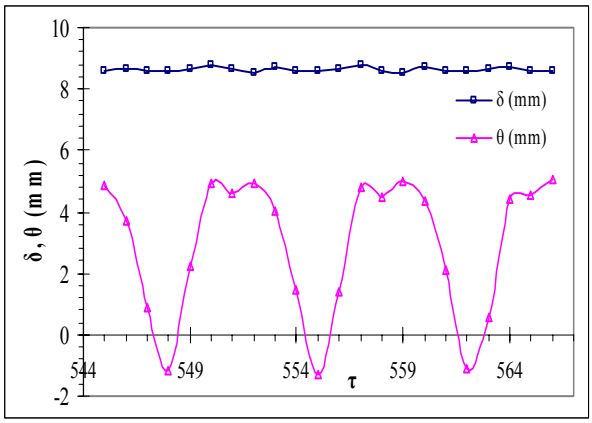

(a)

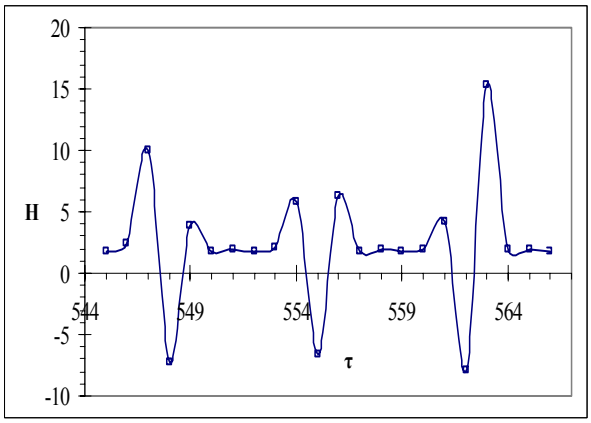

(b)

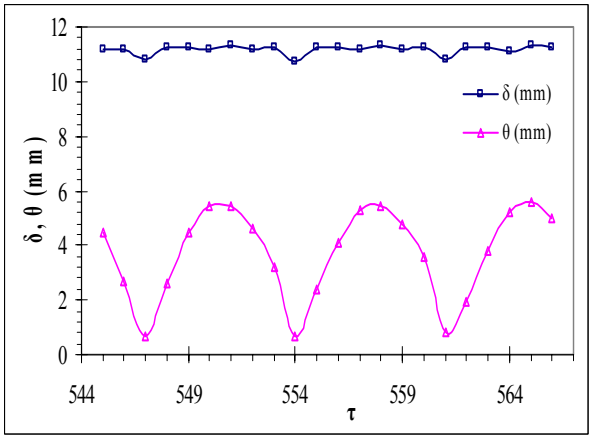

(c)

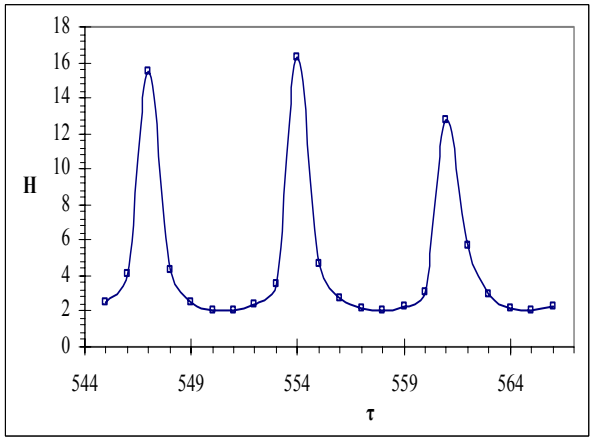

(d)

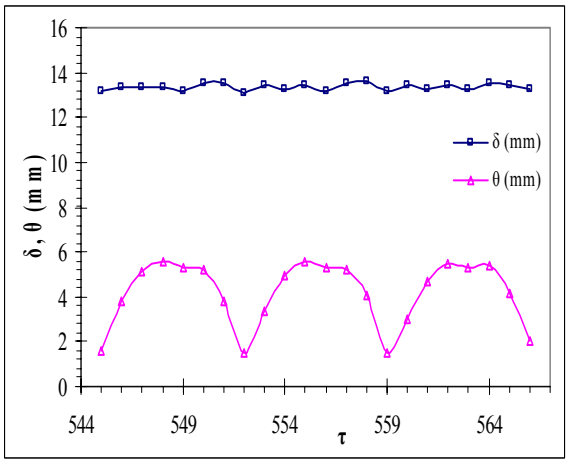

(e)

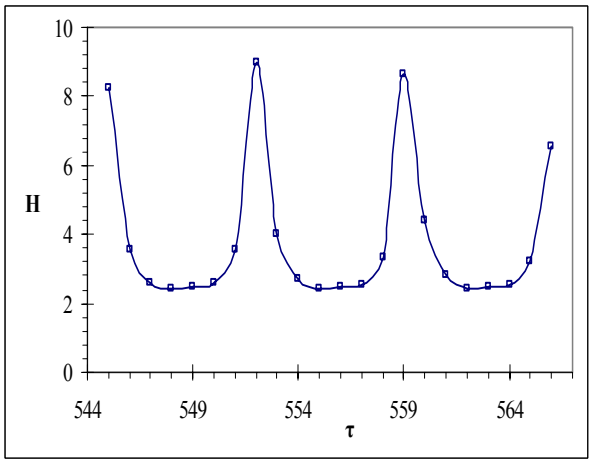

(f)

Figure 5.38 (Continue…)

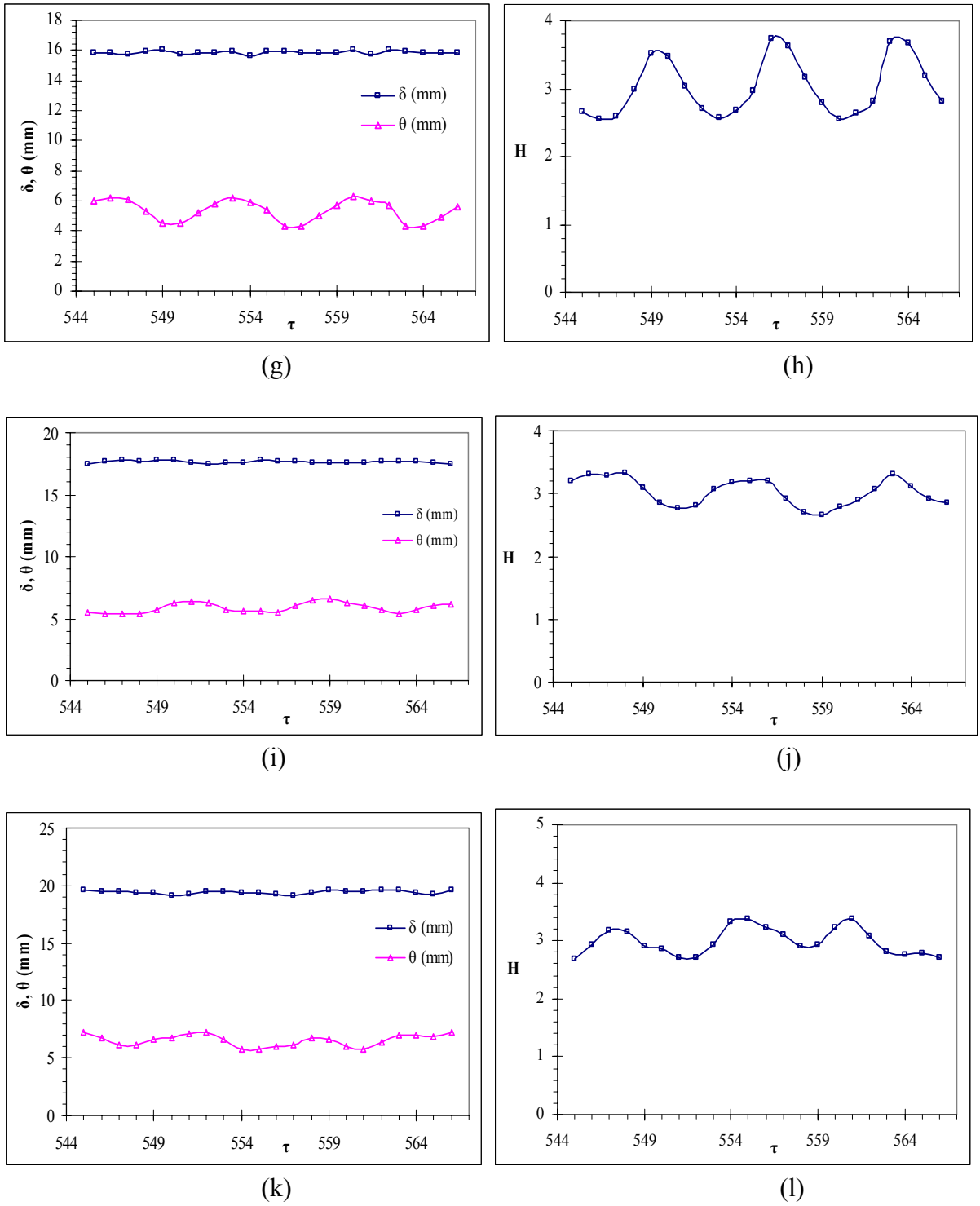

Figure 5.38: Temporal variation of □-displacement thickness (δ), Δ-momentum thickness (θ) and shape factor (H) for Re_{2c} = 500, $x_c/2c$ = -3 $y_c/2c$ = 1, (a,b) Xp =100mm, (c,d) Xp = 200mm, (e,f) Xp =300mm, (g,h) Xp =400mm, (i,j) Xp =500mm, (k,l) Xp =600mm.

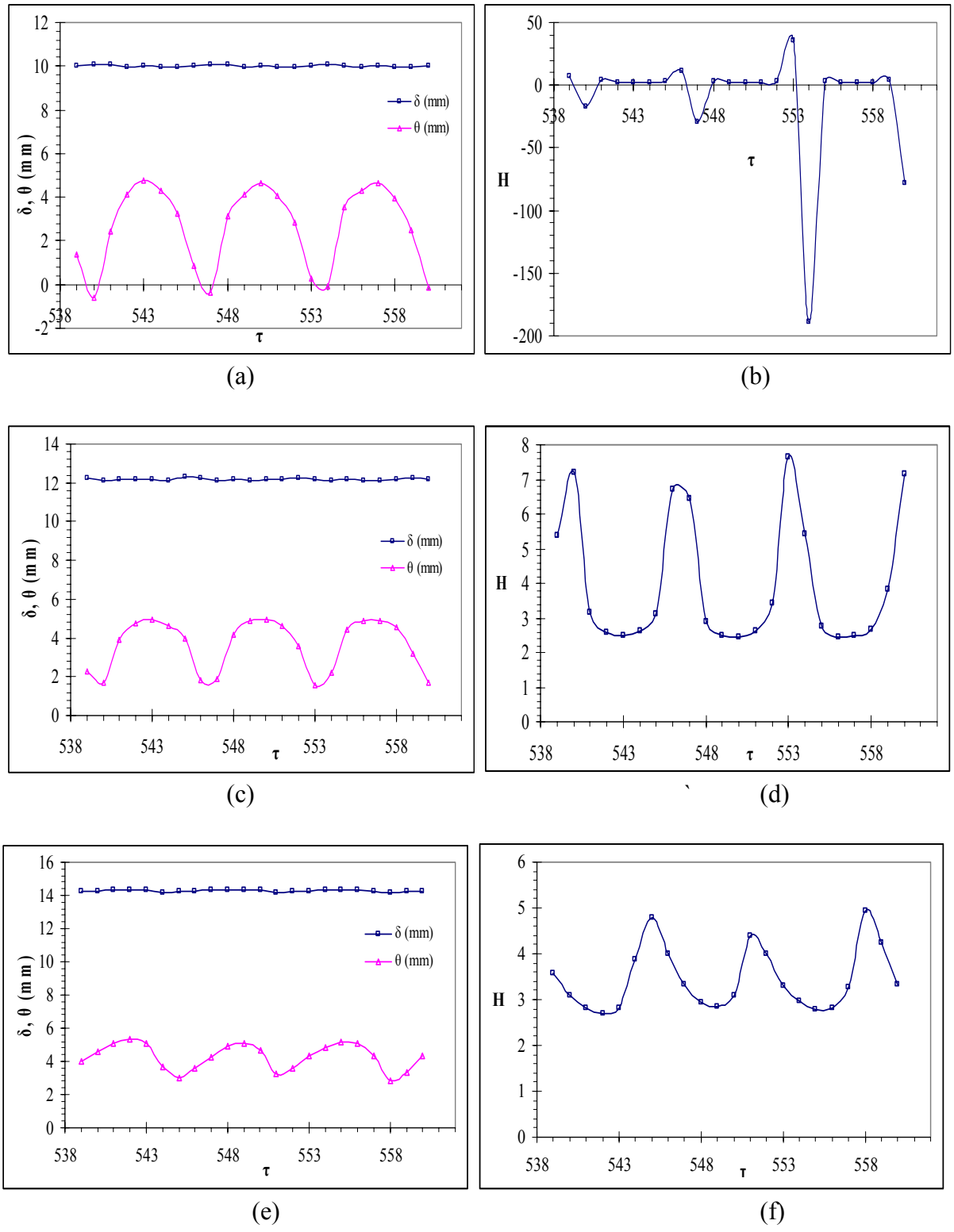

Figure 5.39 (Continue…)

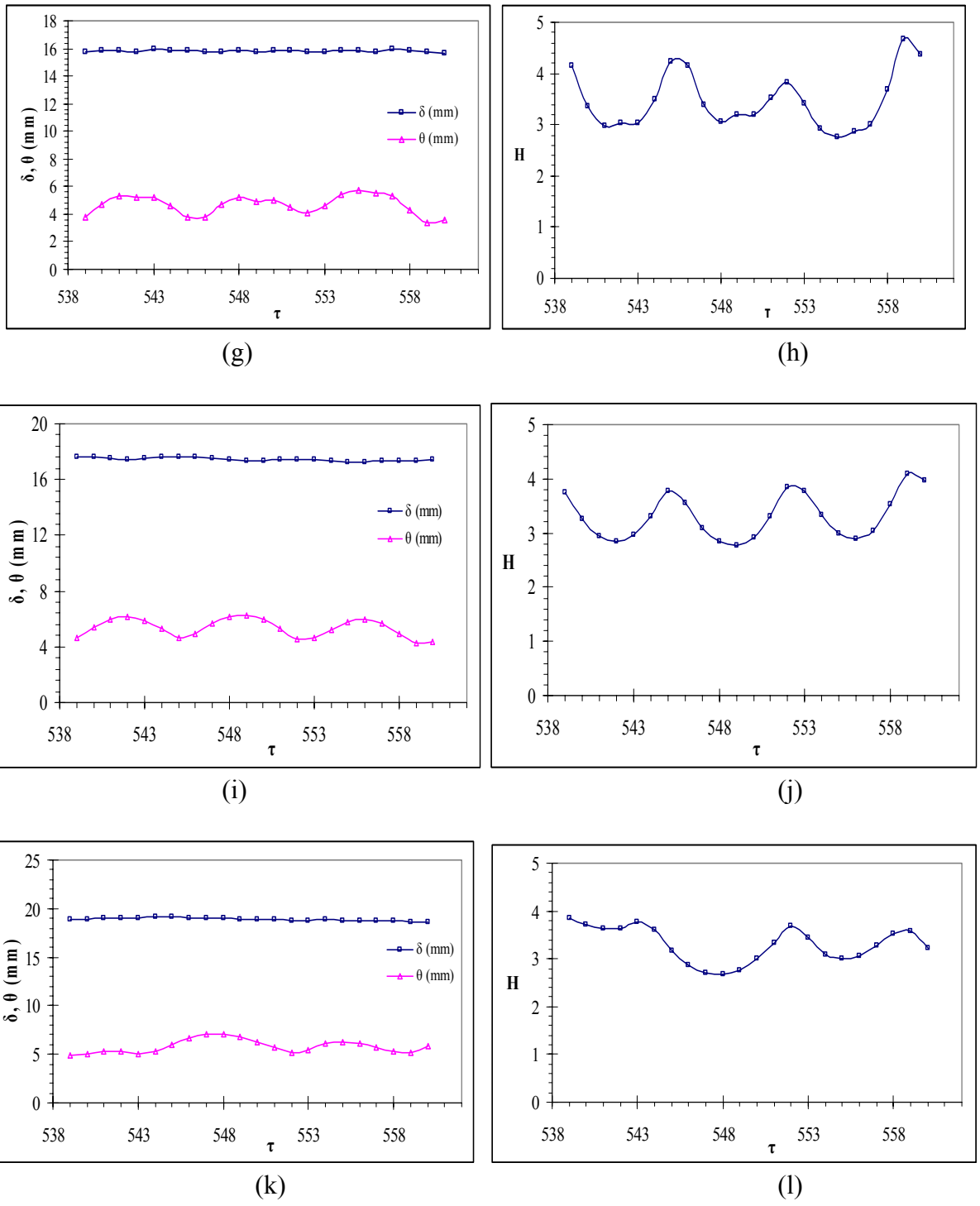

Figure 5.39: Temporal variation of □-displacement thickness (δ), Δ-momentum thickness (θ) and shape factor (H) for Re_{2c} = 500, $x_c/2c$ = 0 $y_c/2c$ = 1, (a,b) Xp =100mm, (c,d) Xp = 200mm, (e,f) Xp =300mm, (g,h) Xp =400mm, (i,j) Xp =500mm, (k,l) Xp =600mm.

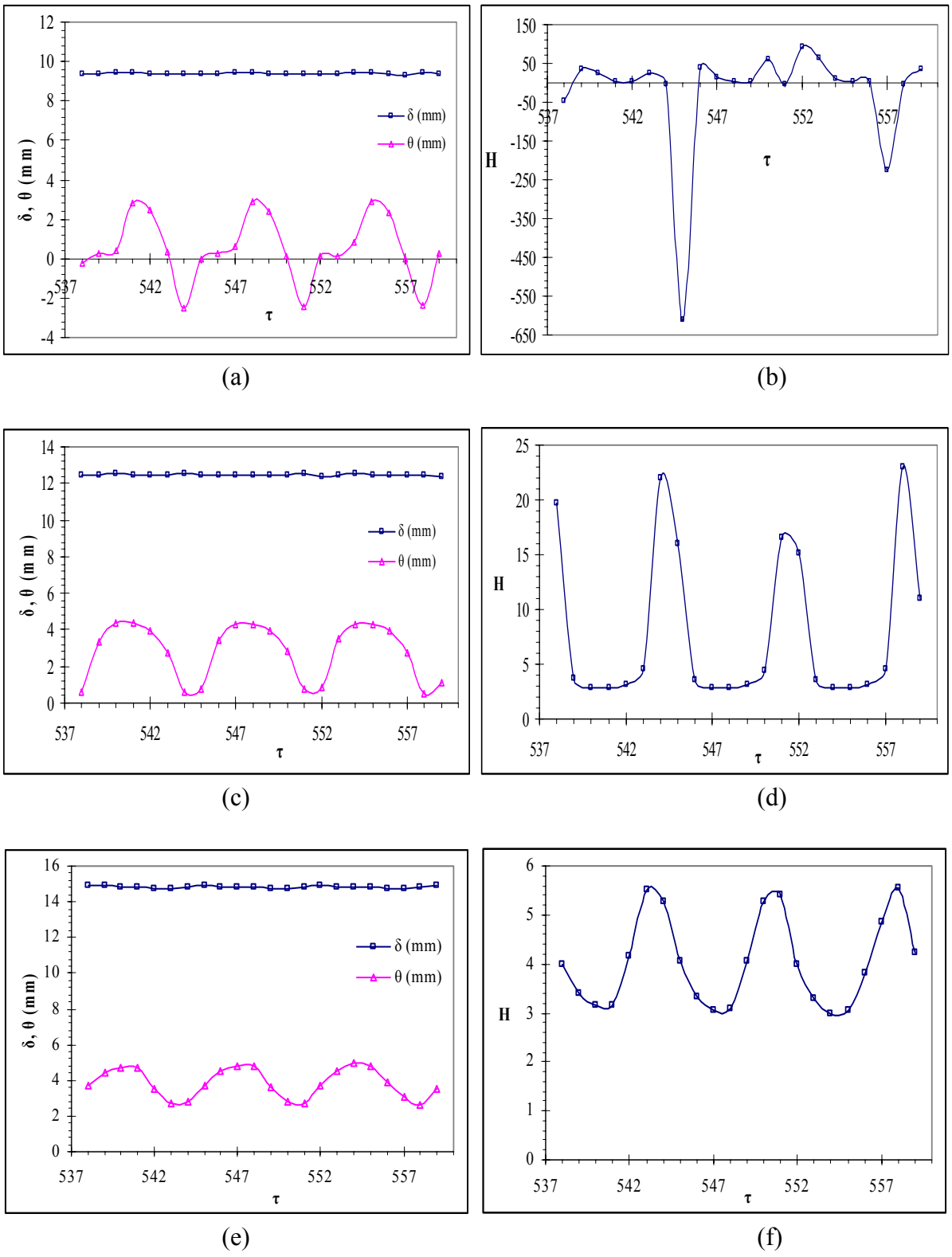

Figure 5.40 (Continue…)

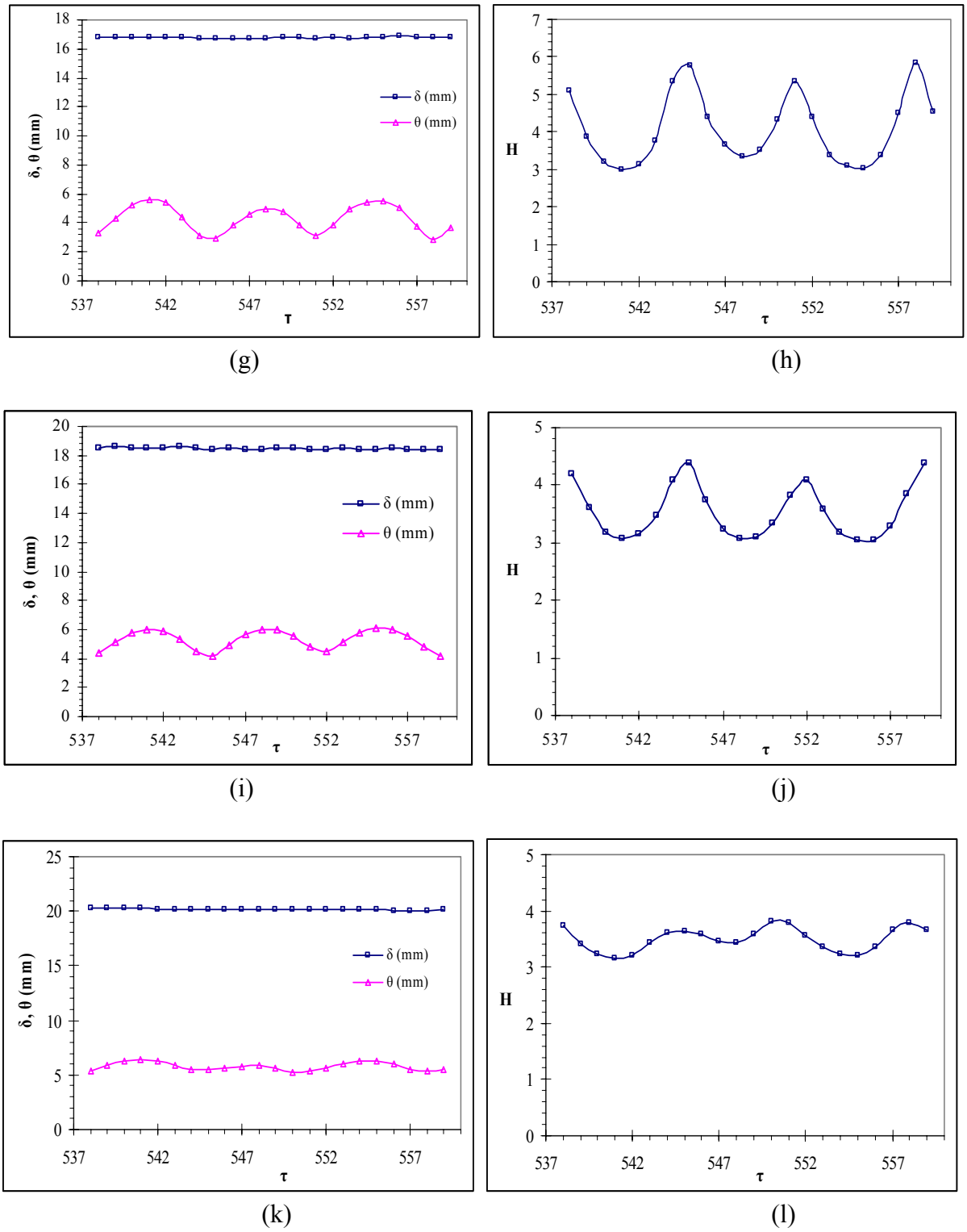

Figure 5.40: Temporal variation of □-displacement thickness (δ), Δ-momentum thickness (θ) and shape factor (H) for Re_{2c} = 500, $x_c/2c$ = 3 $y_c/2c$ = 1, (a,b) Xp =100mm, (c,d) Xp = 200mm, (e,f) Xp =300mm, (g,h) Xp =400mm, (i,j) Xp =500mm, (k,l) Xp =600mm.

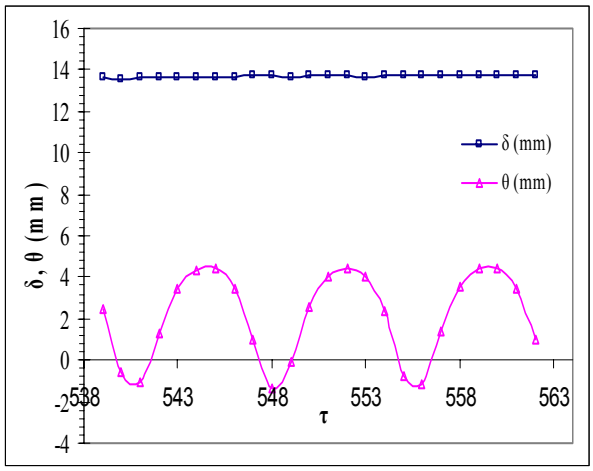

(a)

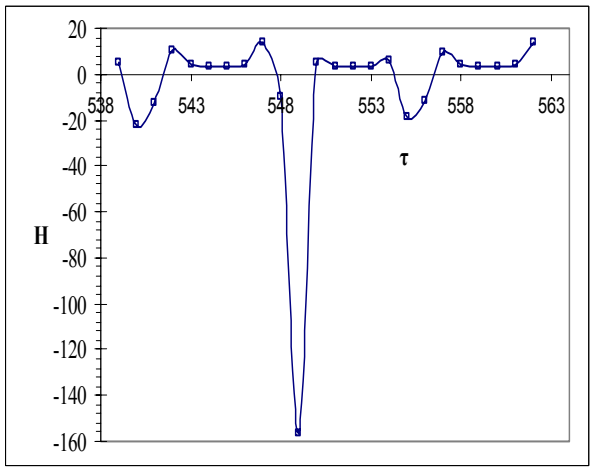

(b)

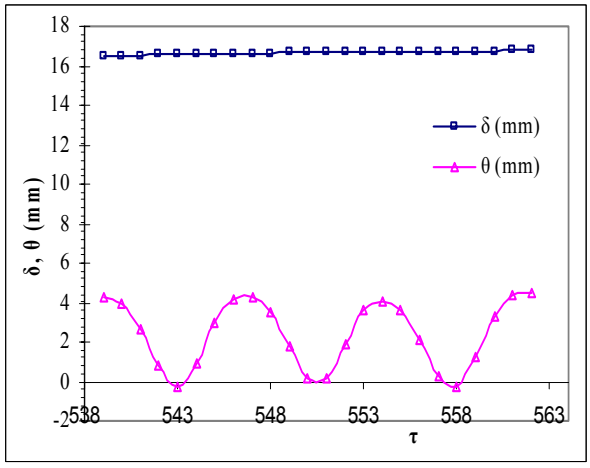

(c)

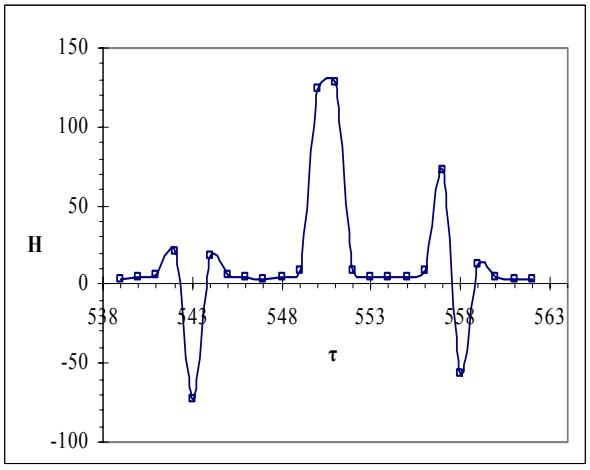

(d)

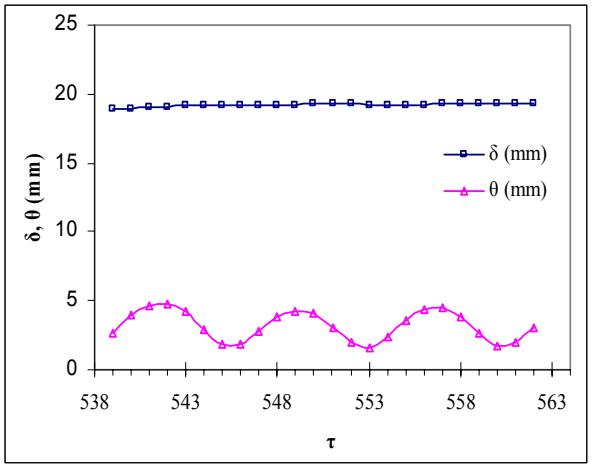

(e)

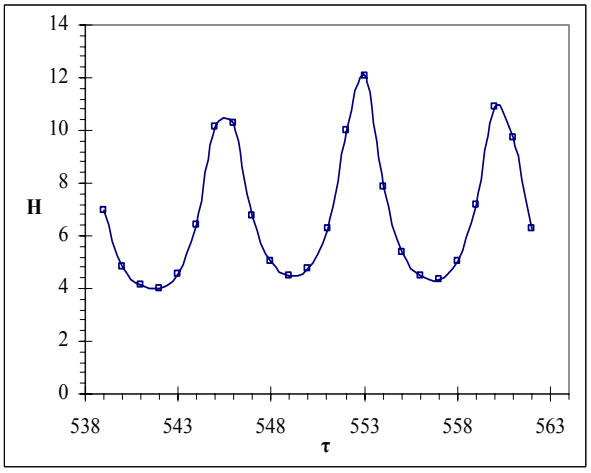

(f)

Figure 5.41 (Continue…)

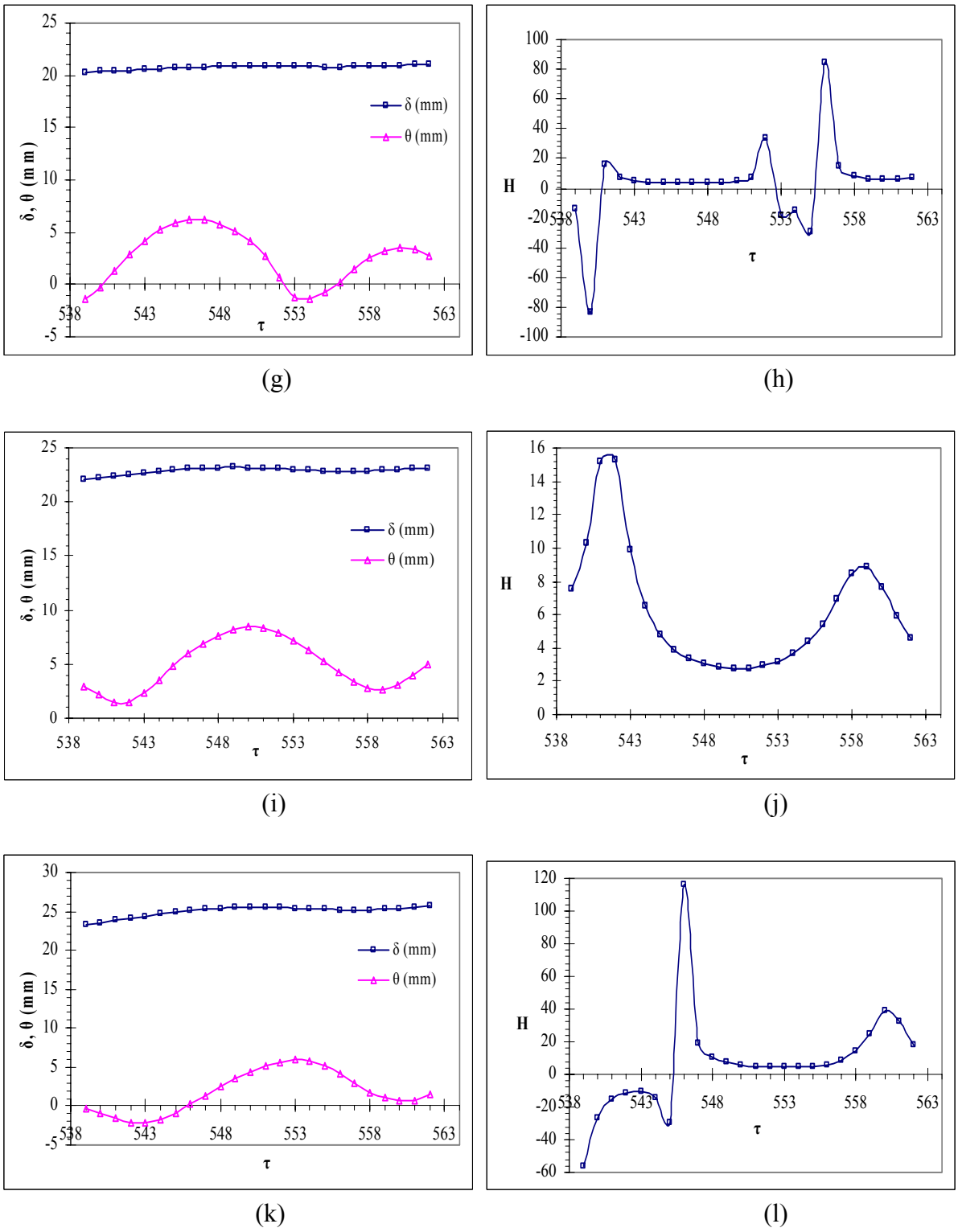

Figure 5.41: Temporal variation of □-displacement thickness (δ), Δ-momentum thickness (θ) and shape factor (H) for Re_{2c} = 500, $x_c/2c$ = 0 $y_c/2c$ = 0.75, (a,b) Xp =100mm, (c,d) Xp = 200mm, (e,f) Xp =300mm, (g,h) Xp =400mm, (i,j) Xp =500mm, (k,l) Xp =600mm.

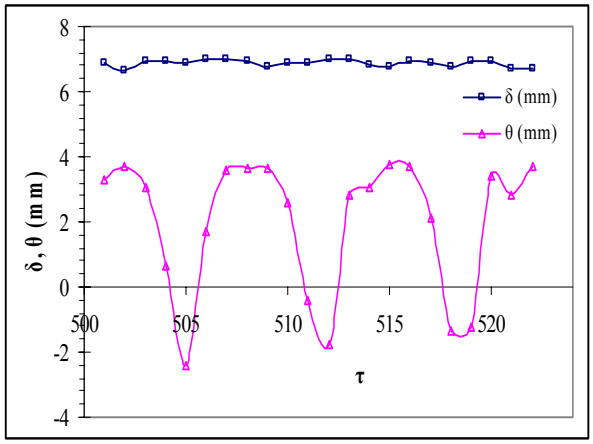

(a)

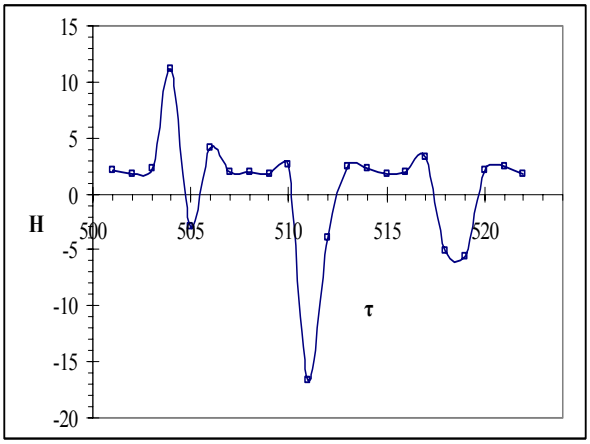

(b)

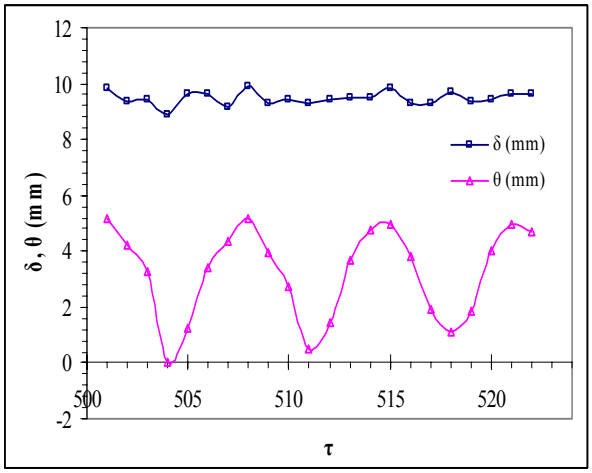

(c)

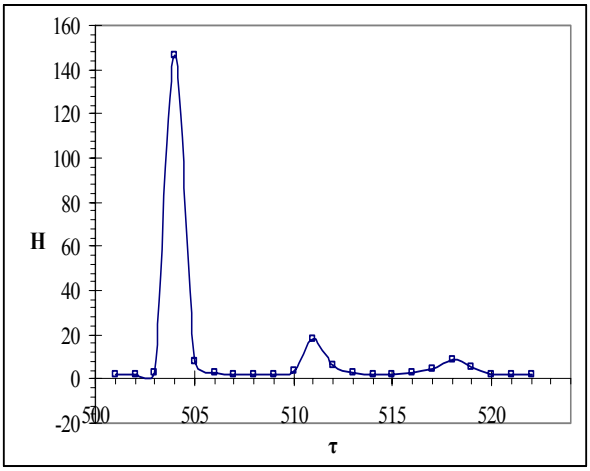

(d)

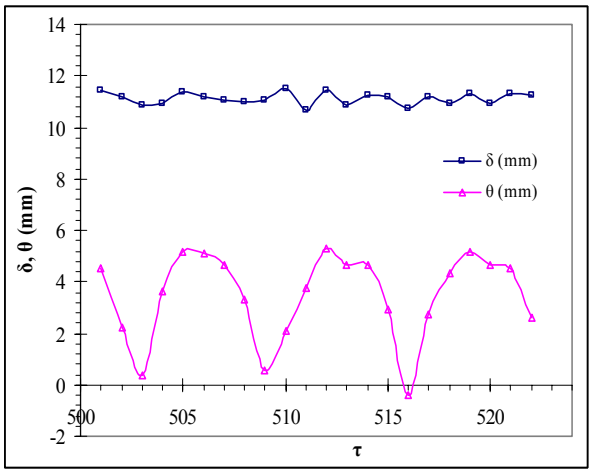

(e)

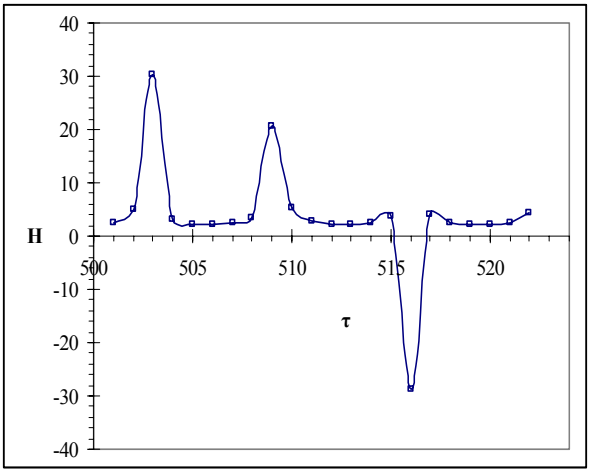

(f)

Figure 5.42 (Continue…)

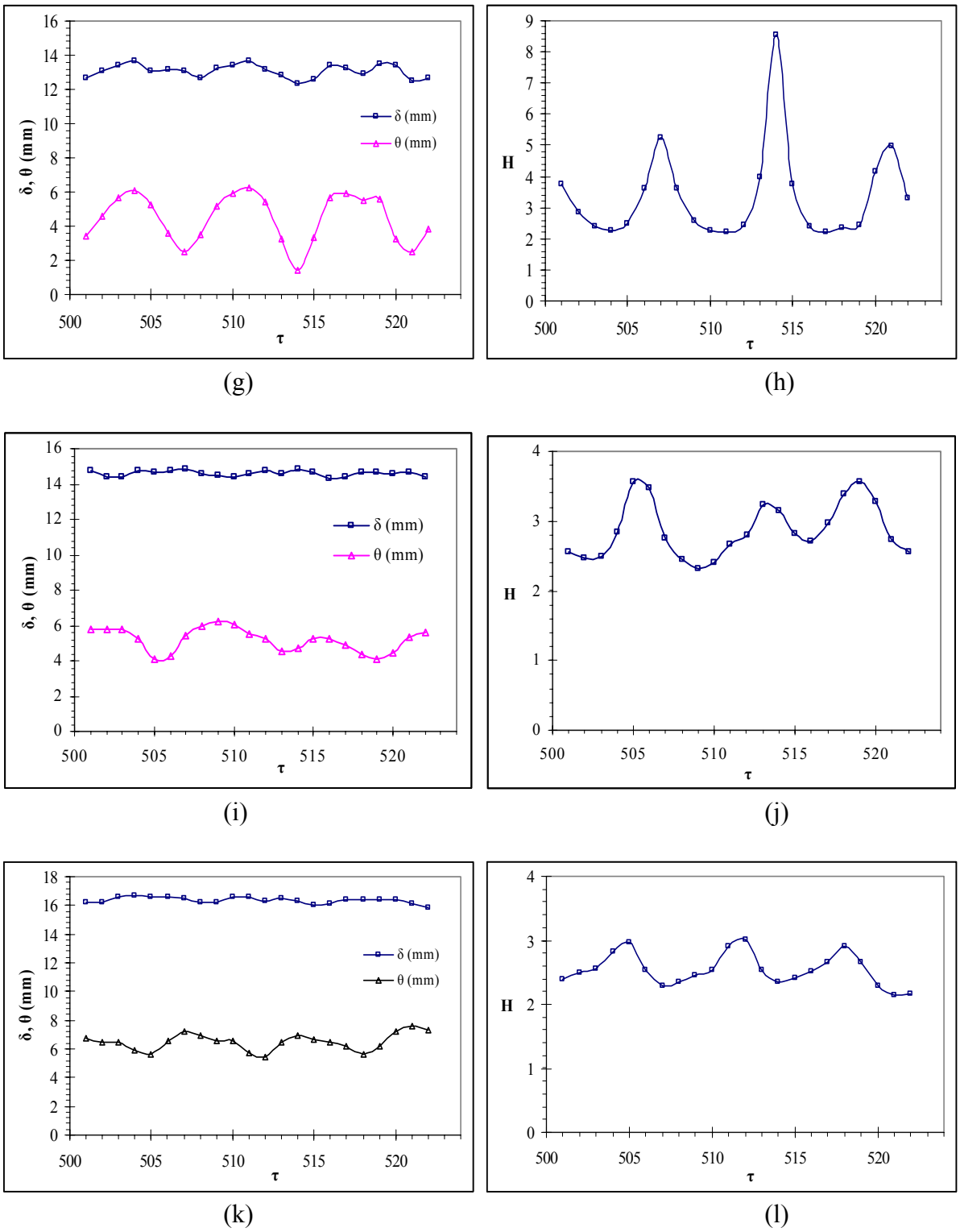

Figure 5.42: Temporal variation of □-displacement thickness (δ), Δ-momentum thickness (θ) and shape factor (H) for Re_{2c} = 800, $x_c/2c$ = -3 $y_c/2c$ = 1, (a,b) Xp =100mm, (c,d) Xp = 200mm, (e,f) Xp =300mm, (g,h) Xp =400mm, (i,j) Xp =500mm, (k,l) Xp =600mm.

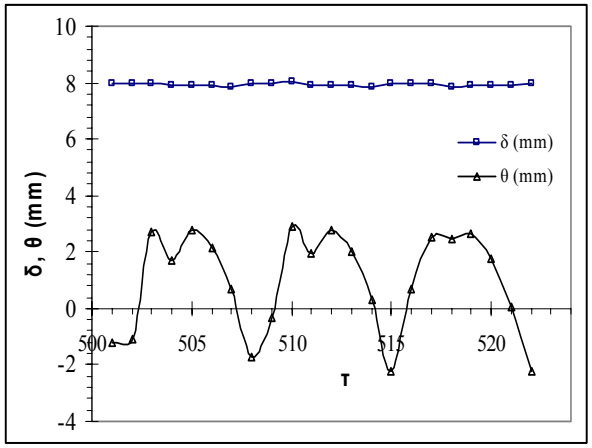

(a)

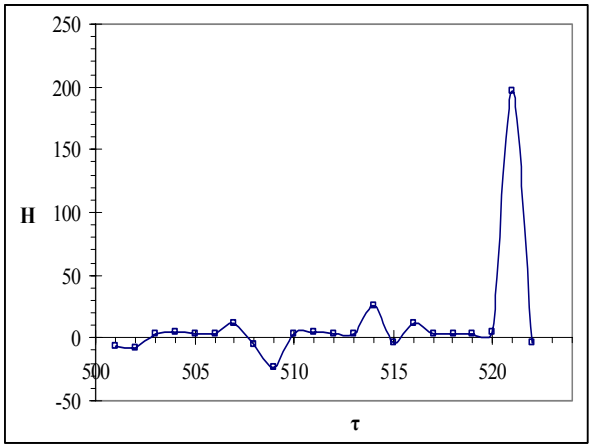

(b)

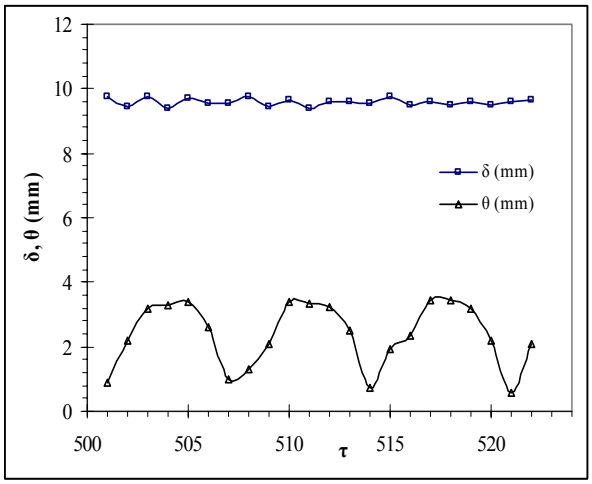

(c)

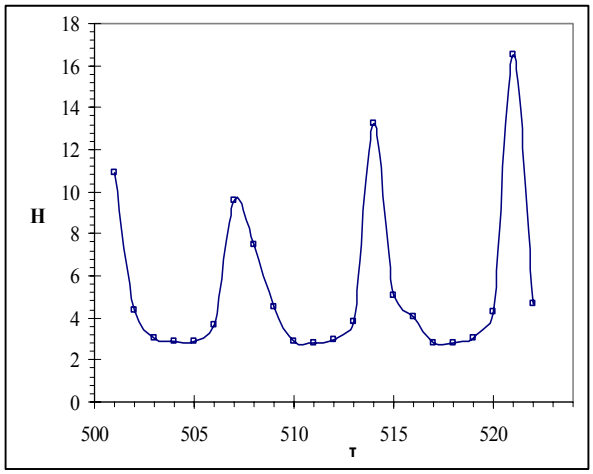

(d)

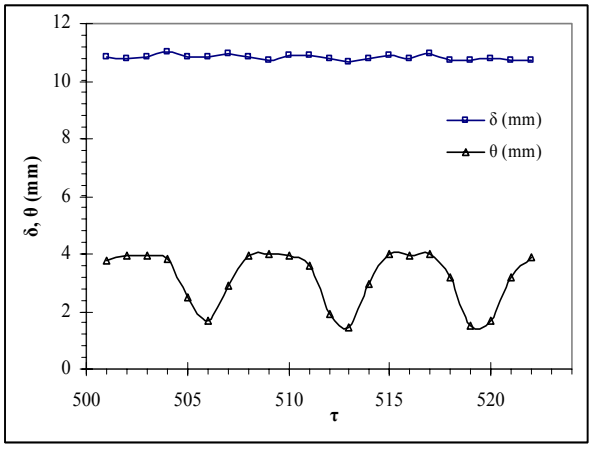

(e)

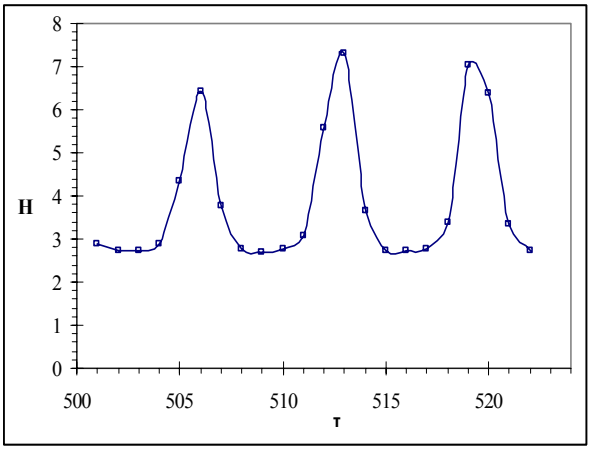

(f)

Figure 5.43 (Continue…)

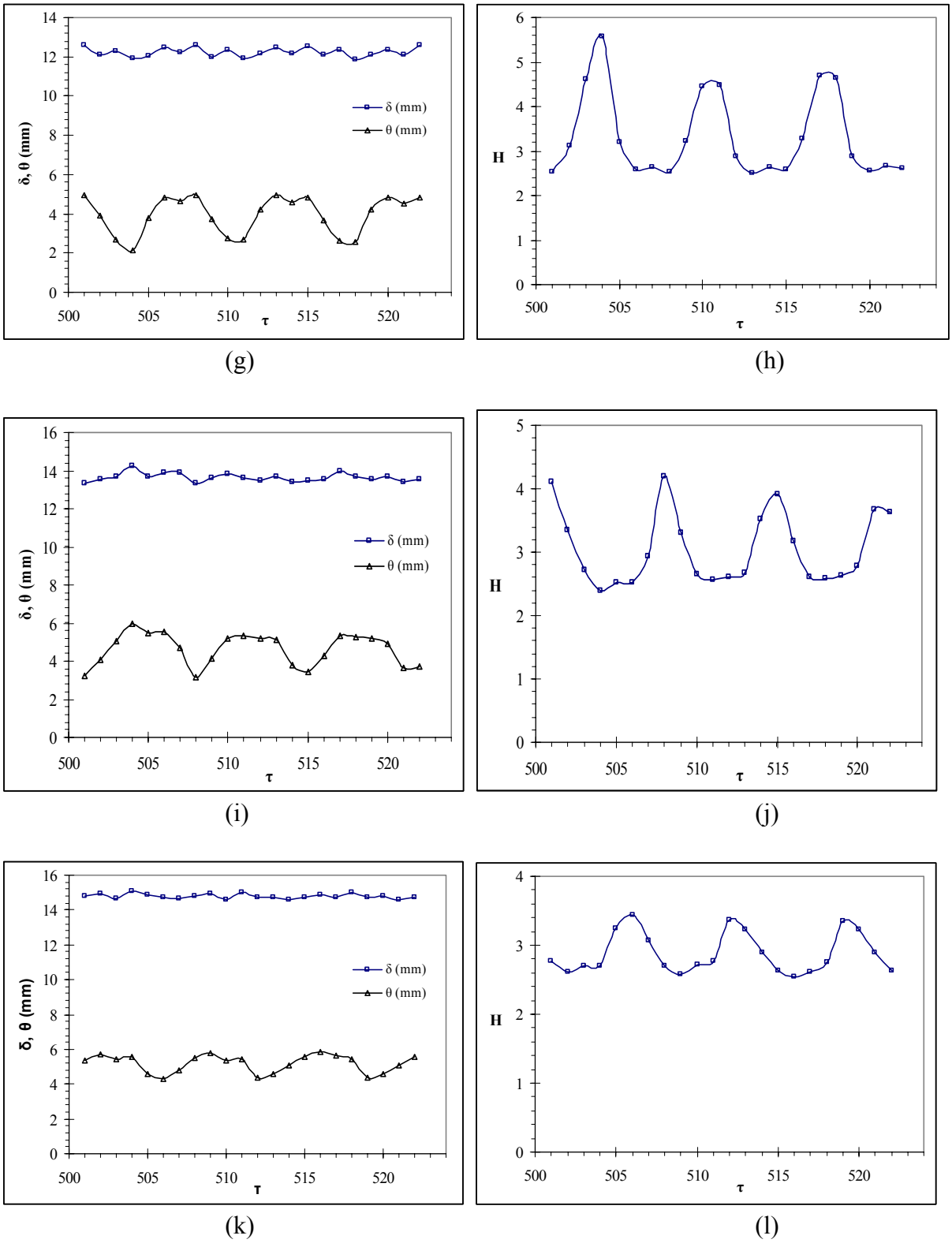

Figure 5.43: Temporal variation of □-displacement thickness (δ), Δ-momentum thickness (θ) and shape factor (H) for Re_{2c} = 800, $x_c/2c$ = 0 $y_c/2c$ = 1, (a,b) Xp =100mm, (c,d) Xp = 200mm, (e,f) Xp =300mm, (g,h) Xp =400mm, (i,j) Xp =500mm, (k,l) Xp =600mm.

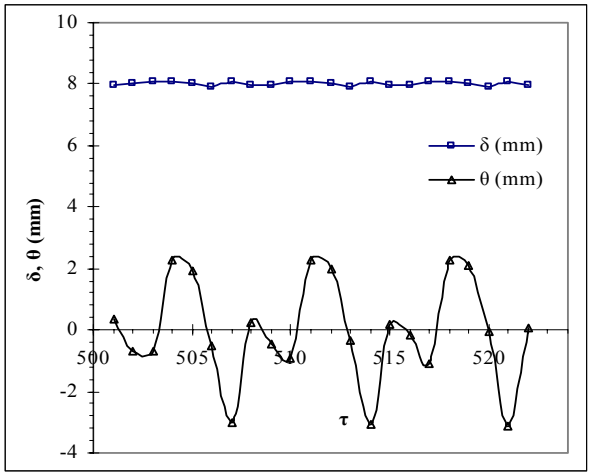

(a)

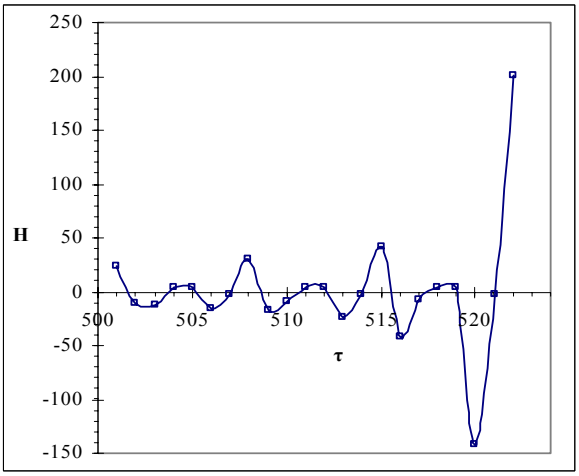

(b)

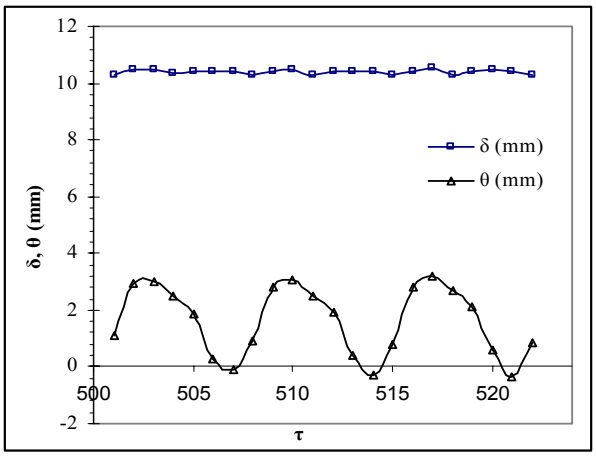

(c)

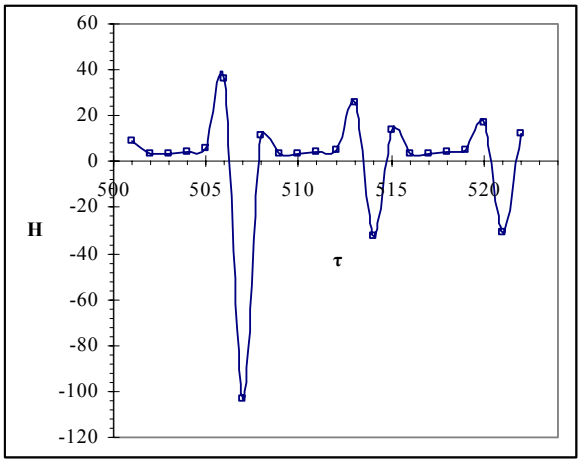

(d)

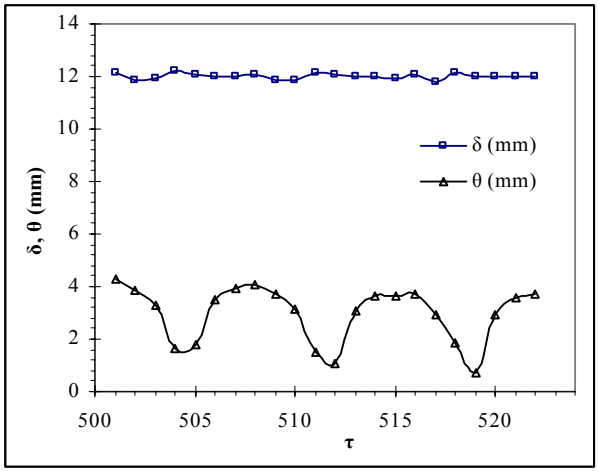

(e)

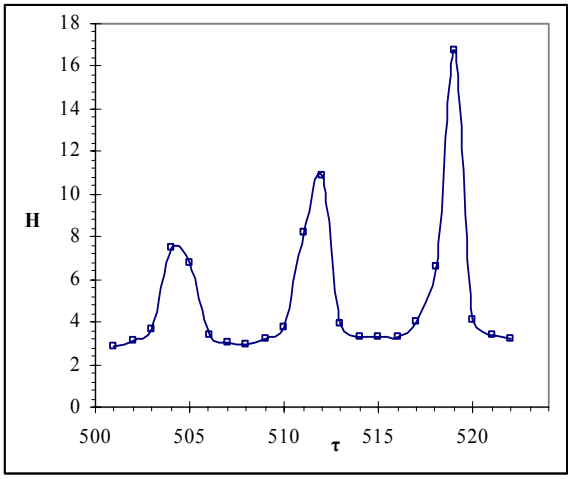

(f)

Figure 5.44 (Continue…)

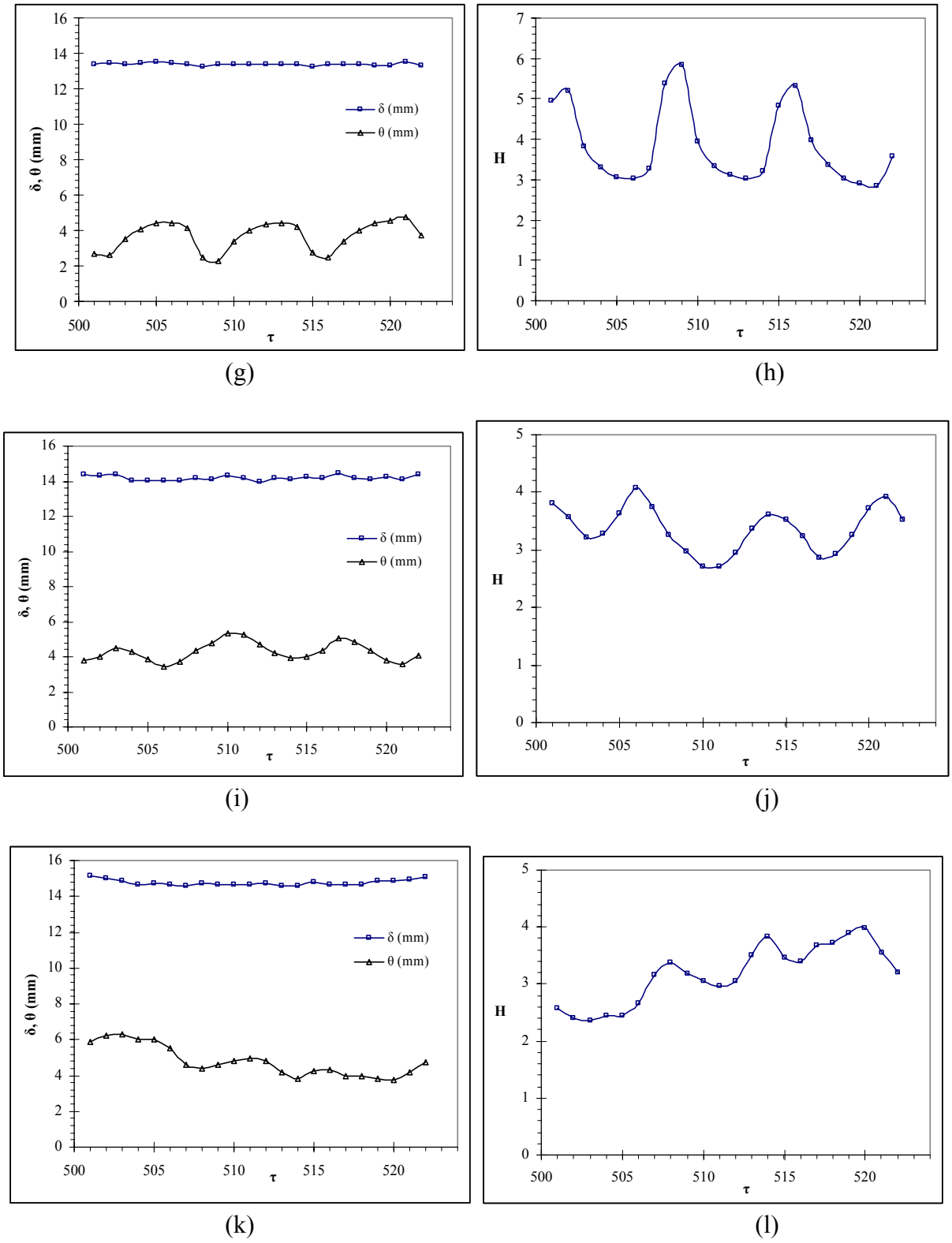

Figure 5.44: Temporal variation of □-displacement thickness (δ), Δ-momentum thickness (θ) and shape factor (H) for Re_{2c} = 800, $x_c/2c$ = 3 $y_c/2c$ = 1, (a,b) Xp =100mm, (c,d) Xp = 200mm, (e,f) Xp =300mm, (g,h) Xp =400mm, (i,j) Xp =500mm, (k,l) Xp =600mm.

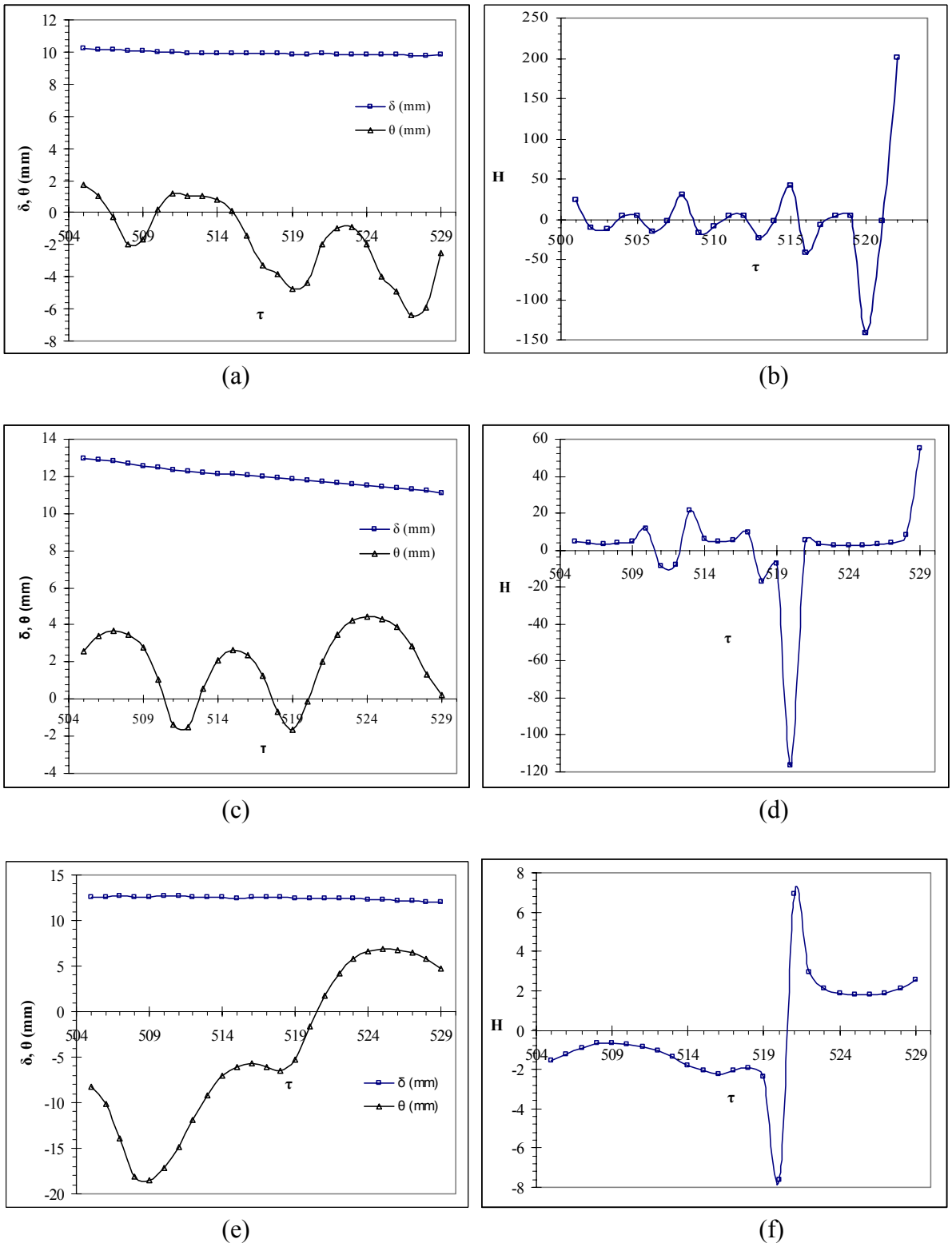

Figure 5.45 (Continue…)

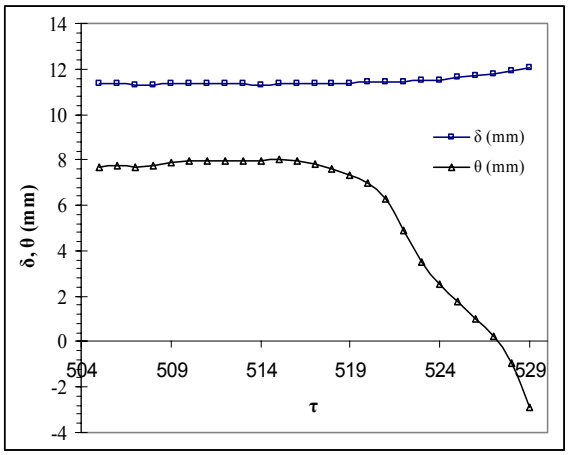

(g)

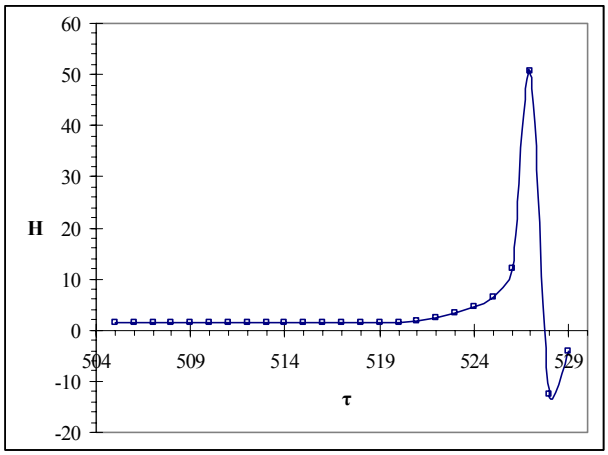

(h)

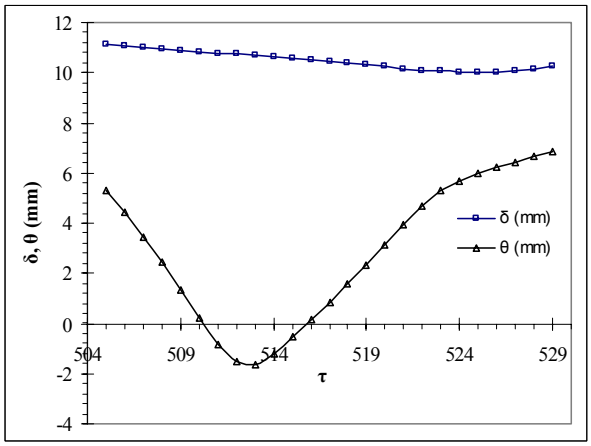

(i)

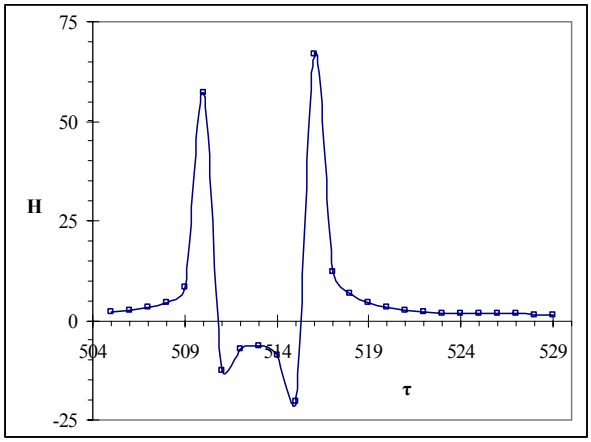

(j)

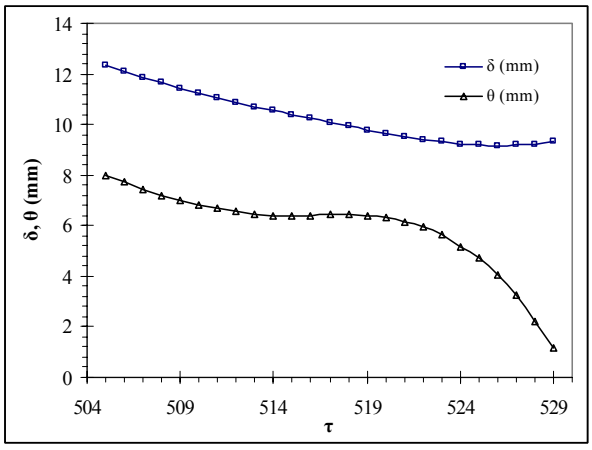

(k)

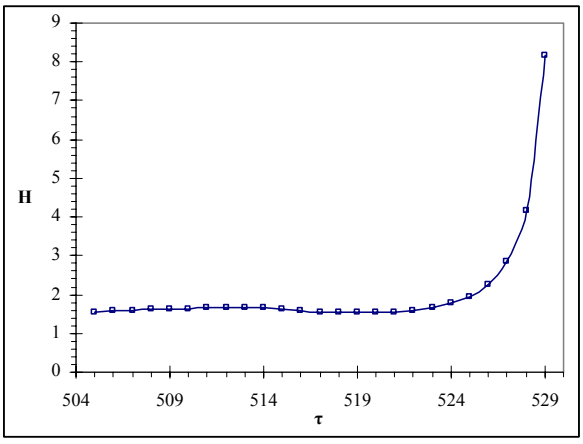

(l)

Figure 5.45: Temporal variation of □-displacement thickness (δ), Δ-momentum thickness (θ) and shape factor (H) for Re_{2c} = 800, $x_c/2c$ = 0 $y_c/2c$ = 0.75, (a,b) Xp =100mm, (c,d) Xp = 200mm, (e,f) Xp =300mm, (g,h) Xp =400mm, (i,j) Xp =500mm, (k,l) Xp =600mm.

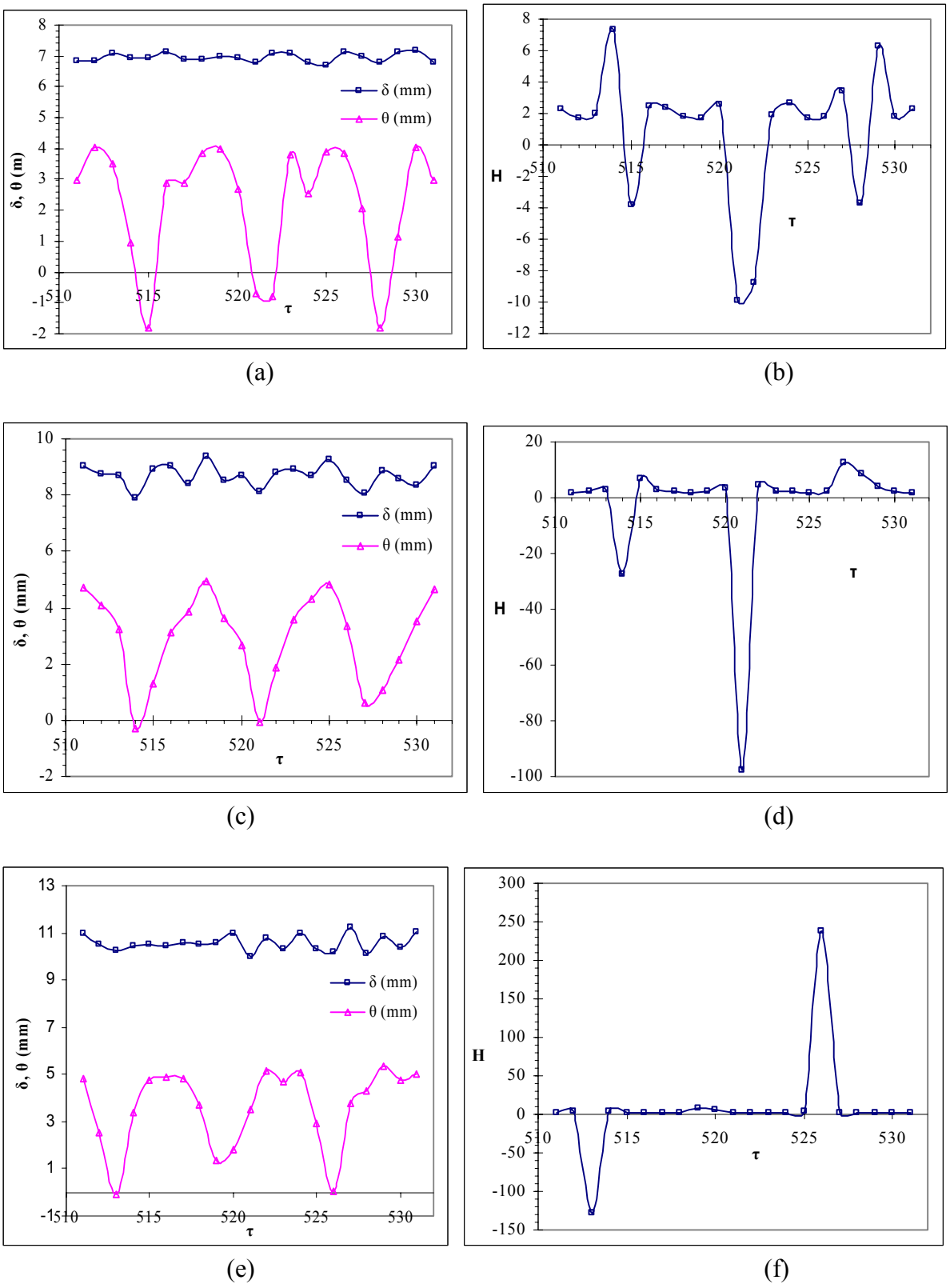

Figure 5.46 (Continue…)

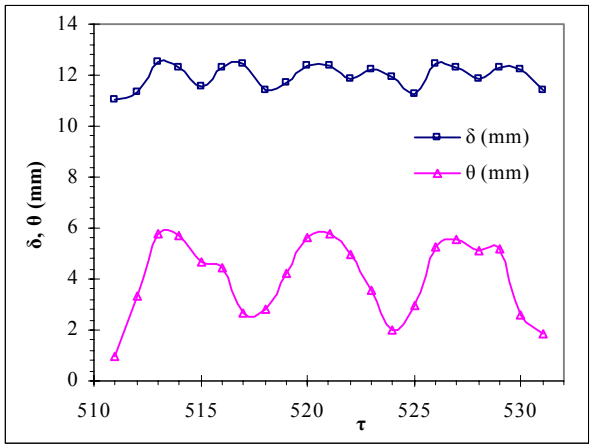

(g)

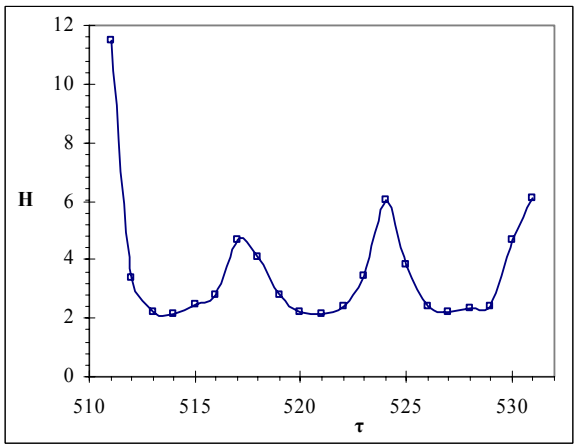

(h)

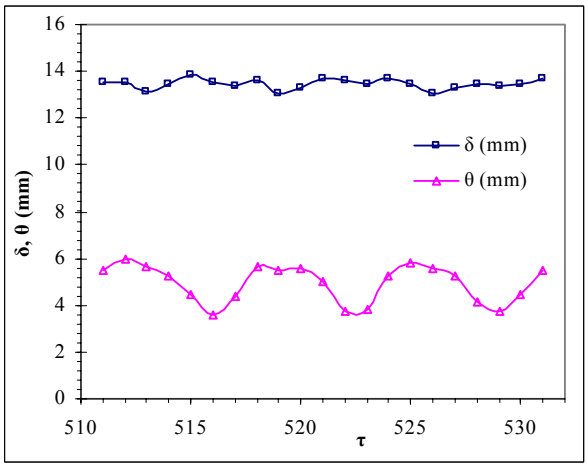

(i)

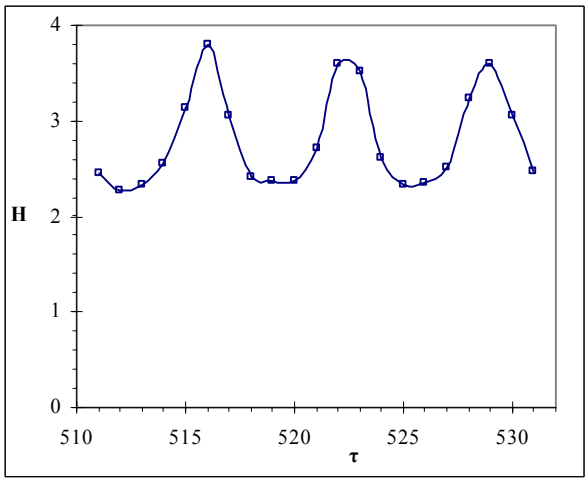

(j)

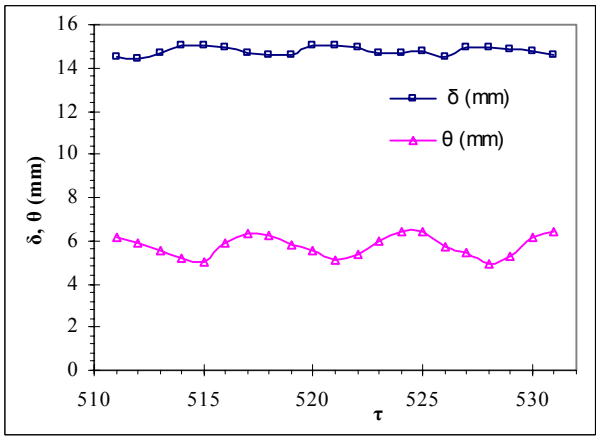

(k)

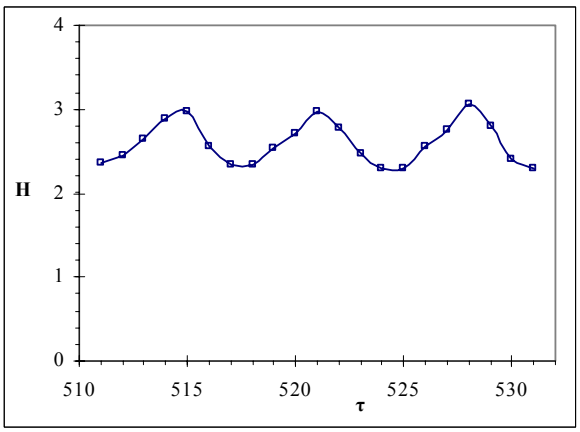

(l)

Figure 5.46: Temporal variation of □-displacement thickness (δ), Δ-momentum thickness (θ) and shape factor (H) for Re_{2c} = 1000, $x_c/2c$ = -3 $y_c/2c$ = 1, (a,b) Xp =100mm, (c,d) Xp = 200mm, (e,f) Xp =300mm, (g,h) Xp =400mm, (i,j) Xp =500mm, (k,l) Xp =600mm.

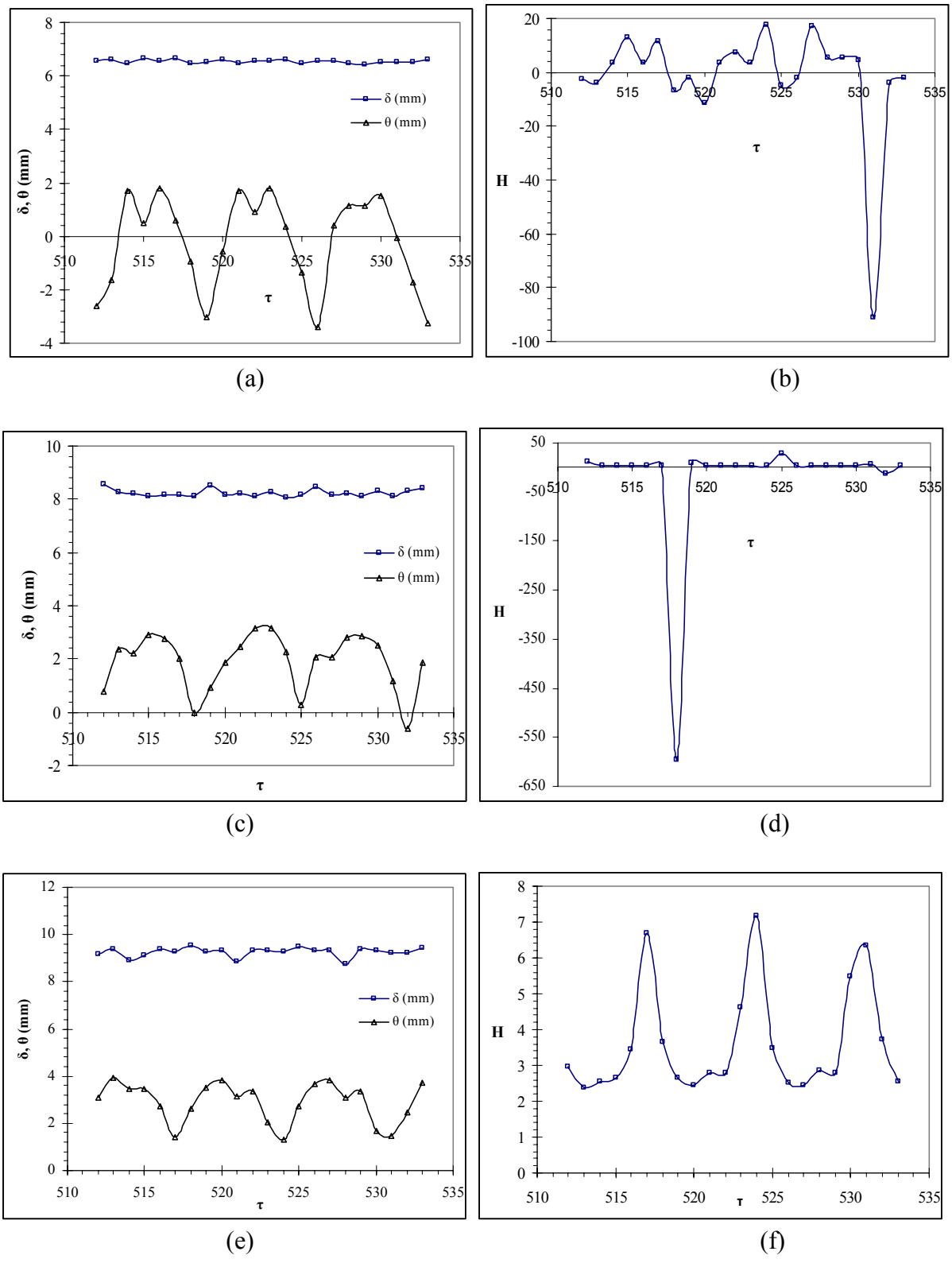

Figure 5.47 (Continue…)

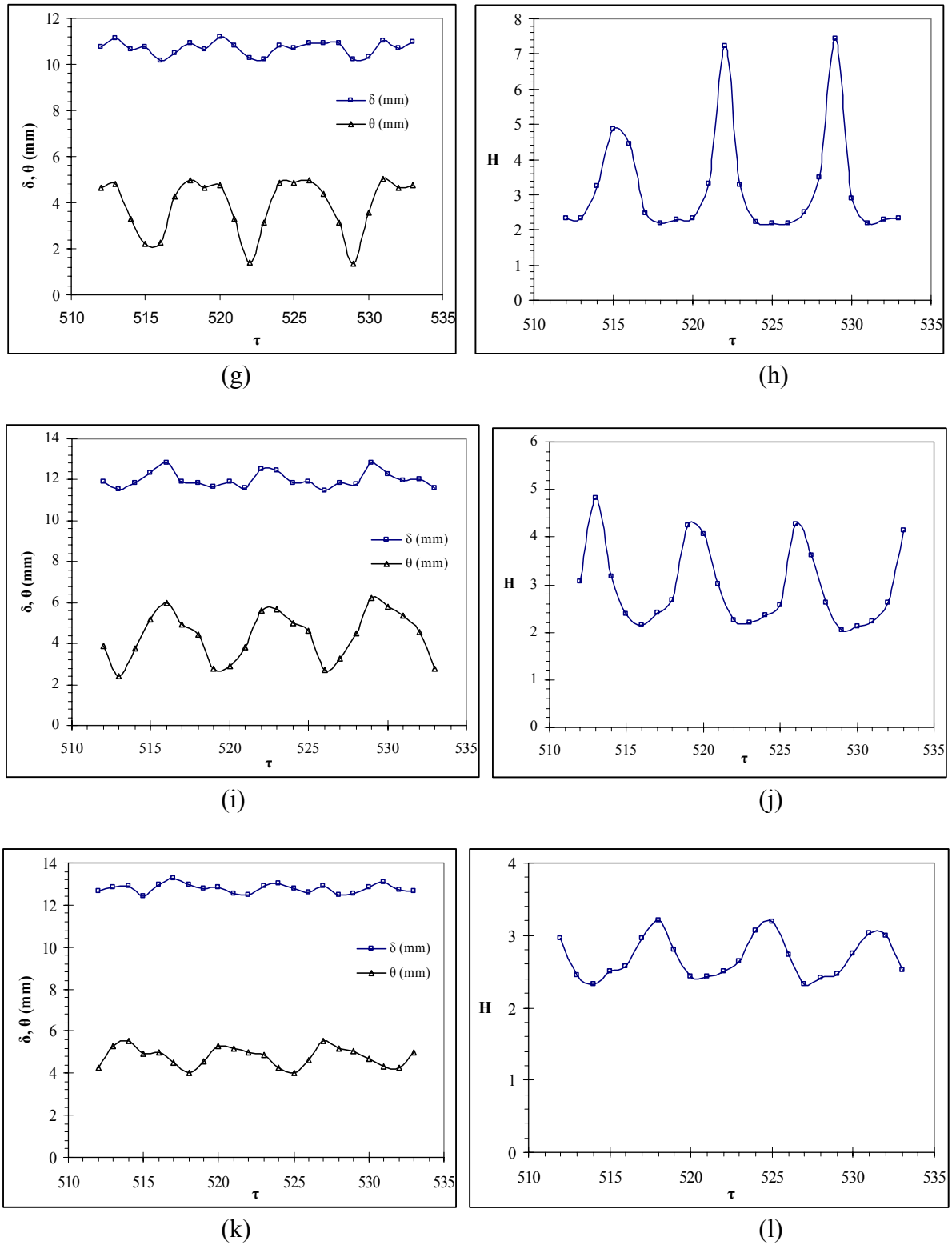

Figure 5.47: Temporal variation of □-displacement thickness (δ), Δ-momentum thickness (θ) and shape factor (H) for Re_{2c} = 1000, $x_c/2c = 0$ $y_c/2c = 1$, (a,b) Xp =100mm, (c,d) Xp = 200mm, (e,f) Xp =300mm, (g,h) Xp =400mm, (i,j) Xp =500mm, (k,l) Xp =600mm.

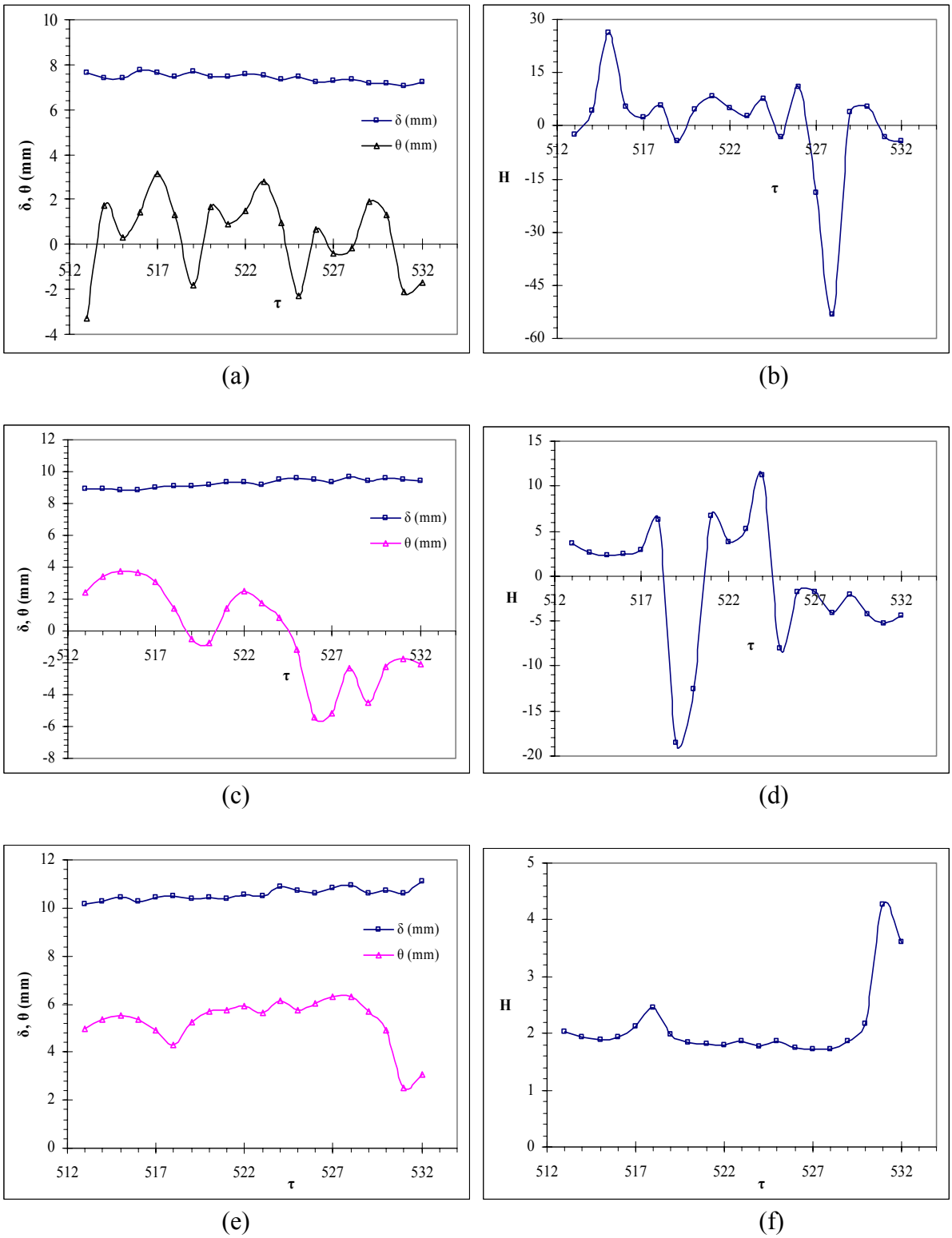

Figure 5.48 (Continue…)

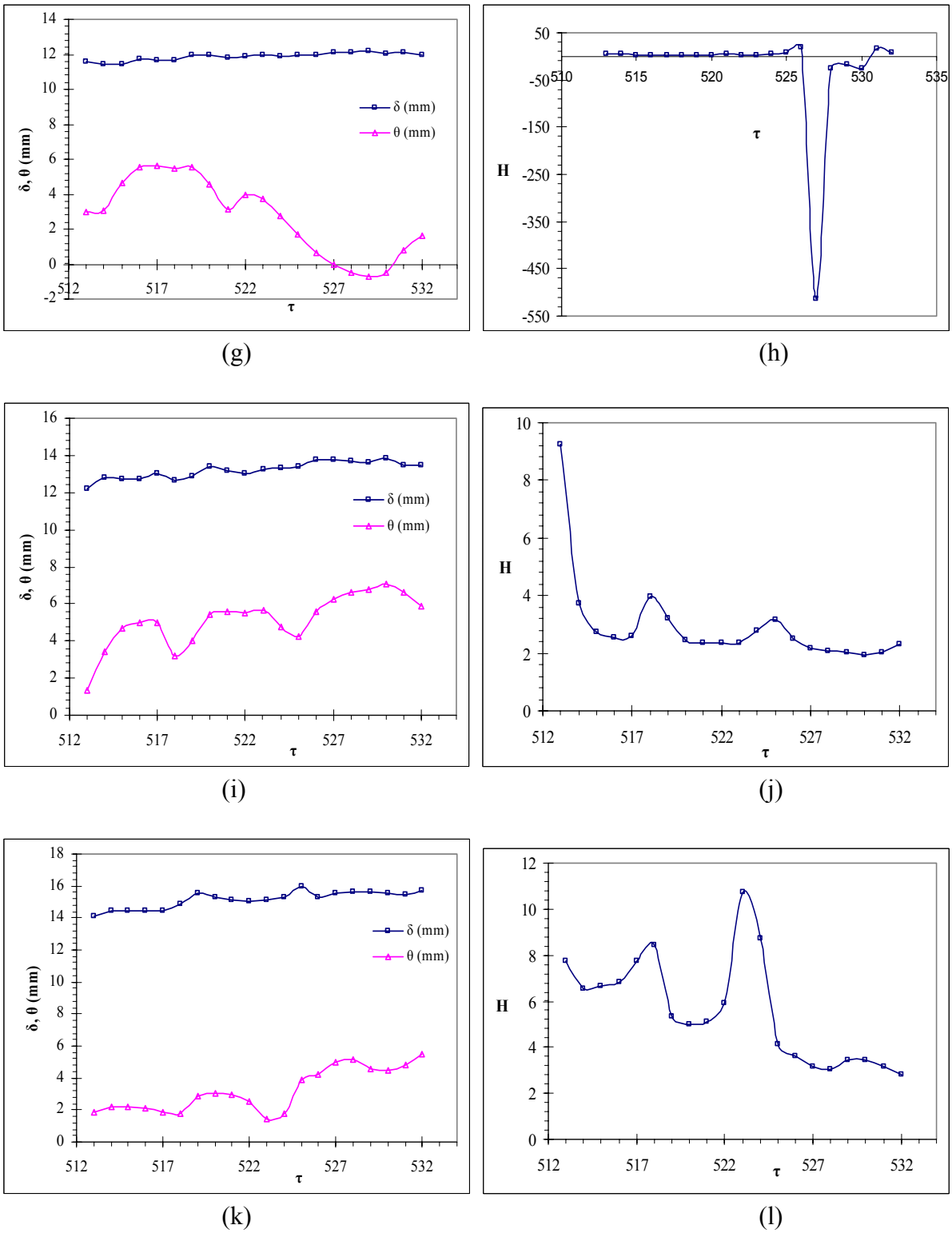

Figure 5.48: Temporal variation of □-displacement thickness (δ), Δ-momentum thickness (θ) and shape factor (H) for Re_{2c} = 1000, $x_c/2c$ = 3 $y_c/2c$ = 1, (a,b) Xp =100mm, (c,d) Xp = 200mm, (e,f) Xp =300mm, (g,h) Xp =400mm, (i,j) Xp =500mm, (k,l) Xp =600mm.

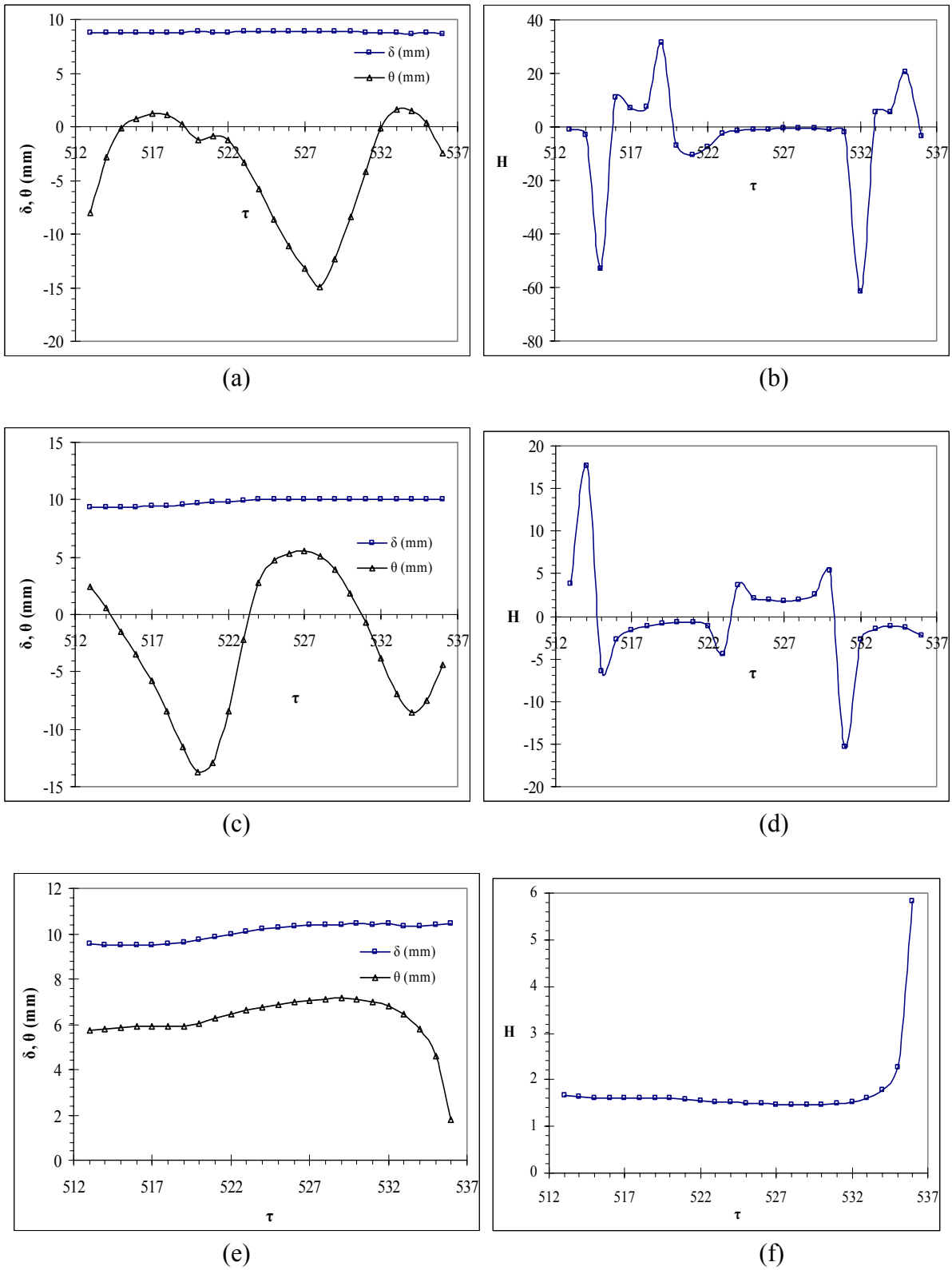

Figure 5.49 (Continue…)

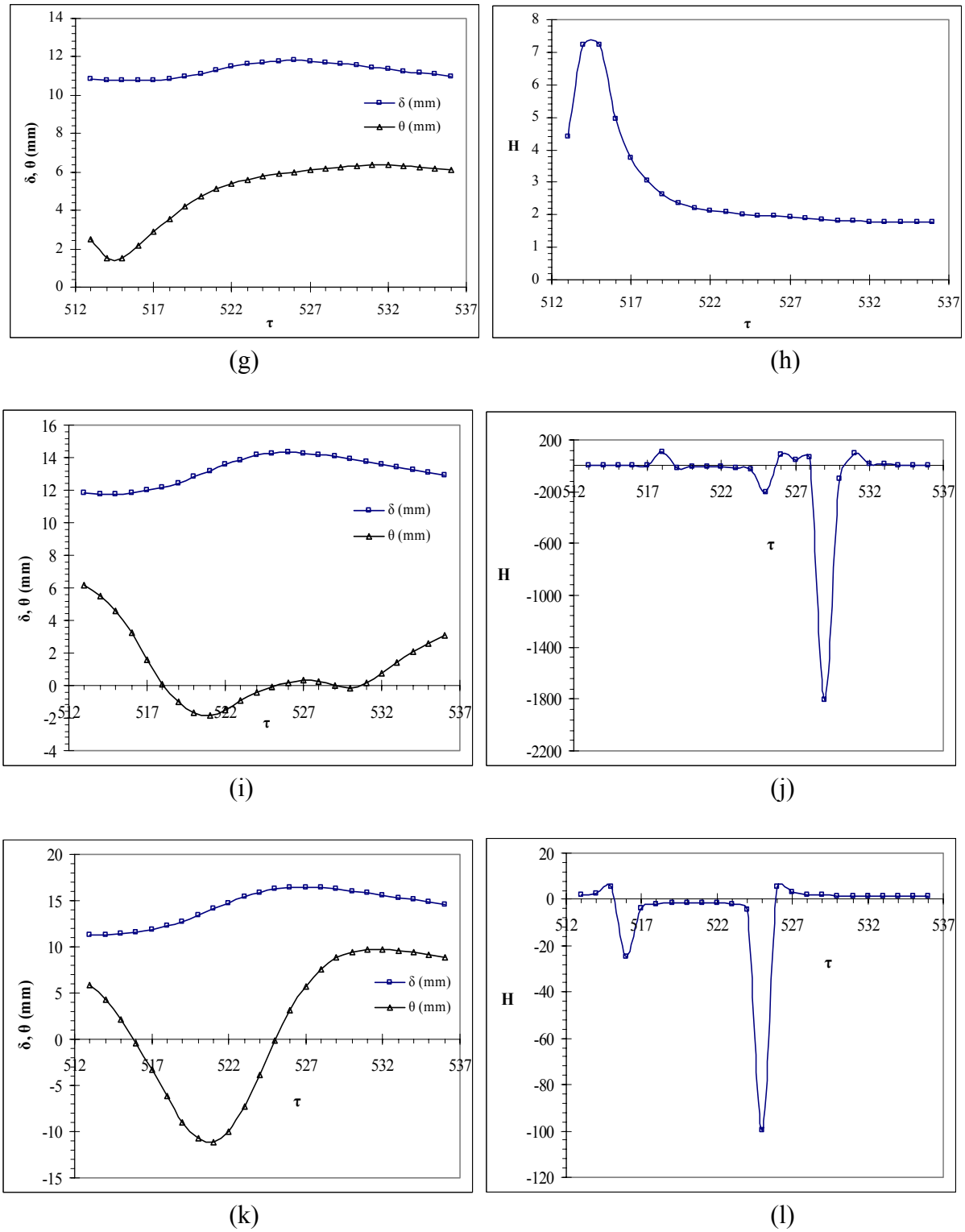

Figure 5.49: Temporal variation of □-displacement thickness (δ), Δ-momentum thickness (θ) and shape factor (H) for Re_{2c} = 1000, $x_c/2c = 0$ $y_c/2c = 0.75$, (a,b) Xp =100mm, (c,d) Xp = 200mm, (e,f) Xp =300mm, (g,h) Xp =400mm, (i,j) Xp =500mm, (k,l) Xp =600mm.

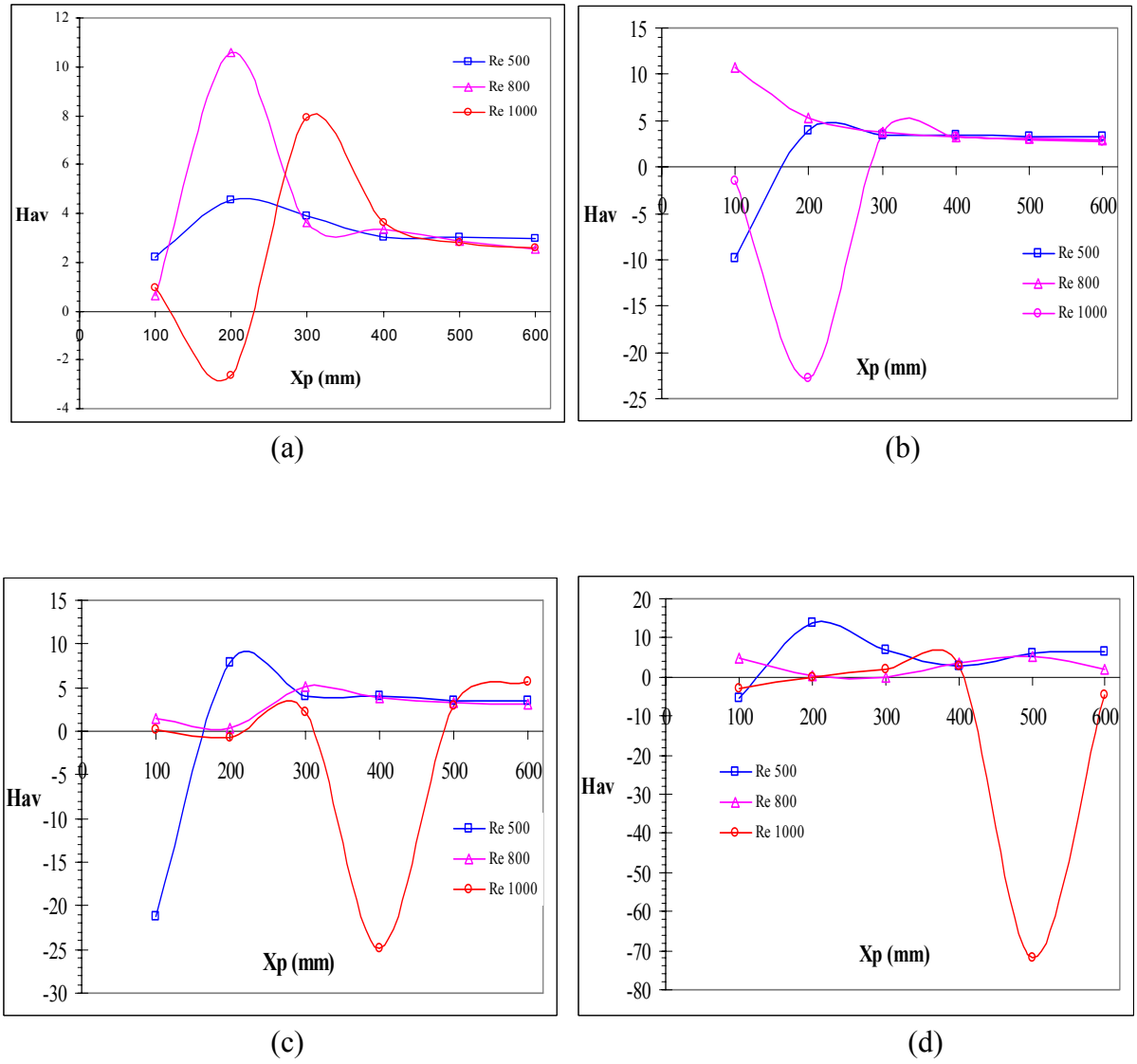

Figure 5.50: Average shape factor (H_{av}) variation with plate stream-wise locations for different Reynolds number for cylinder to plate relative position (a) $x_c/2c = -3$ $y_c/2c = 1$, (b) $x_c/2c = 0$ $y_c/2c = 1$, (c) $x_c/2c = 3$ $y_c/2c = 1$, (d) $x_c/2c = 0$ $y_c/2c = 1$.

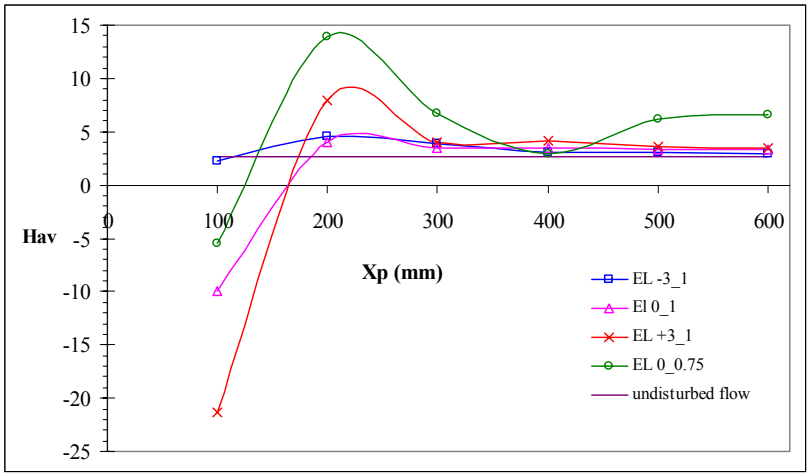

(a)

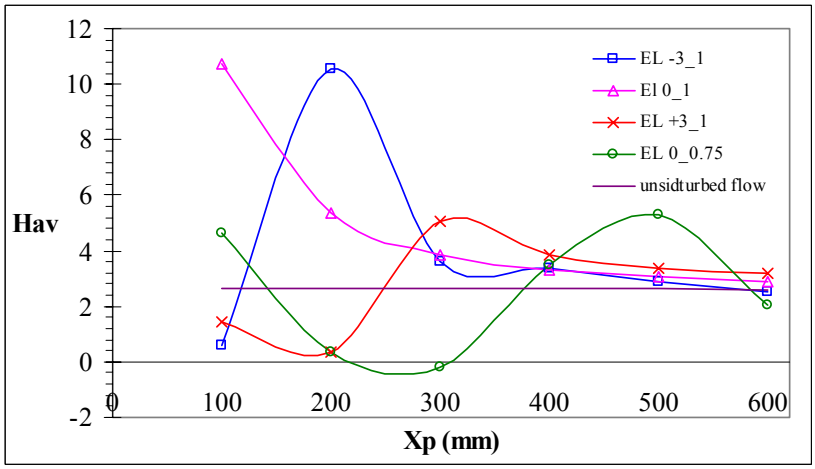

(b)

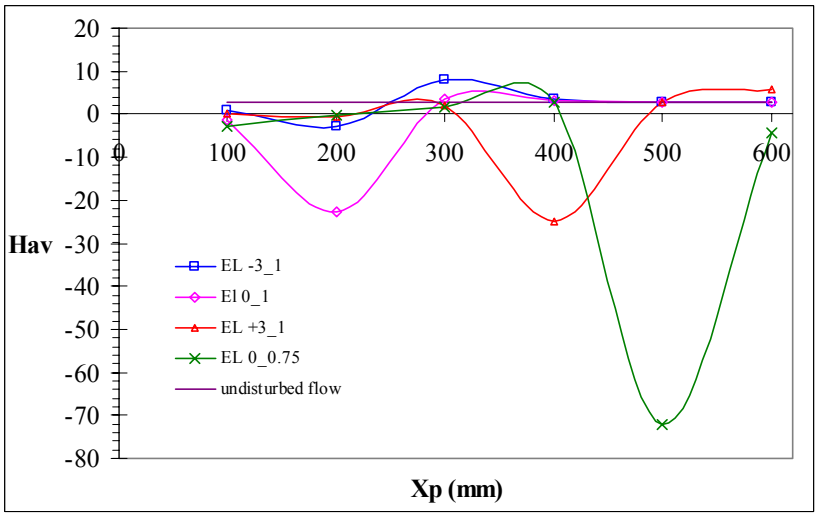

(c)

Figure 5.51: Average shape factor (H_{av}) variation with plate stream-wise locations at different cylinder to plate relative position. for different Reynolds number (a) Re_{2c} = 500, (b) Re_{2c} = 800, .(c) Re_{2c}=1000.

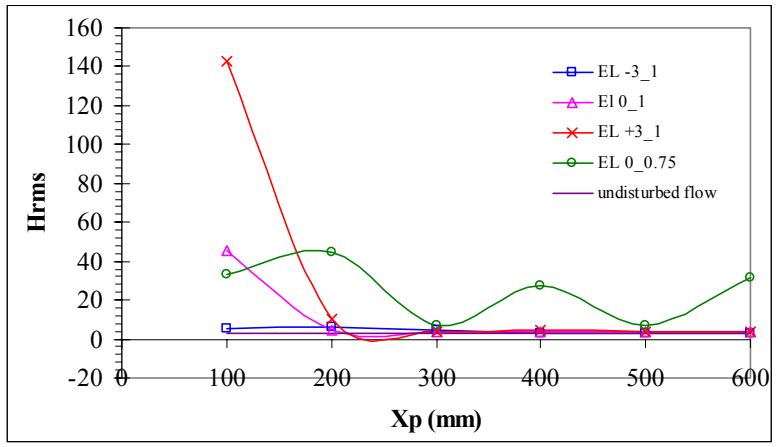

(a)

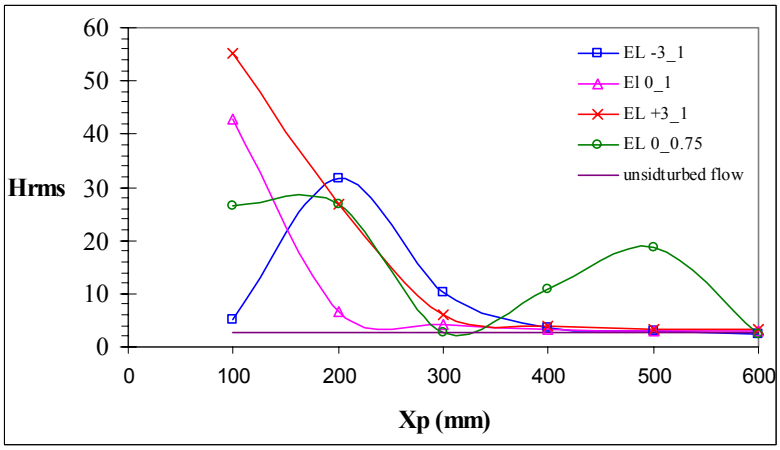

(b)

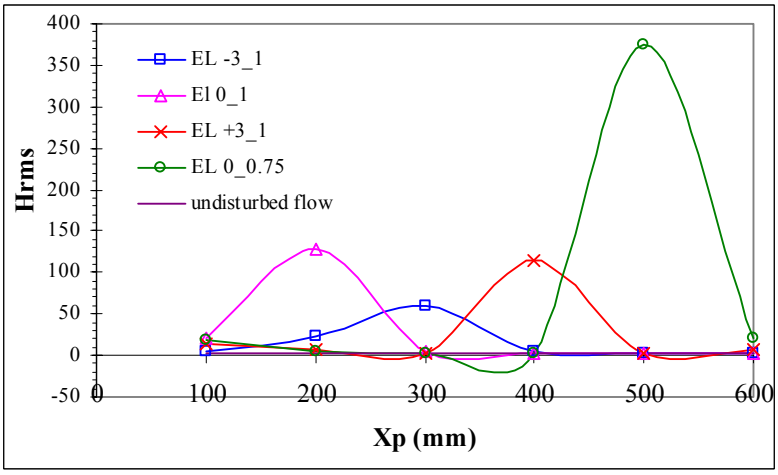

(c)

Figure 5.52: Figure: H_{rms} variation with plate stream-wise locations at different cylinder to plate relative position. for different Reynolds number (a) Re_{2c} = 500, (b) Re_{2c} = 800, .(c) Re_{2c}=1000.

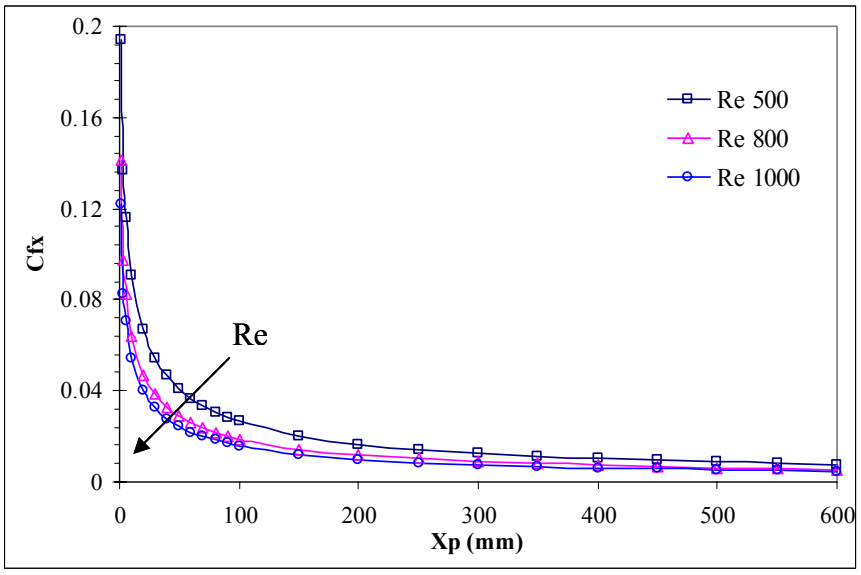

(a)

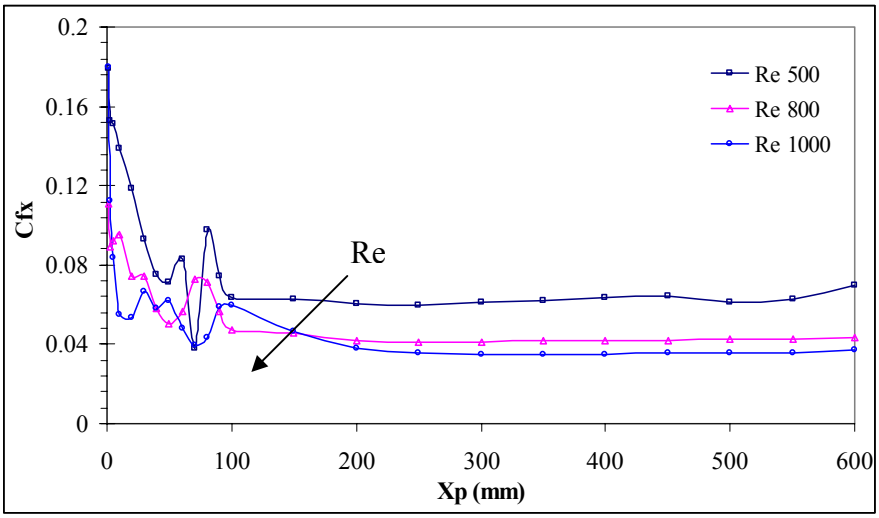

(b)

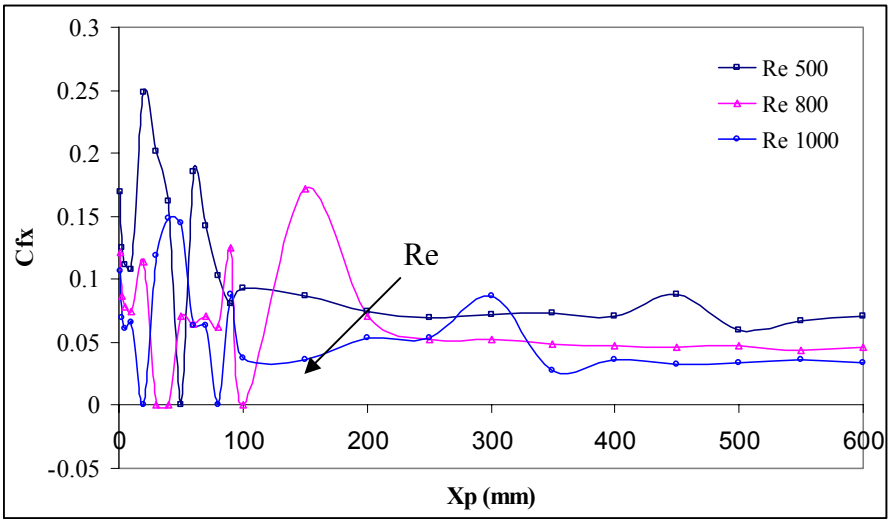

(c)

Figure 5.53 (Continue…)

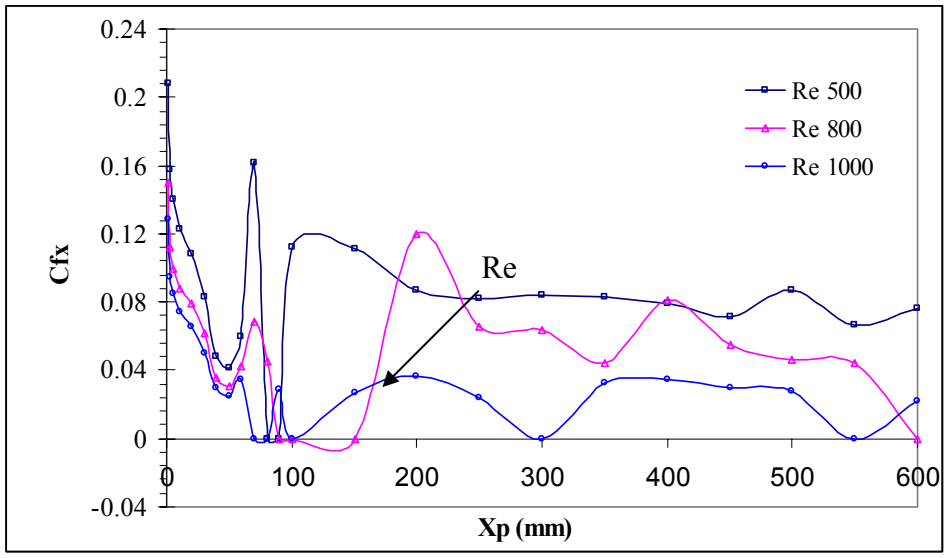

(d)

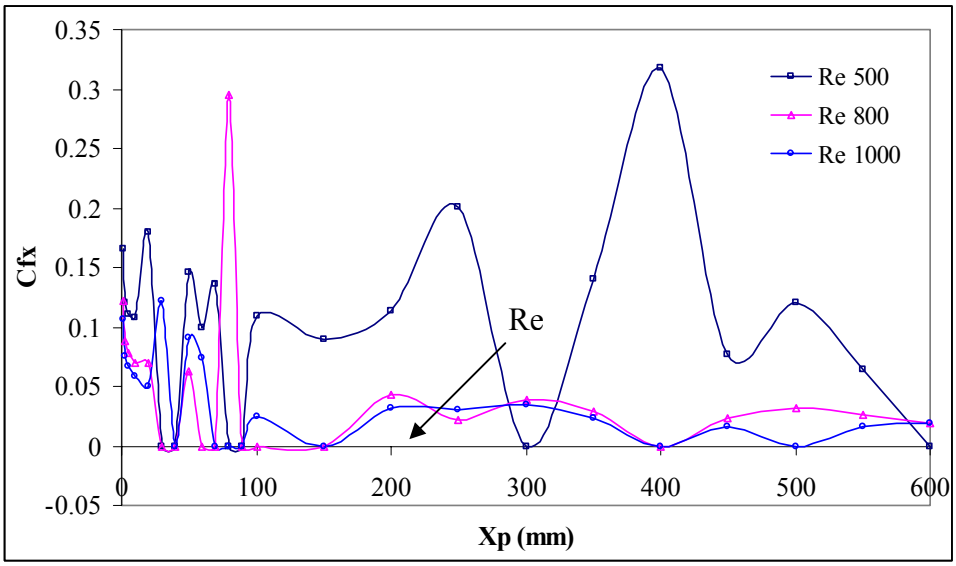

(e)

Figure 5.53: Variation of skin friction coefficient (Cf) with different plate location for $\tau = 500$ □-Re_{2c} 500, Δ-Re_{2c} 800, ○-Re_{2c} 1000, (a) undisturbed flow case and; and also for different elliptic cylinder to plate location, (b) $x_c/2c = -3$ $y_c/2c = 1$, (c) $x_c/2c = 0$ $y_c/2c = 1$, (d) $x_c/2c = 3$ $y_c/2c = 1$, (e) $x_c/2c = 0$ $y_c/2c = 0.75$.

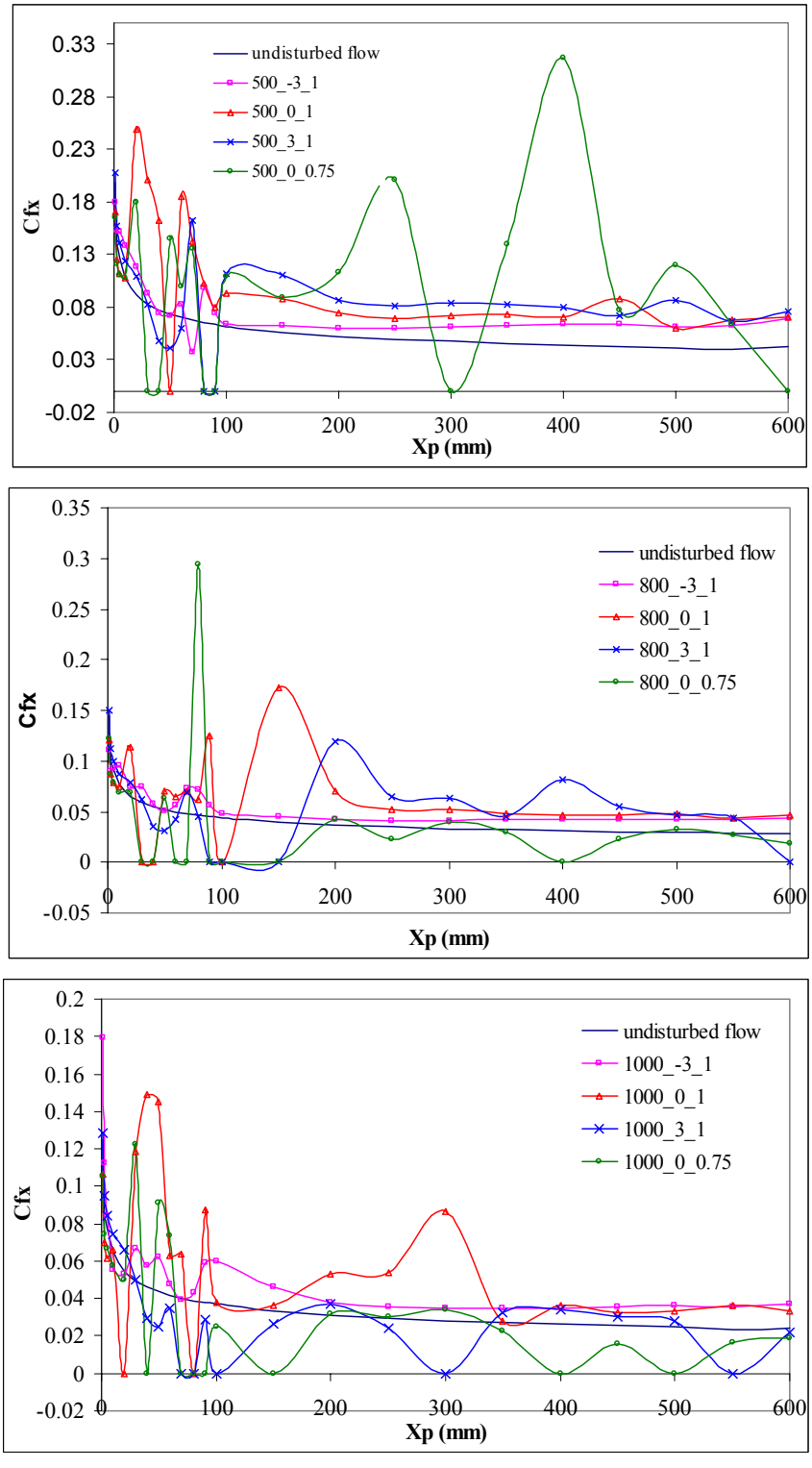

Figure 5.54: Variation of skin friction with different plate axial location for τ = 500, at different elliptic cylinder to plate relative position, for (a) Re_{2c} = 500, (b) Re_{2c} = 800, (c) Re_{2c} = 1000.

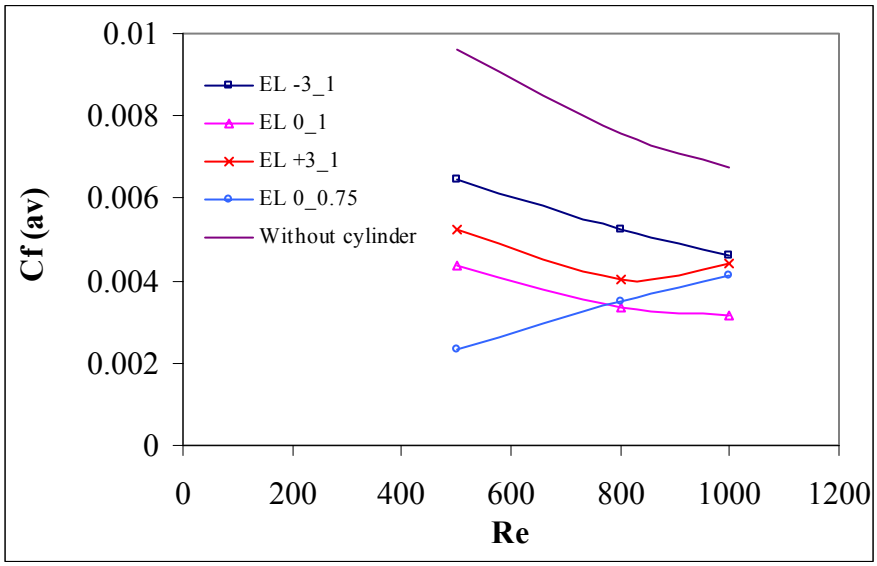

(a)

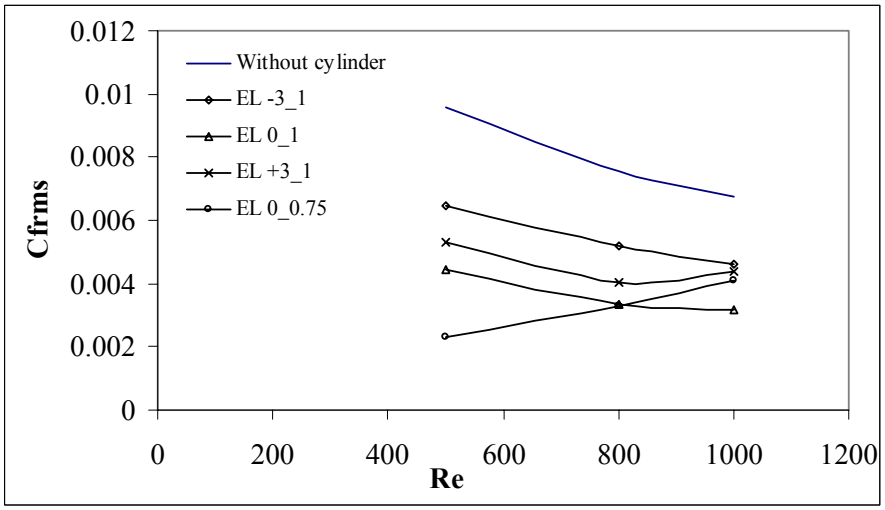

(b)

Figure 5.55: Variation of Cf with respect to Reynolds number at different cylinder to flat plate relative position, (a) for Cf average, and (b) Cf rms.

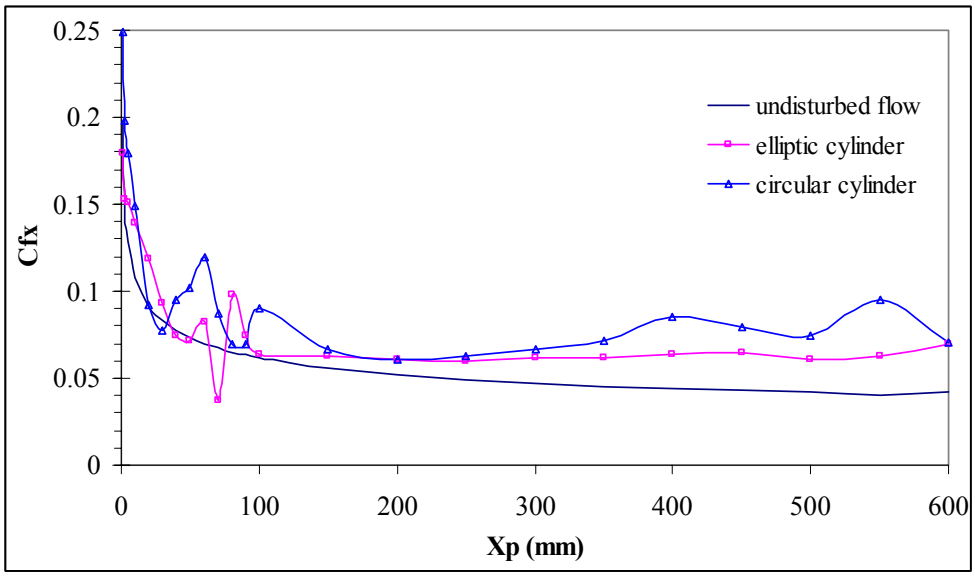

Figure 5.56: Variation of skin friction with the plate axial location for undisturbed flow, disturbed flow with elliptic cylinder and with circular cylinder for τ = 500 Re_{2c}=500 and x_c2c = -3 y_c/2c = 1.